UNIVERSITY OF SOUTHAMPTON

FACULTY OF SCIENCE

DEPARTMENT OF PHYSICS

A POSITION-SENSITIVE DETECTOR FOR HARD X-RAY ASTRONOMY

by

Antony John Bird

A thesis submitted for the degree of

Doctor of Philosophy

November 1990

UNIVERSITY OF SOUTHAMPTON

ABSTRACT

FACULTY OF SCIENCE
PHYSICS

Doctor of Philosophy

A POSITION-SENSITIVE DETECTOR FOR HARD X-RAY ASTRONOMY

by Antony John Bird

Astronomy in the hard X-ray region of the electromagnetic spectrum (20 - 250 keV) provides an essential insight into some of the most energetic processes occurring both in our galaxy and beyond. The current status of hard X-ray astronomy is reviewed, and conclusions concerning the required performance of the next generation of imaging telescopes are reached.

Imaging in this waveband is made difficult by the penetrating nature of the X-ray photons, which makes the use of conventional optics impossible. The techniques applicable to hard X-ray imaging are reviewed, with the emphasis being placed upon modulation imaging in which specially designed apertures are used to modulate the incoming source flux according to the position of the source within the field of view. Hard X-ray detection techniques suitable for use with modulation imagers are reviewed.

The recent development of position-sensitive photomultipliers, which are now available in a variety of configurations, has created a new possibility for the construction of hard X-ray detectors with the spatial resolution necessary to achieve the goal of arc minute imaging with a coded aperture imaging system. One particular type of position-sensitive photomultiplier has been evaluated in conjunction with a thin NaI(Tl) scintillation crystal to examine its potential in a number of X-ray imaging roles. The basic performance of the photomultiplier is assessed, and a method for using such a detector as a hard X-ray imager is developed.

The intrinsic imaging capability of the detector may be relevant in applications where a relatively small detection area is sufficient, but for use in hard X-ray astronomy where the source flux is dominated by the background, a much larger detection area is essential. Methods for constructing large area detectors using position-sensitive photomultipliers are considered, as is the possibility of a position-sensitive phoswich based on the same techniques. Other applications of a compact hard X-ray imaging system are also considered.

For Mum and Dad

ACKNOWLEDGEMENTS

I am greatly indebted to my supervisor, Dr D. Ramsden, for his continual guidance, encouragement and support throughout this work. Also my thanks must go to Dr M. J. Coe and Dr A. J. Dean for their advice and many fruitful discussions.

I would also like to thank the staff of John Caunt Scientific (Ltd), and Mr. John Caunt in particular, for their financial support, advice and technical assistance.

I am also grateful to Dr J. Fleming and the staff of the nuclear medicine department at Southampton General Hospital, and Dr. P. Jackson at Bristol Royal Infirmary, for their assistance and the use of the facilities.

I would like to add a personal thanks to all the members of the High Energy Astrophysics Group at Southampton, both past and present, for their help and advice over the last three years. I believe the following (in no particular order) deserve special mention for their achievements: Kev, Pete, Steve, Laurence, Andy, Terry, Tony G., Andy, Fan, Nan, Zhong and last but not least, Pino.

Finally, I would like to thank the following:

- Dr P. Lanchester for the use of departmental facilities.
- The Science & Engineering Research Council for the award of a CASE research studentship.
- I acknowledge the support provided by the Starlink Project which is funded by the UK SERC.

PREFACE

The author of this thesis was responsible for the assembly and characterisation of the position-sensitive photomultiplier imaging system. He also developed the hardware and software required for the acquisition and analysis of the data obtained from the imager. The work on light guides and position sensitive phoswich detectors described in Chapter 7 was carried out in conjunction with Mr He Zhong, a British Council funded visitor from IHEP, Beijing.

Contents

List of Figures

Chapter 1

INTRODUCTION

Modern astronomy makes use of almost every part of the electromagnetic spectrum from radio waves to gamma rays. The optical waveband was, of course, the first to be exploited by astronomers, followed by radio in the 1930s, and a rapid expansion into the infrared and ultraviolet regions in the 1960s.

After the discovery of X-rays by Röentgen in 1895, it was another 68 years before the detection of a cosmic X-ray source. A group led by Riccardo Giacconi launched a rocket-borne X-ray detector looking for lunar fluorescence, but instead discovered what became known as Scorpius X-1. The subsequent discovery of a second source of cosmic X-rays, Taurus X-1 (the Crab Nebula), led to a number of rocket-borne and balloon-borne observations, which by 1970 had discovered ~20 sources.

The belated discovery of cosmic X-rays can be attributed to several factors. Firstly, the attenuation of the atmosphere in the X-ray region is such that no photons of cosmic origin could ever reach a ground-based detector. Thus the discovery had to wait until rocket-borne, and later, balloon-borne and satellite detectors were a practical proposition. Secondly, the fluxes of X-rays from cosmic sources are very small, such that they are easily lost in background noise, making careful instrument design essential. Finally, the process of detecting an X-ray is not a simple one, due to the penetrating nature of the photon and its interactions with other material.

Today, X-ray astronomy has progressed to the stage that modern instruments, both

balloon-borne and on satellites, are now capable of producing high resolution images with a level of sensitivity which enables thousands of sources to be observed during a reasonable mission lifetime.

This thesis describes work carried out in the development of a detector suitable for imaging observations in the broad energy band from 15 keV - 250 keV, which is commonly referred to as the hard X-ray region.

In **Chapter 2**, a brief review of the current status of observational hard X-ray astronomy will be presented. Following an introduction to the processes believed to give rise to cosmic X-ray emission, the most important classes of galactic and extragalactic sources will be described. The chapter will end with a summary of the observational capabilities required in order to continue the progress currently being made in this field and solve some of the many puzzles which still exist in X-ray astronomy.

Chapter 3 will review the techniques currently used in order to produce hard X-ray images. Since the photons are too energetic to be focussed by normal refracting optics, other methods must be found. The specific requirements of each imaging system in terms of X-ray detectors will be discussed.

In **Chapter 4** the various hard X-ray detectors currently in use will be reviewed. This will include gas detectors, scintillation counters and semiconductor materials, all of which can be used to detect the passage of an X-ray. Particular attention will be given to position sensitive detectors which can locate the point of interaction of an X-ray, a property which is essential in some imaging systems.

Chapter 5 will outline the tests carried out on a small area position sensitive hard X-ray detector based on a position sensitive photomultiplier. The basic characteristics of the detector, that is, energy resolution, response uniformity, spatial resolution and spatial linearity will be evaluated, and their implications discussed.

The testing of this particular detector will be further documented in **Chapter 6** which will concentrate on demonstrating the intrinsic imaging capability of the device. A procedure for enhancing the basic performance of the imager will be developed, and images of both point and extended sources, obtained using a variety of imaging techniques

will be presented.

Chapter 7 will consider the possibilities for making the large area detectors necessary for X-ray astronomy using these relatively small devices. Various techniques, including the construction of a large array of detectors using thick crystals or light guides to overcome the inherent small sensitive area of the photomultipliers, will be discussed. A natural extension to this approach, a position-sensitive phoswich detector, will also be considered.

Taking a contrasting view, **Chapter 8** will focus on some of the possible applications of a small area detector based on a single position sensitive photomultiplier, not necessarily in the field of X-ray astronomy. These include a hard X-ray imager for auroral observations, a compact gamma camera for nuclear medicine, and a variety of industrial applications.

Chapter 2

A REVIEW OF X-RAY ASTRONOMY

2.1 Introduction

Since the discovery, from a rocket-borne X-ray detector in 1962, of an X-ray source in Scorpius, the measurement of X-ray emission from galactic and extragalactic objects has become an essential astrophysical tool.

Astrophysical high energy photon emission is generally grouped into three somewhat arbitrary bands: the soft X-ray band covers photons with energies between 0.1 and 15 keV; the hard X-ray band extends from 15 to 250 keV, and finally, at even higher energies still is the gamma-ray band.

The penetrating nature of hard X-rays and gamma-rays means that they are an excellent probe of the interior of emitting regions, whereas lower energy photons (e.g. optical, infrared) are generally the result of reprocessing of these energetic photons by the intervening material. As such, X-ray observations are essential for the understanding of the fundamental processes giving rise to the observed emission.

In addition, it is now known that a large number of objects emit a large fraction of their energy in the X-ray and gamma-ray regions, such that X-ray observations are the

primary source of information on their character.

Our current knowledge of hard X-ray astronomy is limited to results from a few instruments which have operated in the energy band, with the bulk of observations to date having been made in the softer region of the X-ray spectrum. At these lower energies, many telescopes, for example, the EINSTEIN observatory (launched 1978), EXOSAT (1983, see Figure 2.1), Spacelab 2 (1985) and Ginga (1987), have all supplied excellent data. However the use of gas proportional counter detectors in these instruments meant that they had little or no sensitivity above ~30 keV.

The HEAO-1 satellite carried two instruments (A2 and A4) operating in the hard X-ray band. The A4 instrument completed the first survey of the galactic plane in the energy range 13-180 keV during the period Aug 77 - Jan 79. The map of X-ray emission generated by the HEAO-1 survey is shown in Figure 2.2. The hard X-ray catalogue produced contained ~70 sources, 14 of which were detected at energies $\geq$ 80 keV [93].

Two hard X-ray telescopes are currently in orbit:

The HEXE instrument which is part of the KVANT observatory on the MIR spacecraft, operates in the range 15 – 250 keV, with a 1.6° collimated field of view.

The recently launched SIGMA telescope on the GRANAT spacecraft [39] is designed to operate in the 30 keV – 2 MeV band with an angular resolution of 13′ and a point source location accuracy of 1′40″. This instrument is certain to provide a wealth of hard X-ray data, which should become available over the next few years.

It is hoped that these will provide large numbers of hard X-ray observations with a sensitivity and angular resolution far in excess of that previously achieved.

Much valuable additional data has been provided by a number of balloon-borne experiments. For example, the MIFRASO payload [14] has yielded observations of 9 sources during 2 flights, and the Caltech GRIP telescope [6] has provided high-resolution images of many source regions, with particular emphasis being placed on the observation of supernova 1987A.

This chapter will first briefly discuss the ways in which hard X-rays may be produced in

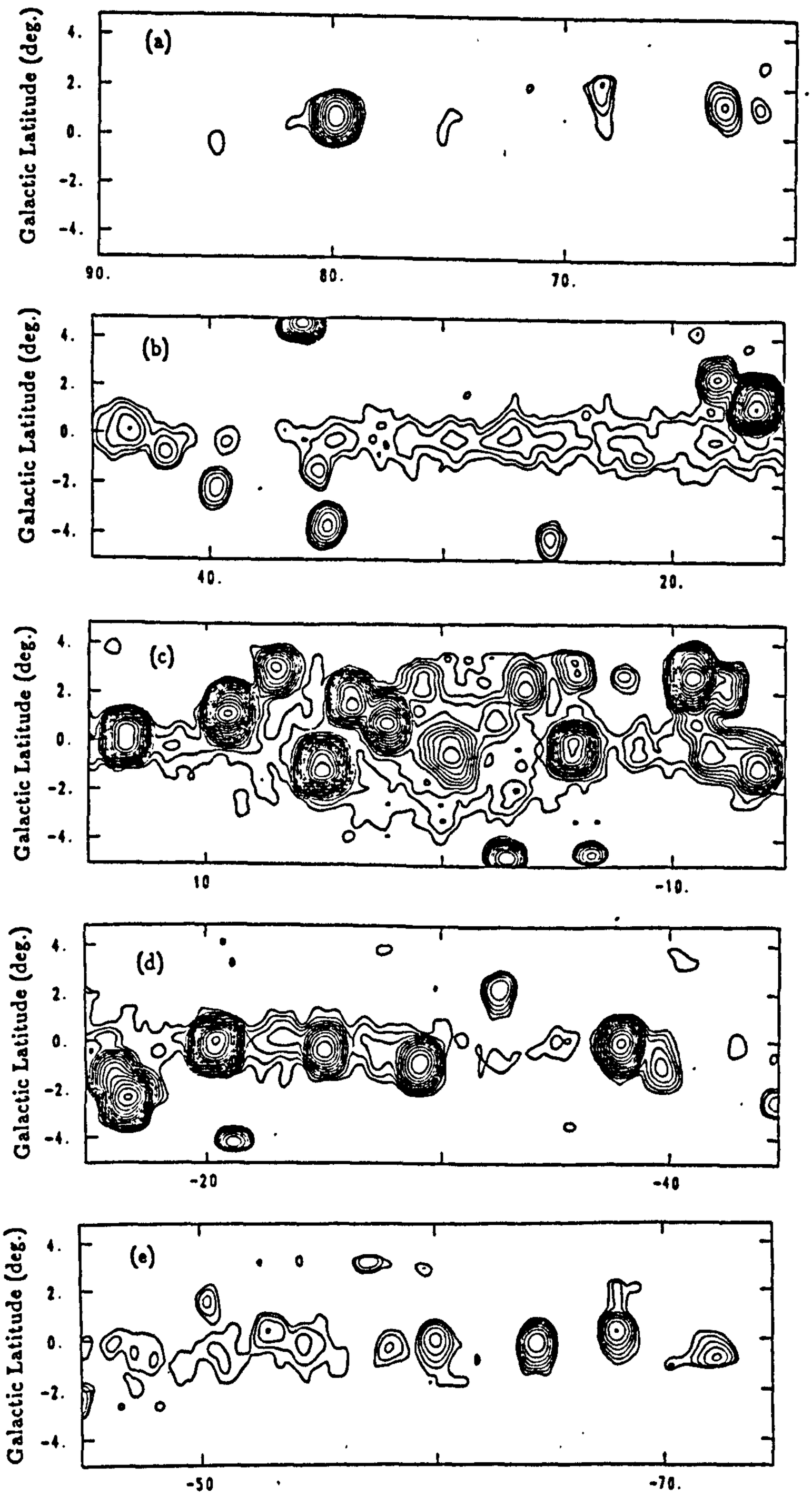

Figure 2.1: *The EXOSAT survey of soft X-ray emission in the region of the galactic centre (from [144])*

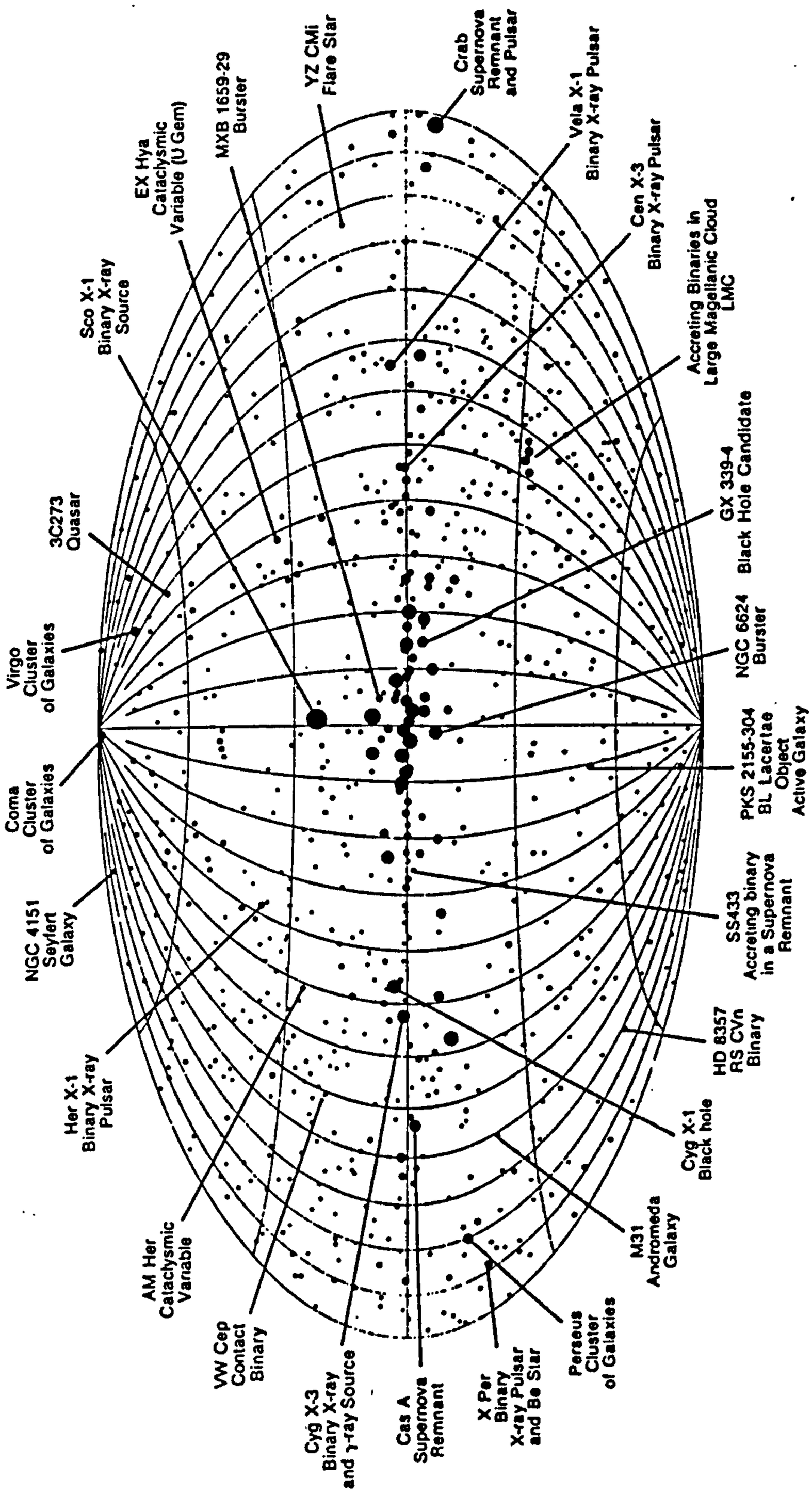

Figure 2.2: *The HEAO1 survey of X-ray emission*

an astrophysical environment, and following this, a review of galactic and extragalactic hard X-ray emitting objects will be presented, along with some of the results obtained so far.

At the end of this chapter, an attempt will be made to identify the requirements for future X-ray telescopes which will follow up the observations made with the current generation of telescopes.

2.2 Emission Mechanisms

The precise mechanisms which can give rise to hard X-ray emission have been described in great detail in many places (see, for example, [70,137]), and so only a brief description will be included here.

The large amounts of energy required to give hard X-ray emission are thought to come from two sources: regions of very hot gases, and the accretion of matter onto a compact object. In the latter case, the energy released when the infalling material is brought to a halt is very great.

In hot gas regions, hard X-rays may come from thermal emission mechanisms:

Blackbody Emission – If the emitting region is optically thick, then the initial emission will be reprocessed to give a blackbody spectrum. Wiens displacement law states that $E_{PEAK} = 4 \times 10^{-7} T$ keV, and thus temperatures $T > 10^8$ K are necessary for hard X-ray emission by this mechanism.

Thermal bremsstrahlung – If the region is optically thin, thermal bremsstrahlung from the acceleration of electrons in the Coulomb fields of other electrons and protons may be emitted, giving rise to an exponential emission spectrum. Temperatures $> 10^7$ K, slightly less than in the case of blackbody emission, are required for hard X-rays to be produced in this way.

Alternatively, various non-thermal mechanisms can give rise to X-ray emission:

Synchrotron radiation – Charged particles in the presence of a magnetic field will circle around the field lines, and therefore undergo an acceleration, emitting radiation. This is known as cyclotron radiation or magneto-bremsstrahlung. If the charged particles (principally electrons) are highly relativistic, then the radiation produced is known as synchrotron radiation. This type of emission is characterised by a power-law spectrum.

Inverse Compton Scattering – If a relativistic electron collides with a low energy photon (eg starlight, microwave background), it can considerably increase the photon energy. Hard X-ray generation by this method requires less energetic electrons than in the synchrotron radiation process. In a process known as Synchrotron Self Compton (SSC), the electrons giving rise to synchrotron emission in the radio/optical region may also be responsible for inverse compton scattering of that emission. The presence of power-law emission in both the radio/optical region and the hard X-ray band is indicative of this process.

2.3 Galactic X-ray sources

The X-ray surveys completed to date have indicated a wide variety of X-ray emitting objects within our own Galaxy on both point and extended scales. Galactic X-ray sources can be divided into several broad groups:

- X-ray binaries - Binary systems which contain a compact object exhibit a wide range of properties, but almost all show some form of X-ray emission.
- The Galactic Centre - this is an extremely complex region in which both point and diffuse X-ray and gamma-ray emitters have been observed.
- Supernova Remnants - many of these are extended sources of X-ray emission. Additionally, supernova 1987A has led to considerable study of the early stages after a supernova explosion, when the high energy emission is largely dominated by radioactive decay.
- Other sources - such as SS433 and Geminga which exhibit X-ray emission but do not, at present, seem to fall into any particular classification.

2.3.1 X-ray binaries

The Galactic plane contains a large number of point X-ray sources as may be judged from inspection of the EINSTEIN and EXOSAT surveys [72,144] (the EXOSAT skymap is shown in Figure 2.1).

The vast majority of these point sources are believed to be X-ray binary systems [148]. These are defined as neutron stars or stellar mass black holes accreting material from a binary companion star. The energy source is the conversion of the gravitational potential of the matter into radiative emission, which for an accretion disk around a neutron star or a black hole occurs at an efficiency of ~10%, a factor of 10 higher than nuclear fusion. Well over one hundred X-ray binaries have now been discovered in the past 25 years from a large number of X-ray observatories.

The various possible configurations of X-ray binary systems are summarised in Table 2.3.1.

Companion star \ Compact object		White dwarf		Neutron star		Black hole
		Unmagnetized	Magnetized	Unmagnetized	Magnetized	
Early-type, massive	O, B supergiant: wind, Roche lobe (?), disc (?)			Unpulsed massive X-ray binaries	Rapidly pulsing massive X-ray binaries [C]	Cygnus X-1 LMC X-3
	Be star: wind, eccentric (?), no disc (?)			Unpulsed X-ray binaries	Slowly pulsing X-ray binaries, [C] only	
Late-type, low-mass ($\leq 2M_\odot$)	Roche lobe, disc (except AM Hers)	Classical novae Dwarf novae Novalike-variables	Intermediate polars AM Hers ([C] only, no disc)	Galactic bulge sources, bursters, globular cluster sources (?)	Her X-1 + two others [C], pulsed	

[C] denotes the presence of accretion columns

Table 2.1: *Summary of X-ray binary sources (from [53])*

X-ray binaries are broadly classified according to the spectral type of the mass donor, which is important as it determines the mode of mass transfer to the compact object, and hence the environment surrounding the compact source.

2.3.1.1 High mass X-ray binaries

The high mass X-ray binaries (HMXRB) contain a very luminous type O or B companion. The O/B companion has a substantial stellar wind, removing between 10^{-6} - 10^{-10} $M_\odot$ per year. A neutron star or black hole in a relatively close orbit will capture a significant

fraction of this, sufficient to power a bright X-ray source. Additional mass transfer may occur through Roche lobe overflow.

HMXRBs may be further sub-divided into supergiant X-ray binaries (SXRBs) and Be X-ray binaries, which have broadly similar X-ray properties. SXRBs tend to have shorter orbital periods (1.4 - 41 days) compared to the Be X-ray binaries (16 - 188 days).

Most SXRB systems contain X-RAY PULSARS, although there are two exceptions: X1700-37 and Cyg X-1. The average luminosity of these systems is in the range 10^{36} - 10^{38} erg/s. The higher luminosity systems have pulse periods of 1 - 10 s, which increase to >100 s for the lower luminosity systems.

Some Be systems are associated with very bright X-ray transients. Pulses with periods of the order of a few seconds are often (but not always) detected. The transients are thought to be caused by mass ejection episodes from the Be star, which is likely to be rotating close to break-up. A further class of Be X-ray binaries are lower luminosity (10^{33} - 10^{35} erg/s) persistent sources.

2.3.1.2 Low mass X-ray binaries

In low mass X-ray binaries (LMXRB), the mass donor is later than type A, and in some cases a white dwarf. The wind of a late type or degenerate mass donor in an LMXRB is insufficient to power a bright X-ray source. Significant mass transfer will only occur if the companion fills its Roche lobe. In Roche lobe overflow, the flow has considerable angular momentum (much more so than from wind flow) and, if there is no other interaction, a ring will form about the compact object. Viscous interactions and angular momentum conservation may cause the ring to spread into an accretion disk.

LMXBs exhibit a wide range of observational characteristics. In general they have soft spectra, and show no strong pulsations, which is thought to be due to a weak or absent magnetic field, which may simply have decayed with time. X-ray bursts are commonly seen from this type of object, and may be due to variable accretion or to bursts of fusion occurring in material which has built up on the surface of the compact object. Additionally, many LMXRBs are seen to exhibit Quasi Periodic Oscillations (QPO),

first discovered in EXOSAT observations of GX 5-1 [141].

A further class of LMXRBs where the accreting compact object is thought to be a white dwarf, is known as the CATACLYSMIC VARIABLES. These are much less luminous objects, of which only 'Am Her type' sources have been found to emit appreciably in the hard X-ray band. The spectrum of Am Her is shown in Figure 2.3 and clearly shows two components, black body with kT=100 eV and thermal bremsstrahlung with kT=10 keV. This is interpreted as being emission from a thin volume of hot gas at the base of accreting columns which are formed by the $\sim 10^8$ G magnetic field indicated by polarization measurements.

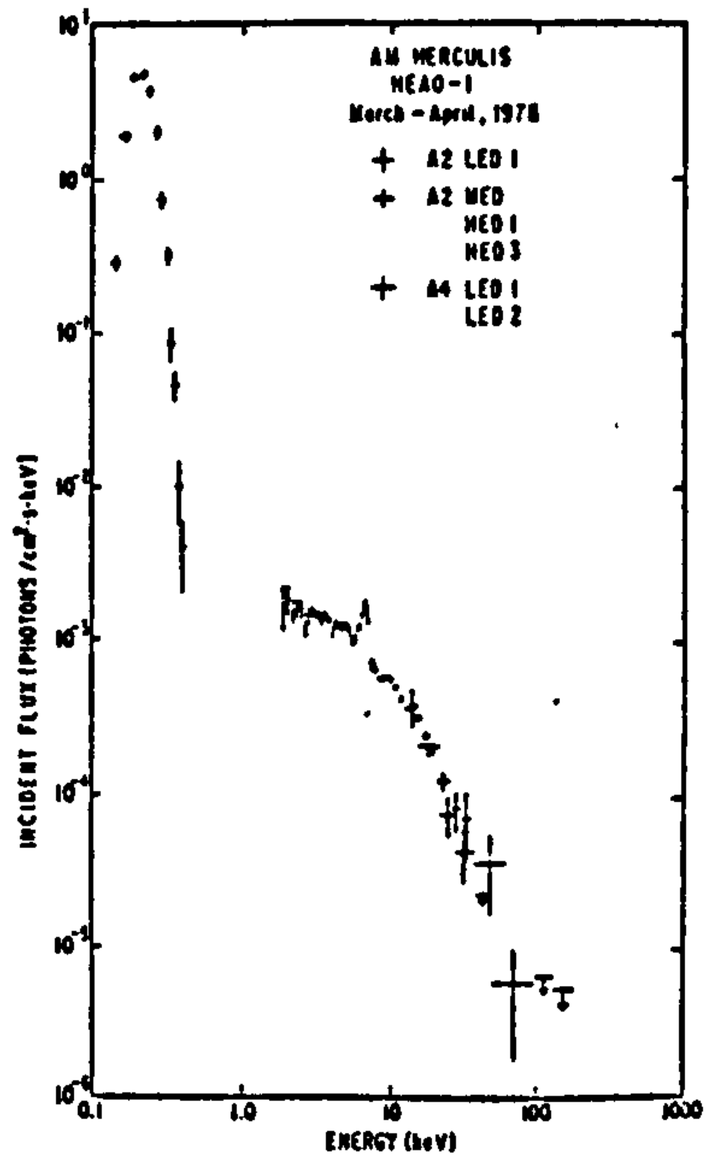

Figure 2.3: *The spectrum of Am Her (from [118])*

2.3.1.3 Black hole candidates

Considering the nature of X-ray binaries containing neutron stars, it is only reasonable to assume that similar systems will exist containing black holes. The most direct method of identifying black hole candidates is the use of optical spectroscopy of the companion star to measure the mass of the compact object. If the mass is well in excess of $\sim$3 $M_\odot$, the maximum theoretical mass of a neutron star, then the compact object must be a black hole. Using this technique, three X-ray binary systems (Cyg X-1, LMC X-3 and A0620-00) are believed to contain black holes. Additionally, LMC X-1 is a 'possible', as are two recently discovered GINGA sources (GS2000+25 and GS2023+33.8).

Since optical spectroscopy of X-ray binaries is difficult, most possibles are now selected from their X-ray character. In particular, a spectrum with a very soft component and a hard power law tail extending out to several hundred keV is currently considered a good indication of the possible presence of a black hole.

2.3.2 The Galactic centre

The Galactic Centre is obscured in the visible band by strong ($\Delta m_v \sim 30$) absorbtion due to the intervening gas and dust clouds. However, in the radio, infrared, X- and gamma-ray regions of the spectrum, where penetration of the intervening material is possible, it assumes its rightful role as a site of fundamental interest for Galactic astrophysics. The immediate vicinity of the Galactic nucleus contains a combination of powerful point sources embedded in an extended emission region. It is thought possible that the compact radio source at the nucleus (SgrA*) may be a weaker form of the those observed in active galaxies. Observations of the Galactic Centre region with the EINSTEIN Observatory [146] revealed there to be 12 point sources within a 1° field of view together with a diffuse emission of about 33 × 18 arc minutes in extent. Extension of the X-ray measurements up to energies of 30 keV by the coded aperture mask X-ray telescope flown on Spacelab 2 [130] likewise detected a number (9) of point sources as well as a 2° diameter diffuse component (Figure 2.4). Towards the higher energy domain of the Spacelab telescope's operational range it was found that the emission from the nuclear region is dominated by one of the surrounding point sources, A1742-294, which is situated about 30 arc minutes from the nucleus.

In the higher energy domain the situation is indicative of the violent activity that is taking place, and although intense fluxes have been measured the picture is far from being clear. High spatial resolution images are required to identify the sources of the hard X-ray and gamma-ray emission.

The HEAO-1 observations which have extended the spectral measurements up to almost 100 keV with about 1° angular resolution, have shown that at least one source with a particularly hard spectrum exists within 0.5° of the Galactic Centre [84]. However, the picture is generally confused by the strong time variability of the hard X-ray sources in this region. Leventhal et al. [92], and Riegler et al. [116] have detected strong and

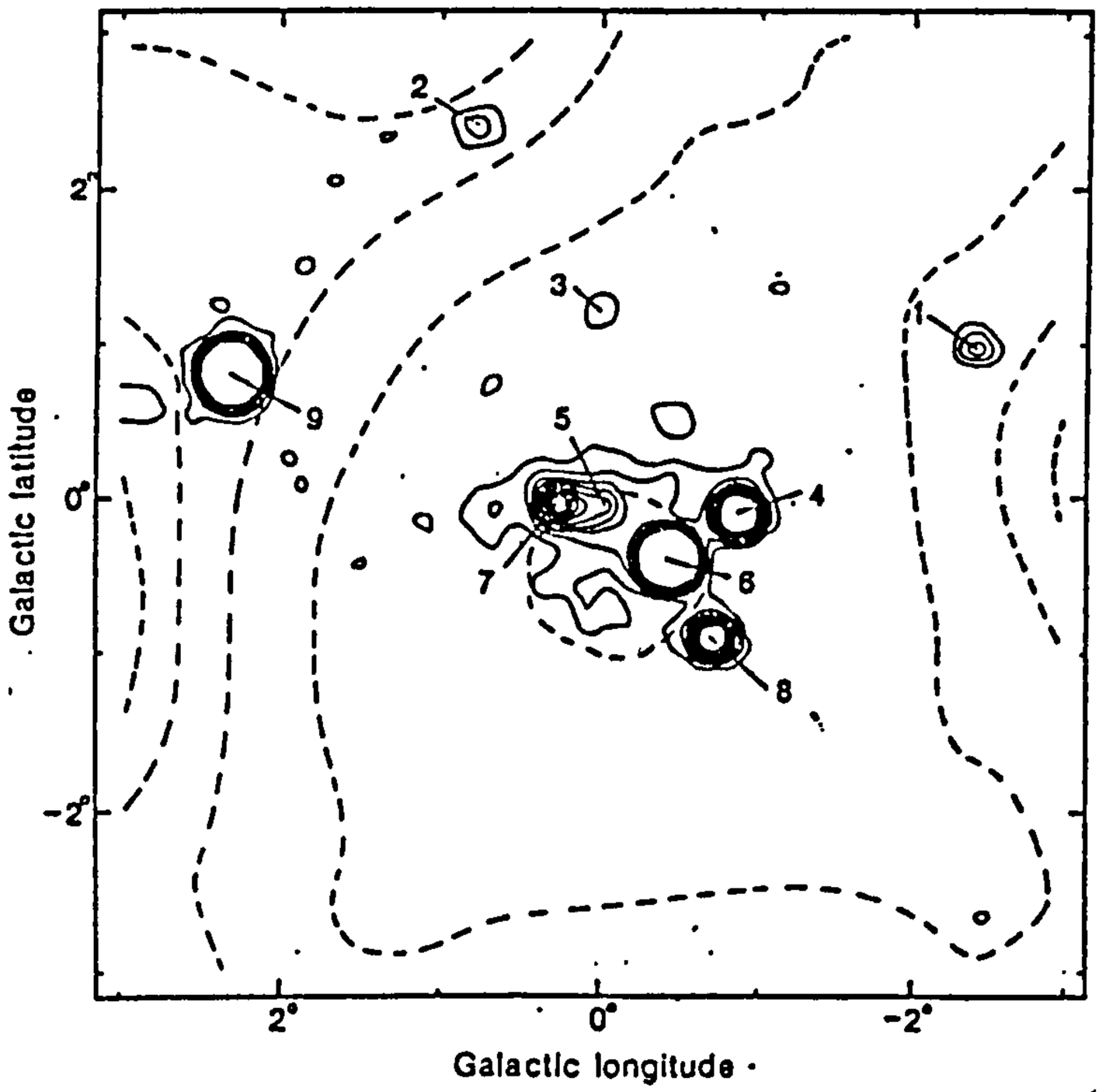

Figure 2.4: *The Spacelab 2 image of the Galactic Centre (from [130])*

variable emission up to about .2 MeV, and although the angular resolutions of their instruments make it difficult to locate the origin to better than a few degrees, the time variability of the emission indicates a point source origin. Coded aperture images of this sky region by the Caltech group [31] with better angular resolution (1.1° FWHM) have tentatively identified a point source emission detected over the range 30 to 200 keV with the X-ray source IE1740.7 - 2942 situated about 0.7 degrees away from the Galactic nucleus. This object also dominated the 2° field of view of the Spacelab 2 coded aperture telescope close to 30 keV, indicating that both Spacelab 2 and the Caltech group have measured the same source. If this source is located at a distance comparable to the centre of the Galaxy, which seems likely on the basis of its position, it is one of the most luminous gamma ray sources in the Galaxy, comparable in output to Cyg X-1.

2.3.3 The extraordinary source - Geminga

Of the point like objects the most fascinating and enigmatic is Geminga (2CG 195+4). This object is the second brightest gamma-ray source in the sky, and emits the vast majority of its energy in the X- and gamma-ray regime [37], with a spectrum characterised

by $L_X/L_{opt} = 3000$ and $L_\gamma/L_X = 1000$. The underluminous optical counterpart points towards a small compact object, possibly one of the typically 10^9 neutron stars that must reside, otherwise undetected, in the Interstellar Medium. If Geminga is such an object then we would expect many more to exist. The unambiguous identification of Geminga, and possibly other X- and gamma-ray emitters of the same new class of object, will provide a vital clue to their understanding. Strenuous efforts have been made to identify Geminga with known emitters at other wavelengths, the most likely candidate being the weak X-ray source 1E0630+178 and an exceedingly faint ($M_B = 26.5$) optical counterpart [68]. However, the precise identification will remain unanswered, together with the nature of the object as a class, until hard X- and gamma-ray telescopes with finer angular resolving power become operational.

2.3.4 Cyg X-3

The spatial structure of this ultra high energy gamma-ray emitting X-ray binary source has been studied by the EXOSAT telescope [149]. The resulting map of the region shows evidence for a low level extended component aligned approximately parallel to the Galactic plane (Figure 2.5). Kifune et al. [81] have suggested that the observed 'wing' structure may be a result of the release of 10^{14} eV electron fluxes, associated with the UHE gamma-ray emission, into the surrounding medium which produce synchrotron radiation. The X-ray structure extends over a few degrees. Higher resolution images are required to confirm the true nature of the wings, and the implications for the processes occurring in Cyg X-3 and other similar sources.

2.3.5 SS 433

This source first attracted interest due to its optical and IR spectra which implied, through doppler shifts, that bulk motions with velocities ~0.25c were occurring. This is supported by observations of red and blue shifted ^{24}Mg gamma-ray line emission at 1.5 and 1.2 MeV, again implying a velocity of 0.25c. Einstein observations [145] showed the X-ray emission to be in the form of two oppositely-directed jets over 40′ across (Figure 2.6). The observed doppler shifts are thought to come from a 164 day periodic

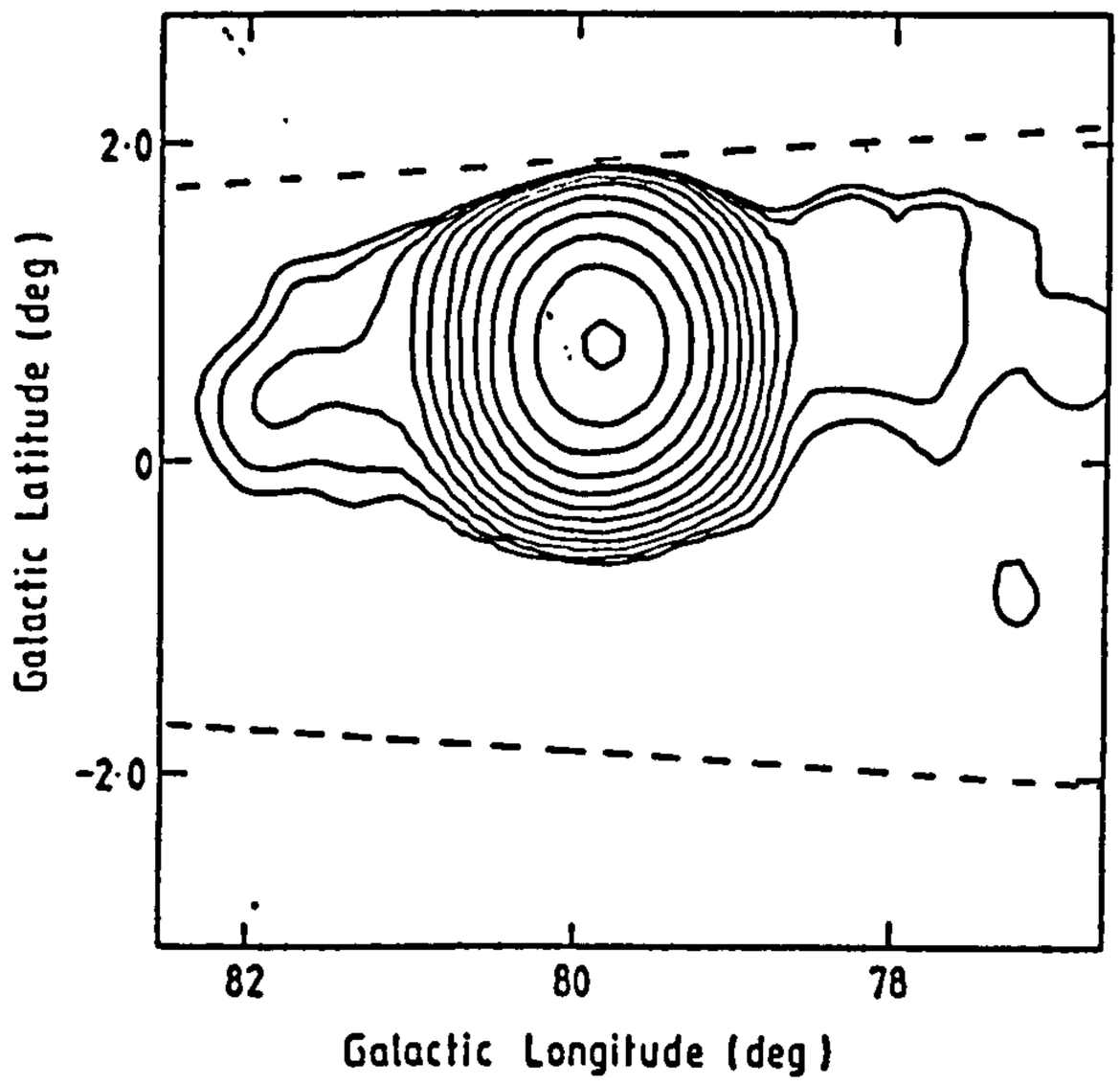

Figure 2.5: *EXOSAT image of Cygnus X-3 (from [81])*

precession of the jets, which has been confirmed by radio measurements.

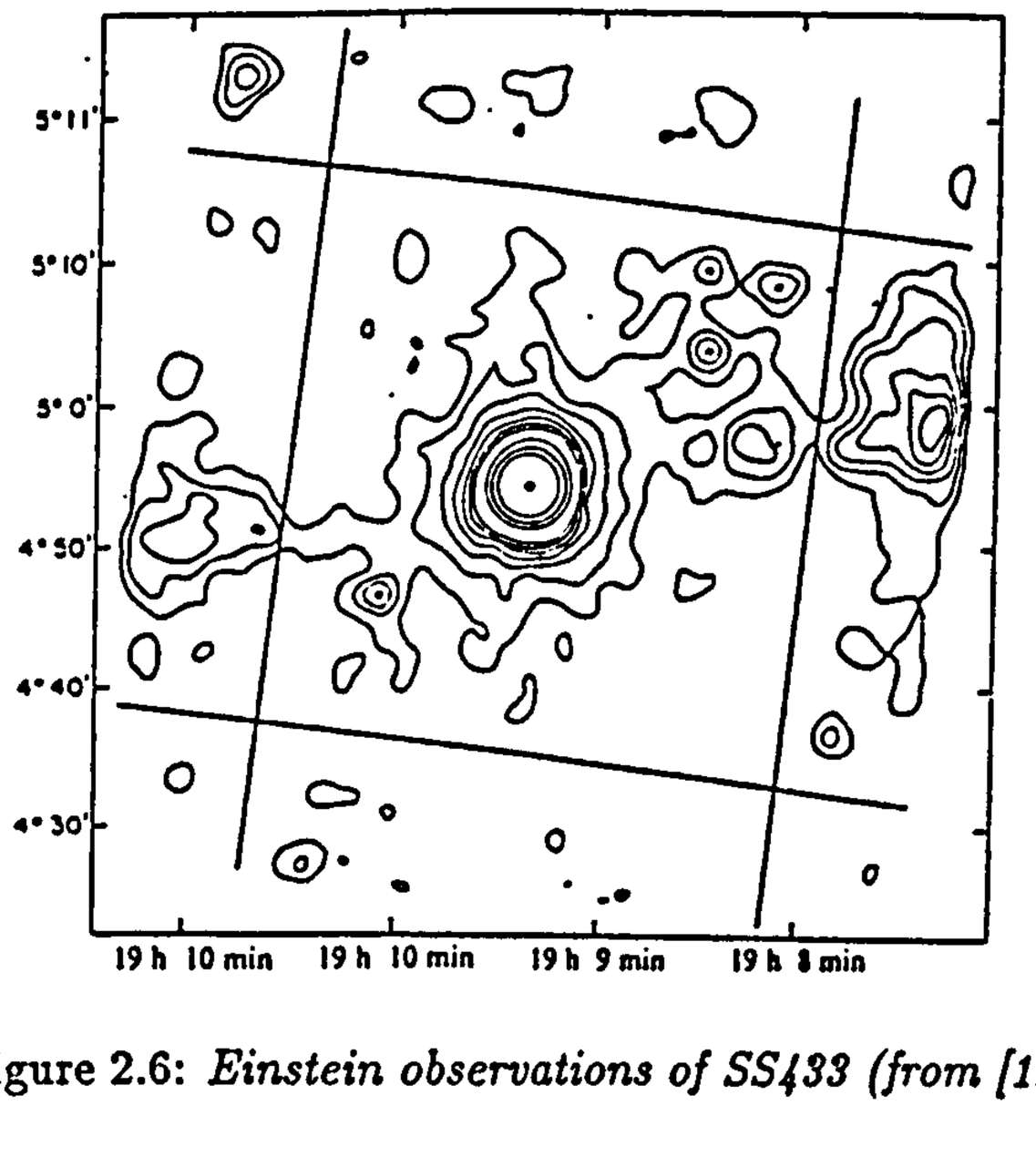

Figure 2.6: *Einstein observations of SS433 (from [145])*

The precise mechanism for X-ray generation is as yet uncertain, although one possibility is thermal emission from heating where the jets interact with the surrounding medium. In an alternative scenario, the emission could be due to synchrotron radiation from particles within the jets themselves. To unravel the mysteries of this source will require high-resolution observations with both hard X-ray and gamma-ray telescopes.

2.3.6 Supernova remnants

SS 433 is imbedded within a supernova remnant, and there are many other examples of supernova remnants (SNR) which constitute structured galactic X-ray sources (see, for example, Ashcenbach *et al.* [11]). A considerable number of these objects have been imaged by the EINSTEIN and EXOSAT observatories ranging from the youngest examples, such as Cas A which is 300 years old, to the Cygnus loop which is probably more than 50,000 years old. The approximate angular scales of some of the SNR are as follows: Puppis A (1°), IC 443 (30′), Cygnus loop (3°), Tycho (7′) ,Cas A (5′), SN 1006 (25′), Vela (degrees). Generally the spectra indicate that the emission mechanism is thermal bremsstrahlung, which is believed to derive from a shell source in the region of the expanding shock front. In some examples, however, (e.g. SN 1000) it appears that the emission spectrum follows a power law, which may be produced by the synchrotron radiation of energetic electrons produced by a central (but unobserved) pulsar.

2.3.6.1 The Crab Nebula & Pulsar

The Crab Nebula, the expanding shell from a supernova in 1054, is a spectacular extended object which has been observed to emit radiation in all wavebands from radio to high energy gamma rays.

The spectrum is well determined, with a synchrotron origin for the radio, optical and X-ray emission. At hard X-ray energies, the Crab is the brightest non-variable source, which has led to it becoming one of the most common targets for study. The hard X-ray spectrum comprises two power law components with a break at ~80 keV, the indices being $\alpha = 1.99$ below that energy, and 2.42 above it.

In 1968, the puzzle of the origin of the high energy emission was partially solved with the discovery of a pulsar within the nebula. The pulsar is now believed to contribute up to 10% of the total observed emission. It is the fastest known X-ray pulsar, with a period of 33 ms. The pulse profile is shown in Figure 2.7, and has the same double-peaked shape as the optical/radio pulse profile.

The first studies of the extended emission from the Crab Nebula were carried out

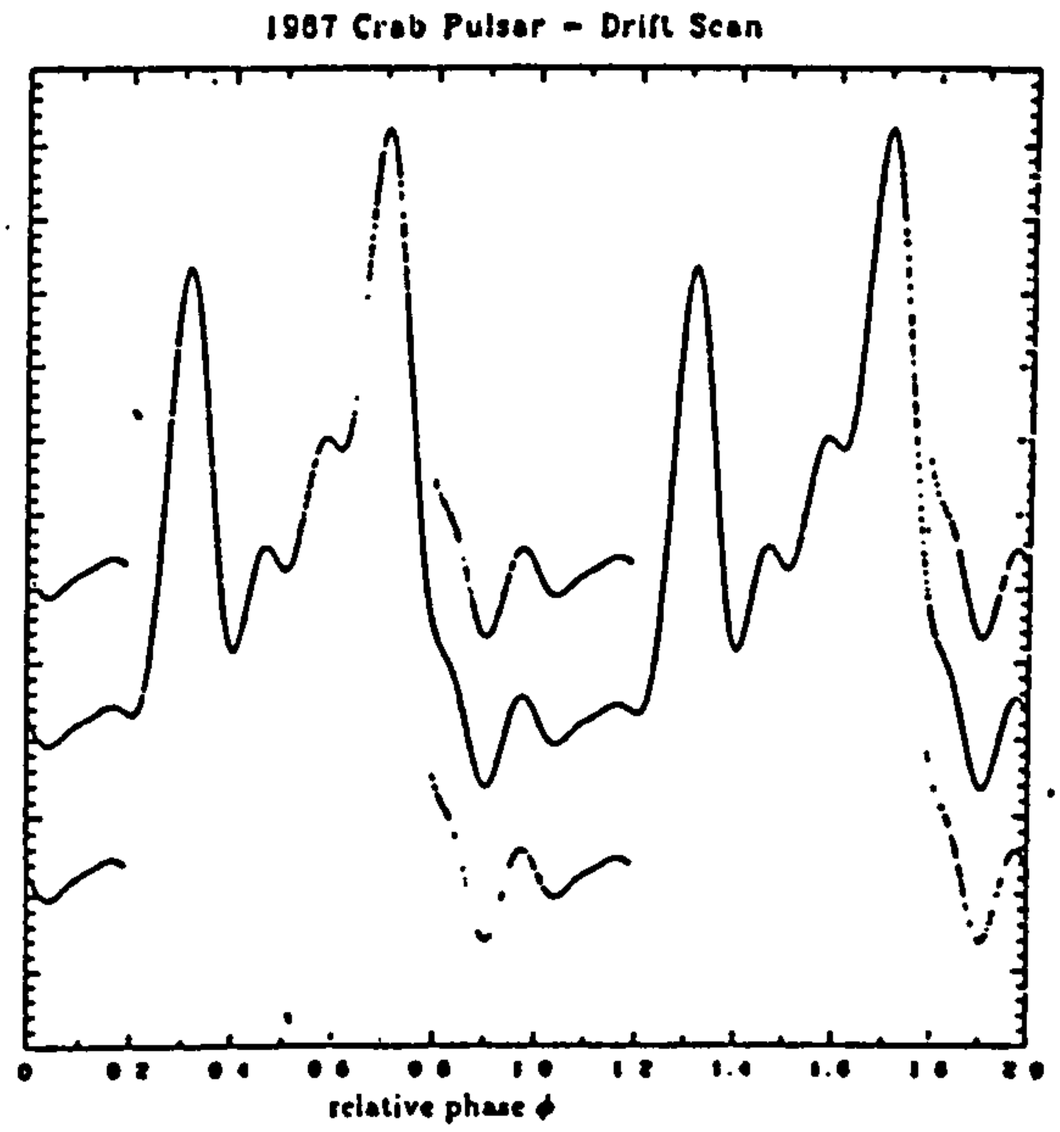

Figure 2.7: *The X-ray pulse profile of the Crab pulsar (from [18])*

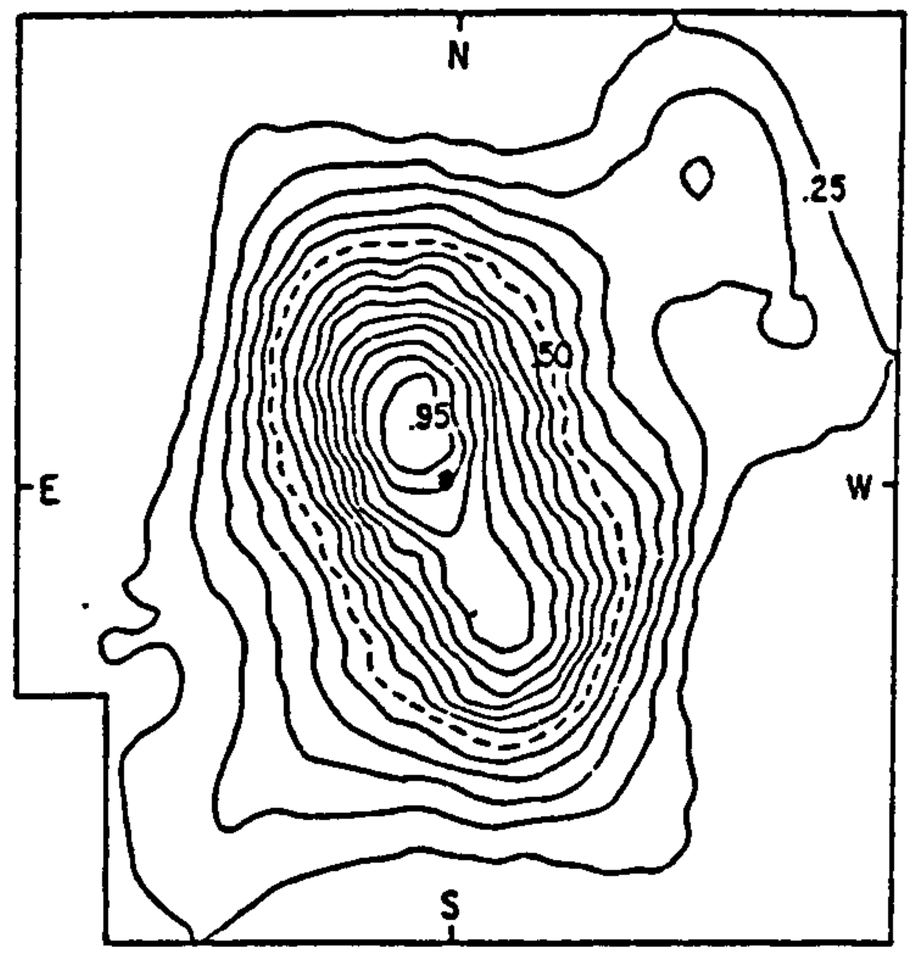

Figure 2.8: *Scanning collimator image of the Crab Nebula (from [111])*

using lunar occultations. More recently, images have been obtained using a scanning modulation collimator [96,111] with an angular resolution of 22″. An image in the 42-63 keV waveband is shown in Figure 2.8, and shows the following features:

i) The hard X-ray emission is elongated in the NE-SW direction, perpendicular to the optical long axis and parallel to the local magnetic field. This elongation is more pronounced at the higher energies (see also Figure 3.4).

ii) No emission feature is observed at the pulsar position.

iii) The offset between the emission centroid and the pulsar seems to decrease with increasing photon energy.

These features are strong evidence for a toroidal-shaped magnetic field enhancement due to a shock front at a distance of $r \sim 3 \times 10^{17}$ cm [96]. The observed double-peaked structure may then be explained as a simple geometric effect caused by viewing the torus almost side-on.

Further observations at higher energy and with improved resolution will be required in order to clarify the precise processes occurring in this complex object.

2.3.6.2 Supernova 1987A

Supernova 1987A was (and still is) one of the most exciting astrophysical events this century. On February 24th 1987, Sk -69° 202, a blue supergiant in the Large Magellanic Cloud exploded. It was the first opportunity to observe a relatively nearby supernova with sensitive instrumentation across the entire electromagnetic spectrum, and as this was also the first supernova for which data on the progenitor was available, the event became an ideal opportunity to evaluate and improve the theories of stellar evolution and nuclear astrophysics which were used to predict its evolution with time.

The first detection of hard X-ray emission was made by the Ginga satellite [43] in June 1987, after which the flux was seen to rise until early September (Figure 2.9), reflecting an decrease in the opacity of the surrounding material. This rise continued until February 88, after which it began a gradual decline [10]. This was in good agreement with the predictions of models, provided that sufficient mixing was invoked to give the correct initial hard X-ray flux.

Slightly later, hard X-ray emission over the range 20 - 300 keV was detected by the HEXE instrument on the Mir-Kvant observatory [132]. They measured the spectrum (Figure 2.10) to have a power law index of ~1.4, with evidence of flattening at lower energies. This spectrum was believed to originate from Compton scattering of higher energy photons created in the $^{56}Ni \rightarrow {}^{56}Co \rightarrow {}^{56}Fe$ decay sequence. In November 1987, an image of the area surrounding SN 1987A was obtained by the GRIP telescope [32], and this is shown in Figure 2.11.

The detection of a neutrino burst coincident in time with the supernova has led to the belief that a pulsar may have been formed. However, to date, no direct evidence has been found to confirm the existence of such a compact object, although the detection of pulsed emission would require the expanding supernova to have become reasonably transparent.

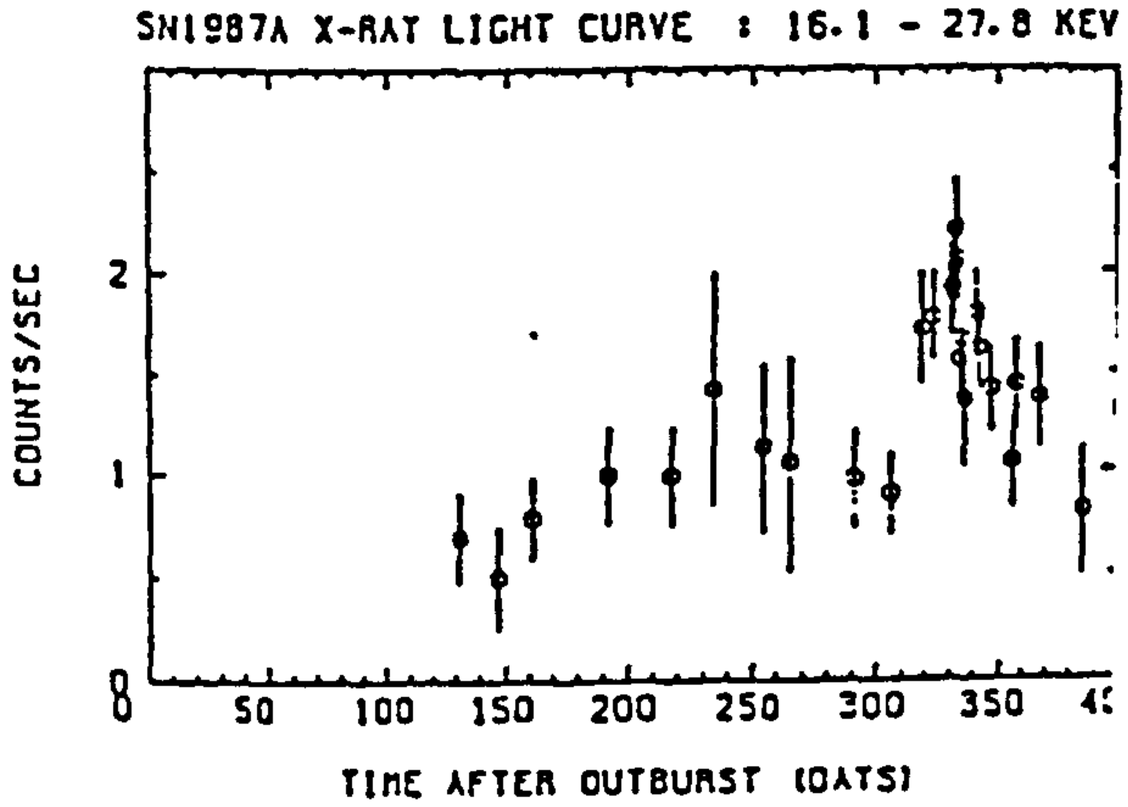

Figure 2.9: *The X-ray light curve of SN1987A (from [10])*

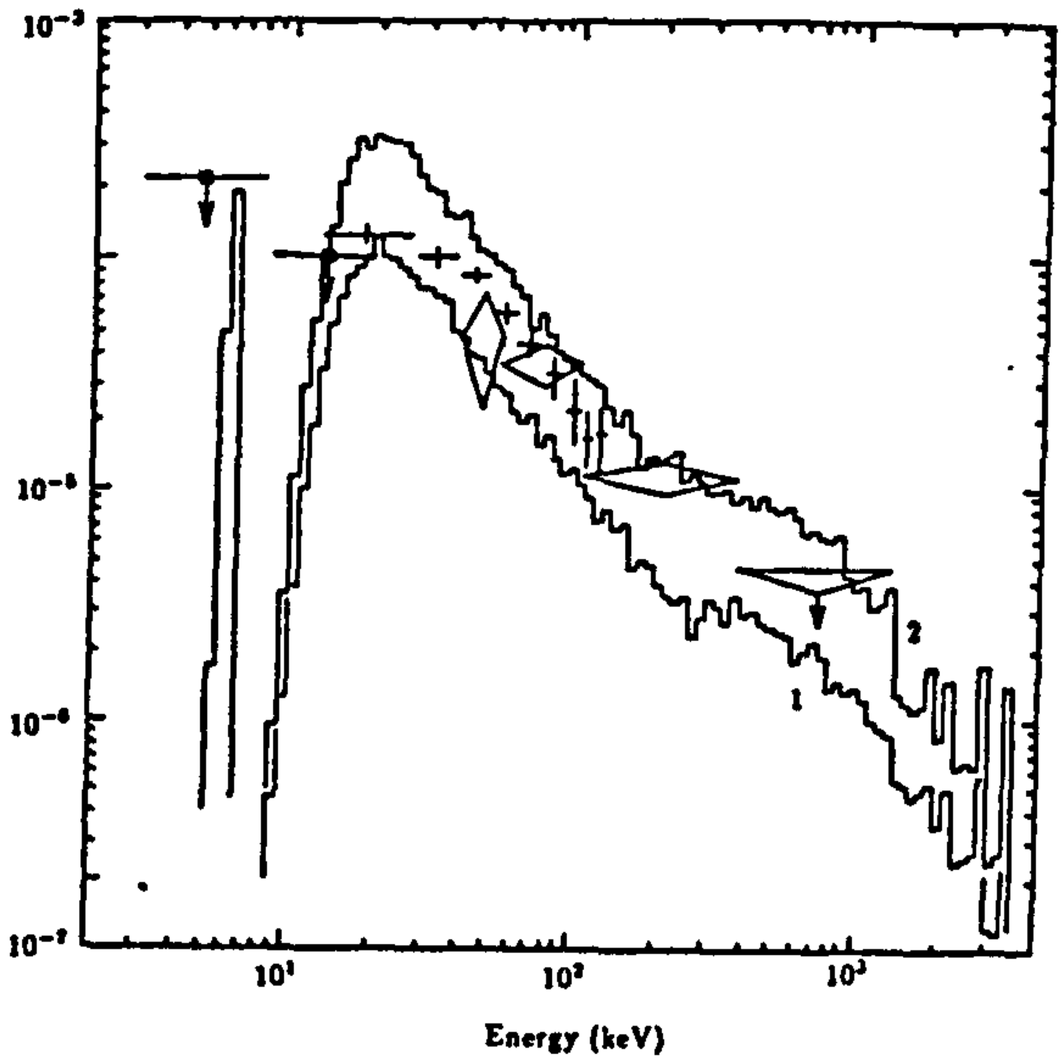

Figure 2.10: *The Hard X-ray spectrum of SN1987A (from [132])*

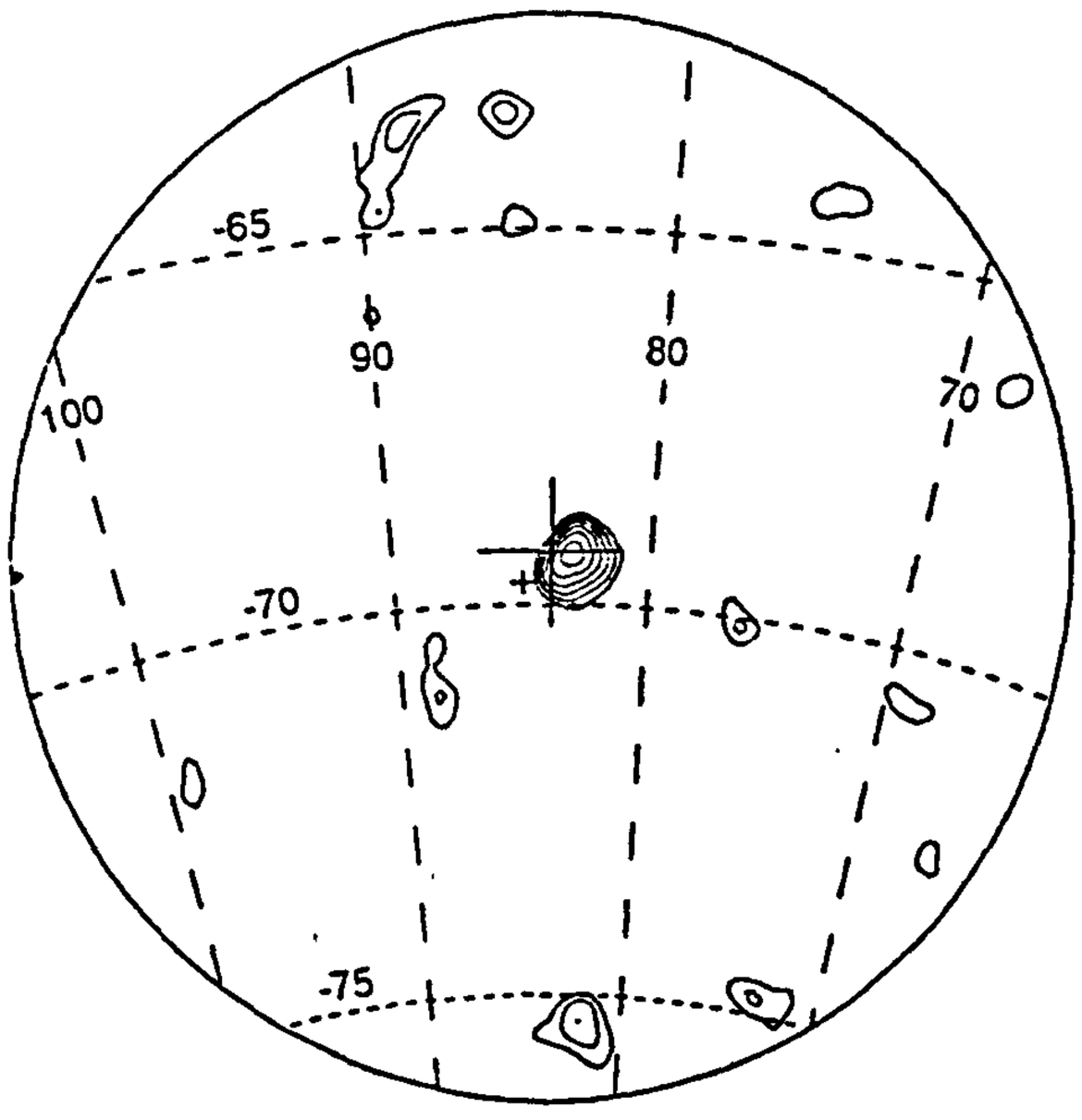

Figure 2.11: *GRIP telescope image of SN1987A (from [32])*

2.4 Extragalactic Sources

As for the Galactic scenario, a wide variety of object types emitting on a wide range of angular scales are encountered when the astronomer contemplates the extragalactic sky. Sources of interest range from the 'point-like' active galactic nuclei (AGN) through structured objects such as nearby galaxies and clusters of galaxies, to the cosmic diffuse background (CDB) at the farthest end of the angular scale.

2.4.1 Active galactic nuclei

Active galactic nuclei, as their name suggests, are galaxies in which most of the power emitted is believed to come from a small region near the core. Their extremely high luminosity cannot be explained by normal stellar processes, and this, coupled to the rapid variability and non-thermal spectra observed, leads to the belief that they are powered by massive ($\sim 10^8 M_\odot$) black holes.

The limited hard X-ray and γ-ray observations of AGN which are available indicate that a substantial fraction of their energy is emitted in this band, making further observations essential to a greater understanding of the nature of these sources.

AGN have been subdivided into 4 main groups: Seyfert galaxies, radio galaxies, BL Lacertae objects and Quasi-Stellar objects (Quasars), reflecting the general emission characteristics.

2.4.1.1 Seyfert galaxies

Seyfert galaxies are normally defined by their optical properties. Morphologically, Seyferts are spiral galaxies with a bright compact nucleus, from which intense emission lines are observed. Type I Seyferts exhibit both broad and narrow emission lines (believed to come from different regions surrounding the central source), whereas only the narrow lines are seen from Seyfert IIs.

Seyfert Is are found to be more luminous in hard X-rays, and this is consistent with

the theory that Seyfert IIs are simply Seyfert Is viewed edge-on so that the emission is attenuated by the galactic plane.

The hard X-ray spectra of Seyfert galaxies may be described by a single power law. A mean spectrum [117] has a photon index (α) of 1.68 ± 0.15 (Figure 2.12), suggesting a synchrotron origin, possibly by SSC scattering of the electrons producing the radio/IR continuum also observed.

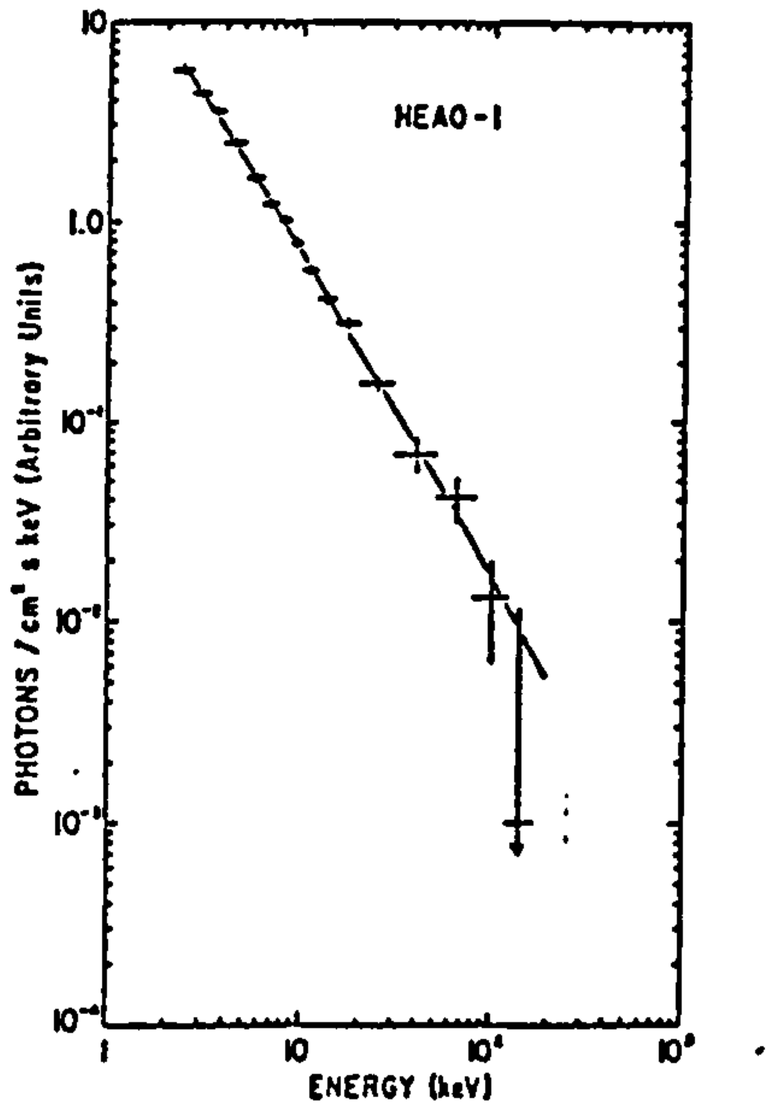

Figure 2.12: *Mean X-ray spectrum of Seyfert galaxies (from [117])*

Seyfert galaxies exhibit variability over a wide range of timescales. A survey in 1981 [101] showed that 50% of a sample of 28 AGN varied in flux by a factor of 2 over timescales of ≤ 1 year. NGC 4051 has been observed to show repeated variability on a timescale of $\sim$1 hour [90], which has been interpreted as an accretion disk rotating about a central 10^6 $M_\odot$ black hole.

2.4.1.2 Radio Galaxies

Cen A is the only radio galaxy to have been detected in hard X-rays or gamma-rays. This object is a strong, variable radio source at a distance of $\sim$5 Mpc, with two huge lobes of radio emission separated on the sky by 5°, colinear with two minor lobes separated by 4′ on either side of the nucleus, one of which has been associated with a jet [49].

The X-ray spectrum of Cen A is shown in Figure 2.13, and is best fit by two power laws of 1.6 and 2.0, with the break coming at ~140 keV. More recently, a single power law of slope 1.59 over the range 70-500 keV has been measured [56].

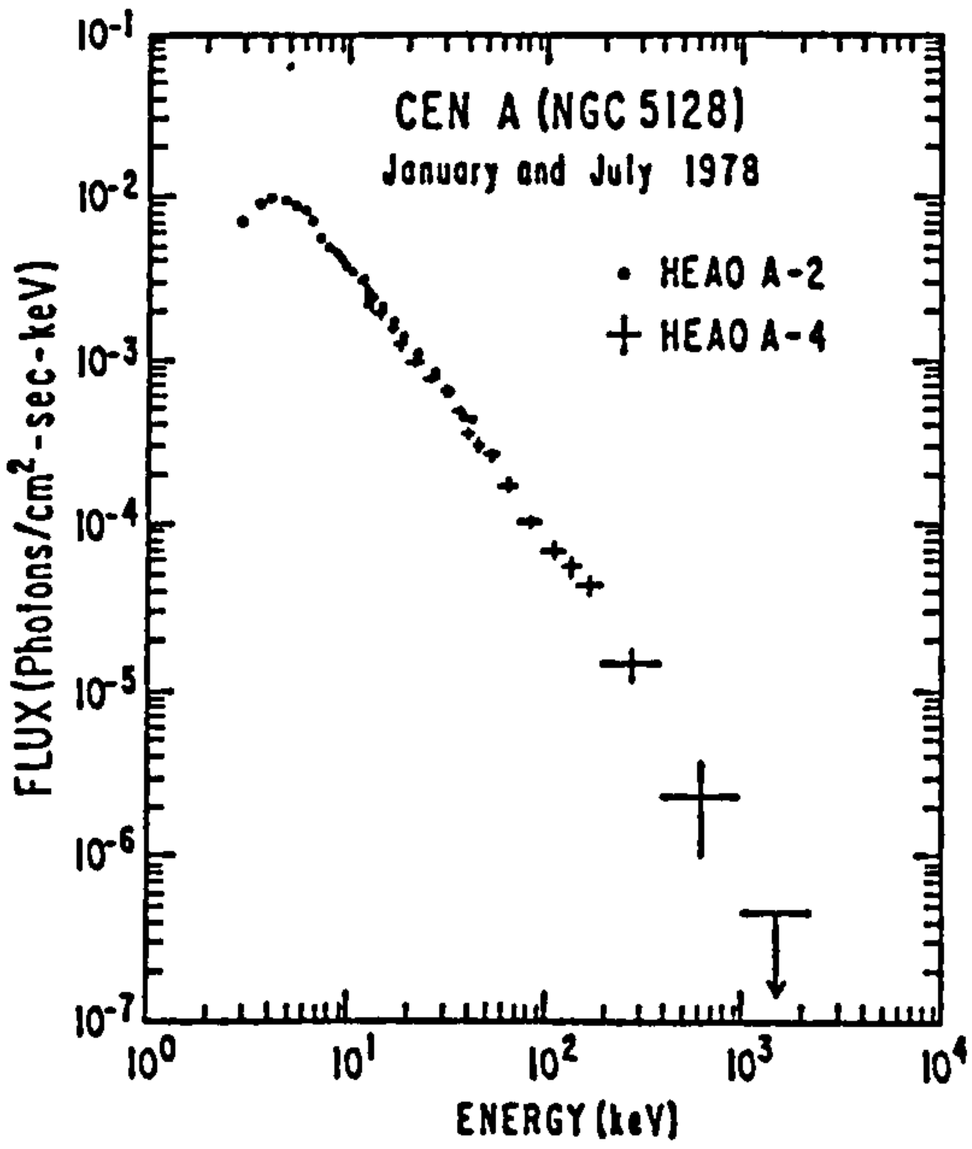

Figure 2.13: *X-ray spectrum of Cen A (from [13])*

Variability over a wide range of timescales from a few hours (~25%) to years (a factor of 5 change over the period 1970-77) has been observed.

There is considerable interest in the precise origin of the hard X-ray emission. The observed variability indicates the origin to be a compact central object, but telescopes sufficiently sensitive to diffuse emission have not yet investigated the giant radio lobes, which may also emit X-rays. This is clearly a prime candidate for high-sensitivity, high-resolution imaging observations in the hard X-ray waveband.

2.4.1.3 BL Lac objects

Named after the prototype BL Lacertae, BL Lac objects have non-thermal spectra, but, in contrast to Seyfert galaxies have very weak or no emission lines.

There is little data in the hard X-ray band, but soft/medium X-ray observations indicate steep power-law spectra ($\alpha \sim 2.5$), with possible evidence of a hard tail above ~10 keV. The spectrum of PKS 2155-304 is shown in Figure 2.14, and demonstrates both these

features. Unlike in Seyfert galaxies, there is also evidence of spectral variability over a period of days.

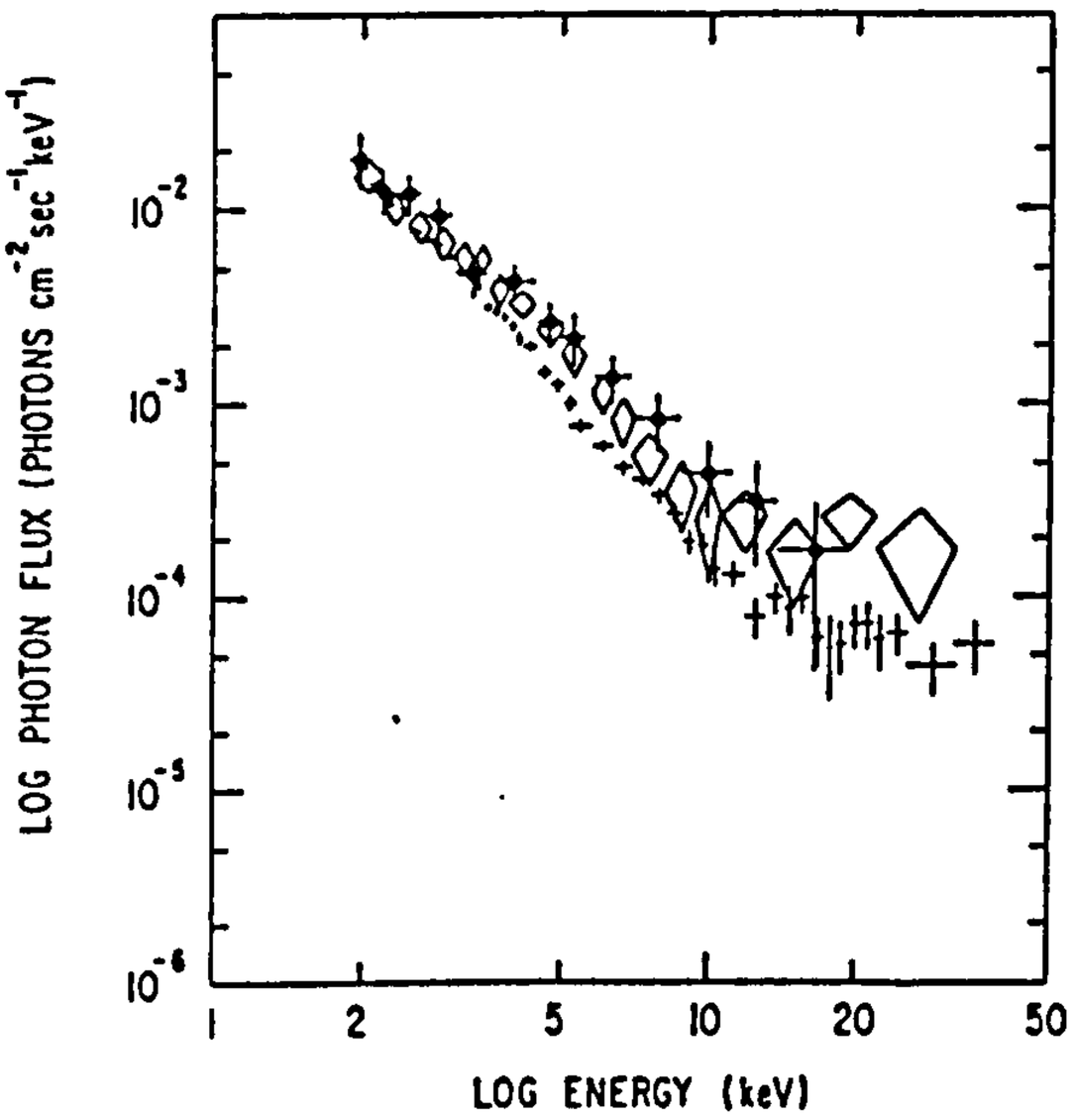

Figure 2.14: *X-ray spectrum of PKS 2155-304, a BL Lacertae object, showing variablitity over the period Nov 77 – Nov 78 (from [140])*

Strong flux variability is shown over timescales from minutes to months. 3C 66A, a luminous BL Lac, varied by a factor of 10 in 6 months, whilst much more rapid variations (1 minute) have been reported in H0323+022.

The models for this type of source suggest a synchrotron source for the optical/UV/soft X-ray continuum, with the hard tail resulting from SSC scattering of the radio-producing electrons. The lack of hard X-ray data, and studies of variability in general, prevent these models from being constrained further at present.

2.4.1.4 Quasi-Stellar Objects (Quasars)

Quasars are point-like sources with redshifts which imply that they are both at very great distances and of very high luminosity ($L_X \sim 10^{46}$ erg/s). Their spectra are generally characterised by power laws over a wide range of spectral index. With the exception of 3C 273, few successful observations have been made in the hard X-ray band.

3C273 is the source of most of our knowledge of quasars as it is both luminous and

relatively nearby, and it has been well-studied at all wavelengths. The output from 3C 273 is greatest in the hard X-ray/soft γ-ray band which dominates the spectrum (Figure 2.15), making it an excellent target for study in this region. The X-ray spectrum of 3C 273 (Figure 2.16) shows some sign of variability, and is rather complex. HEAO A-2 measurements are best fit by three components: a power law ($\alpha = 1.2$) in the region 2-9 keV, a flatter component up to 30 keV, with an additional steeper component at higher energies. The HEAO A-4 data was consistent with a single power law ($\alpha = 1.7$) over the range 20-120 keV. Variability in the detected flux of ~50% over a few years has been observed, and appears to be correlated with the spectral variations.

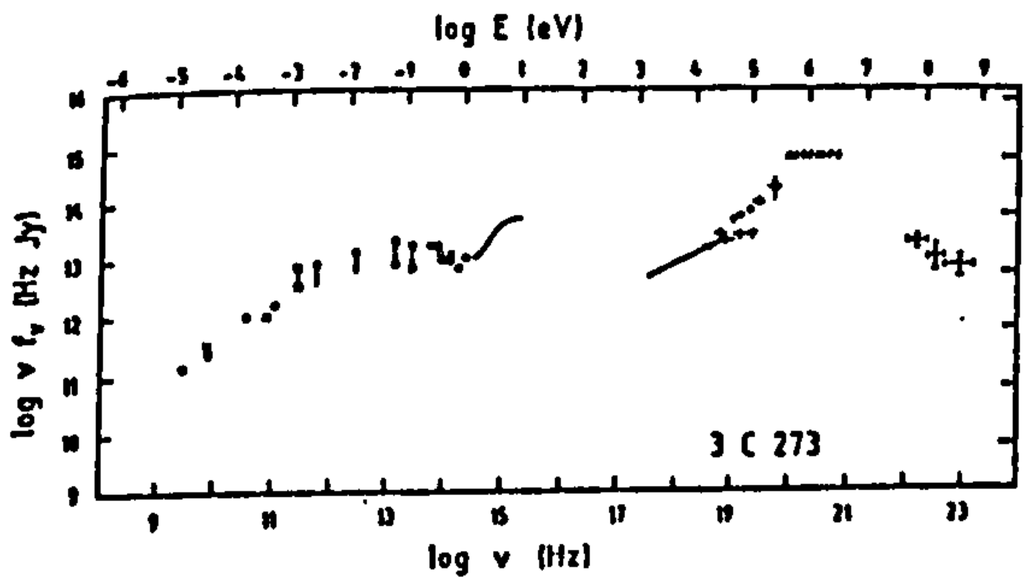

Figure 2.15: *Full spectrum of 3C273, showing the dominant nature of the X- and gamma-ray emission (from [21])*

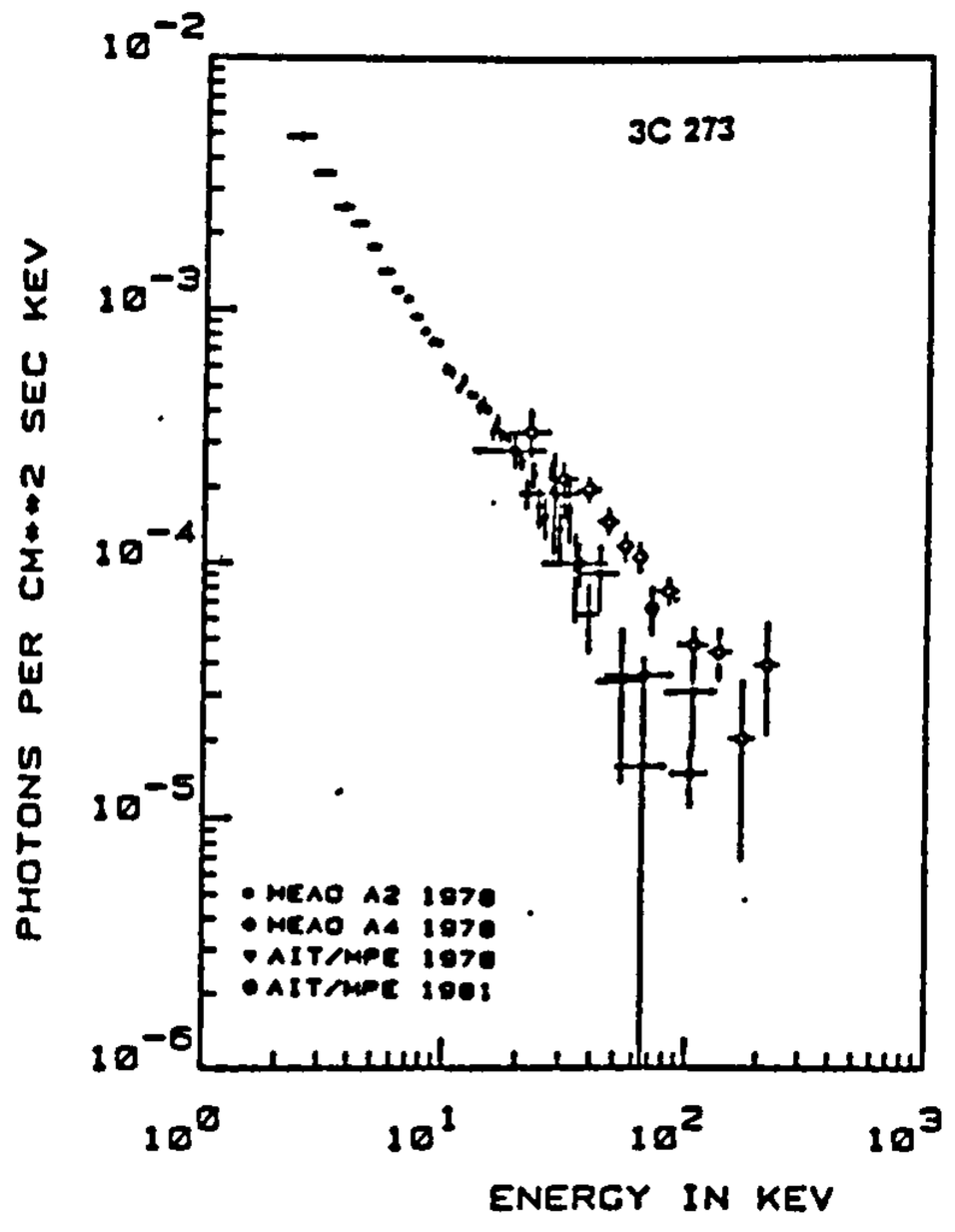

Figure 2.16: *The hard X-ray spectrum of 3C273 (from [21])*

Several quasars has been seen to have jet structures when viewed with high resolution radio studies, and a soft X-ray jet has been observed in 3C 273. The observation of similar structures from this and other quasars in the hard X-ray band would require an angular resolution of $\sim 1'$, but would be extremely important for the understanding of these intriguing objects.

2.4.2 Clusters of galaxies

Clusters of galaxies not only provide sources of interest to the hard X-ray astronomer in their own right but also provide regions of enhanced numbers of AGN for study. Clusters of galaxies are known to be a well defined class of X-ray emitters in the energy range 1-10 keV, but very few measurements have been reported at energies above 30 keV where there is generally an indication of a hard tail emission over and above the thermal bremsstrahlung emission which dominates in the 1-10 keV X-ray band (Figure 2.17). This effect has been reported from Coma, Virgo, Perseus, A2142, 3C129, A401, A225 and A2256 [17,91,114]. For Perseus the emission is clearly dominated by NGC 1275, but for other clusters the situation is less clear. It is important to ascertain whether this hard emission is due to the presence of AGN or whether it is due to the Compton scattering of the microwave background photons by relativistic electrons in the intracluster region.

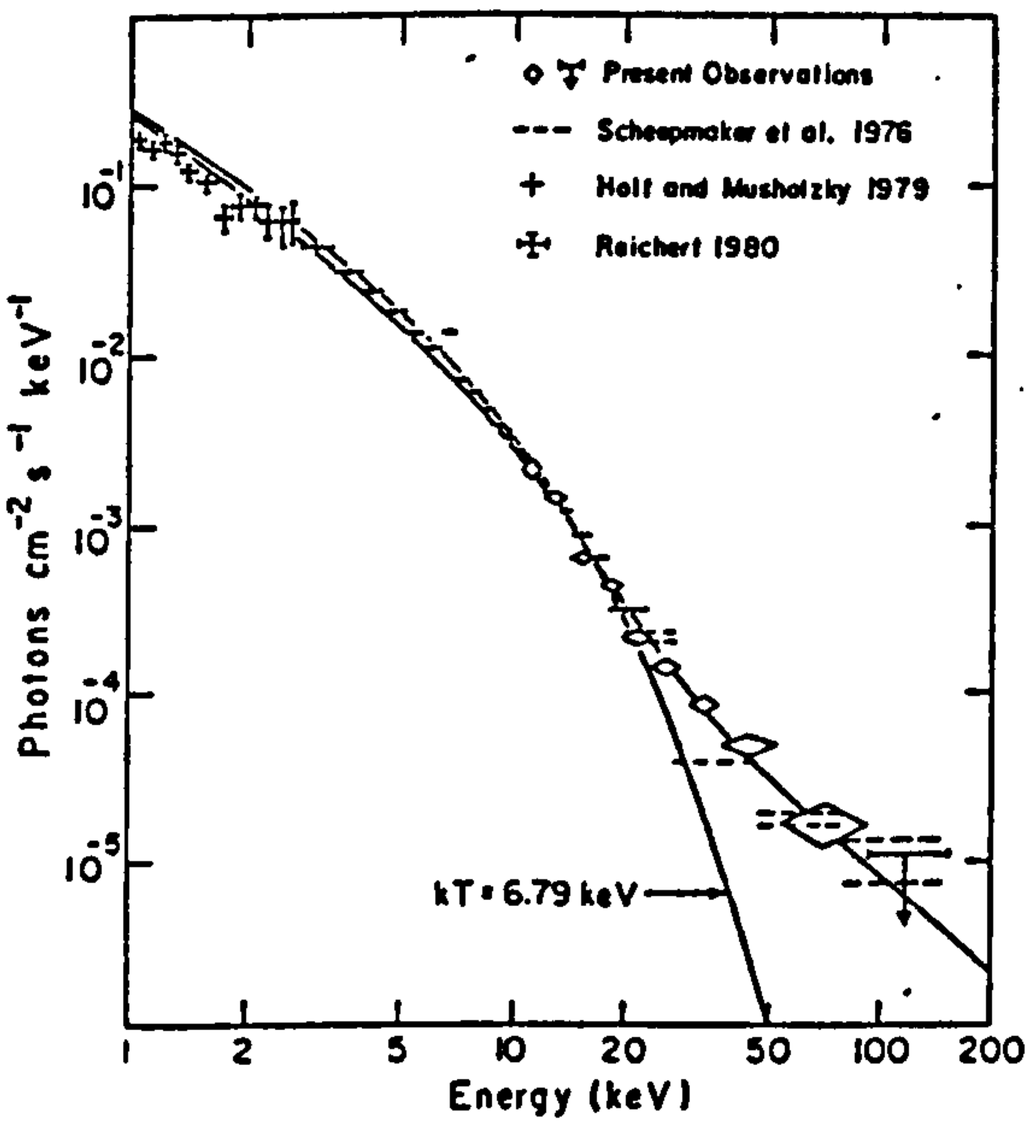

Figure 2.17: *Typical spectrum of a cluster of galaxies, in this case the Perseus cluster (from [114])*

The Virgo cluster was recently studied by the coded aperture X-ray telescope on board Spacelab 2 [69] (Figure 2.18). These images demonstrated that much of the hard X-ray emission originates in NGC 4388 which is classified as a type 2 Seyfert Galaxy. It had previously been suggested that the hard tail comes from M87 which dominates the 1-10 keV X-ray emission. This result illustrates the benefits of imaging studies of clusters of galaxies in an unexplored waveband, which have provided a completely new insight into

both the cluster dynamics and the morphology of AGN. The capability to locate point sources of hard X-ray emission to about one arc minute within a field of view of typically 10 square degrees is required for further study of the Virgo cluster.

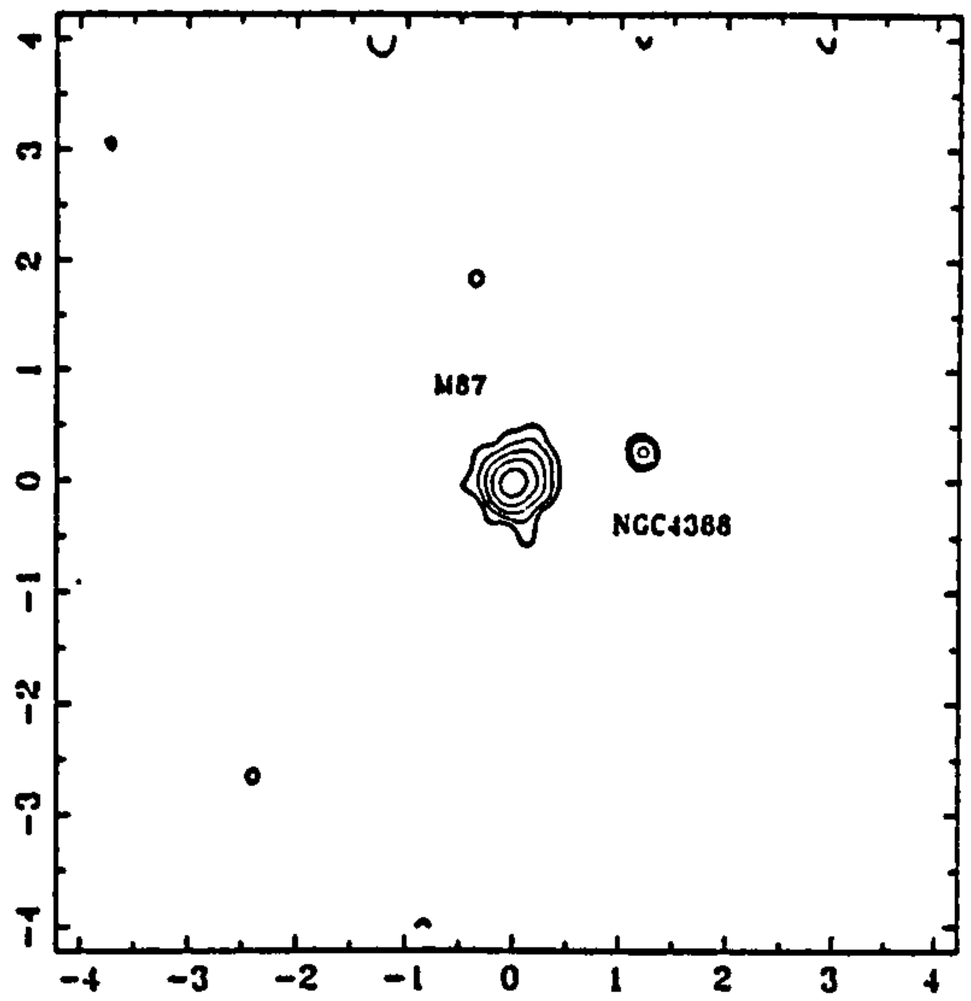

Figure 2.18: *Spacelab 2 image of the Virgo cluster (from [69])*

The situation appears to be somewhat different for the Coma cluster. In the 1-10 keV band, the emission mechanism is due to thermal bremsstrahlung from a diffuse hot intra-cluster gas. X-ray images (e.g. from Gorenstein et al. [60]) show elongated X-ray emission with a central uniform core decaying more slowly than the distribution of galaxies. The EXOSAT/CMA serendipitous search has shown the presence of 5 compact sources within the cluster.

2.4.3 Nearby galaxies

The brightest members of the local group of galaxies will make interesting targets for future hard X-ray imaging studies. Interesting sources of a type similar to those found in our Galaxy should be visible in the Magellanic Clouds e.g. the black hole candidate LMC X-3, the UHE gamma-ray source LMC X-1, the 50 msec pulsar, the SN remnant N49, possibly the site of the March 5 1979 gamma-ray burst, and, of course SN 1987A. To study the LMC, a field of view of about 10° FWHM is required and a point source location capability of typically 1 arc minute for the identification of point sources.

Observations of normal galaxies within the local group with the EINSTEIN observatory and EXOSAT (e.g. Trinchieri *et al.* [136] for M33, Fabbiano *et al.* [48] for M31) demonstrate that these galaxies are similar to the Milky Way galaxy. The X-ray images are composed of a series of point X-ray sources, bright nuclei, diffuse emission from the galactic plane and a hard component which is most likely the result of the integrated contribution of several lower luminosity discrete sources, similar to the ones observed in the Milky Way, e.g. compact accreting systems and young SNRs.

2.4.4 The cosmic diffuse background

The spectrum of the isotropic cosmic diffuse background is shown in Figure 2.19, and is best described by a thermal bremsstrahlung spectrum below ~10 keV, with a power law at higher energies. It is believed that most of this emission is due to unresolved extragalactic sources. Seyfert galaxies could contribute as much as 60% of the observed emission [15] with contributions of ~10% from each of the other classes of active galactic nuclei. However, the uncertainties in these estimates mean that they do not rule out the presence of a true diffuse component to the measured background.

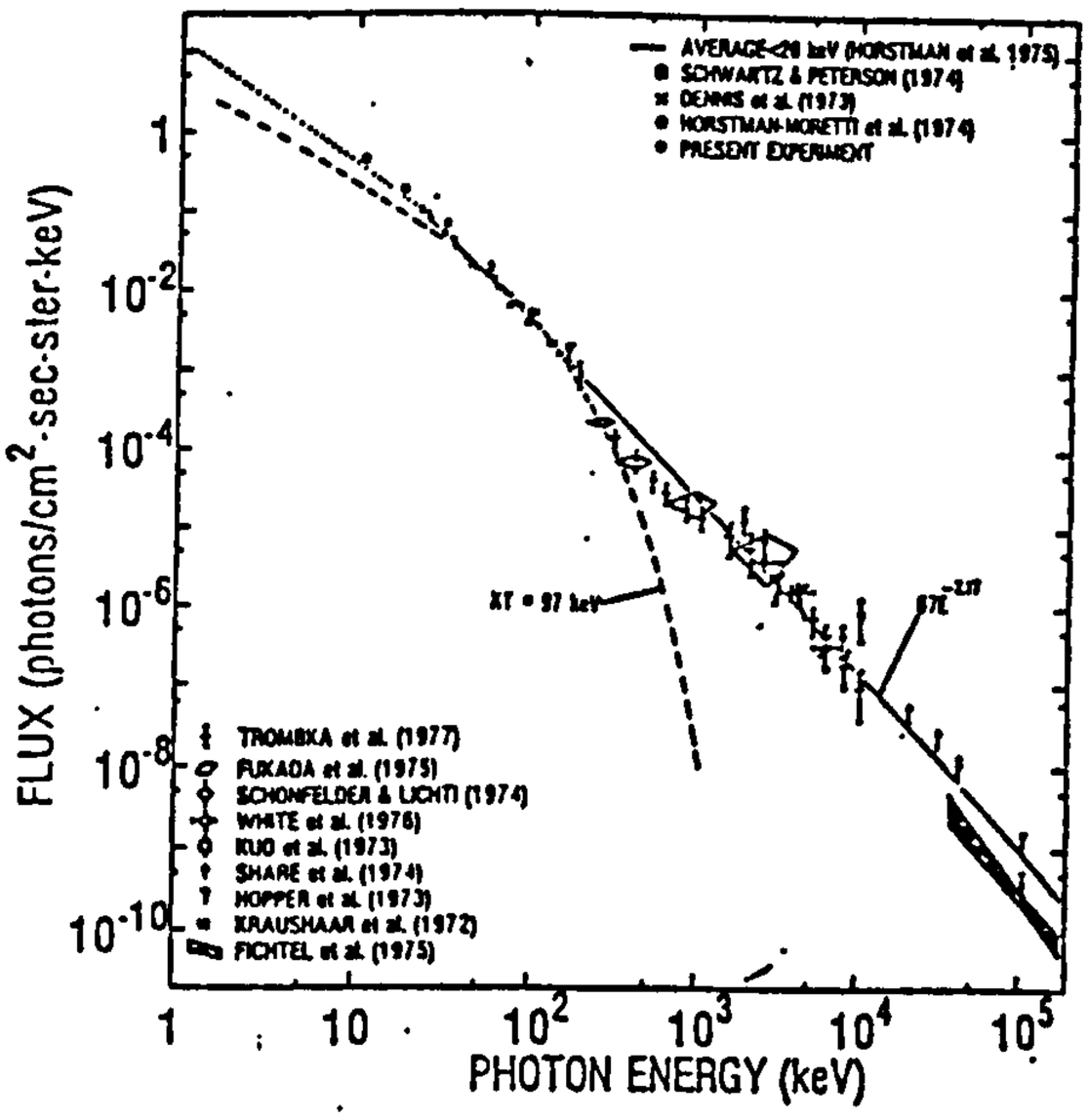

Figure 2.19: *Spectrum of the isotropic cosmic diffuse background (from [82])*

2.5 Conclusions - Key Performance Requirements Of Hard X-Ray Telescopes

Regardless of the imaging technique employed, there are several basic performance requirements for hard X-ray telescopes if they are to contribute significantly to the further understanding of the astrophysical objects being studied.

2.5.1 Sensitivity

Clearly high sensitivity over as broad an operating range as possible is essential. The design of telescopes can be biased towards high sensitivity towards point or diffuse sources, or continuum or line emission, but rarely all four. For a general survey instrument all these requirements must be balanced. High sensitivity has several clear advantages:

- High sensitivity, combined with a wide field of view, is essential for a survey type instrument which must make sensitive observations of the whole sky within a practical mission lifetime.
- More sources can be detected, allowing larger samples of various objects to be obtained for, e.g. morphological studies.
- Non-periodic variability studies become possible.
- The large numbers of new sources which may be detected increases the chance that entirely new classes of object may be discovered.

2.5.2 Angular resolution

As the sensitivity of a telescope increases, the problem of source confusion becomes more severe, and hence telescopes with good angular resolving power will be essential. Good resolving power allows spectral contamination between nearby sources to be reduced during spectroscopic studies. Additionally, high angular resolution is essential for the observation of structure within extended sources. One of the most difficult tasks, the observation of structure within AGN, would require angular resolution better than

1′, whilst the study of other classes of X-ray emitters requires more modest angular resolution.

2.5.3 Point source location accuracy

With the advent of multi-waveband studies, it is clearly vital that sources of emission can be accurately located in order to facilitate their identification with known (or yet to be discovered) sources in other wavebands. As will be discussed in the introduction to the next chapter, an accuracy of typically $\sim 1'$ is necessary before counterpart identification becomes a practical proposition.

2.5.4 Field of View

Some of the larger sources, such as nearby galaxies and clusters of galaxies, require a field of view of $\sim 10°$ in order to view them with a single pointing. A large field of view is clearly important for a survey instrument which must observe the whole sky within a fixed mission lifetime. A large field of view has the further advantage that it increases the chance of serendipitous source discoveries during specific pointing observations.

2.5.5 Spectral resolution

The accurate determination of continuum spectra and the detection of line features requires only moderate spectral resolution ($\sim 10\%$ at 150 keV) such as may be provided by scintillation detectors. However the accurate measurement of spectral features such as cyclotron lines, which contain vital information on the processes occurring in the source, requires the use of special instruments such as germanium spectrometers which offer very high spectral resolution.

Chapter 3

HARD X-RAY IMAGING TECHNIQUES

3.1 Introduction

The previous chapter provided a brief outline of the challenges facing X-ray astronomy and served to indicate the progress in observational capability which will be required in order to succeed in the aims outlined there.

So far, most observations in the hard X-ray band have been made using collimated telescopes. In such instruments the field of view is restricted to a few degrees by either active or passive shielding, so that the angular resolution of the telescope is determined by the field of view. Such an instrument offers none of the advantages of true imaging which will be introduced later in this section. An example of this type of instrument is the MIFRASO balloon-borne telescope [14], a successful instrument with a total detector area of 3200 cm^2 passively collimated to provide a $2° \times 2°$ field of view.

In order to provide coverage of the hard X-ray waveband (15 – 250 keV) in such a way that the results may be correlated with observations in other wavebands, there is a clear need for X-ray telescopes capable of high angular resolution measurements. In a $1° \times 1°$ field in the galactic plane, there may be some 15000 stars brighter than magnitude 18. This value translates to ~5 sources within a $1'$ error circle, and so to overcome the

problems of source confusion and enable unambiguous source identification requires an angular resolution of this order.

An imaging telescope has many advantages over a non-imaging one. The most obvious advantage is simply that point sources can be located with high precision within a much larger field of view, and thus a single observation may contain many resolvable sources increasing the amount of science provided by the telescope many times. As demonstrated by the Spacelab 2 low energy X-ray telescope images of the galactic centre, an imaging telescope can resolve multiple sources within a complex region which would lead to confusion in a non-imaging telescope. This will become increasingly important as the sensitivity of telescopes improves, and the number of detectable sources increases.

An imaging telescope allows simultaneous measurements of both the background counting rate (obtained from an empty sky region) and the source flux. This assessment of the background is continuous, such that a varying background due to, for example, passage through radiation belts, may be continually monitored. With a non-imaging telescope, background assessment can only be achieved by periodically moving the telescope off the source onto a (supposedly) empty sky region, reducing the on-source time of any observation.

Whereas a collimated telescope such as MIFRASO may be particularly valuable in studying the spectral and temporal variations in known or likely candidate X-ray emitters, a wide-field imager is essential if an instrument is to carry out a comprehensive survey of the hard X-ray sky. It may be estimated that an imaging telescope with a large detection area (3000 cm^2) and a field of view of $\sim 10°$, in a highly eccentric orbit, could detect in excess of 1000 sources in a mission spanning 2 years. Such a survey could never be undertaken with a collimated telescope.

However, it is not possible to produce hard X-ray images by the methods employed in other wavebands. Specifically, hard X-ray photons cannot be refracted or reflected, making conventional focussing optics impossible. Grazing incidence optics, as employed in the mirror system for the Einstein X-ray satellite observatory [57] and ROSAT [4], can only be used at energies up to a few keV. Consequently, a hard X-ray image must be formed by an indirect method. Furthermore, in astronomical imaging at these high energies, the flux from the source may be small compared with the background. This

implies that long observations with large detectors will be required to obtain a statistically significant detection, and any imaging technique used should make efficient use of the incident source photons.

Due to the lack of focussing optics which will work in the hard X-ray waveband, other techniques have been developed to provide an imaging capability. The technique upon which all recent hard X-ray telescopes have been based is that of indirect imaging by flux modulation. Telescopes of this type modulate the incoming photon flux to encode the position of the source into the pattern observed at the detector. This pattern can then be computer processed to yield the original source distribution. The modulation may be either temporal or spatial depending on the type of aperture and detector used. Examples of this type of imaging are Coded Aperture Mask (CAM) imaging, Rotation Modulation Collimator (RMC) imaging and Fourier Transform Collimator (FTC) imaging.

This chapter will review the techniques applicable to hard X-ray imaging systems. Where relevant, examples will be drawn from those telescopes already designed or in operation which feature these techniques. A comparison of the various imaging schemes will be given, along with an indication of their suitability for use in conjunction with various types of detector.

3.2 General Principles of Modulation Imaging

Modulation imaging is an indirect imaging method whereby a specially designed aperture is placed between the source and detector. The detector then records a flux distribution which bears no obvious relation to the source being observed but is, in fact, the modulated incoming source flux. A knowledge of the nature of the modulation pattern may then be used to reconstruct the true source distribution. The modulation may either be a function of time or position across the detector, and these techniques are hence known as temporal or spatial modulation respectively. In a telescope employing temporal modulation, the location of the source is derived from the characteristic rise and fall in the photon flux with time, and it is therefore not necessary to use a position sensitive detector. Conversely, a spatial modulation imager requires a position sensitive detector in order to record the spatially modulated flux.

Assuming a linear system, that is, one in which the modulation is independent of source parameters such as photon energy, the detected flux distribution, D, can be generally represented mathematically [8] by the following (see also Figure 3.1):

$$D(x,y,\phi) = \int_{-\infty}^{\infty}\int_{-\infty}^{\infty} A(x,y,\xi,\eta,\phi)S(\xi,\eta)d\xi d\eta \tag{3.1}$$

where $S(\xi,\eta)$ represents the source distribution and $A(x,y,\xi,\eta,\phi)$ the modulation when the modulator is at a position ϕ relative to the detector.

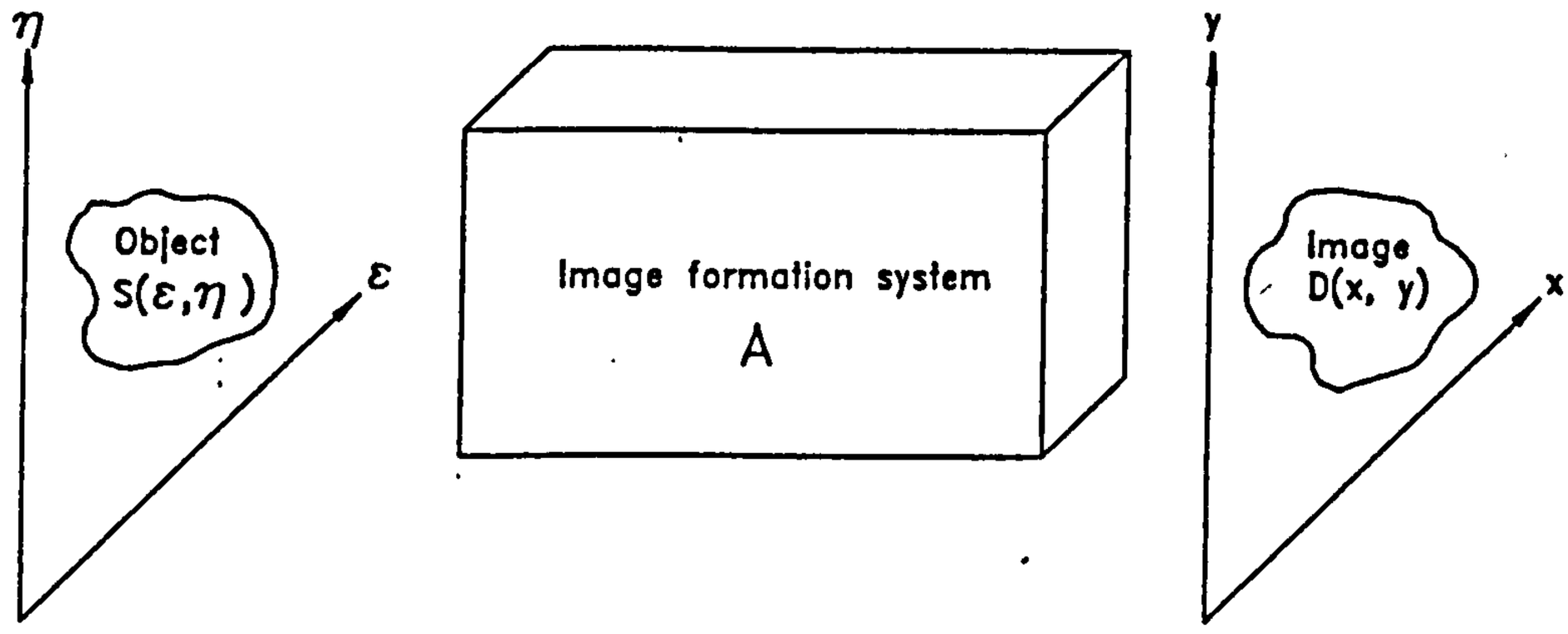

Figure 3.1: *A generalised imaging system*

For spatial modulation systems, the detector and modulator are permanently aligned, and so there is no ϕ dependence.

$$D(x,y) = \int_{-\infty}^{\infty}\int_{-\infty}^{\infty} A(x,y,\xi,\eta,)S(\xi,\eta)d\xi d\eta \tag{3.2}$$

whereas in a temporal modulation system the detector used is not position sensitive, and we have

$$D(\phi) = \int_{-\infty}^{\infty}\int_{-\infty}^{\infty} A(\xi,\eta,\phi)S(\xi,\eta)d\xi d\eta \tag{3.3}$$

In both cases, an estimate of the source distribution can be obtained by a number of methods, the two most commonly used being cross-correlation and inverse transform deconvolution. In a cross-correlation, the recorded data is compared with that expected for a point source at each point in the field of view, and the positions with the highest correlation are given the highest probability of emission. Inverse fourier transform methods are made possible by the mathematical properties of the chosen apertures which sample the object scene at certain spatial frequencies.

3.3 Temporal Modulation Imaging

In an imaging system employing temporal modulation, the incoming photon flux is modulated by the movement between the source and the detector of one or more grids made from alternating opaque and transparent stripes. These grids may be moved across the source either by scanning or rotating the entire telescope. The position of the source is then encoded into the variation of count-rate seen at the detector. As it is only the detected count rate which determines the source position, there is no need for a position-sensitive detector, and it is this simplification of the detector which is the main advantage of the temporal modulation imagers.

The simplest system is a single linear-scan modulation collimator which gives a one-dimensional profile of the source distribution. If the telescope is rotated about a fixed axis, a two-dimensional image may be obtained. In both cases, the image quality may be improved by the combination of data from several modules with slightly different imaging characteristics.

An additional advantage of the temporal modulation imaging systems is that the telescope platform need not be completely stabilised. For a rotating modulation collimator, a spin stabilised platform is ideal and this allowed early experiments of this type to be rocket-borne.

However, temporal modulation imaging systems do have some disadvantages. In their basic form they are unsuitable for the observation of variable and transient sources such as gamma-ray bursts since the source variability interferes with the modulation

process. Additionally, as the grids used have a transmission of 50%, a standard bi-grid collimator has an average aperture transmission of only 25%. This reduced sensitivity is characteristic of this type of system, and the situation may be made even worse if additional grids are used to improve the imaging characteristics.

Most temporal modulation imagers used to date have operated in the soft X-ray band where the grids can be made thin and hence narrow (with corresponding high angular resolution) while still attenuating the incident photons sufficiently. In the hard X-ray band, several millimetres of highly absorbing material is required in order to provide a sufficient modulation depth, and to avoid vignetting, the stripes must be of at least the same width as this thickness. This clearly implies a theoretical limit to the angular resolution which may be attained with such a system.

3.3.1 Linear-scan Modulation Collimator

In 1965, the linear-scan modulation collimator (LMC) was proposed by M. Oda [106] as an imaging technique which could improve on the simple slat collimator. The general principle is shown in Figure 3.2. A modulation collimator consists of two or more grids, each having parallel linear slits, separated by a distance D which is large compared with the slit width d. As the collimator is scanned across a source (usually by rocking the telescope) the source flux is modulated. The count rate at the detector varies as a function of time with a sawtooth shape, and contained within this modulated signal is information on the source distribution in one dimension. The background is not modulated, thus allowing simultaneous assessment of the source and background levels.

Unfortunately there is a periodic ambiguity within the information due to the period of the modulation pattern, P, which is given by

$$P = \frac{2d}{D} \tag{3.4}$$

The angular resolution of a bi-grid modulation collimator can be written as:

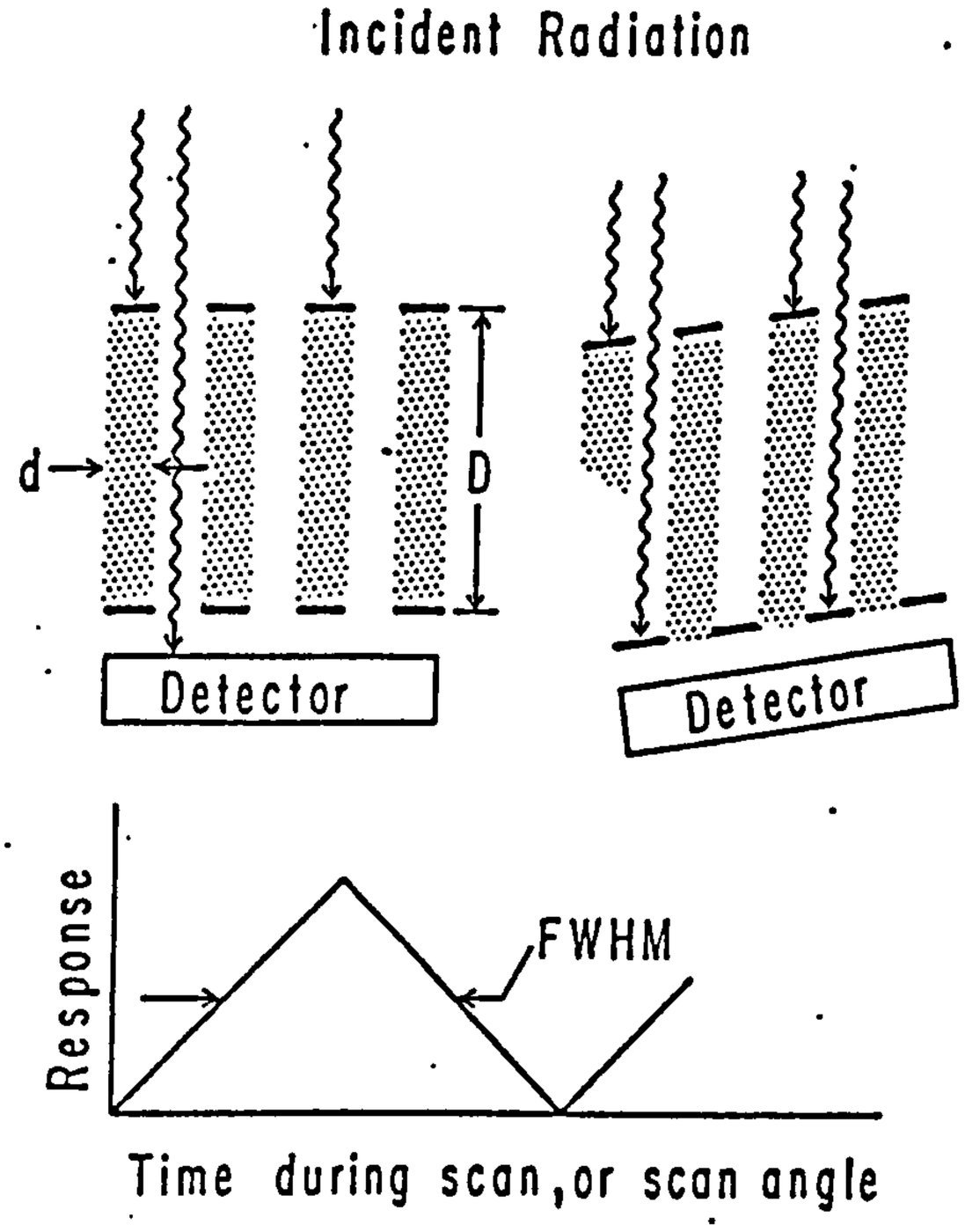

Figure 3.2: *Principle of the bi-grid collimator (from [75])*

$$\Delta = \frac{d}{D} \tag{3.5}$$

The ambiguities can be reduced by placing additional grids into the modulator. This increases the ratio of P to Δ and hence the imaging capability of the system is enhanced (Figure 3.3). However, as each grid has a transmission of only 50% this can only be done at the expense of reduced aperture transmission.

As such a collimator system in fact measures a single Fourier component of the source scene [75], it has been proposed [97] that many such collimators with different orientations and grid spacings can be used to survey many Fourier components of a scene. The data from these individual detectors can then be recombined by inverse fourier transform to form an image in a process strongly analogous to the aperture synthesis techniques used in radio astronomy. This type of imaging system is known as a multi-pitch modulation collimator.

A LMC telescope was used to locate the position of Sco X-1 to an accuracy of $\sim 1'$

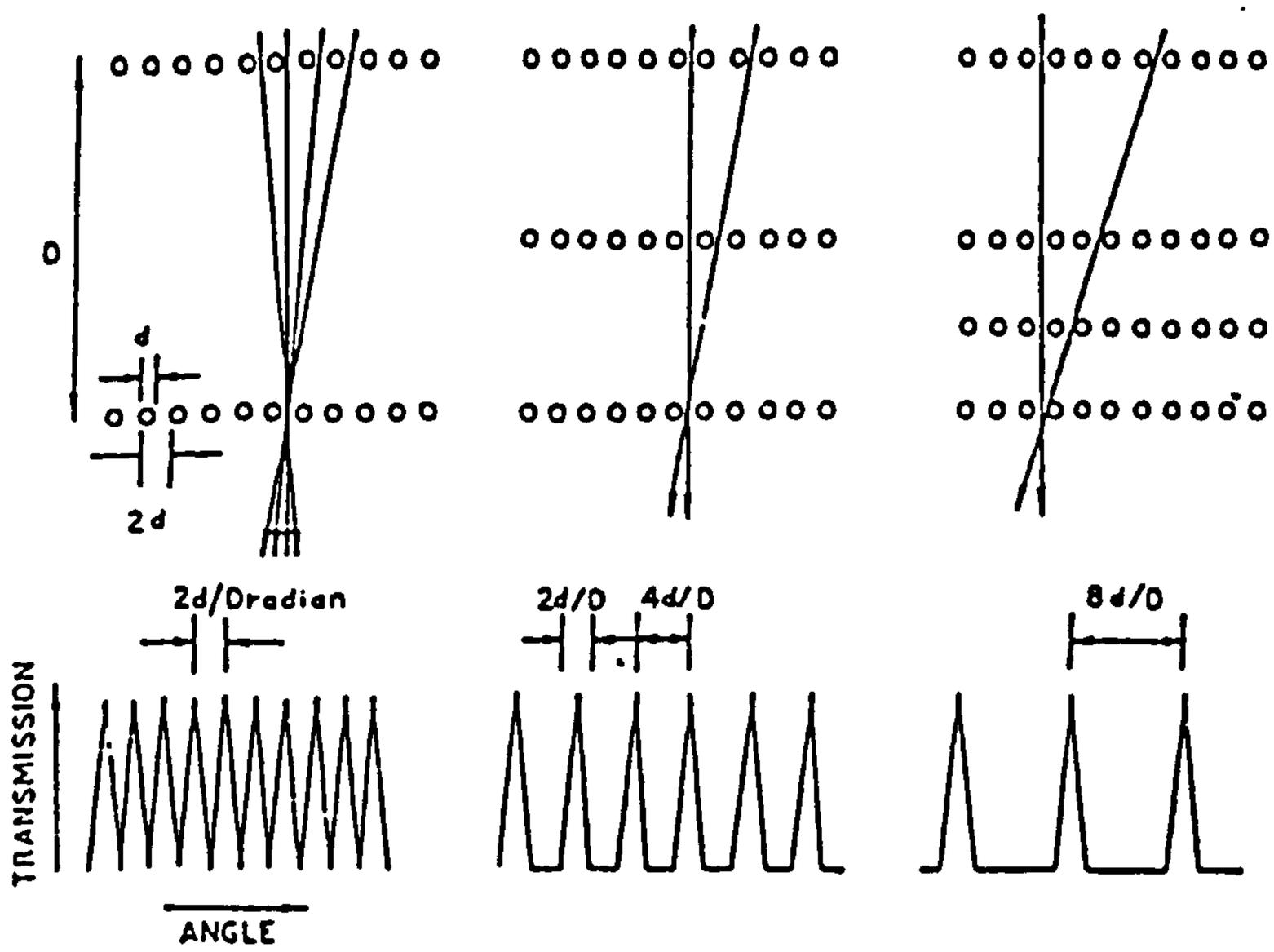

Figure 3.3: *Multi-grid LMC*

[96]. This was a multi-grid collimator which used the vernier effect between two sets of collimators with slightly different period P to resolve the ambiguities present in the image.

Pelling, 1987 [111] reports X-ray observations of the Crab Nebula using a scanning modulation collimator. The instrument used was a 4-grid collimator having an overall length of 1.5m. Each 1 mm thick modulator grid had a line pitch of 300 μm, giving an angular resolution of 22″. An image of the non-pulsed emission in two energy bands covering the range 22–64 keV is shown in Figure 3.4. This was obtained by a maximum entropy deconvolution of the two-dimensional X-ray brightness distribution.

3.3.2 Rotating Modulation Collimator

A rotating modulation collimator consists of two identical grids of equal-width opaque and transparent rulings, as in a linear modulation collimator. In the case of the RMC, however, the modulation is no longer produced by scanning across the source but by pointing the collimator in one direction and rotating the system about a fixed axis. The source flux from any direction within the field of view is modulated in a complex but unique way, with the characteristic features of fourier frequency spectrum and phase

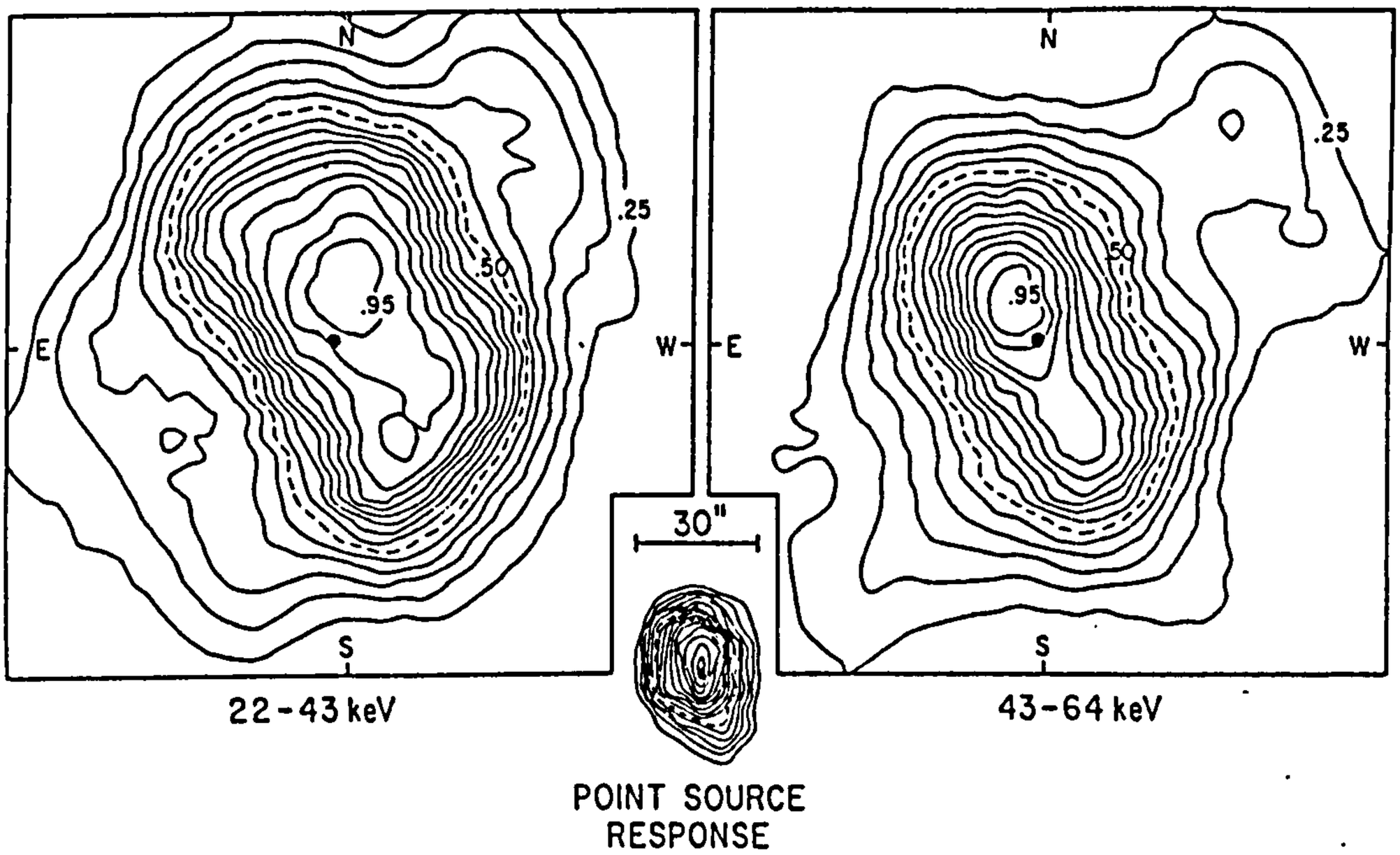

Figure 3.4: *An image of the Crab pulsar obtained with an LMC (from [111])*

being dependent on the angle between the rotation axis and the source and the azimuthal angle respectively (Figure 3.5).

The original source distribution can then be recovered either by using an inverse fourier transform [123] or by cross-correlation between the observed modulation pattern and the expected pattern for a point source at each pixel in the field of view [35].

As with the linear scan modulation collimator, the RMC preferentially samples the image at one spatial frequency causing the auto-correlation function to be a peak surrounded by large circular sidelobes (Figure 3.6a). This problem may be reduced by using a number of modules sampling at different frequencies, such that when the images from these are added together with a suitable weighting, each will contribute to the central peak whilst the sidelobes are significantly reduced, resulting in a much improved system point-spread function (Figure 3.6b). This type of instrument is known as a multi-pitch RMC [34].

A further enhancement of the basic RMC design is the phoswich RMC [38], in which the lower grid is replaced with two segmented detectors (Figure 3.7). This has two advantages:

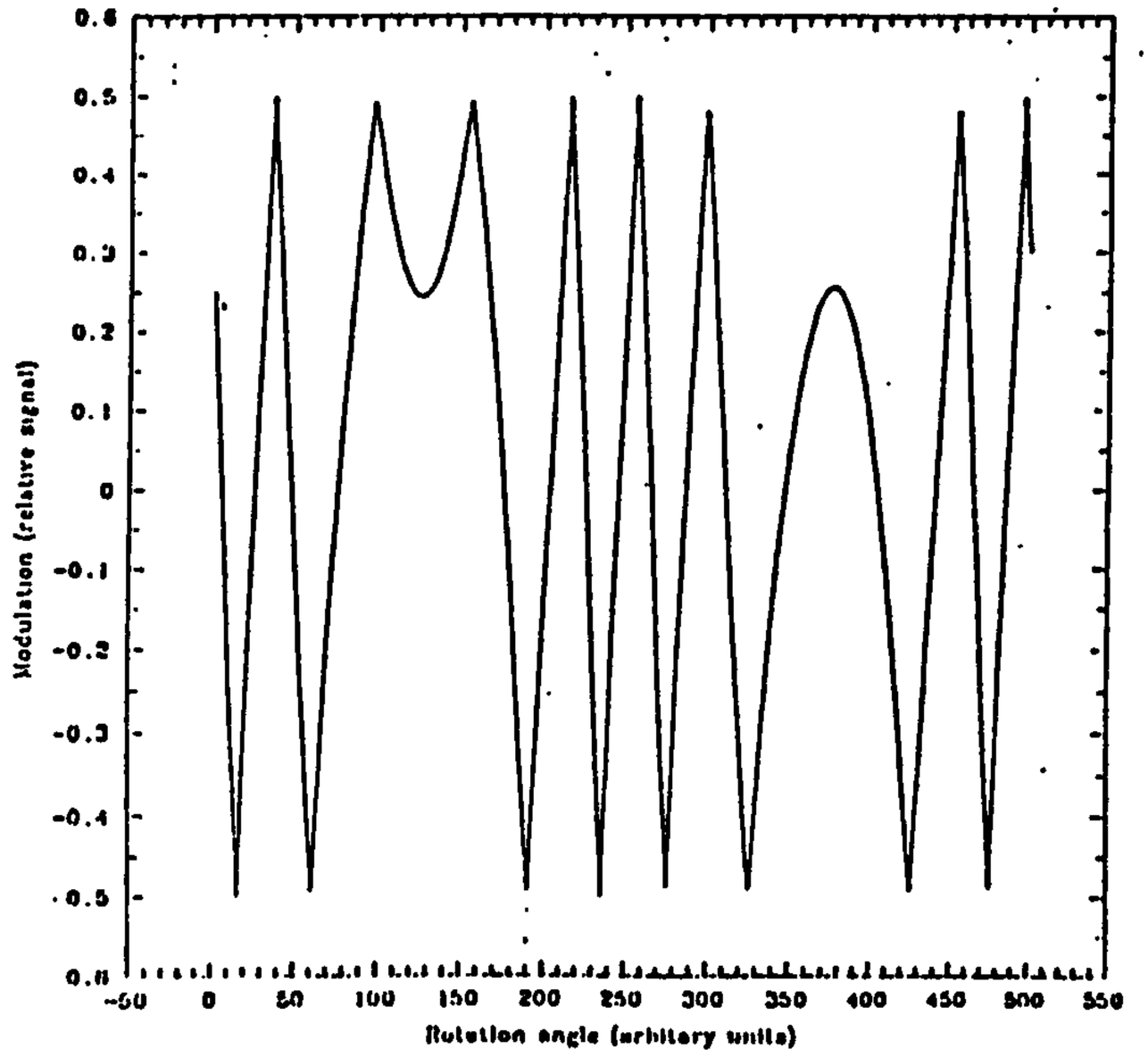

Figure 3.5: *Typical modulation of a RMC (from [55])*

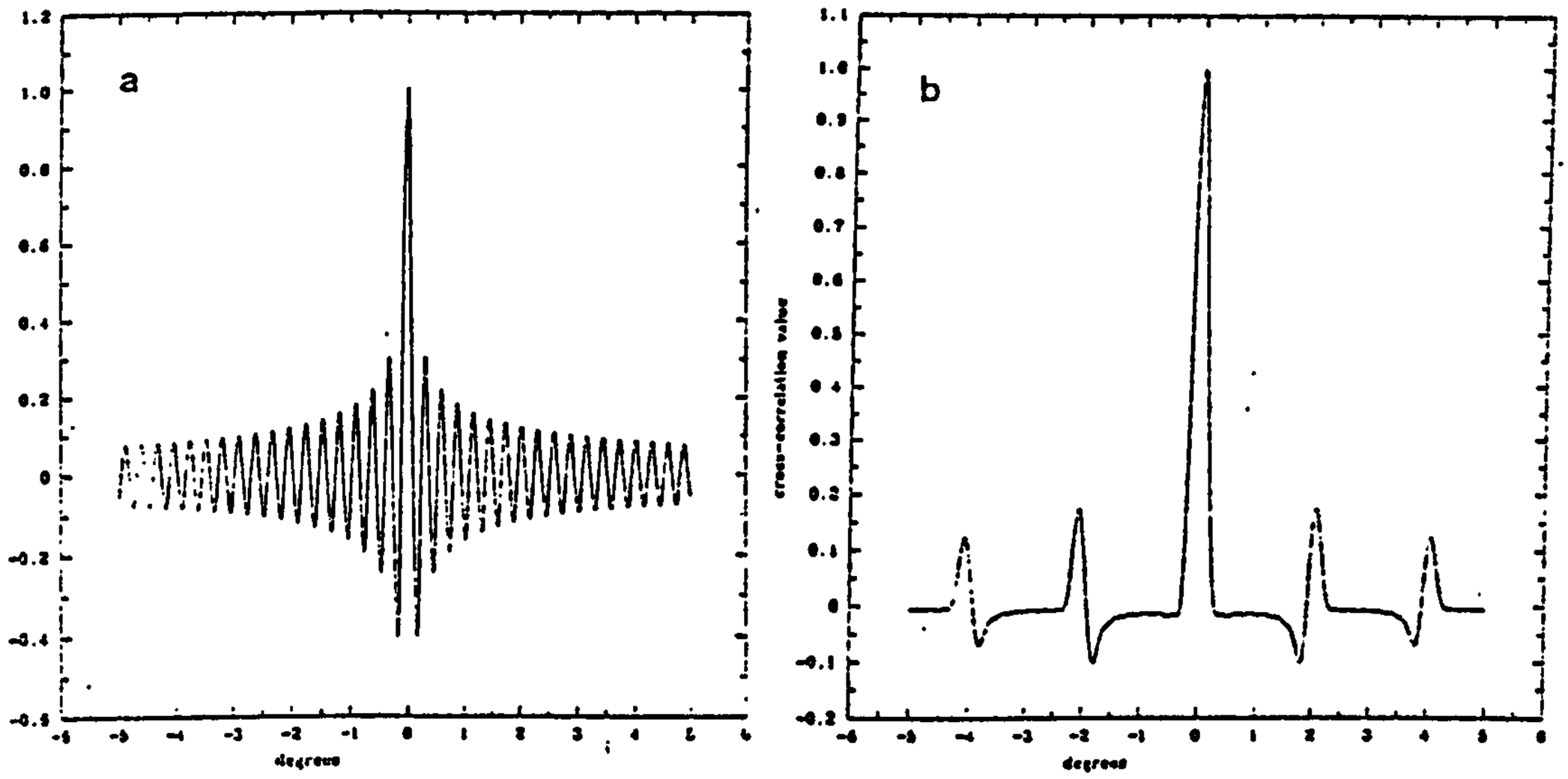

Figure 3.6: *Point-spread function for (a) a single RMC (b) a multi-pitch RMC (from [55])*

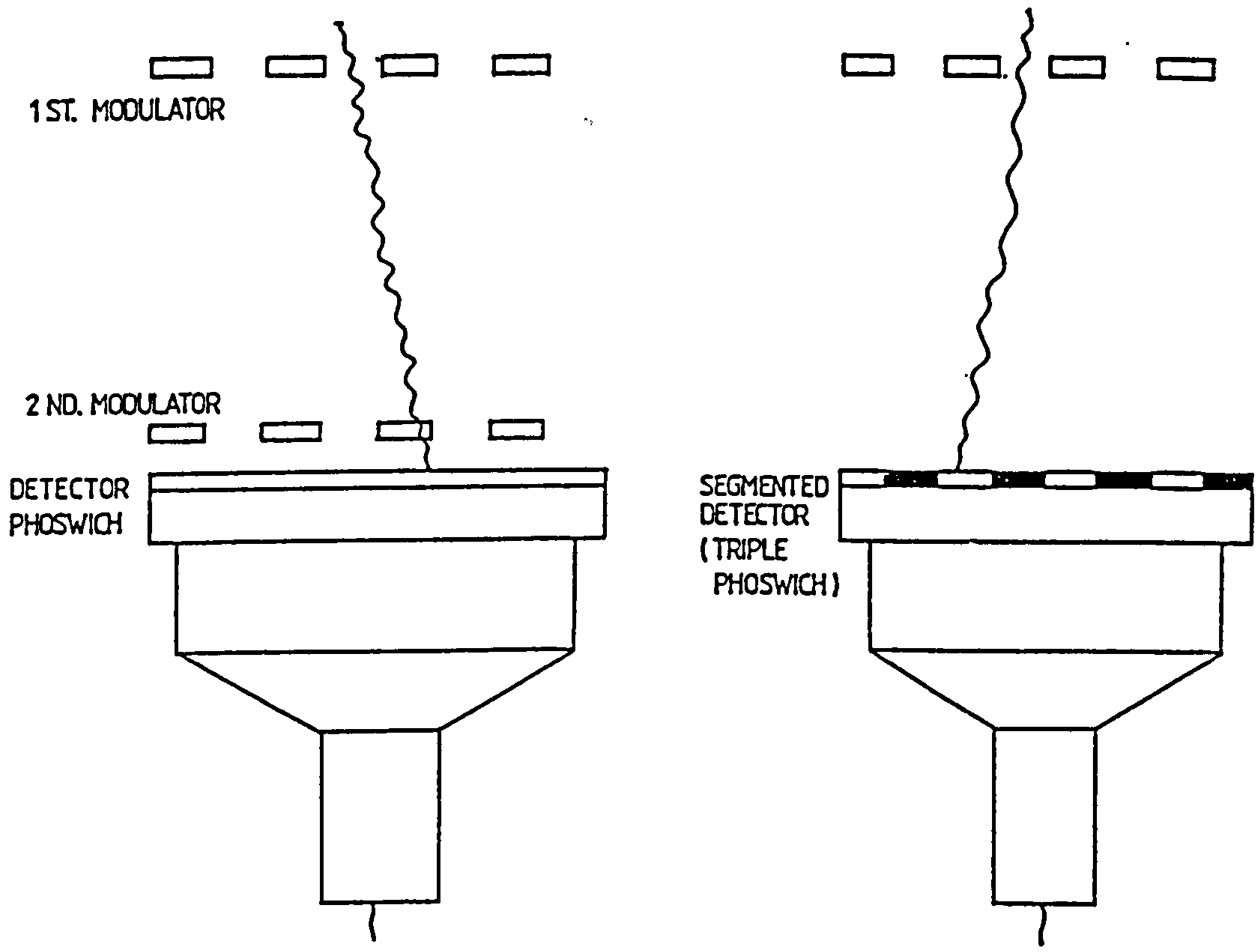

Figure 3.7: *The principle of (left) a classic RMC, and (right) a phoswich RMC*

i) The sensitivity of the telescope is doubled as the single-grid collimator has a transmission of 50%.

ii) The detector becomes useful for the observation of variable sources such as some X-ray binaries and AGN. The standard bi-grid RMC is not suitable for these observations as the time structure of the emission interferes with the temporal modulation of the imager. In a phoswich RMC, the sum of the detector signals can monitor the flux, and hence the variability, whilst the ratio of individual detector counts to the total count measures the modulation. The RMC detector used on the WATCH experiment [95] successfully observed gamma ray bursts over a field of view of 120° using this technique.

RMCs have been used to a considerable extent in X-ray astronomy. The first experiments were rocket-borne and took advantage of the spin of their launch vehicles. In the early 1970s, 3 RMC telescopes operating in the 2-10 keV band were launched on spin-stabilised *Skylark* rockets. More recently, two RMCs for operation in the 2-11 keV energy band with a total effective area of 356 cm^2 were carried on the SAS-3 satellite. The grids were

formed from 75μm diameter tungsten wires, and were separated by 112mm and 58mm, giving angular resolutions of 2.3 and 4.5 arc min respectively, over a field of view of 12° by 12° [46].

In the case of SAS-3 the energy range was determined by the argon-filled proportional counter detectors used, but it is clear that extension of this technique to higher energies requires more consideration of the mechanical aspects of the system. A RMC has been constructed for use up to 100 keV using 2 mm molybdenum wires and a phoswich detector with a sensitive area of 760 cm^2 [135]. The multi-pitch RMC telescope for the proposed CHIXSAT experiment was designed to operate over the 20 - 200 keV energy range with a sensitive area of 3000 cm^2. The proposed telescope consisted of 14 modules, each a separate phoswich RMC with a thick (4mm) lead or tungsten collimator grid required to provide modulation at the hard X-ray energies.

3.4 Spatial Modulation Imaging

The second class of modulation imaging systems consists of those which employ spatial modulation of the incident photon flux. A pair of grids, or a mask comprising opaque and transparent elements, is used to cast a shadow of each source in the field of view onto a position-sensitive detector,and if the aperture is designed in such a way that the shadow cast by a source in any part of the field of view is unique, the shadow may be used to reconstruct the source distribution.

The detectors required in such systems are very different to those used in temporal modulation imagers. The need for spatial resolution in at least one dimension imposes more complexity on the detector. Furthermore, the source, mask and detector must be kept permanently aligned, and this places great importance on the pointing accuracy and stability of the telescope platform, whether it is a balloon-borne or satellite instrument.

The two techniques which will be discussed are Coded Aperture imaging using a mask consisting of opaque and transparent elements, and the Fourier Transform Telescope which combines a bi-grid collimator and a position-sensitive detector.

3.4.1 Coded Aperture Imaging

In coded aperture imaging systems, a mask consisting of an array of opaque and transparent elements is set between the source(s) and a position sensitive detection plane, and hence every source within the field of view projects a shadow of the aperture on to the detection plane. The aperture must be designed such that the shadow projected by a source at any position within the field of view is unique and hence this shadow may be used to reconstruct the source position. This is shown schematically in Figure 3.8. The area of the aperture projected onto the detector by a point source is referred to as the basic pattern or the working zone. A complete mask is normally constructed from a 2 x 2 mosaic of the basic pattern, with one row and one column removed to avoid any ambiguities in the source location, this geometry giving the largest possible field of view for any given detector size [25].

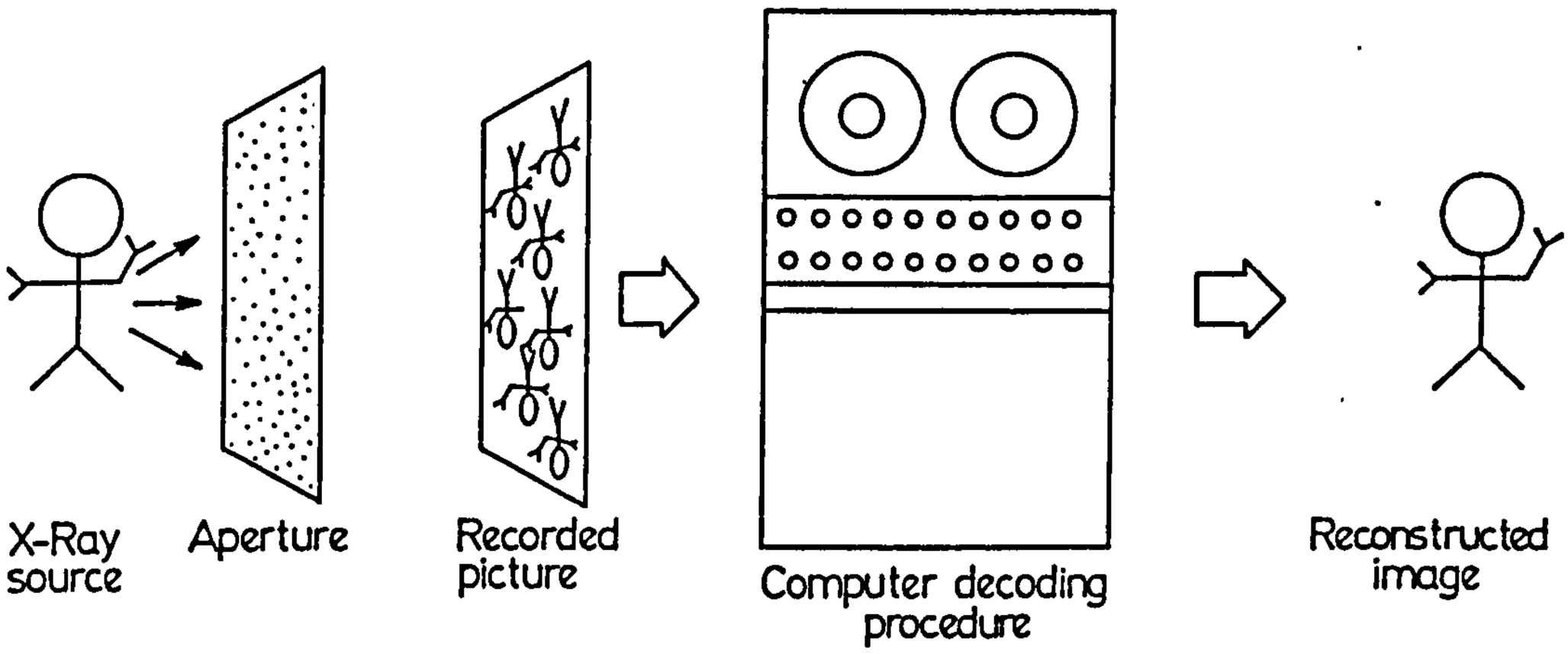

Figure 3.8: *Principle of Coded Aperture imaging*

The angular resolution of a coded aperture system is defined as

$$\Delta = \frac{d}{D} \tag{3.6}$$

where d is the characteristic size of the mask elements, and D the distance between the mask and detector. The point-source location accuracy is determined by the accuracy with which the mask shadow on the detector may be located, and hence is dependent on the detector resolution. In all cases the detector resolution should be small compared

with the mask size to prevent the misbinning of photons causing a serious reduction in the signal-to-noise ratio of the image. For a telescope with a mask-detector separation of 3m, achieving a point-source location accuracy of 1′ requires a detector with a spatial resolution of < 1 mm, a level of performance currently beyond hard X-ray detectors.

3.4.1.1 Image formation & reconstruction

If the source plane is denoted by $S(x, y)$ and the aperture transmission function by $A(x, y)$, then the spatial distribution of the detected flux may be written

$$D(x, y) = A(x, y) * S(x, y) + B(x, y) \tag{3.7}$$

where $*$ is the convolution operator and B represents the source independent detector background. An estimate of the object $\hat{S}$ may be obtained by filtering the recorded shadow with a suitable function $G(x, y)$, in a process known as a cross-correlation deconvolution.

$$\hat{S}(x, y) = G(x, y) * A(x, y) * S(x, y) + G(x, y) * B(x, y) \tag{3.8}$$

Choosing G to be the inverse of A would, theoretically, yield a perfect estimate of the source distribution in the absence of noise. In practice, the near-singularity of A may cause a large amplification of the noise term, and both A and G must be carefully selected to minimise the noise introduced to the estimate. The progress in the development of apertures for this type of application may be seen from the following brief descriptions:

Fresnel Zone Plate The Fresnel Zone Plate (FZP) [104] is a circularly symmetric aperture with a theoretical transmission of $A(r) = \cos r^2$. In practice, this must be approximated by a series of concentric transparent and opaque annuli of equal area with radius $r_n = r_0\sqrt{n}$, where r_0 is the radius of the central disc which may be either transparent or opaque (Figure 3.9(a)). An ideal FZP possesses optimum imaging characteristics, however, the use of this discrete transmission function results in a point spread function, defined by the autocorrelation $A*A$, of a

central peak surrounded by a series of lobes which degrade the imaging performance (Figure 3.9(b)).

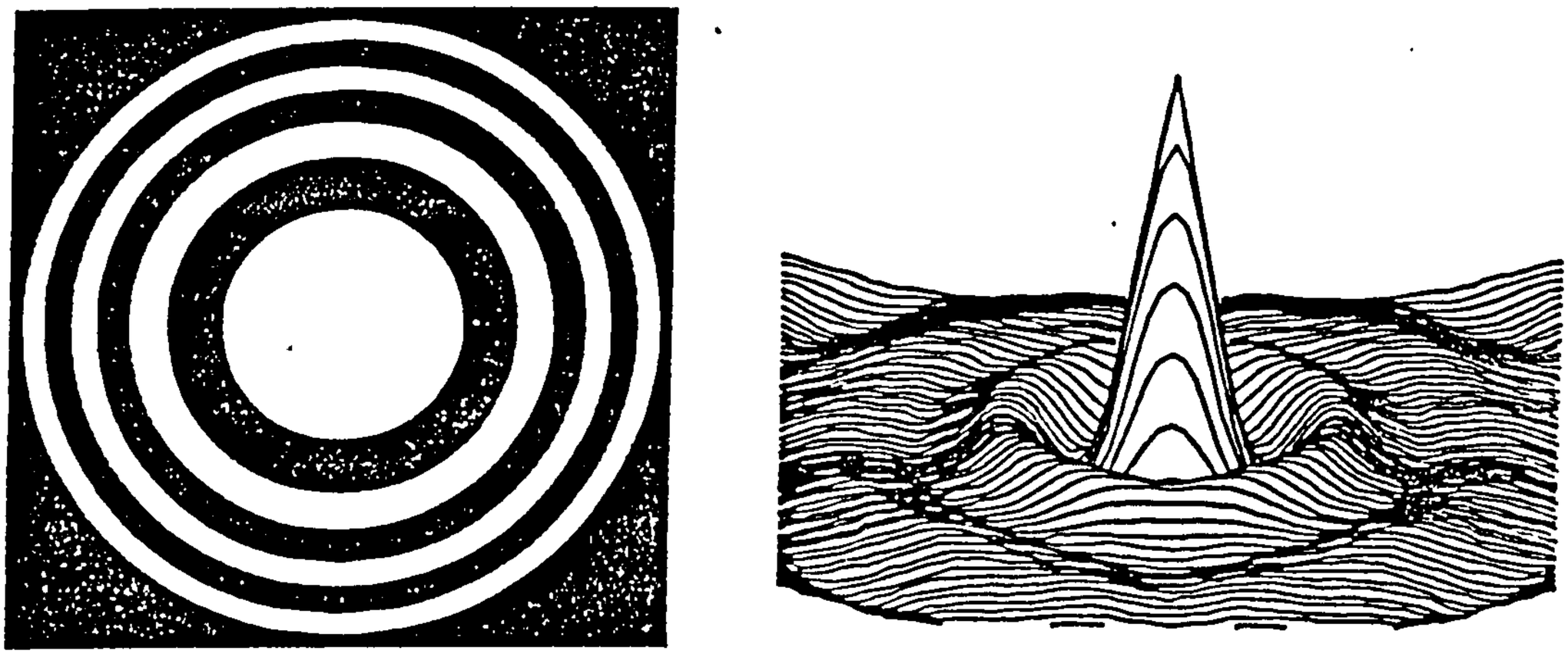

Figure 3.9: *(left) A Fresnel zone plate and (right) its autocorrelation function (from [25])*

Random Pinhole Masks Dicke [41] proposed the use of apertures of randomly spaced pinholes having an overall transmission of 50% for applications in X-ray and γ-ray astronomy. An example is shown as Figure 3.10(a). This technique is a logical extension of the single pinhole, which despite having optimum imaging characteristics, is of limited application due to a conflict between resolution and sensitivity. Random pinhole masks are limited by non-ideal imaging properties in the form of considerable structure in the autocorrelation function caused by preferential sampling of some spatial frequencies which can give rise to spurious peaks within an image. Random pinhole arrays have been successfully used for pinhole imaging of solar X-rays [22], and were also proposed for use in a X-ray burst detector operating in the 30-600 keV energy region [142].

Non- and Uniformly-Redundant Arrays To overcome the problems inherent in random masks, Golay [59] proposed the Non-Redundant Array (NRA) within which the separation between any two holes occurs once and once only. The autocorrelation of such an aperture is a single peak on a flat background with no sidelobes within a distance δ (where the maximum hole separation is 2δ). The transparency of a NRA ranges from ~1% to ~20% making them more suitable for use in nuclear medicine [50]. A typical NRA is shown in Figure 3.10(b). NRAs may in fact be regarded as a subset of the larger group of mask designs known

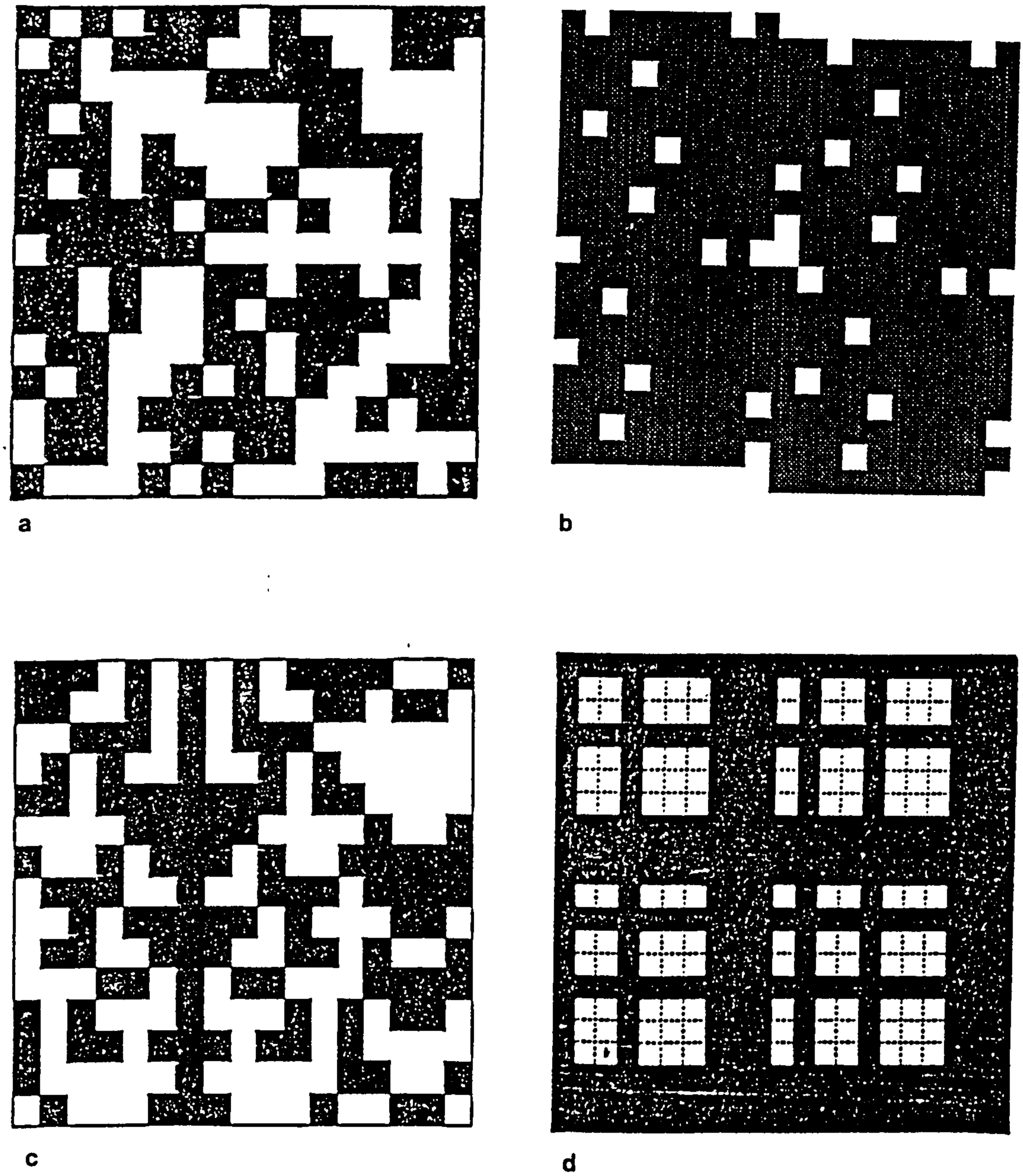

Figure 3.10: *Coded Aperture Masks: (a) Random pinhole array (b) Non-redundant array (c) Uniformly redundant array (d) Pseudo-noise product array*

as Uniformly Redundant Arrays (URAs). Proposed by Fenimore & Cannon [51], the feature of these designs is that each hole separation occurs the same number of times. NRAs and URAs may be constructed by various mathematical methods, and are formed from two types of Cyclic Difference Set, namely Hadamard and Singer sets. The transmission of masks constructed from Hadamard difference sets is always ~50%, making them popular for use in X- and γ-ray astronomy. Both NRA and URA masks have optimum imaging characteristics. By using a modified decoding array G such that

$$G_{jk} = \begin{cases} 1 & \text{if } A_{jk} = 1 \\ \tau/(\tau - 1) & \text{if } A_{jk} = 0 \end{cases}$$

the flat background can be removed from the deconvolved image. This type of deconvolution is referred to as 'balanced' due to the weighting assigned to the pixels. URA mask designs have been used in many astronomy missions operating over a wide range of energies using a variety of detectors. Examples are the SIGMA telescope on GRANAT which employs a 29 x 31 element URA [39] (shown as Figure 3.10(c)), the ZEBRA balloon-borne telescope with a 9 x 7 Hadamard pattern [143], and EXITE with a 11 x 13 URA array [64]. Other telescopes, both proposed and operational, employing URA masks are DGT [102], GAMMA-1 [5] and GRIS [134].

A further subset of the URA is the Hexagonal URA (HURA) [52] constructed from hexagonal elements. This type of mask has special rotational properties, and is ideal for use with a circular detector. A HURA mask has been successfully used in conjunction with a gamma camera in the Gamma-Ray Imaging Payload (GRIP) experiment [6] which operates in the hard X-ray and soft γ-ray band.

Pseudo-Noise Product Masks URAs and NRAs are limited to certain dimensions by the finite number of cyclic difference sets which may be used in their construction. A new family of masks known as Pseudo-Noise Product (PNP) masks have been developed to allow a wider range of mask dimensions, with some interesting additional properties. PNP masks are constructed from the direct product of two 50% 'transparent' pseudo-noise sequences and therefore have a transmission of ~25%. In addition they are always self-supporting. An example is shown in Figure 3.10(d). The autocorrelation of a PNP mask is a peak superimposed on a

cross structure. This cross structure may be removed by the use of a more suitable decoding array, giving a system with optimum imaging characteristics.

The choice of aperture type depends largely on the source distribution to be imaged. It can be shown that for a source which fills a substantial fraction of the field of view, a mask of lower transmission such as an NRA will give a higher signal-to-noise ratio. However, for astronomical use the URA is a standard choice, since it has 50% transmission, is optimum for the more sparse source distributions encountered in X-ray astronomy, and is never more than a factor of $\sqrt{2}$ worse than an NRA, even for the most uniform source distributions.

3.4.2 Fourier Transform Imaging

The term 'Fourier Transform Collimator' (FTC) may be used to describe several related imaging systems. Here it will be used to refer to a class of imagers based on the modulation collimator described in Section 3.3.1, but which have been adapted to spatial modulation instead of temporal modulation.

In the case of the FTC, the upper and lower grids of the collimator have a slightly different pitch [75,108]. As the detector is held stationary, the modulation of the flux is spatial rather than temporal, and a point source viewed by such a collimator has a count rate distribution with an approximately triangular profile on a spatial scale coarse compared to the grid dimensions (Figure 3.11). The period of this triangular pattern is given by

$$P = \frac{a_1 a_2}{a_2 - a_1} \tag{3.9}$$

The coarseness of the profile, this means that the detector used needs only a relatively modest position resolution in one dimension, provided that the profile of the flux falling on the detector can be adequately sampled.

As in the case of the LMC, each module measures a specific Fourier component of the angular distribution of the source [33]. For hard X-ray imaging, a set of Fourier components is recorded using a set of subcollimators with an appropriate range of grid

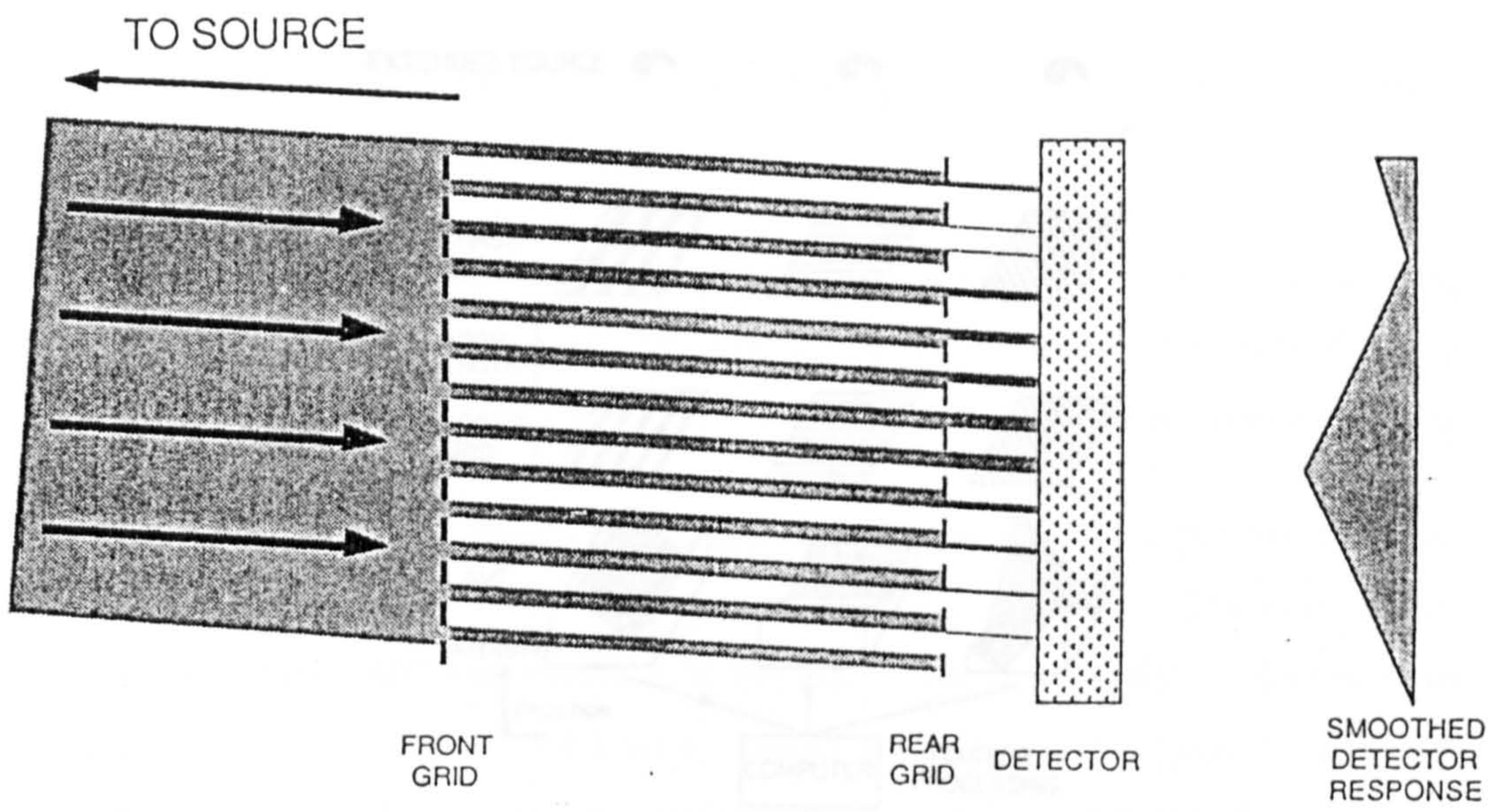

Figure 3.11: *General principle of the Fourier Transform Collimator (from [115])*

spacings and orientations. These data can then be recombined in a Fourier inversion process (Figure 3.12).

The angular resolution of a FTC telescope is again given by

$$\Delta = \frac{d}{D} \tag{3.10}$$

where d is the upper grid width and D the distance separating the two grids. It can be seen that the angular resolution does not depend on the detector resolution, which primarily influences the number of Fourier components sampled. In a practical system, a detector resolution of 1-2 cm in one dimension is sufficient to obtain arc second resolution with a grid separation of a few metres. Having resolution in two dimensions allows some of the grid alignment criteria to be relaxed. The detector resolution for a comparable system employing the coded mask technique would be <1 mm. The factors which fundamentally limit the potential resolution of this system are:

i) X-ray diffraction at the apertures.

ii) The ability to manufacture opaque grids at very fine pitches.

iii) The grid separation which can be allowed in a practical instrument.

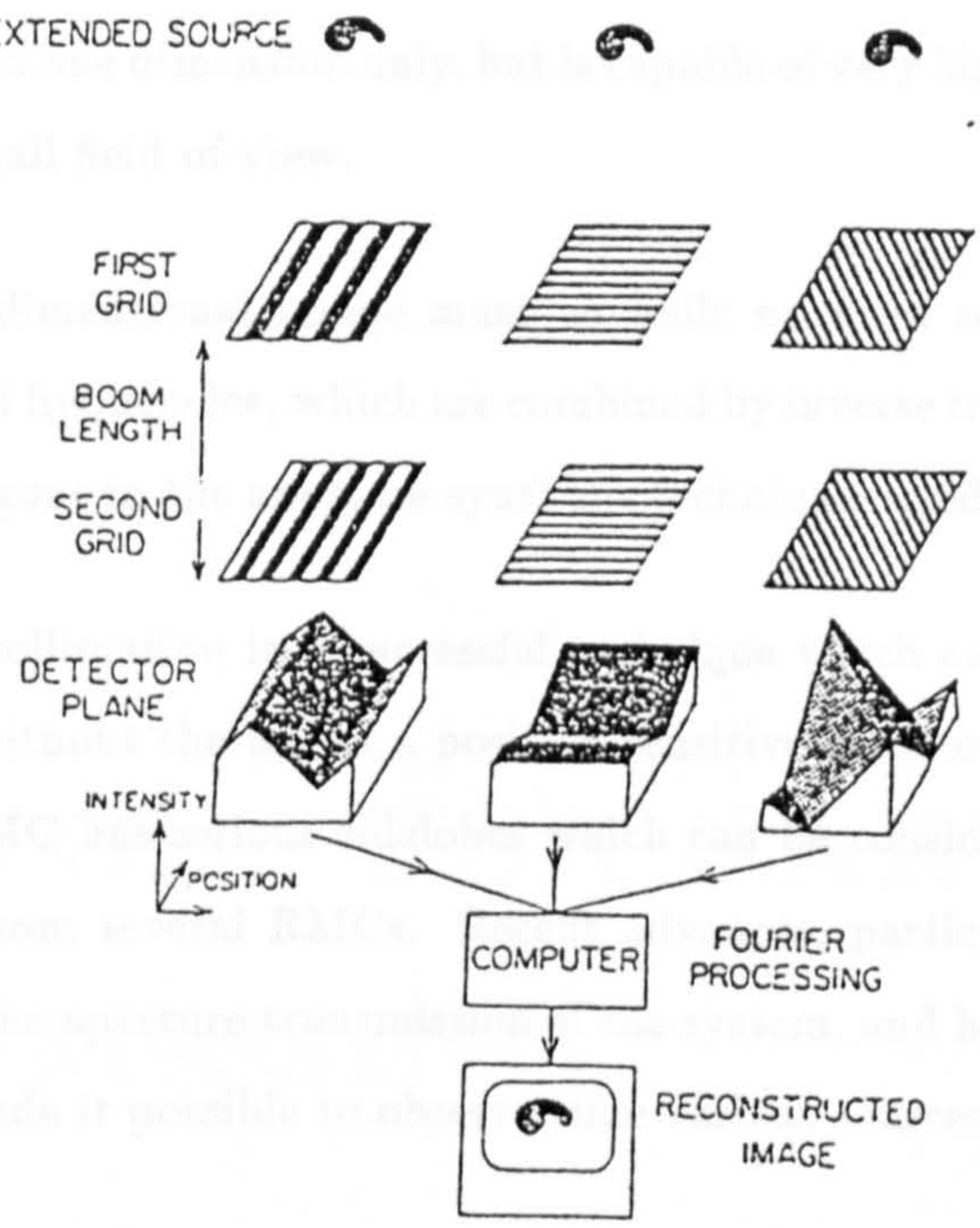

Figure 3.12: *Principle of the Fourier Transform Telescope (from [33])*

With the high attainable angular resolution by this method, the FTC has been applied primarily to the imaging of solar flare X-rays where the low sensitivity is of no great importance due to the relatively large flux present. The most ambitious proposal to date is for the shuttle-based Pinhole/Occulter Facility, with two grids of width $\sim 50\mu$m separated by a 50m boom to give a spatial resolution of 0.2 arc seconds [115]. Most solar observations have been confined to relatively low photon energies. Extension of this technique to cover the entire hard X-ray band requires new developments in the construction of thick grids.

3.5 Concluding remarks

The linear modulation collimator was introduced as a replacement for the simple slit collimator, but the periodic ambiguities present within the image from a simple bi-grid collimator rule it out for imaging anything but isolated point sources. These ambiguities can be reduced, but only by inserting extra grids and further reducing the mean aperture transmission.

The closely related Fourier Transform Collimator requires a position sensitive detector

with coarse resolution in one dimension only, but is capable of very high angular resolution observations over a small field of view.

In both cases, a two-dimensional image must be built up from scans taken at many orientations and spatial frequencies, which are combined by inverse transform methods, in a process closely analogous to the aperture synthesis techniques used in radio astronomy.

Rotation modulation collimation is a successful technique which can provide true two-dimensional imaging without the use of a position sensitive detector. The point spread function of a single RMC has serious sidelobes which can be considerably decreased by the addition of data from several RMCs. Recent advances, particularly the phoswich RMC, have increased the aperture transmission of the system, and hence the instrument sensitivity, and also made it possible to observe time variant sources.

All the systems employing grid collimators are suitable for high angular resolution applications and are limited only by the availability of suitable grids, the requirements for detectors being relatively simple to meet. To operate in the hard X-ray band, grid thicknesses of up to 5mm are necessary, and these be constructed to very high tolerances to avoid degrading the image quality. Crannell [33] has described ways of constructing tungsten grids of this thickness with apertures as small as 50μm.

Coded aperture imaging, however, is currently limited by the available position-sensitive detector technology. To avoid a significant reduction in signal-to-noise ratio, the mask elements should be at least twice as large as the detector resolution. Therefore, the angular resolution of the telescope, which is proportional to the mask element size, is limited by the detector resolution. At low energies below $\sim$ 50 keV, gas proportional counters can provide resolutions $\sim$1 mm. Above this energy, when the detectors are mainly scintillation counters, resolutions of $\sim$ 5mm are more practical. Advances in the fields of position-sensitive photomultipliers and discrete semiconductor detectors should greatly improve this situation.

Chapter 4

DETECTORS FOR HARD X-RAY IMAGING

4.1 Introduction

The descriptions of imaging techniques given in the previous chapter concentrated on the formation of the X-ray image but paid little attention to the way in which the image is recorded. In this chapter, the many detectors which may be used to record the incident X-ray flux will be reviewed, and their relative merits and applications discussed.

The first X-ray detector to be used, photographic emulsion, is in some ways still to be surpassed. The resolution of photographic emulsion is superb, but modern electronic X-ray detectors have other requirements to meet besides this. They should be capable of distinguishing the properties of incident radiations (energy, charge etc.) in order to both increase the scientific returns and reduce the background present in the image. In addition, as discussed in the previous chapter, due to the impracticality of direct focussing of X-rays, the flux at the detector may have been highly coded by the aperture and will require computer processing. All modern detectors ultimately convert X-rays to electronic signals which may be stored in digital form and processed as necessary.

All practical hard X-ray detectors record the amount of energy deposited within them due to an interaction between the material making up the detector and an incident

X-ray. The geometry of the detector and the way in which the energy deposit is recorded together determine which other characteristics of the incident radiation (e.g. type, position, polarization) may be determined. As the bias of this work is towards those imaging systems which employ spatial modulation of the incoming photons, the discussion of X-ray detectors in this chapter will naturally tend towards those detectors capable of determining the interaction position with the spatial resolution necessary for such systems.

The requirements for a position-sensitive detector which arose from the discussions of X-ray imaging techniques in Chapter 3 were:

- A detector spatial resolution of $\leq$2mm is required in order to build a telescope with the kind of angular resolution which has been shown to be necessary for applications in hard X-ray astronomy.
- The determination of the broad shape of the energy spectrum of the incident radiation requires the measurement of any energy deposit to better than ~10%. The investigation of features in emission spectra (e.g. gamma-ray lines) requires the use of detectors with much higher energy resolution.
- In order to produce a telescope with good sensitivity, it must be possible to construct a detector with a large uniformly-sensitive area.

The following requirements may be added to those listed above in order to specify a detector for use in practical astronomical applications:

- The detector should operate with high efficiency over a wide range of incident photon energies. Most detectors are only effective over a restricted range of energies, due to the nature of the fundamental interaction processes.
- A detector should be capable of recognising and rejecting at least some background events. Additionally, care must be taken to minimise the background by e.g. careful shielding and choice of materials. As an example, the neutron cross-section depends mainly on the detector volume and must be kept as low as possible.
- For use in a space environment, both the detector mass and power consumption must be carefully limited.

This chapter will first describe the ways in which hard X-ray photons can interact with matter, allowing them to be detected. Following this, several of the more common detectors will be discussed, with the emphasis being placed on their relative performances and their potential for application in X-ray imaging.

4.2 The Interactions of X-rays and Matter

In order to design a working detector of X-rays, it is necessary to understand the ways in which these photons interact with matter. Since photons carry no charge, their main interaction is with the electromagnetic field of the atom or its electrons. Photonuclear reactions can occur, but have a much lower probability. The primary interactions of X-rays with matter result in the production of energetic charged particles and it is these charged particles and their secondary interactions that transfer energy to the matter and make the incident photon detectable. Energetic photons interact with matter by means of six principal processes:

1. The photoelectric effect.
2. Rayleigh scattering.
3. The Compton effect.
4. Pair Production.
5. Resonance elastic scattering (Mössbauer effect).
6. Photodisintegration.

In the context of hard X-ray detection, only processes (1),(3) and (4) are of significant interest, and since the hard X-ray band under consideration (15–250 keV) prohibits pair production, photoelectric absorption and Compton scattering are the dominant processes.

The probability of an incident photon interacting in any of these ways is expressed as a cross-section per atom. The total cross-section will clearly be the sum of the cross-sections for the different interactions. The *linear attenuation coefficient*, μ is defined as

the total cross-section per atom multiplied by the number of atoms per unit volume. The attenuation of the X-rays is of the form

$$I = I_o e^{-\mu x} \tag{4.1}$$

where μ will be strongly energy dependent and x is the thickness of absorber through which the X-ray has passed. Graphs showing the linear attenuation coefficients for the three major interactions in sodium iodide (a common detector material) and lead (a shielding material) are shown as Figures 4.1 and 4.2 respectively.

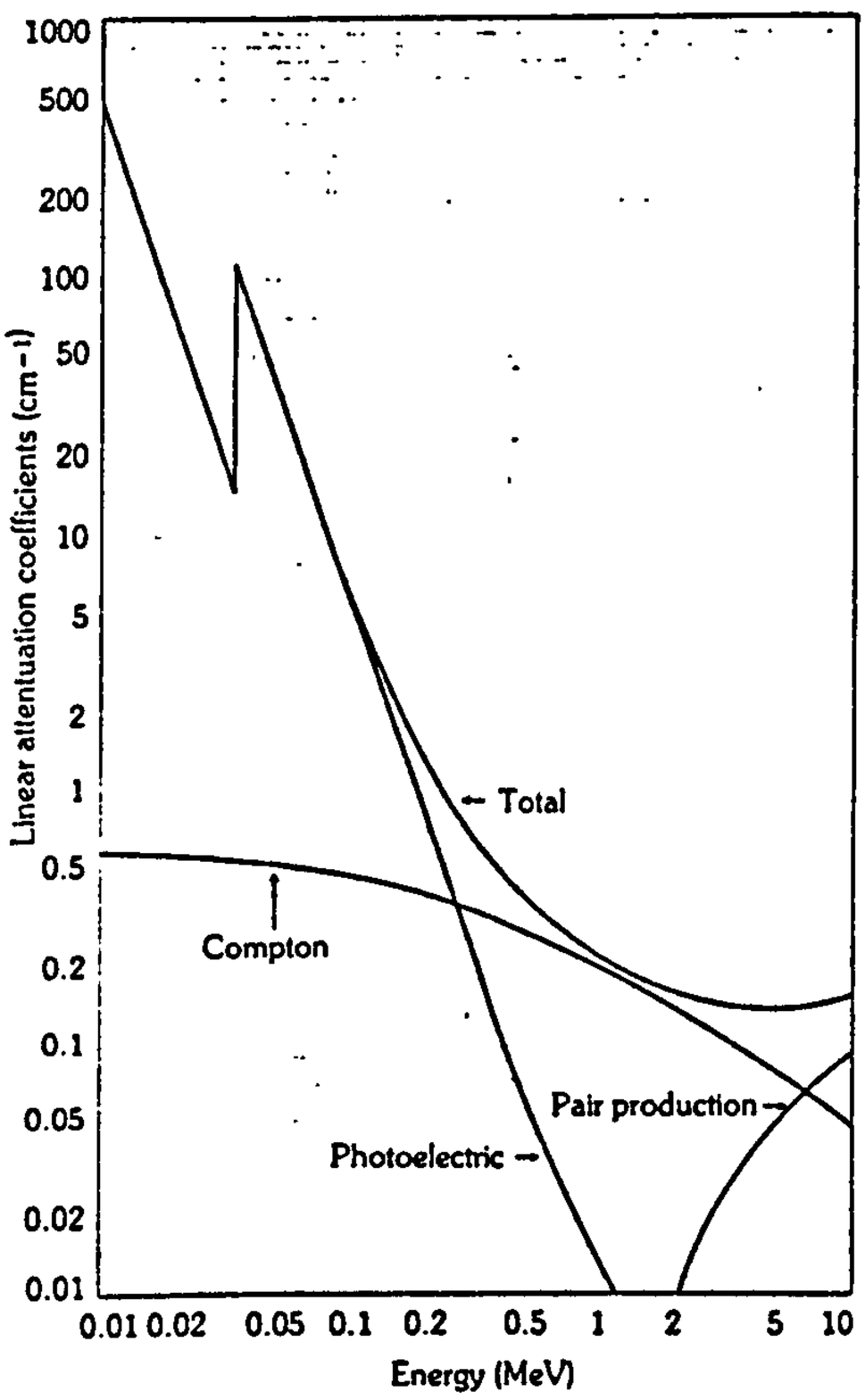

Figure 4.1: *The attenuation of X-rays in sodium iodide*

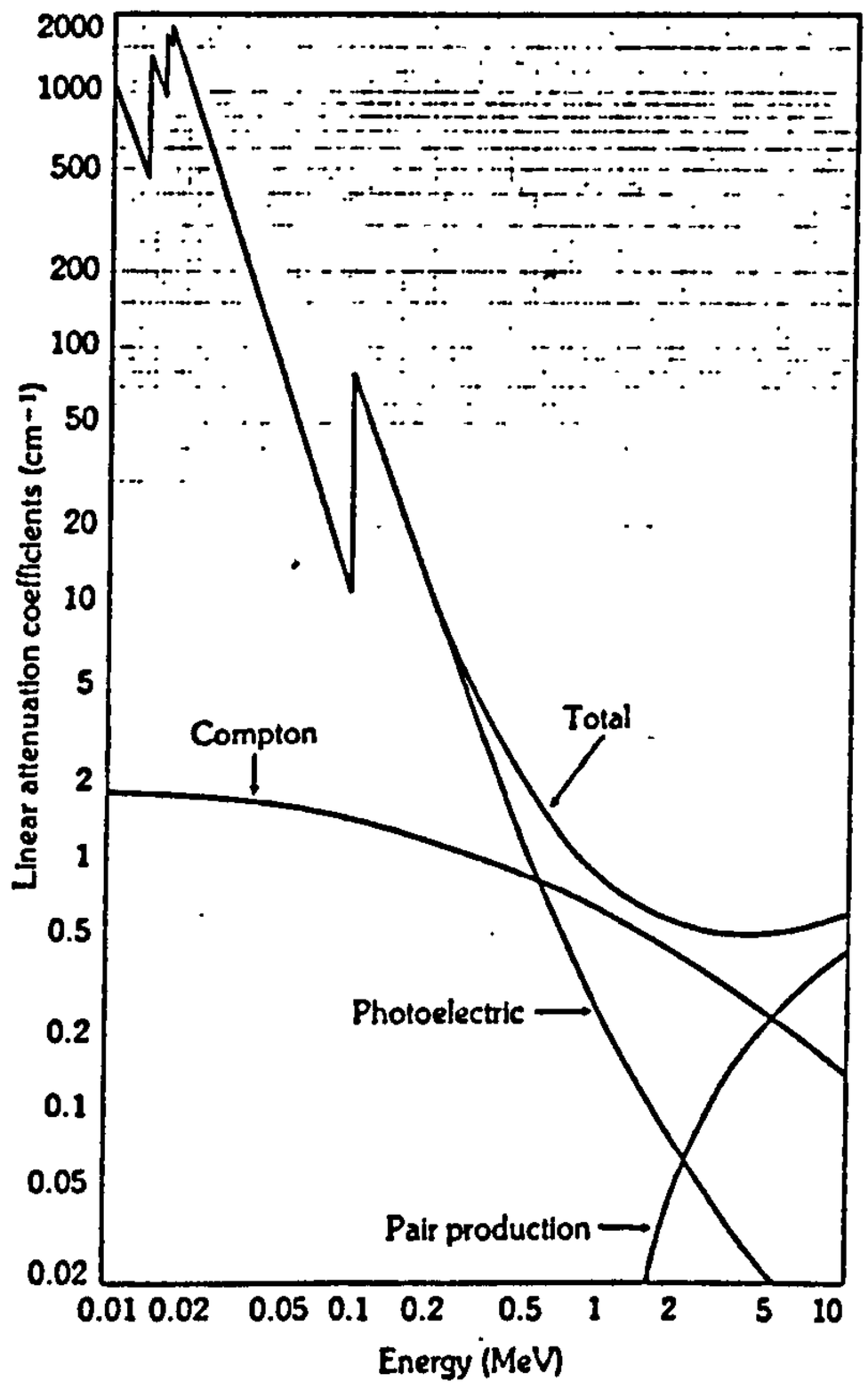

Figure 4.2: *The attenuation of X-rays in lead*

4.2.1 The Photoelectric Effect

The photoelectric process is the predominant interaction for photons of relatively low energy. In photoelectric collisions, the entire energy of the incident photon $h\nu$ is absorbed by one atom. An electron, usually from the K or L shell of the atom, is ejected with an energy given by

$$E = h\nu - B_e \tag{4.2}$$

where B_e is the binding energy of the ejected electron and h is Planck's constant. For energetic photons where $h\nu >> B_e$, i.e. greater than a few hundred keV, the electron carries off almost all of the incident photon energy. The vacancy in the inner shell is then filled by an electron from a higher level, with the emission of X-rays at energies characteristic of the material or Auger electrons. These processes are illustrated in Figure 4.3.

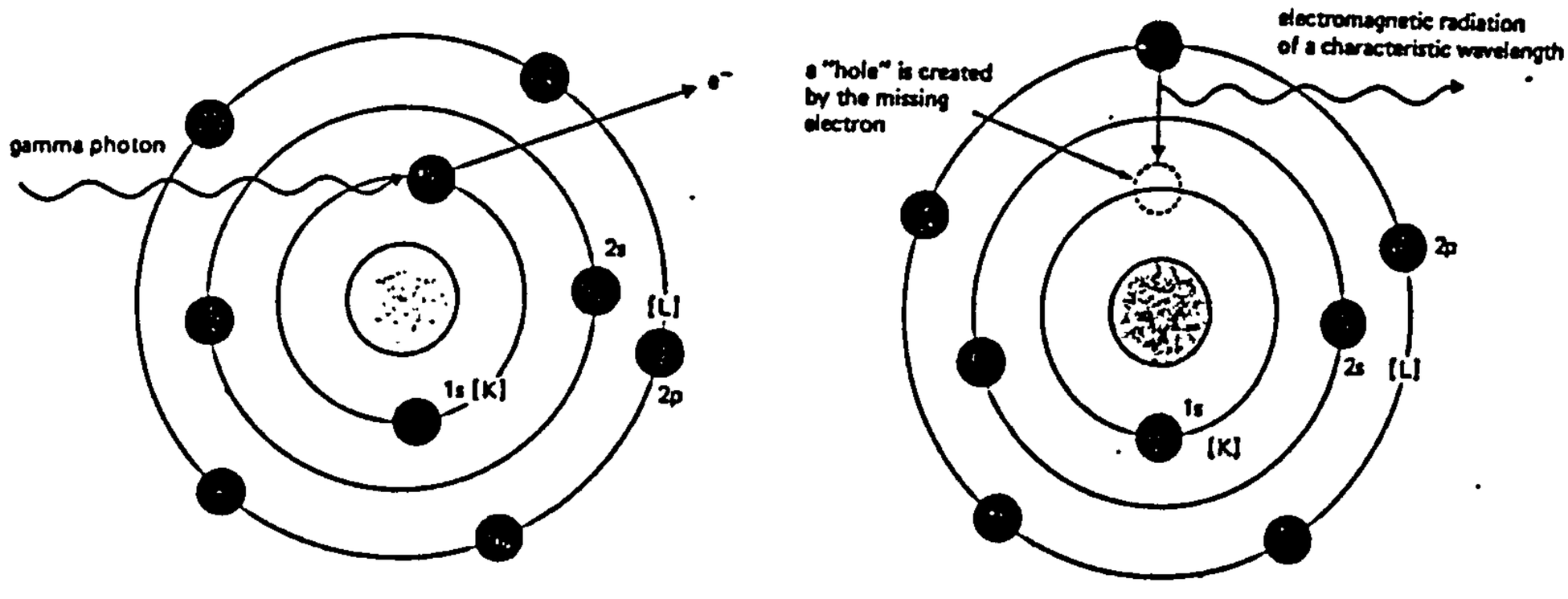

Figure 4.3: *The photoelectric effect*

X-rays are usually absorbed close to the site of the initial photoelectric interaction, but in some cases may escape from the material. The cross-section for photoelectric absorption of a photon with energy E, in a material of atomic number Z can be approximated by:

$$\sigma_{pe} = \text{const}\frac{Z^4}{E^3} \tag{4.3}$$

The strong Z dependence means that high-Z materials play an important role in the design of X-ray detectors. High-Z materials such as lead and tungsten are used when it is important to reduce the incident fluxes to the lowest possible levels, both in shielding a detector, and in some cases as a part of the imaging process. In addition, high-Z materials are preferred in some detectors as they offer a greater probability of interaction, enhancing the sensitivity of the detector.

The expression given in Equation 4.3 indicates the general shape of the attenuation curves, but superimposed upon this are sharp features known as absorption edges, which are clearly visible on the attenuation curves in Figure 4.2. These are caused by the sudden availability of more electrons as the binding energy of a new electron shell is exceeded, with a corresponding jump in the photoelectric cross-section.

4.2.2 Compton Scattering

Compton scattering occurs when a photon collides with an electron in the absorbing material and is deflected, transferring some fraction of its energy to the electron. If the electron is initially in a state with a binding energy which is low compared with the photon energy, it can be considered as a free electron, and the interaction can be regarded as an ordinary elastic collision.

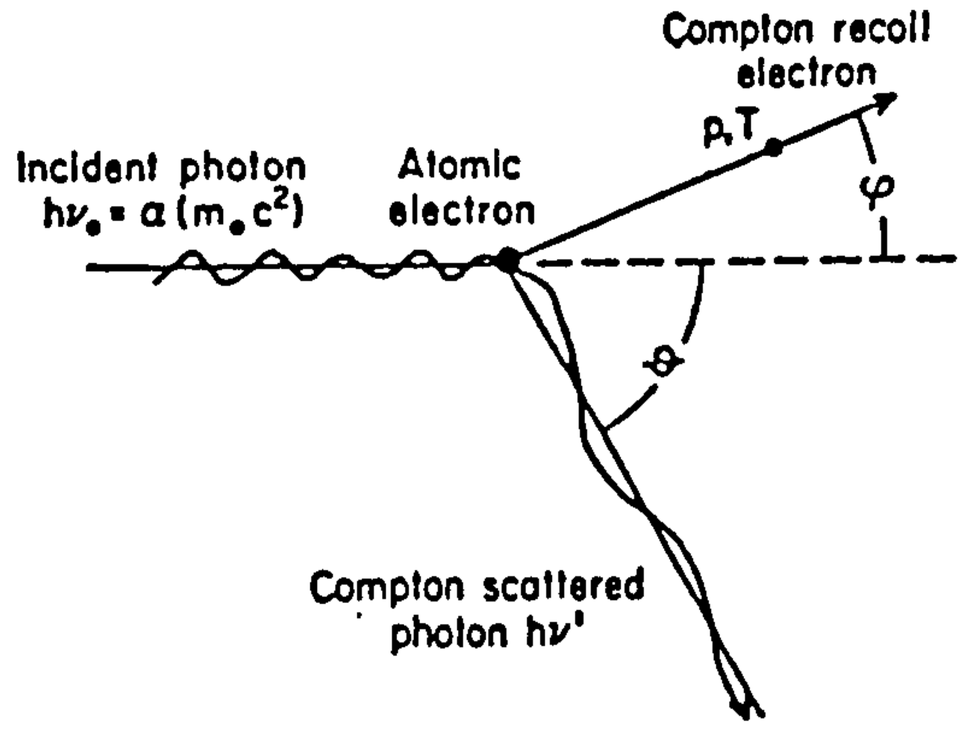

Figure 4.4: *Compton scattering*

If the photon is scattered through an angle θ, and has its energy reduced from $h\nu$ to $h\nu'$ (Figure 4.4), then it can be shown [44] that

$$h\nu' = \frac{h\nu}{1 + \alpha(1 - \cos\theta)} \tag{4.4}$$

where $\alpha = \frac{h\nu}{m_0c^2}$ and m_0c^2 is the rest mass of the electron. The energy transferred to the electron E_{e^-} is given by $h\nu - h\nu'$ and is

$$E_{e^-} = h\nu\frac{\alpha(1 - \cos\theta)}{1 + \alpha(1 - \cos\theta)} \tag{4.5}$$

All scattering angles from $\theta = 0$ to $\theta = \pi$ can occur in the detector, and so a continuum of energies can be transferred to the electron. For $\theta = 0$, that is, a grazing collision, the energy transfer is negligible. The maximum energy transfer will be caused by a head-on collision, and is therefore given by evaluating Equation 4.5 for the case $\theta = \pi$, where

$$E_{e^-_{MAX}} = h\nu\frac{2\alpha}{1 + 2\alpha} \tag{4.6}$$

The distribution of electron energies gives rise to the characteristic spectrum shown in Figure 4.5 and demonstrates the gap between the incident photon energy and the *Compton edge*. This gap is given by

$$E_{GAP} = h\nu\frac{1}{1 + 2\alpha} \tag{4.7}$$

For relatively low energy photons, the assumption that the struck electron can be considered to be free is not strictly true, and this results in some modification to the electron energy distribution. In particular the Compton edge is no longer sharp and the spectrum is modified to that shown in Figure 4.5.

4.3 X-Ray Detectors

The most common X-ray detectors may be divided into broad groups which in general indicate the type of material in which the X-ray interacts. These groups are:

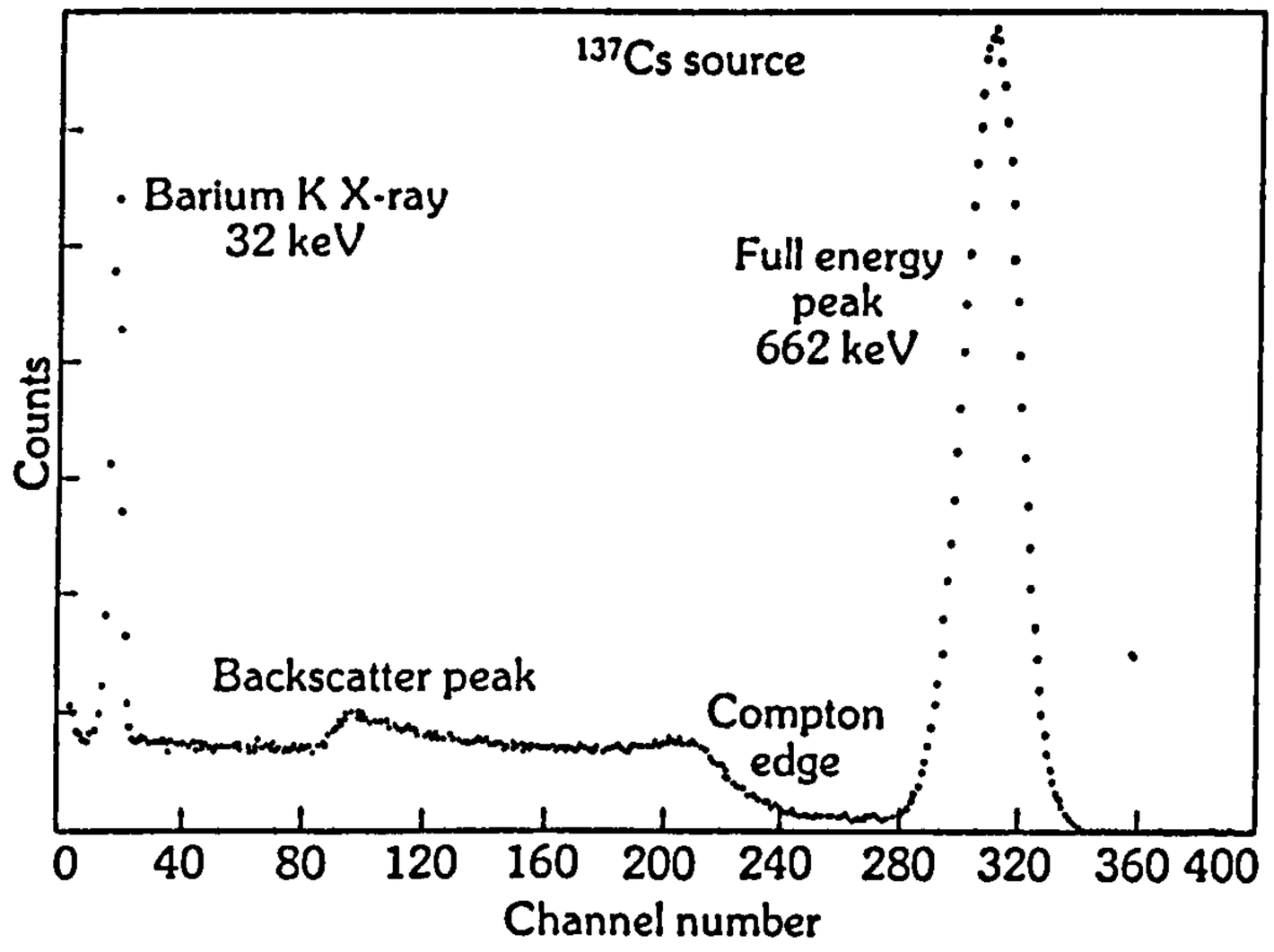

Figure 4.5: *Typical spectrum showing features resulting from Compton scattering*

- Gas detectors
- Semiconductor detectors
- Scintillation detectors

In addition, there are a large number of detectors which employ a combination of detection techniques and cannot be categorised in a simple way (e.g. the gas scintillation proportional counter). Some of these various detector types will now be discussed in more detail, and their strengths and weaknesses in different areas discussed.

4.3.1 Gas Detectors

The term 'gas detector' encompasses an extremely wide variety of detectors, all of which rely on the collection at one or more electrodes of ionization which has been induced in a gas by the passage of an X-ray.

A typical gas detector consists of a sealed chamber containing one or more electrodes (in some cases the chamber itself is an electrode), filled with a mixture of gases, with a potential applied across the electrodes. When an X-ray photon interacts with the gas, an energetic electron is produced which loses energy by ionizing the surrounding gas. The

ions and electrons created will be attracted to, and collected, at the electrodes where they may be detected.

The behaviour of the detector depends largely on the potential applied across the electrodes, the most commonly used detectors being:

- The Geiger-Müller tube.

  This is a gas detector operating at very high voltage, such that any X-ray interaction causes an avalanche of secondary ions throughout the volume of the tube. It therefore simply records the detection of the photon, but has no energy resolution, and is limited to counting applications.

- The proportional counter.

  Proportional counters are suitable for the detection of low energy (< 10 keV) X-rays, but above that energy the range of the secondary electron in the gas reduces the detection efficiency to an impractical level.

- The multi-wire high-pressure proportional counter.

  This extension of the proportional counter principle uses grids of wires in order to allow the position of the photon interaction to be measured. The use of high pressures (many atmospheres) allows the counter to be used up to energies ~100 keV. In modern X-ray astronomy, the multi-wire proportional counter (MWPC) is commonly used for imaging telescopes operating in the 1 - 200 keV range [19,131,138].

4.3.1.1 Proportional Counters

In a proportional counter, the voltage between the electrodes is sufficiently high to ensure that the chance of recombination of the ions and electrons created is very small, but not so high that an incoming photon causes a massive avalanche of ionization as in a Geiger-Müller counter. In this way, provided that the photon energy is totally absorbed within the detector, the charge collected at the output is proportional to the energy of the incident photon.

When an X-ray enters the detector it may be absorbed by photoelectric absorption,

with the ejection of an energetic electron. The excited atom subsequently de-excites by emitting either a fluorescent X-ray or an Auger electron (see section 4.2.1). The energetic electrons cause ionization as they pass through the gas, creating ion-electron pairs which drift towards the electrodes in the field.

Near the anode, the field is intense enough to accelerate the electrons to energies such that their passage creates further ionization. This rapid creation of electrons and ions is known as a Townsend Avalanche, and can give rise to a gas gain of between 10^3 and 10^5. As all of the electrons created are collected at the anode, the size of the output pulse is proportional to the energy of the incident particle or photon. The output will rise according to the arrival time of the electrons at the anode, which is typically <1 μs.

In practical terms, a proportional counter is constructed by mounting an insulated anode in a container which acts as the cathode. To permit the entrance of low energy photons, a very thin, low attenuation, i.e. low-Z, window (e.g. Mylar) can be used. Thin windows have the disadvantage that gas can leak through them, and the gas must be continuously replenished to maintain the pressure within the detector. For use in space, or with pressurised gases, the window must be thicker, and is often made from a metal such as beryllium. These thicker windows restrict the low energy threshold to above $\sim$1 keV [94]. The upper energy limit of the detector is determined by the cross-section presented by the gas, and its ability to absorb the total energy of the incoming photon. To raise this upper energy limit, the pressure of the gas within the counter can be increased to several atmospheres. This is unfortunately incompatible with the thin container walls and window needed to operate at very low energy, and this limits the energy range over which any proportional counter can operate. Additionally, the energy resolution of a proportional counter falls with increasing gas pressure due to the higher probability of ion recombination.

The gas in a proportional counter is usually a mixture of an inert noble gas such as xenon or argon, and a polyatomic gas such as CH_4 or CO_2, known as the quench gas. A noble gas is preferred as energy is not likely to be lost to rotational or vibrational excitation of the molecules. The quench gas is present to inhibit various undesirable processes which would occur in a pure noble gas.

The efficiency of a proportional counter is determined by both the transparency of the

window and the probability of absorbing all the photon energy within the counter. A typical dependence of efficiency on energy is shown in Figure 4.6.

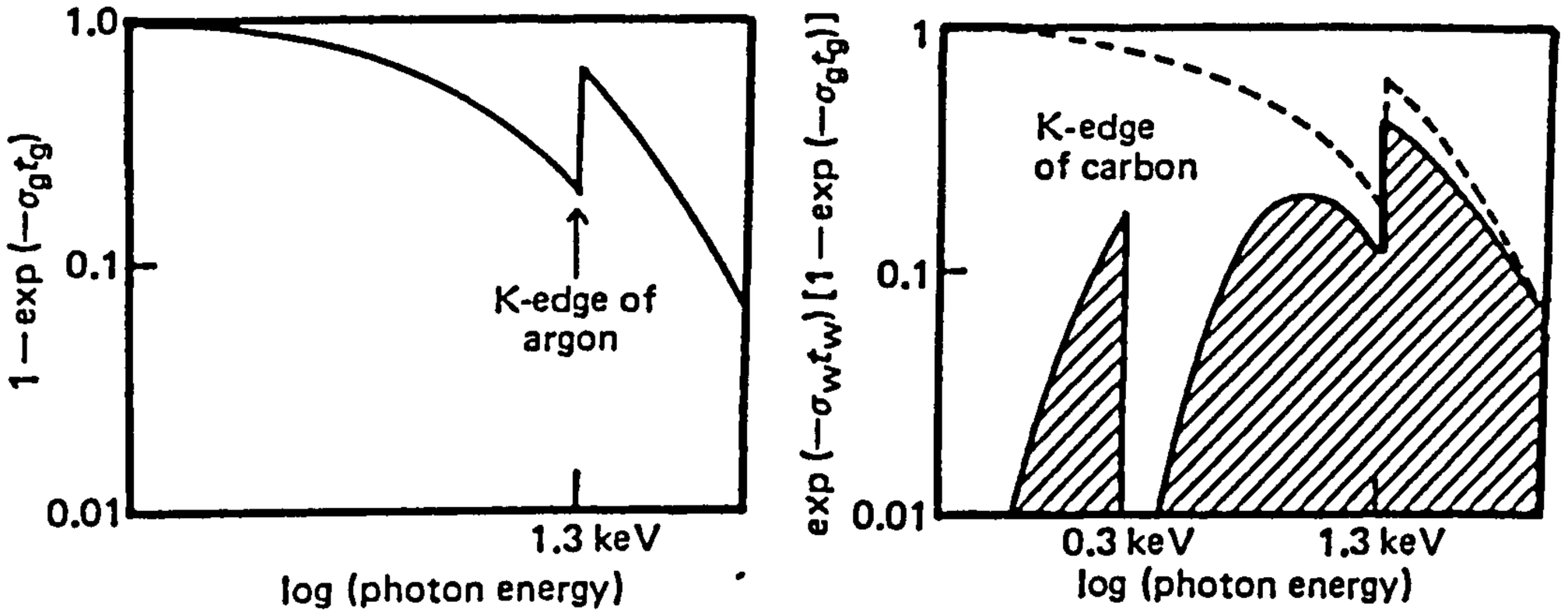

Figure 4.6: *Detection efficiency as a function of energy for a proportional counter (left) with no window, and (right) with organic window (from [94])*

On average, 30 eV are required to produce an ion-electron pair, so for a 10 keV photon ~330 electrons are collected. Assuming Poissonian statistics, this gives a theoretical energy resolution of 6% FWHM at 10 keV.

4.3.1.2 Multi-Wire Proportional Counters

The electron avalanche in a proportional counter is generally highly localized at the anode, and this makes it possible to extract positional data from a detector of slightly modified design. A typical multi-wire proportional counter (MWPC) [16] consists of a plane of closely spaced ~ 20μm diameter anode wires, sandwiched between two cathode planes 5 - 20 mm away from the anode plane. A typical detector configuration is shown in Figure 4.7. The wires in the cathode planes, which can be thicker than the anode wires, are in general arranged mutually orthogonally in order to give position readout in two dimensions. Working voltages for a MWPC are higher than for a single wire proportional counter (~5kV instead of ~1.5kV).

Various schemes have been devised for reading out the co-ordinates of an event in a MWPC. Most rely on determining the centroid of the charge collected at the cathode planes which has been found to have a Gaussian distribution with a width determined

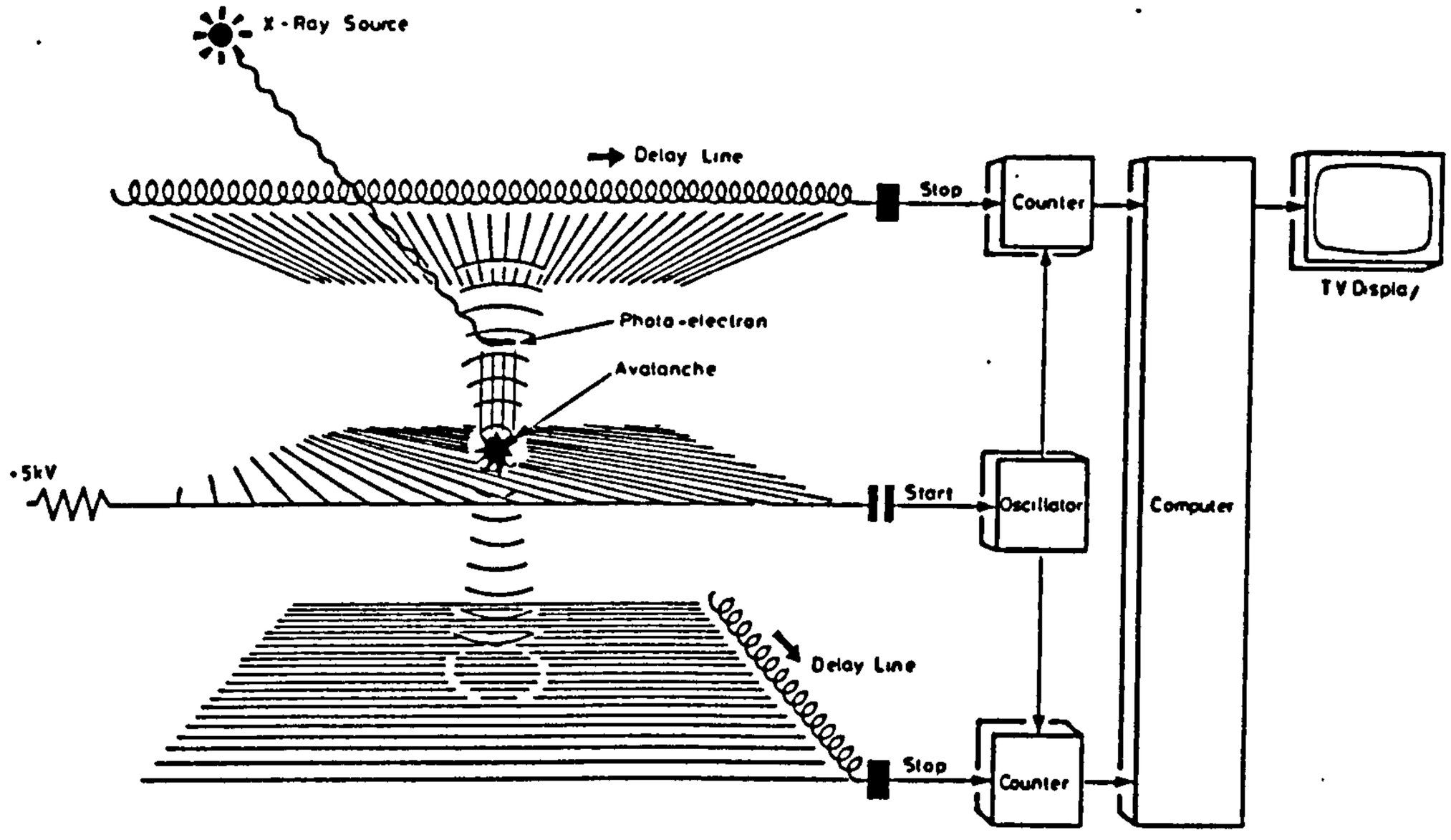

Figure 4.7: *Schematic diagram of a typical multi-wire proportional counter (from [16])*

by the anode-cathode distance.

As a MWPC may have several hundred cathode wires, steps must be taken to reduce the amount of signal processing required. One approach is to group several adjacent outputs together to form strips, and the signals from these strips are then measured, the position of the initial event being determined from the centroid of these group outputs. Alternatively, the individual cathode wires can be connected to delay lines, and timing analysis of the output signals can be used to find the event position.

The multi-wire proportional counters used on the Spacelab 2 X-ray telescope [131] serve as a good example of this type of detector. These were two xenon-filled MWPCs pressurised to 1.5 bar, with a total area of $\sim$2000cm^2. These were used in conjunction with coded masks to form two telescopes operating in the 2.5-30 keV energy range, one with coarse angular resolution, and one producing a finer image of a smaller field of view.

The POKER balloon payload carried two MWPCs with a total sensitive area of 1.1 m^2 [19]. A pressure of 3 bars allowed the proportional counters to be operated in the energy range 20 - 180 keV.

4.3.1.3 Gas Scintillation Proportional Counters

A gas scintillation proportional counter (Figure 4.8) [128,127] consists of a gas cell filled with a noble gas. Wire mesh electrodes are used to define two regions within the chamber. The first is a drift region (D) where photoelectric absorption of an incident photon may occur, creating an electron cloud which drifts in the low electric field. In the second scintillation region (S) the higher field accelerates the electrons to an energy at which they can excite the noble gases to produce their characteristic UV emission.

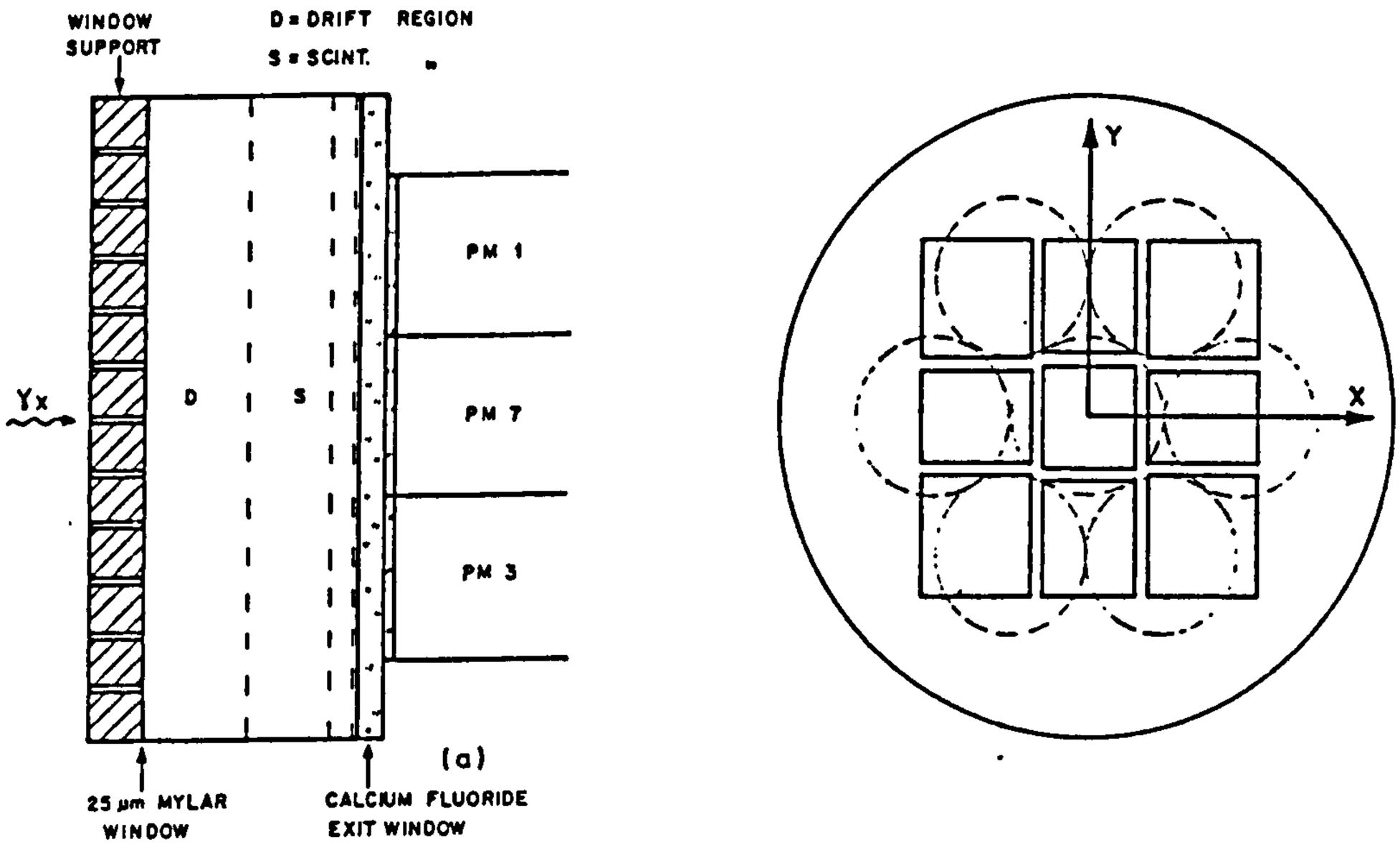

Figure 4.8: *A gas scintillation proportional counter incorporating Anger camera readout (from [128])*

The UV emission can be detected in a number of ways e.g. (i) by photomultipliers with UV transmitting windows operating in an Anger camera mode, (ii) by a microchannel plate, (iii) by a multi-wire proportional counter to which has been added a small amount of a gas which can be ionised by the UV light (TEA for krypton scintillation, and TMAE for xenon).

The energy range of gas scintillation counters is limited by the same factors as for normal gas detectors, but they offer better spectral resolution (typically ~9% at 6 keV). The spatial resolution which can be achieved depends upon the type of readout employed,

but has been demonstrated to be < 1 mm [128].

4.3.2 Semiconductor Detectors

The principle of a semiconductor detector is similar to that of a proportional counter, except that in this case the gas is replaced by a solid. This greatly increases the density of the absorbing medium, and means that the detector can be used for the detection of higher energy photons than a proportional counter.

As the energy required to move an electron into the conduction band of a semiconductor is small relative to that required in other materials, the number of electrons excited by an incoming photon is much larger than for other types of detector. Thus the statistical fluctuations in the number of electrons are far less significant, and hence semiconductor detectors can provide very good spectral resolution.

The basic operation of a semiconductor detector is shown in Figure 4.9. When a p-n junction is reverse-biased, a depletion region forms around the junction. This region should be of a size comparable to the range of the radiation to be detected, and various techniques are used to achieve this, including the use of cylindrical geometry detectors and the addition of impurities.

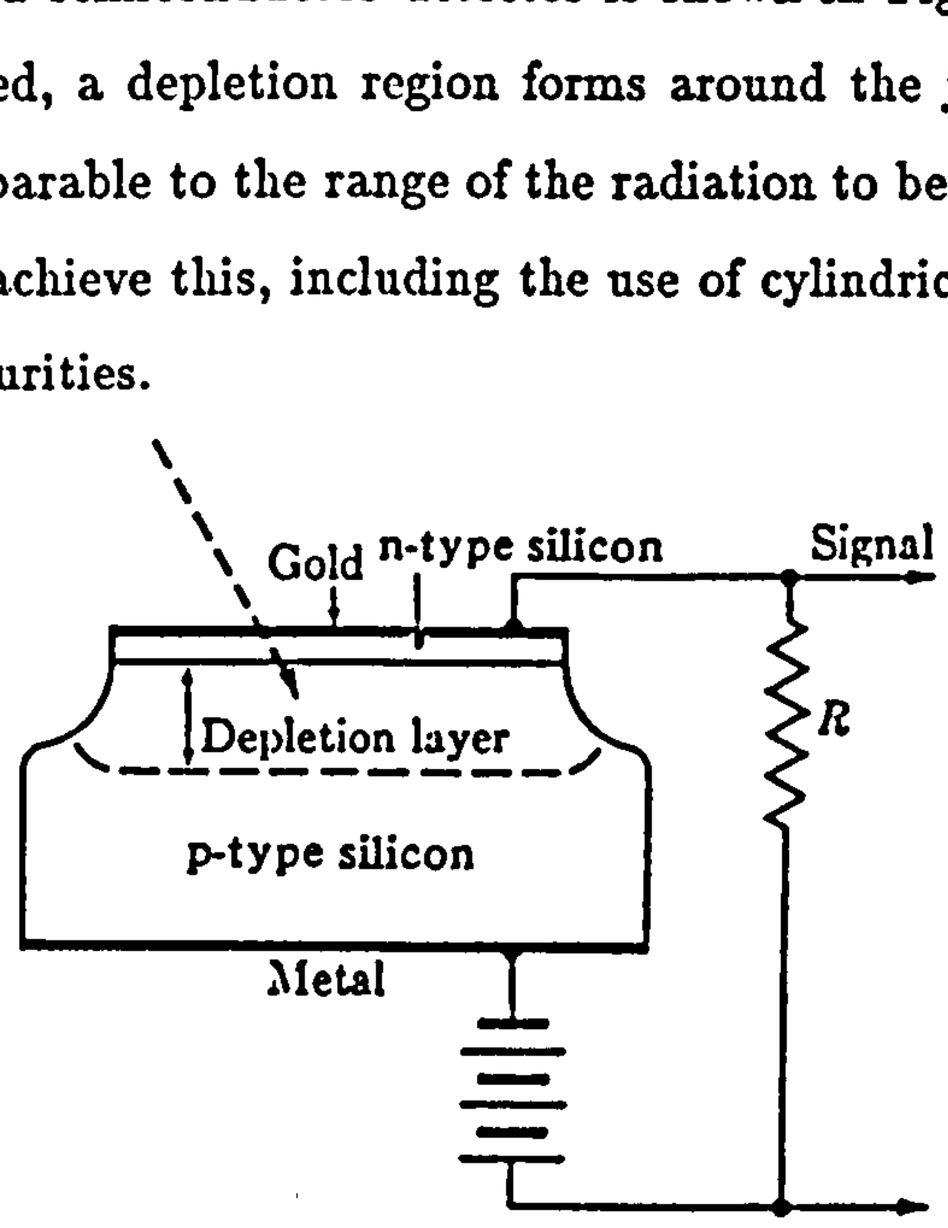

Figure 4.9: *A p-n junction detector*

Silicon and germanium are the most important semiconductor materials in current use, and their main properties are shown in Table 4.1, along with those for some promising recent materials.

	Si	Ge	HgI_2	CdTe
Highest Atomic Number	14	32	80	52
Density (g/cm^3)	2.33	5.33	6.4	6.06
Band Gap (eV)	1.08	0.75	2.13	1.47
Energy/e^--hole pair	3.65	2.95	2.13	1.47

Table 4.1: *Properties of semiconductor detector materials*

Germanium is the preferred material for hard X-ray and γ-ray detection as it has a much higher detection probability than silicon for energetic photons. As the energy required to produce an electron-hole pair is much smaller than the ionization potential of a gas in a proportional counter, the energy resolution achievable with a germanium detector is far superior to that from a gas detector. For this reason, germanium detectors are mainly used in spectroscopy applications.

As they have a low detection probability for photons with energies greater than ~30 keV, silicon diodes are more commonly employed for soft X-ray detection and as photodetectors for use in arrays of individual scintillation detectors, a technique which will be described in more detail in Section 4.3.4.

Semiconductor detectors are generally rather small, but one method which may be used to increase the sensitive volume of a semiconductor detector is that of lithium drifting. If lithium ions are diffused into either Ge or Si, and the material is then heated while a reverse bias voltage is applied, the Li ions drift from the n region to the p region, forming an accurately compensated intrinsic region. This intrinsic region forms the sensitive volume of the detector. Such devices are known as Ge(Li) and Si(Li) detectors, or p-i-n junction devices. The major disadvantage of such detectors is that even at room temperatures, the Li ions tend to drift back into the junction region, seriously reducing the sensitivity of the detector. For this reason they must be stored and operated at liquid nitrogen temperatures.

The recent development of very pure germanium with an impurity concentration of $< 10^{10}$ atoms/cm^3 can be used instead of a lithium drifted semiconductor. The increased purity means that a significant depletion depth can be produced by a practical voltage. The major advantage of a hyper-pure germanium (HPGe) detector is that it can be stored

at room temperature, although it must still be cooled during operation. Several balloon flights are planned to evaluate these materials.

Although usually used as simple spectrometers, an interesting example of germanium detectors being used in an imaging system is the gamma-ray spectrometer for the proposed INTEGRAL mission. This imaging spectrometer comprises an array of 9 large high-purity germanium detectors, cooled to 85K and having a total detection volume of 2600 cm^3. The γ-ray spectrometer is designed to operate over the energy range 15 keV - 10 MeV, with typical energy resolution being $E/\Delta E$ ~500 at 1 MeV. Imaging is achieved by an active coded aperture system which gives a final deconvolved image which is a 3×3 element map of a 12×12 degree portion of the sky, giving 4 degree angular resolution, and a point source location accuracy of 30′ (10σ).

With sufficient development work, mercuric iodide could become a very important material for X- and gamma-ray detection. With a high density and containing only high-Z elements, it has a high attenuation coefficient, and its large band gap means that HgI_2 detectors can be stored and operated at room temperature. However, there are some problems associated with this material. Firstly, mercury has a K-edge at 83 keV, which is inconvenient for hard X-ray measurements in this region. Secondly, mercuric iodide detectors are difficult to manufacture in large sizes, with the largest crystals currently being ~ 4 cm^2 [74,77], which is small compared with available germanium detectors. Finally, the energy resolution of HgI_2 detectors is yet to approach the theoretical limit, and a typical performance is ~10% at 662 keV [20] which is inferior to a good NaI(Tl) scintillation counter. Mercuric iodide detectors have been investigated for use in scintillator readout [77,100,99] and are capable of high energy resolution measurements in this application. A spectral resolution of 4.98% at 662 keV has been obtained in conjunction with a CsI(Tl) crystal. The spectral response of HgI_2, which is high over the range 380 - 560 nm allows it to be used to read out other scintillators such as NaI(Tl) which are not suitable for use with silicon photodiodes.

Cadmium telluride is another material with similar properties to mercuric iodide. It may be operated at room temperature, has good stopping power, and has a K-edge at 32 keV. CdTe detectors have the same problems of small size and poor resolution as HgI_2, and additionally have a particularly large neutron cross-section due to the presence of

cadmium. This final problem could result in an unacceptably high background in a space environment.

4.3.2.1 Position-sensitive semiconductor detectors

To date there has been considerable work on developing semiconductor detectors with intrinsic spatial resolution.

The advanced techniques for diode fabrication, particularly in silicon, enable large arrays of diodes to be manufactured on a single silicon wafer. The individual devices may vary in size from a few microns (the so-called silicon pixel detectors) to several millimetres. The latter group of detectors will be discussed in Section 4.3.4.1 for their application to the detection of scintillation light.

An alternative approach is to collect the charge from a single diode on a large number of electrodes which are arranged such that the charges detected at each individual electrode can be used to reconstruct the event location. For example, in a technique strongly analogous to the multi-wire proportional counter, orthogonal sets of strip electrodes on the upper and lower surface of a diode may be used [110].

Of more direct relevance to the detection of hard X-rays and especially gamma-rays are segmented germanium detectors. These may be made up of a number of individual diodes, but may alternatively use a number of electrodes to notionally divide a single detector into a number of segments. At higher energies, above a few hundred keV, this type of detector will have a lower background as beta decay events (single site) and gamma-ray events (multi-site) may be distinguished.

4.3.3 Scintillation Detectors

The detection of radiation with a scintillating material is one of the oldest techniques, dating from the 1920s when Rutherford used it to detect alpha particles.

In contrast to gas and semiconductor detectors, scintillation detectors rely on the excitation of atoms rather than the production of ionization. On absorbing energy from

the incident radiation, an atom in the scintillator undergoes excitation to a higher electron state, which is followed by a return to the ground state with the emission of light of a wavelength determined by the gap between the energy levels. Provided the scintillation material is transparent to light of this wavelength, this light may be observed by a suitable instrument at the surface of the material. X-ray scintillation detectors work in two stages: the conversion of the X-ray photon to an optical pulse, and the subsequent detection of the optical pulse.

Again, the discussion here will centre on designing instruments with good spatial resolution which may be used in imaging detectors. This can be achieved in several ways:

1. If many small scintillators and photodetectors are placed in an array of essentially independent detectors, then a position sensitive detection plane will result. For this case, the achievable spatial resolution will be limited by the size of each individual detector.

2. If a single scintillator is viewed by two or more small photodetectors, the amount of light falling on each detector will be related to the distance from the origin of the light, allowing the position of the interaction to be calculated.

3. One or more photodetectors with intrinsic spatial resolution may be used to view a scintillator. If the photodetectors have a large sensitive area, this approach should offer a reduction in the amount and complexity of signal processing electronics required for a detector of a given size. In this case, the resolution of the system will be dictated by the resolution of the photodetector.

The techniques for position-sensitive readout of a scintillator will be described in greater detail in Section 4.3.4.1. It is first necessary to review the materials which are most commonly used as scintillators, in order to enable the selection of the most suitable material for a given application, and also to understand the requirements for the photodetectors which will operate in conjunction with them.

The main requirements for an effective scintillation material are as follows:

- For hard X-ray detection, high density materials are needed in order to ensure a

high interaction probability. The high density of suitable scintillation materials allows the construction of detectors which are efficient at energies far in excess of those covered by gas detectors.

- The conversion of the X-ray photon to visible light should be as efficient as possible in order to give a high fluorescent light yield.
- The light yield should be linearly dependent upon the energy deposited within the scintillator.
- The material should have a high transparency to the emitted light. In many cases, some impurity is added to the scintillator to shift the emitted wavelength away from the absorption band.
- The decay time of the scintillation light output should be well defined. Fast scintillators are mainly used in anti-coincidence systems. A range of scintillators with different decay times is essential for phoswich systems which rely on pulse-shape discrimination to distinguish energy deposits in different crystals.
- The refractive index of the material should be such that the scintillator and photodetector(s) may be optically coupled to give a high light collection efficiency.
- The emitted scintillation light should be at a wavelength compatible with the photodetectors available. Figure 4.10 shows typical response curves for two types of photomultiplier photocathode, along with the emission spectra of some common scintillators.
- The material should be chemically and mechanically stable. For example, hygroscopic crystals such as NaI(Tl) require special packaging to ensure their performance is not degraded by moisture take-up over a period of time.

No single scintillator can achieve all of these goals, and so a wide range of materials has been developed. Some of the more important scintillation materials are shown in Table 4.2. These are mainly inorganic crystal scintillators, as it is these which are most often used in hard X-ray detection, although plastic scintillators have applications in charged particle detection, and are often used to reduce background in space-borne detectors.

Material	Peak Emission (nm)	Decay Const (μs)	Refractive Index	Density (g/cm^3)	Hygroscopic	Efficiency
Inorganic crystals						
NaI(Tl)	415	0.23	1.85	3.67	Yes	100
NaI [1]	303	0.06	1.85	3.67	Yes	200
CsI(Tl)	550	1.0	1.80	4.51	No	45
CsI(Na)	420	0.63	1.84	4.51	Yes	85
CsI [1]	400	0.2	1.80	4.51	No	220
BGO	480	0.3	2.15	7.13	No	13
$CdWO_4$	540	5.0	2.25	7.9	No	40
CaF_2(Eu)	435	0.94	1.44	3.18	No	50
BaF_2	225	0.8 ns	1.49	4.88	No	4
	310	0.62				20
CsF	390	5 ns	1.48	4.64	Very	5
LiI(Eu)	470	0.6	1.96	4.08	Yes	35
$ZnWO_4$	480	5.0	2.14	7.8	No	28
GSO(Ce)	430	0.06	-	6.71	No	20
CeF_3	310	2 ns	1.68	6.16	No	3
	340	31 ns				3
Plastic scintillators						
NE102A	423	2.4 ns	1.58	1.03	No	30
NE110	406	3.3 ns	1.58	1.03	No	30

Table 4.2: *Some common scintillation materials.*

Data compiled from [2,62,7,76,107,112]

[1] Measured at 77 K

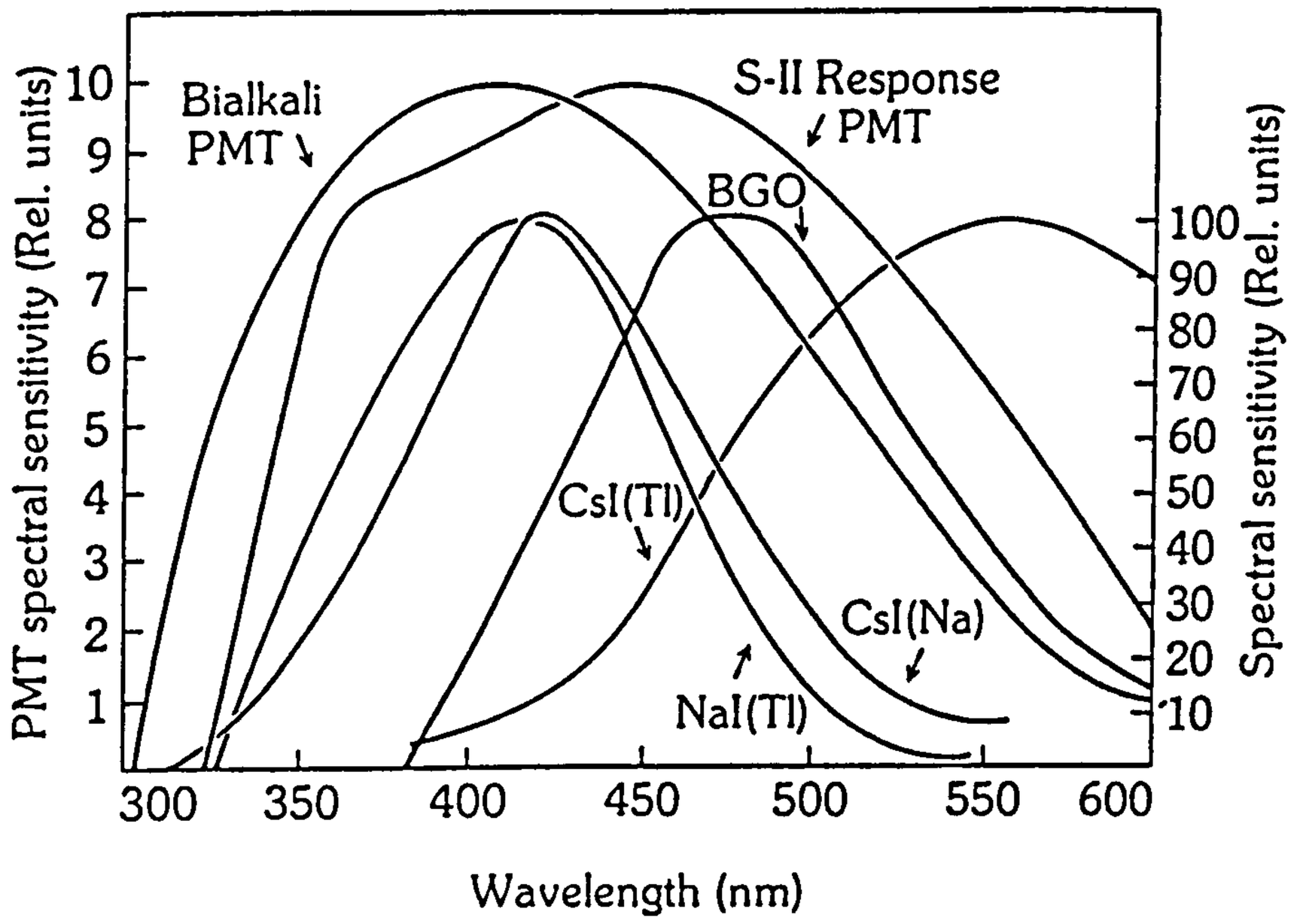

Figure 4.10: *Emission spectra of some common scintillators*

Many of these materials have been developed for specific applications, and so are of limited use for X-ray astronomy. Some of the more common materials currently in use, and also those with promising properties which have yet to be applied in this field, are worth mentioning in more detail:

NaI(Tl) Thallium doped sodium iodide has become the standard choice of inorganic crystal scintillator for many applications in X-ray detection and spectroscopy [71]. Large crystals can be grown, allowing sensitive large-area detectors to be constructed relatively inexpensively. The light yield at room temperature is very high with a peak emission at 415nm [29] which matches standard photomultipliers well, and hence the light yield of NaI(Tl) is generally used as the standard against which other materials are measured. The decay of the light output is relatively fast, allowing NaI(Tl) to be used in high count rate applications such as medical imaging. However, NaI(Tl) is strongly hygroscopic, and in air rapidly forms an oxide layer which seriously degrades its performance. For this reason, NaI(Tl) crystals are packaged in sealed containers which must be evacuated if meant for use in low pressure environments. In addition, NaI(Tl) crystals are quite fragile placing extra importance on the packaging.

CsI(Tl) The light yield of CsI(Tl) is only around half that of NaI(Tl), but the material

does have several important advantages. Firstly, the high X-ray attenuation means that relative to NaI(Tl), a smaller volume of material is required to form a detector operating over the same energy range. In addition, the material is easier to work with since it is non hygroscopic, and may be formed to make detectors with unusual geometries. The peak emission is at 550 nm, which is not well matched to standard photomultipliers, but CsI(Tl) has been successfully used in conjunction with silicon photodiodes which may be made sensitive to light of this wavelength [63,120]. The difference in decay times between NaI(Tl) and CsI(Tl) is significant. It has been demonstrated [150] that events from the two crystals can be distinguished by pulse shape discrimination, allowing their use together in phoswich detectors.

CsI(Na) When doped with sodium, the peak emission of CsI shifts to 420nm, making it more suitable for use with standard photomultipliers. In addition, the light yield is increased to around 80% of NaI(Tl). Unfortunately, the presence of sodium makes CsI(Na) hygroscopic. Again, the decay constant of 0.63μs allows CsI(Na) to be used with NaI(Tl) in phoswich detectors.

Pure Alkyl Halides The scintillation properties of the pure alkyl halides, and in particular NaI and CsI deserve special mention. Although relatively inefficient at room temperatures, their performance is strongly temperature dependent, and at low temperatures they have some very desirable properties. At 80K, the scintillation efficiency of NaI is twice that of room temperature NaI(Tl). The temperature dependence of the light yield and the decay time of NaI is shown an Figures 4.11 and 4.12 respectively.

At these low temperatures, the peak emission is in the ultraviolet region at 303nm. However, there are several practical difficulties limiting the operation of scintillators at such low temperatures:

1. Standard photomultipliers cannot be cooled to these temperatures, although Persyk et al. [112] have shown that special quartz-window photomultipliers may be operated at liquid nitrogen temperatures. Alternatively a long quartz light pipe can be used to insulate the PMT from the crystal.
2. No satisfactory light coupling fluid has been found which will operate at these temperatures. Some success has been noted by using air and gas interfaces between crystal and PMT, and the solid optical coupling used in

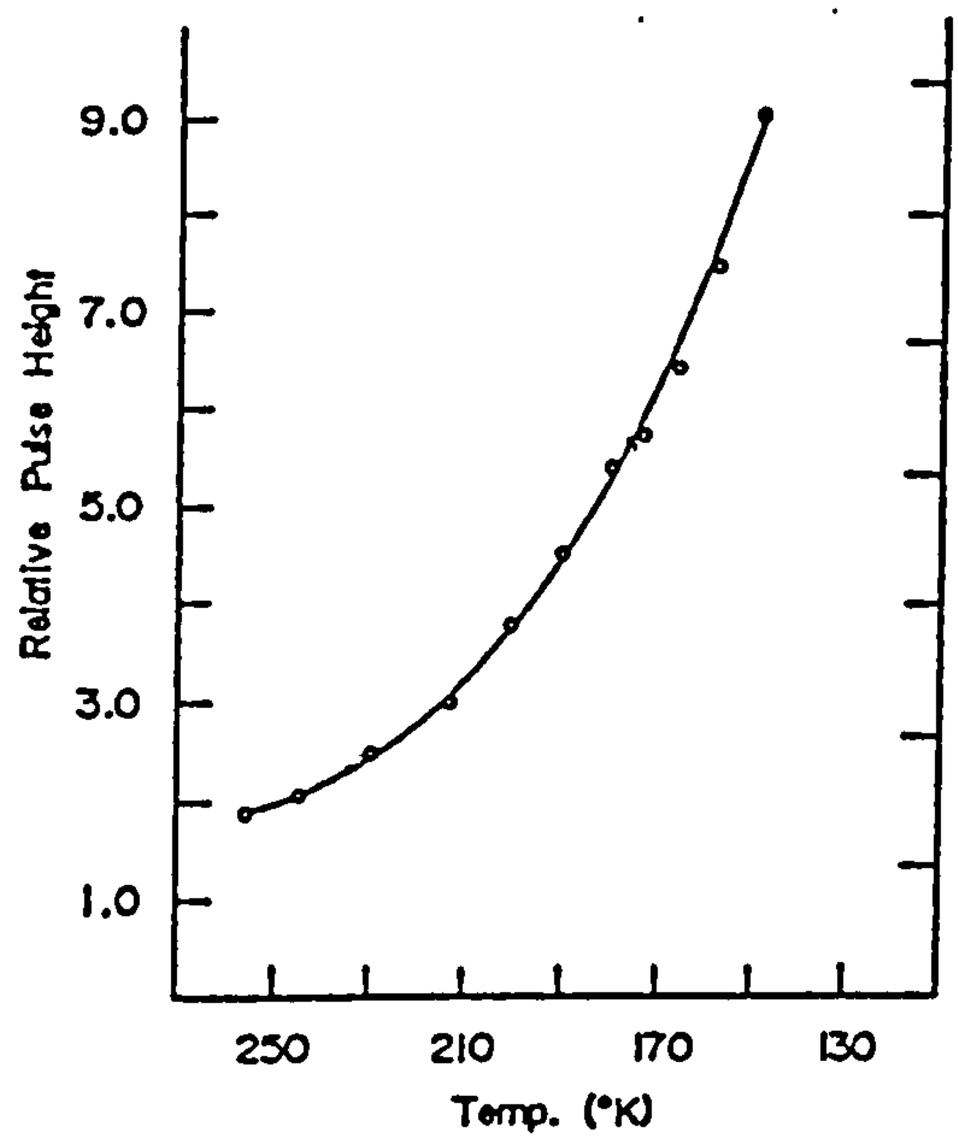

Figure 4.11: *Temperature dependence of the scintillation efficiency of pure NaI*

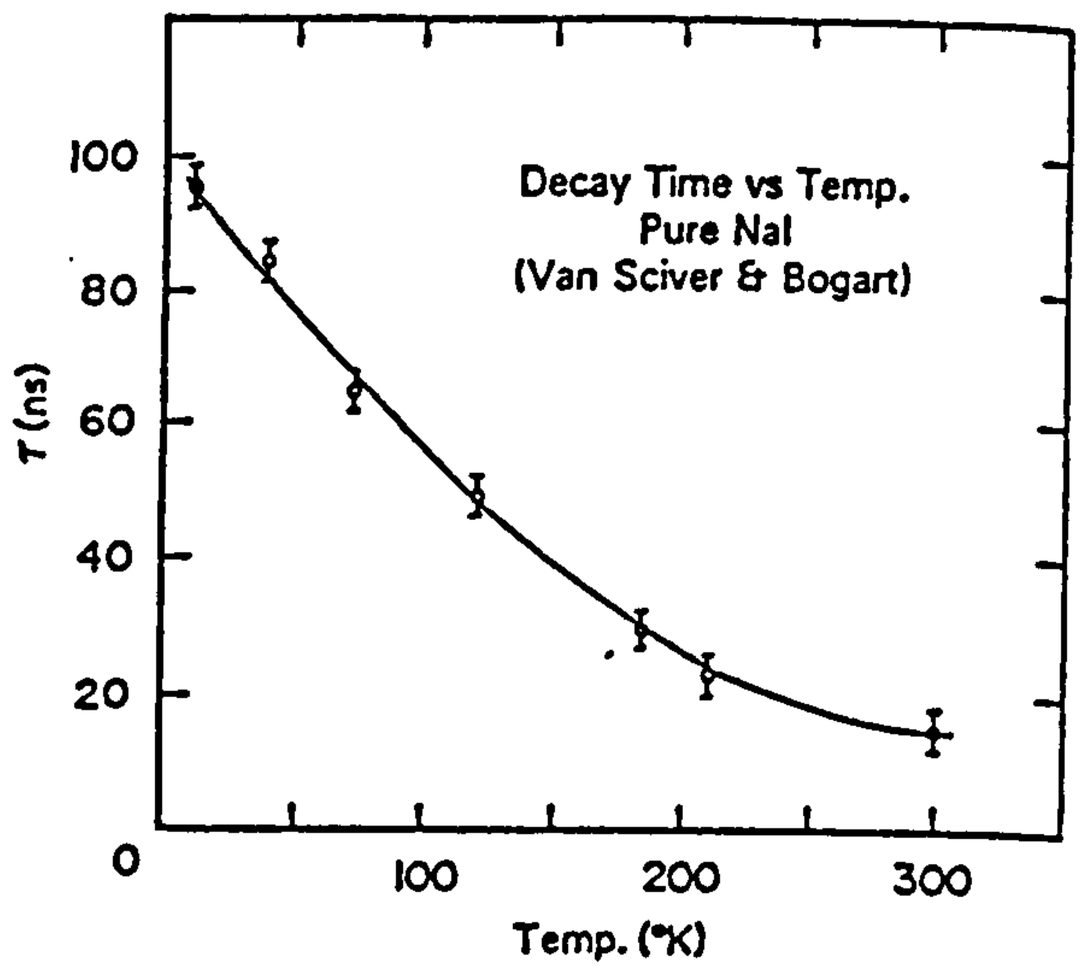

Figure 4.12: *Temperature dependence of the decay time of pure NaI*

space applications is satisfactory at these low temperatures.

3. It is believed that self-absorption of the scintillation light may limit practical crystal thicknesses to ~15mm, although recent results have cast doubt on this, at least in the case of pure CsI.

Pure CsI may prove a useful material both when cooled and at room temperature. At 77K the light yield from CsI is 2.2 times that of NaI(Tl), and is centred at 410nm. The problems outlined above concerning low temperature scintillation counting apply equally to CsI. At room temperature the light output is much smaller, at around 10% of NaI(Tl), but the fast decay time of 10 ns has led it to be considered as a possible fast veto crystal. Pure CsI is non-hygroscopic.

BaF_2 Barium fluoride is an interesting inorganic crystal which exhibits two light decay constants. BaF_2 gives both a weak fast pulse at 220 nm, and another slower, higher intensity pulse at 320nm. The decay constant of the fast component is 0.6 ns, making it useful in fast veto applications.

Plastic Scintillators Plastic scintillators are made by dissolving an organic scintillator in a solvent which polymerises. Although they have a lower interaction probability for X-ray photons, they are commonly used in X-ray detectors to reduce the

background due to charged particles. The light output is very fast, typically a few nanoseconds, allowing them to be used in veto systems.

Phosphor Screens Several phosphors are used in the construction of fluorescent screens for use in combination with X-ray film to give a higher detection efficiency at the expense of some resolution. The most important are calcium tungstate ($CaWO_4$) and terbium-activated rare-earth oxysulphides (X_2O_2S with X being gadolinium, lanthanum or yttrium) [147].

4.3.4 Scintillation Detection

All the scintillation materials described in the last section would not be of any practical use without some means to accurately detect the scintillation light which they emit. This emission is generally in the form of visible or ultra-violet light pulses of very low intensity.

Photomultiplier tubes (PMTs) and silicon photodiodes are the most common devices used for scintillation detection. Historically, PMTs have been the most important, but photodiodes have some important advantages which have caused an increase in their application in this area. A brief comparison of the two types of device is given in Table 4.3, and the spectral response functions are shown in Figure 4.13.

	Photomultiplier	Si Photodiode
Quantum Efficiency	10-20%	60%
Power requirements	HT ~ 2 kV	Bias ~ 30 V
Peak Response	~ 400 nm	~ 900 nm
Intrinsic amplification	~ 10^5	None
Size & mass	Large, heavy	Small, light
Use in B fields	Susceptible	No effect

Table 4.3: *A comparison of PMTs and photodiodes*

Photomultipliers The sensitivity of a PMT depends on the efficiency of conversion of light photons at the photocathode, and on the degree and linearity of electron multiplication in the multiplier section. The photocathode is a material of low work function allowing photons in the visible and ultra-violet region to eject electrons.

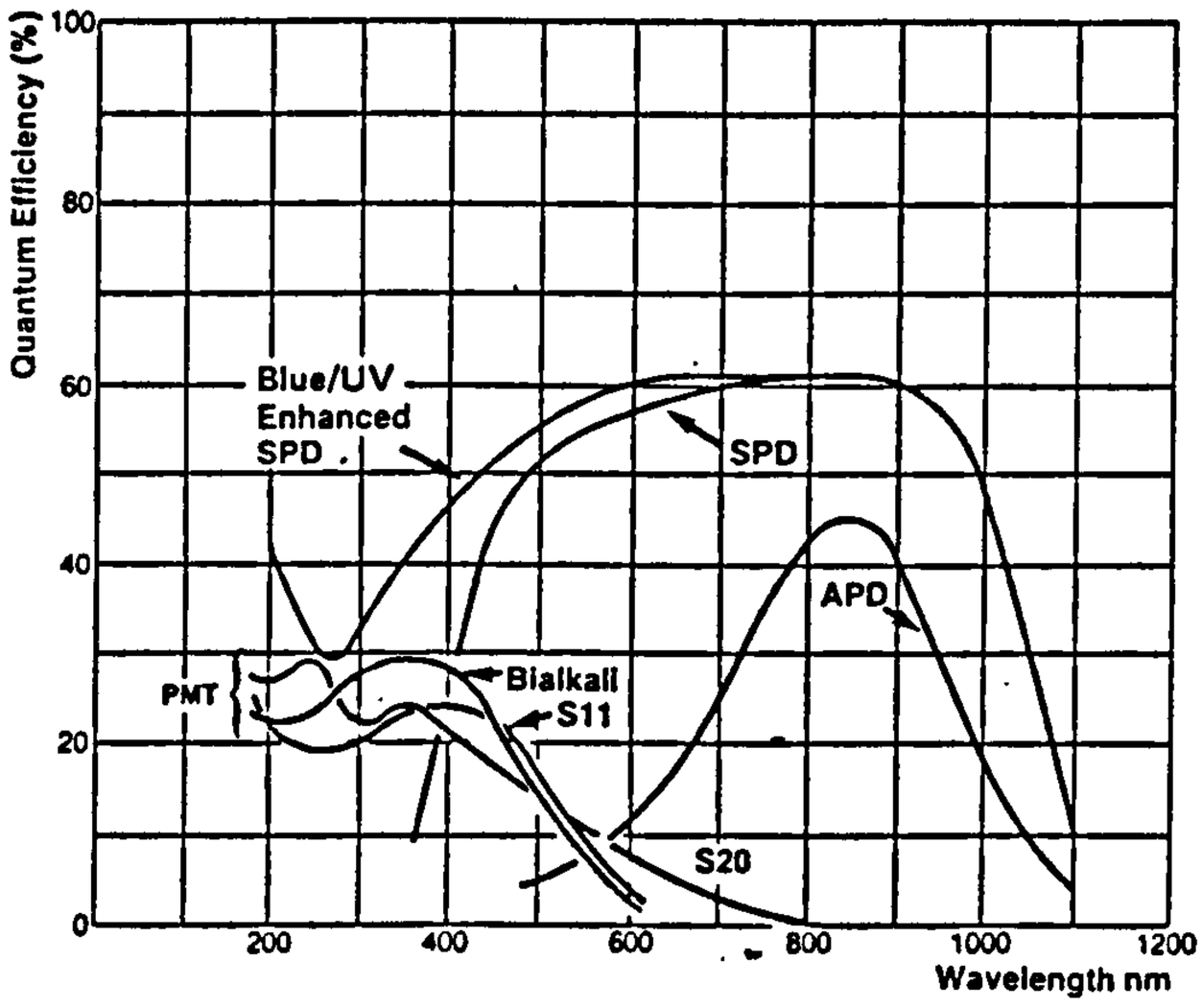

Figure 4.13: *Quantum efficiency of photodetectors*

The photocathode response is wavelength dependent, and depends on the material used, with almost all having a peak response around 440nm. After emission, the electrons must be accelerated by an applied voltage to reach an energy sufficient to cause multiple emission of secondary electrons at the first dynode; subsequently the same conditions must be met at each successive pair of dynodes. To achieve this, each dynode is connected to a resistive divider chain which distributes a high supply voltage to each dynode (Figure 4.14). Some typical dynode structures are shown in Figure 4.15. Several precautions must be observed when using PMTs:

- Operating a photomultiplier at too high a voltage causes charge to build up within the device, and prevents linear operation.
- The flow of electrons between the dynodes may be affected by electric and magnetic fields.
- The gain of a photomultiplier tube is temperature-sensitive, and care must be taken to prevent heating from the voltage-divider network.

Photodiodes In recent years, the use of silicon photodiodes in conjunction with certain scintillators has become increasingly common. The peak spectral response of Si diodes limits their use to scintillators with 'red' output, CsI(Tl) [119,120] and BGO [40,65] being two examples. Photodiodes allow the construction of more compact detectors with simpler power requirements, and are suitable for use in

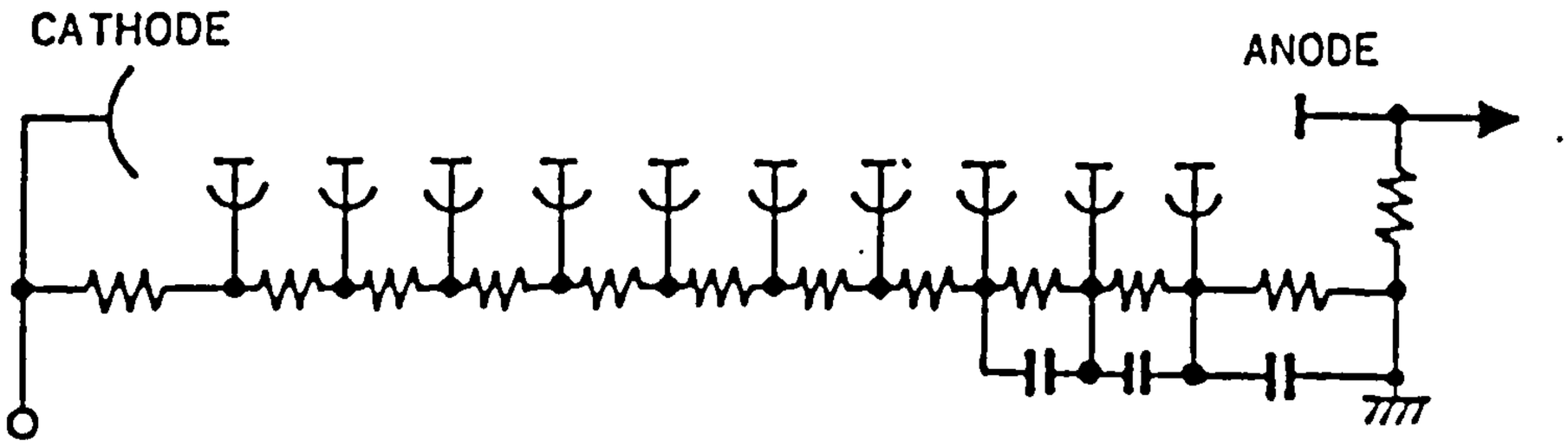

Figure 4.14: *A typical PMT dynode supply*

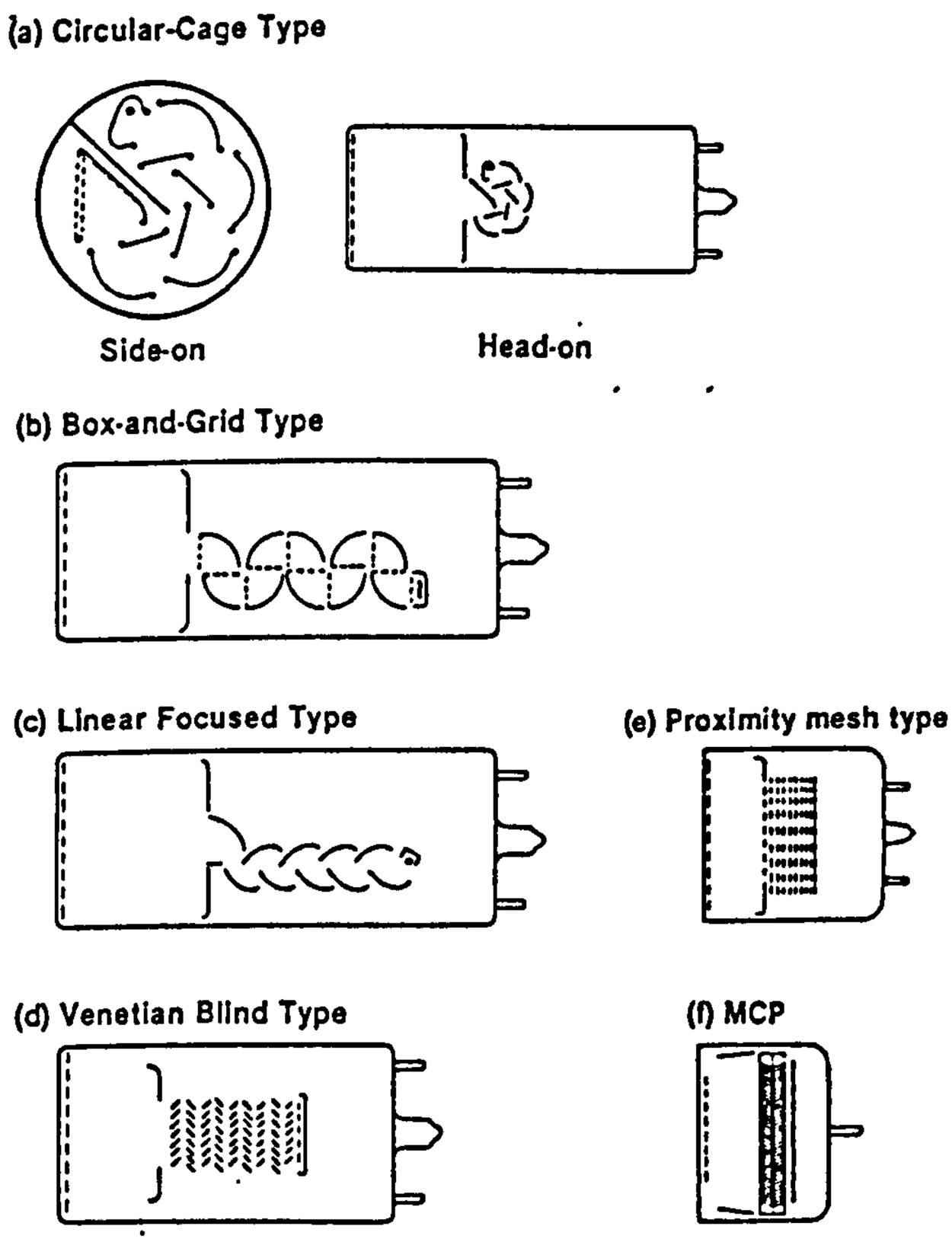

Figure 4.15: *Some typical PMT dynode structures*

strong magnetic environments. The major disadvantage of the photodiode is the lack of internal amplification which means that the output must be amplified by very low-noise electronics. It has been shown [79,124] that this can only be achieved with low capacitance diodes and well matched amplifiers. This has important implications for the dimensions, materials and operating conditions for photodiodes. Current photodiode / scintillator / amplifier combinations are affected by noise at $\sim$ 60keV and cannot be used below that energy. In addition to this, the small area of currently available photodiodes implies considerable complexity for the readout of a large-area detector. Various diode designs have been proposed to overcome this, but are all in the early stages of development. Drift diodes [45] have lower capacitance than standard diodes of the same are, improving the theoretical noise performance which can be achieved. Avalanche photodiodes are operated at higher bias voltages than conventional diodes, and offer a degree of internal amplification, again resulting in an improvement in noise performance. Some very promising results have been obtained with these devices, but they are currently only available in restrictively small sizes.

4.3.4.1 Position-Sensitive Scintillation Detection

Position sensitive scintillation readout schemes are based upon the use of multiple photodetectors or variants of photodetectors which provide intrinsic position resolution. Three general approaches can be envisaged:

1. An array of individual small detectors.

2. Using multiple photodetectors to view a single crystal.

3. The use of position-sensitive photodetectors.

The first approach requires the construction of miniature detectors, and is most likely to be accomplished by using arrays of small crystals viewed by photodiodes. The use of high density amplifier circuitry would allow modules of up to 64 individual detectors to be constructed on a single silicon wafer. A prototype silicon photodiode/CsI(Tl) detector array being developed at Southampton University [105] is shown in Figure 4.16.

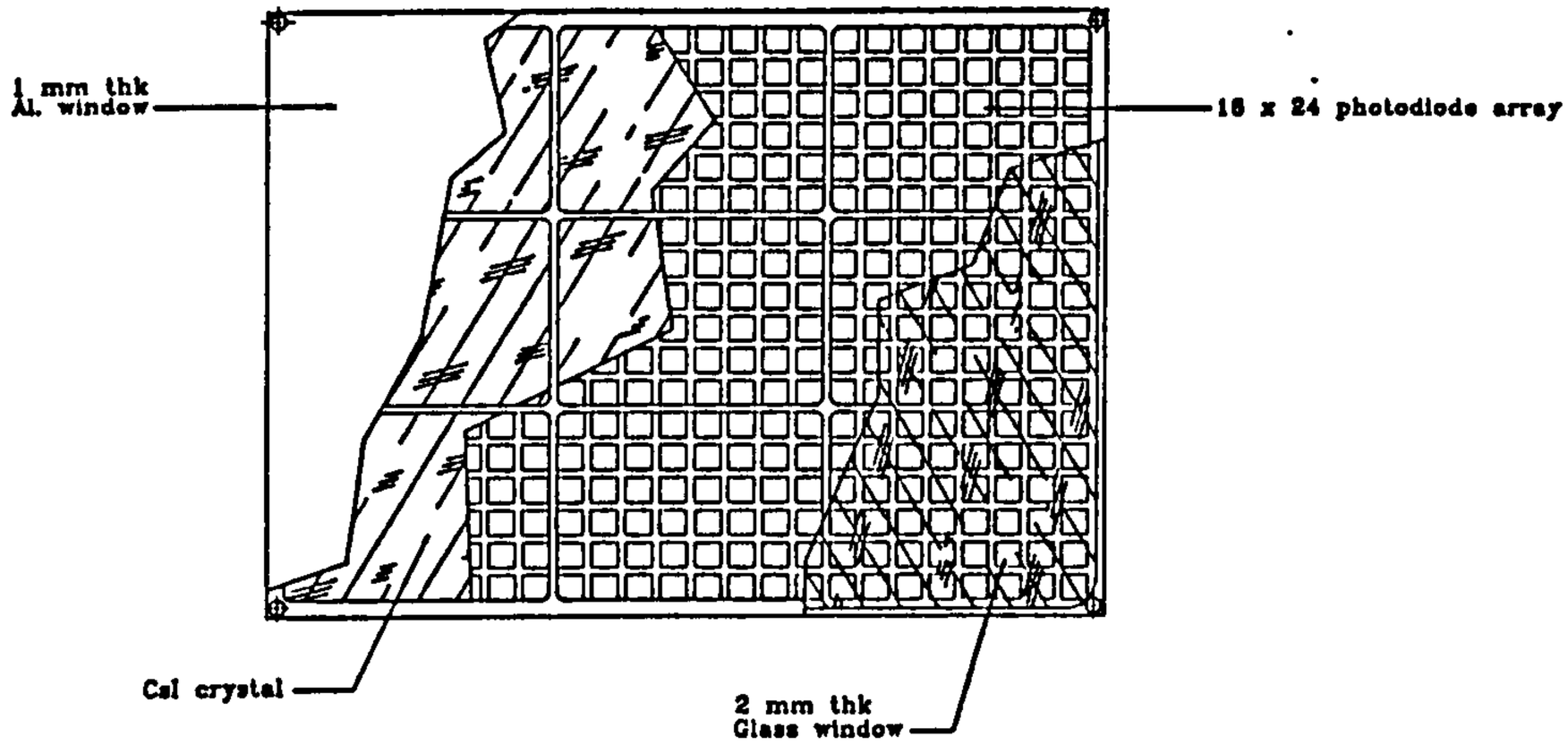

Figure 4.16: *A prototype CsI(Tl)/Si diode detector array*

Both (2) and (3) rely on the fact that scintillation light from an X-ray interaction will spread to each surface of the scintillator. When combined with the geometry and surface finish of the scintillator, the variation in intensity over the surface may be used to determine the position of the initial interaction. In practice, this variation in intensity can be measured either with multiple photodetectors, or a single position-sensitive detector.

A simple linear position-sensitive scintillator can be made by viewing a scintillator bar with a photodetector mounted at each end [26,27]. An example is shown as Figure 4.17. This system relies on exponential attenuation of the scintillation light intensity as it travels along the bar, and the position of the interaction (along the bar) is given by

$$x = \frac{1}{2\alpha} \ln \frac{E_B}{E_A} \tag{4.8}$$

where E_A and E_B are the signals in the two photodetectors and α is the light attenuation coefficient per unit length. If many of these bars are placed side-by-side, a two-dimensional position-sensitive detector may be formed. This is the principle used in the ZEBRA detector [28] which has 5.8 x 5 x 50 cm NaI(Tl) crystals viewed by photomultipliers. Figure 4.18 shows the positional resolution along the bar achieved by this system. A two-dimensional array of much smaller bar detectors is proposed for the INTEGRAL mission. In this case, CsI(Tl) bars are viewed by silicon photodiodes, and make up a 3-dimensional position-sensitive detector with a volume of 37,500cm^3. In such

systems, the position resolution along the axes orthogonal to the major axis of the bars is limited to the bar dimensions.

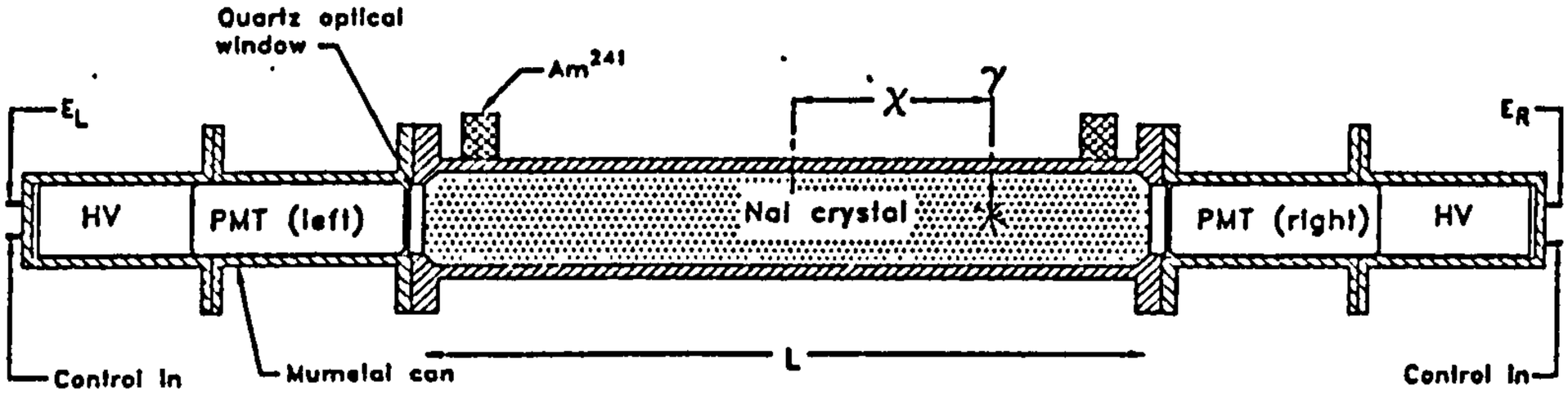

Figure 4.17: *A linear position-sensitive scintillator*

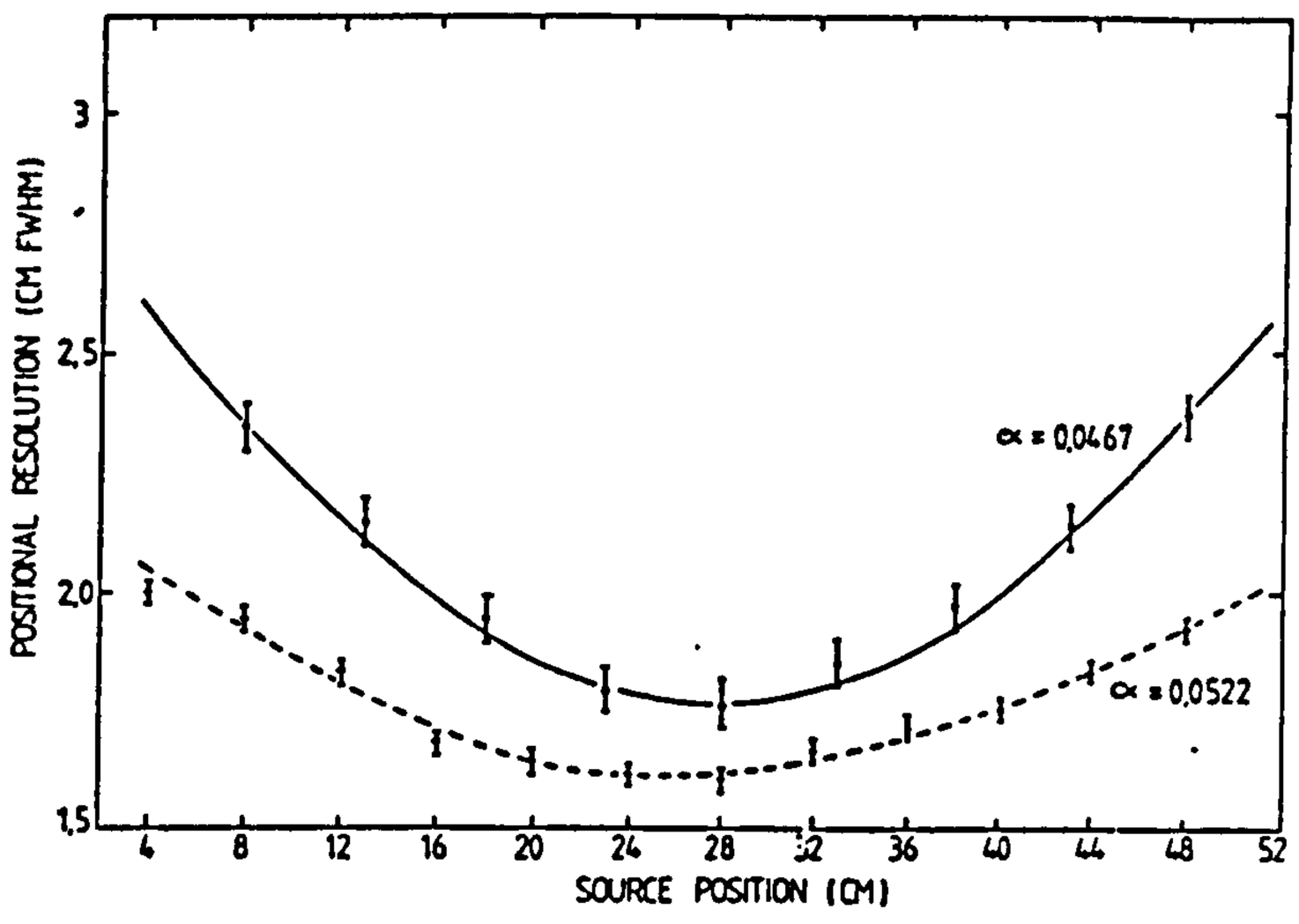

Figure 4.18: *Position resolution along a ZEBRA detector bar (from [28])*

If more than two photodetectors are used to view a single scintillator, it becomes possible to calculate the source position in two dimensions. The most common use of this technique is in the Anger camera [9,126], which uses the ratios of signals in 7 or more photomultipliers to accurately determine the interaction location (Figure 4.19). An X-ray photon passing through the collimator interacts in the crystal, and the intensity of the light pulse seen by each photomultiplier will be dependent on its distance from the event.

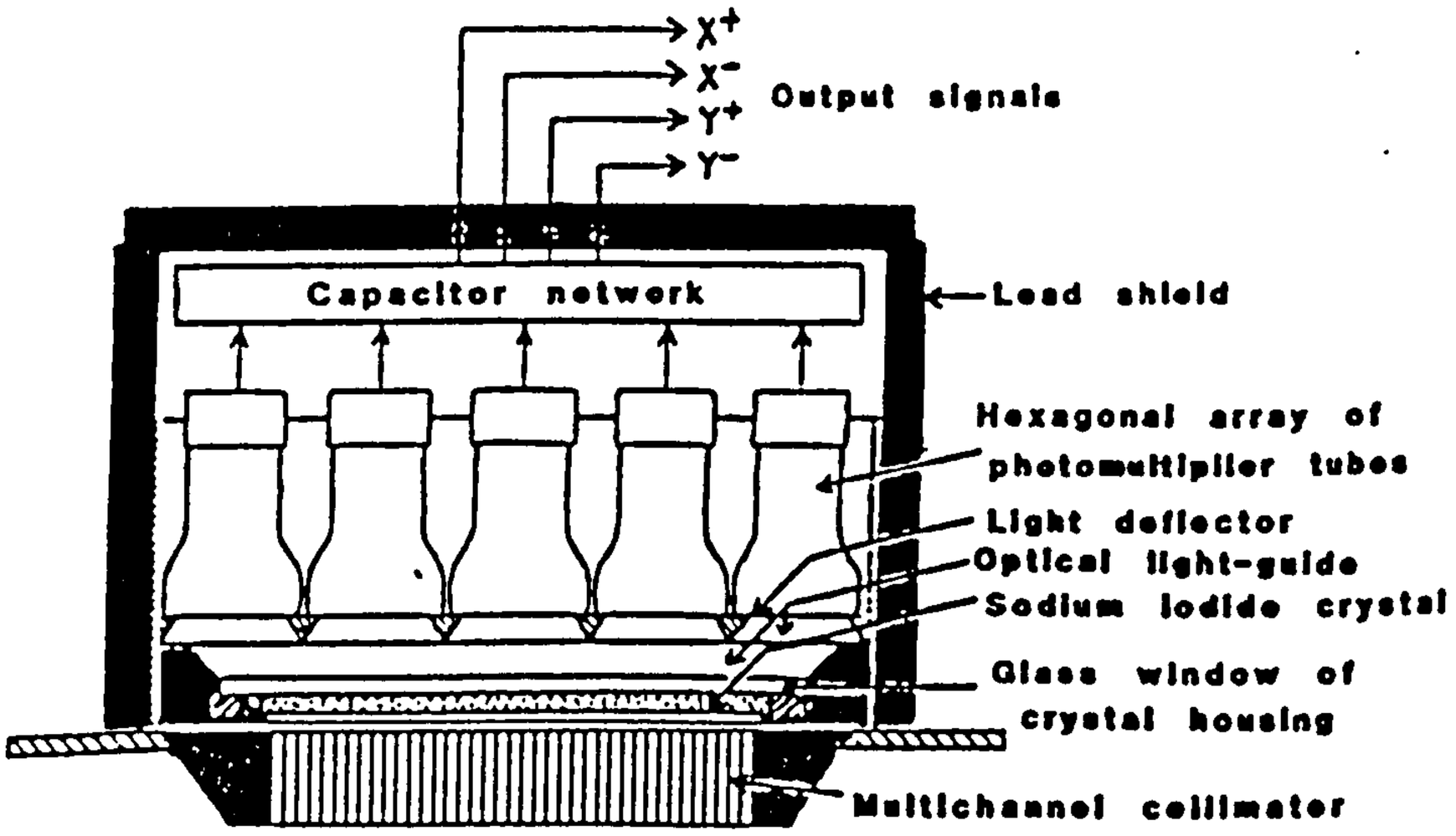

Figure 4.19: *Anger camera principle*

If axes are defined, the tube outputs can be processed by analogue or digital means to give both the position and energy of the photon. From this description, an intrinsic disadvantage of the Anger camera principle is clear: as each tube must be surrounded by 6 others to function properly, the area covered by the outermost ring of photomultipliers cannot be considered to be useful for imaging. Thus the useful area is always considerably smaller than the detector physical area.

Anger cameras are the standard clinical X-ray imaging tool and have also been used in several X-ray telescopes. The key parameters of two of these instruments, GRIP [30] and SIGMA [98] are shown in Table 4.4.

	GRIP	SIGMA
Detector area (cm^2)	1320	1963
Effective area (cm^2)	615	825
Number of PMTs	19	61
Spatial Resolution FWHM (mm)	7.0	4.7

Table 4.4: *X-ray telescopes employing Anger cameras*

4.3.4.2 Position-sensitive Photodetectors

Several photodetectors have now been developed which are capable of determining the position of any incident illumination. Most work on the same principle as the photomultiplier described in Section 4.3.4; that is, an incident photon ejects an electron from a photocathode, this photoelectron initiates a shower of electrons within the device, and the charge generated is collected on an output surface from which the signal is derived. To create a position sensitive detector requires the use of special techniques in the areas of electron amplification and charge collection.

The photoelectrons emitted from the photocathode are usually proximity focussed onto the gain stage; that is the two surfaces are mounted no more than a few millimetres apart to prevent loss of positional resolution and to reduce distortions in the final image.

The electron amplification is achieved by a system designed to preserve the position and geometry of the electron shower initiated at the photocathode. Various designs have been suggested including :

- Metal foil dynodes containing a regular pattern of apertures [23].
- A Venetian blind dynode structure with a co-aligned magnetic field [86].
- A fine mesh dynode [85].
- A microchannel plate (see section 4.3.5).

When the electron shower arrives at the output generating surface, which may be either the anode or the last dynode, its position of arrival must be encoded into the output signals. Again, various methods have been employed to achieve this (Fig 4.20):

1. An array of discrete anodes.

   Usually referred to as a multianode photomultiplier, this type of device has been adopted in various fields [23,122]. As many as 88 discrete anodes have been housed within a single PMT enclosure, and spatial resolutions as good as 1.4mm FWHM have been reported [133]. A derivative of this type of tube has been demonstrated

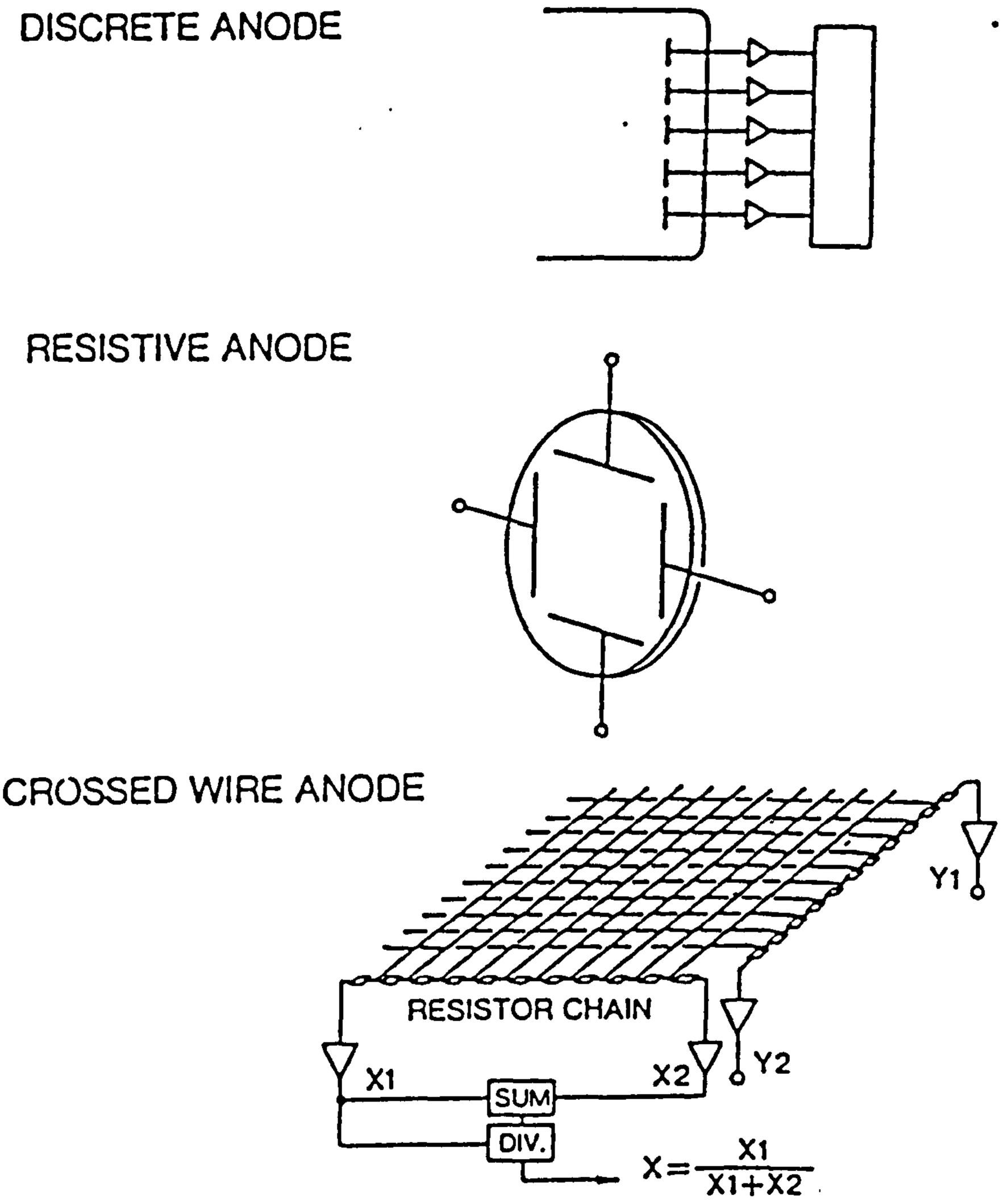

Figure 4.20: *Position-sensitive anodes*

working in high magnetic field environments with a spatial resolution of 2.6mm FWHM. These impressive performance figures should be balanced against the complexity of the necessary readout electronics, where many channels of data must be processed simultaneously. High count rates may be handled by this type of anode and this may be important in some applications.

2. A resistive anode.

   A single resistive anode has the advantage that only 4 output signals are generated and hence the readout electronics are much simplified. The main disadvantage is the long time constant associated with the readout which causes difficulties in high count-rate applications.

3. A crossed-wire anode.

   The crossed-wire anode combines the ease of readout of the resistive anode with the high rate capabilities of discrete anodes. Again only 4 output signals are generated. For this reason it has found favour in several designs of position sensitive PMT.

4. A wedge and strip anode.

   This is a conductive device comprising three insulated electrodes and relying on the unique division of charge amongst the electrodes for any x and y position. The position of the incident charge is easily calculated from the three digitised outputs [89].

Almost all combinations of these are possible, the most promising at present being position sensitive photomultipliers using mesh dynodes and a crossed wire anode, and imagers using a microchannel plate with a wedge and strip anode.

4.3.5 Microchannel Plates

The microchannel plate (MCP) is an ingenious electron amplification device which has many applications in X-ray detectors, but does not really fit into any of the detector groups described so far. The basic construction is of a plate pierced by numerous tiny holes, each only $\sim 25\mu$m across, and it is this hole size which gives the MCP its very high spatial resolution. The top surface of the plate is an electrode with a negative potential of ~2 kV relative to the base. Any electrons within a hole (or channel) are

accelerated downwards, colliding with the walls of the channel. Secondary electrons are emitted along the surface of the tubular channel whose resistive properties permit the maintenance of a continuous voltage gradient (Figure 4.21), giving rise to a large cascade with amplifications of the order of 10^4 being possible. At the exit of the MCP, the electrons spray out of the channel where they may be detected, most commonly with a wedge and strip anode [89].

Microchannel plates may be used in photomultipliers and other applications as a simple electron amplifier. Alternatively, the top surface of the plate may be coated with a photoelectron emitter [83], commonly evaporated CsI, to allow direct detection of low energy X-rays [54]. For the detection of higher energy photons, a detector comprising two MCPs has been suggested [103]. A 5 cm thick upper plate with a high lead content is used as a converter to give a reasonable detection efficiency (10% at 511 keV), whilst the second MCP is used as an amplification stage.

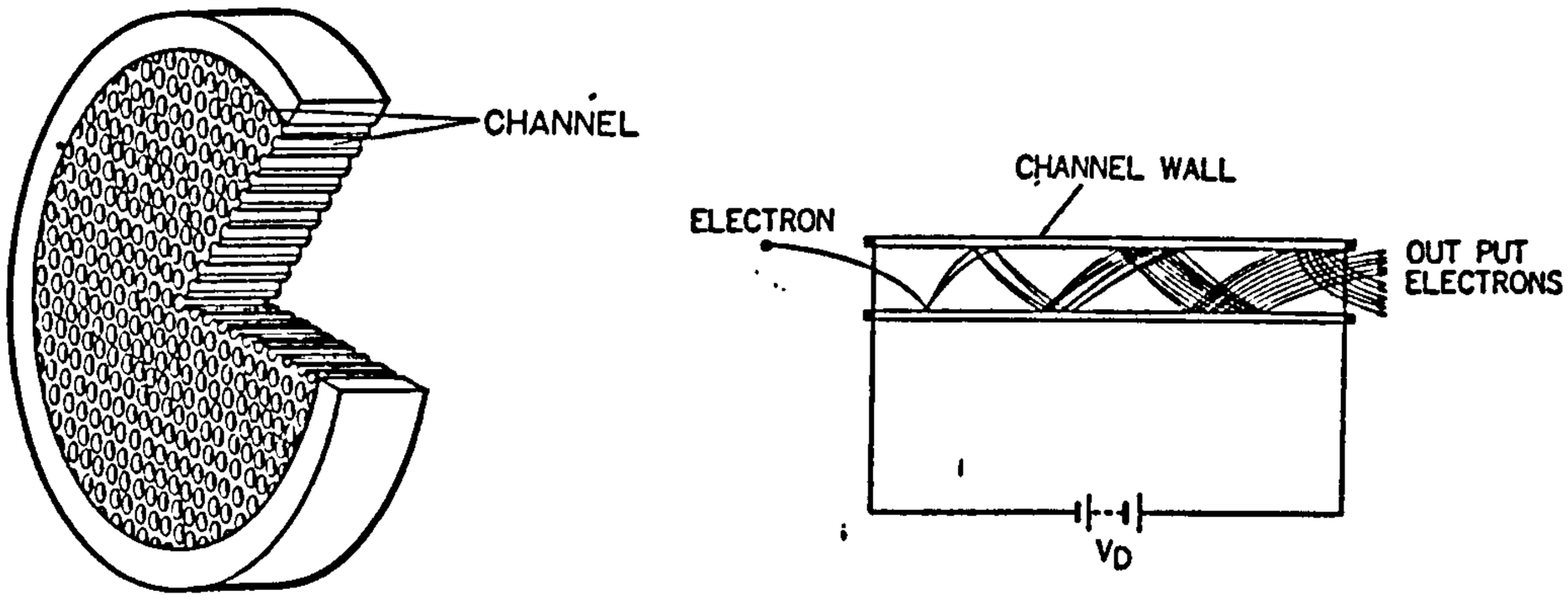

Figure 4.21: *(a) A microchannel plate and (b) detail of a single channel*

4.4 Conclusions

This chapter has reviewed some of the techniques available for constructing position sensitive X-ray detectors.

At low energies of $\leq$ 100 keV, the multi-wire proportional counter provides both moderate spectral resolution, and accurate location of the incident radiation. The upper limit to

their energy response is defined by the low interaction probability for energetic photons, even when the gas in the detector is pressurised to several atmospheres.

Germanium detectors are best applied to high resolution spectroscopy work. The cost of such detectors and the need to operate them at very low temperatures makes the construction of large-area position sensitive germanium arrays for imaging work impractical.

Scintillation detectors are efficient over the entire hard X-ray waveband, and are suited to the development of several types of position sensitive detector when coupled with photomultipliers or silicon photodiodes.

The remainder of this thesis will concentrate on the development of a position sensitive scintillation detector based on just one of the many options described in this chapter: a recently developed position sensitive photomultiplier viewing a single thin sodium iodide crystal.

Chapter 5

TESTS OF A POSITION SENSITIVE PHOTOMULTIPLIER

5.1 Introduction

The previous chapter has shown the benefits which arise from the use of a position sensitive detector when developing an X-ray imaging system. With the scintillator and photomultiplier tube proving to be such a successful detector combination it is only natural that attempts should be made to extract positional information from it. The Anger camera discussed in Section 4.3.4.1 (see also Figure 4.19) has been successful in this respect, but the use of multiple PMTs to derive positional information leads to inefficient use of detector area and complexity in the handling of the output signals.

An alternative approach is to use a single photomultiplier which has intrinsic positional resolution. Several techniques have been put forward to achieve this aim, and these were reviewed towards the end of the previous chapter in the section describing position sensitive photodetectors, of which they are but one type.

There are now many designs of photomultiplier offering some form of position sensitivity. The important features of some of these are summarised in Table 5.1.

Manufacturer	Model	Sensitive Area (cm^2	P'cathode Material	Dynode Type	Anode Type	Spatial Res (mm)
Hamamatsu	R1224	3.14	Various	2 stage MCP	4 x 4 matrix	2.9
	R1712	2.54	Various	2 stage MCP	8 x 8 matrix	1.5
	R2486	19.6	Bialkali	Mesh	Crossed wire	0.3
	R2487	24.75	Bialkali	Mesh	Crossed wire	0.3
	R3292	78.5	Bialkali	Mesh	Crossed wire	-
	R3309	1.53	Bialkali	Linear focus	4 x 1 matrix	-
	-	4.9	Multialkali	2 stage MCP	10 x 10 matrix	-
	R3384	16.0	Bialkali	Mesh	16 x 16 matrix	6.0
	R3835	10.17	Bialkali	Mesh	8 x 8 matrix	5.4
Philips	XP4702	4.0	Bialkali	Aperture grid	8 x 8 matrix	-

Table 5.1: *Position-sensitive photomultipliers*

In this chapter, the discussion centres on one particular design of position-sensitive PMT, namely the Hamamatsu R2487-02 which was selected for assessment of its value in a hard X-ray imaging detector. The initial tests of two of these PMTs in conjunction with a NaI(Tl) scintillation crystal will be described, with the emphasis being placed on the determination of the positional resolution performance attainable. The inherent non-linearities of the devices will also be discussed with a view to testing the imaging capabilities of the detector.

5.2 The Hamamatsu R2487 series

The Hamamatsu R2487 series is one of a range of position sensitive PMTs designed for use in nuclear medicine, high energy physics and astronomy. The R2487 is a 3 inch square device, which gives it certain advantages when it comes to constructing a large array of PMTs. A 5 inch diameter circular version (R3292) is now available, and the manufacturers intend to apply the same techniques to an 8 inch diameter tube in the future.

A schematic diagram of the R2487-02, a variant of the R2487 employing resistive chain outputs, is shown in Figure 5.1. Light enters the photomultiplier through a flat

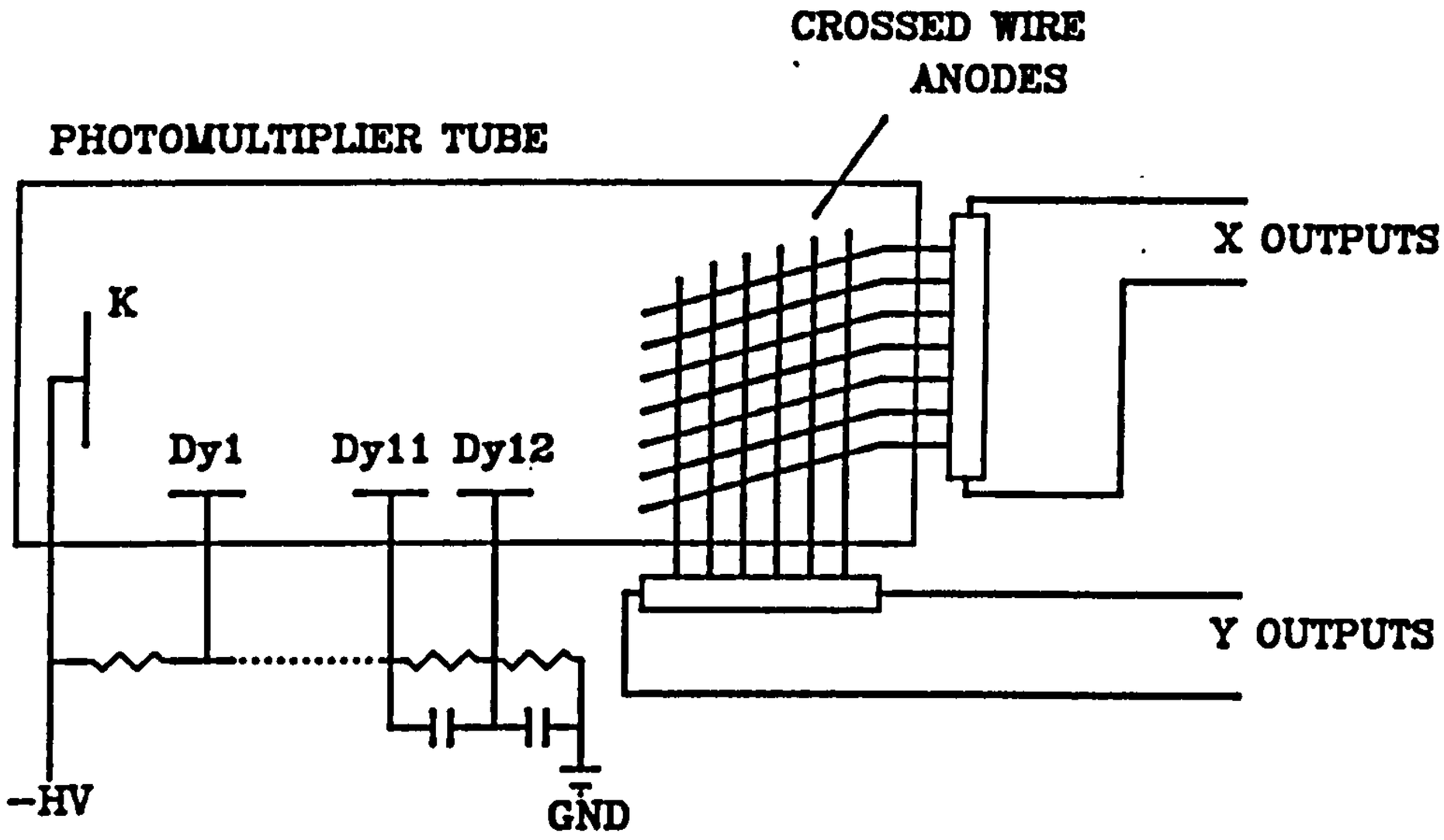

Figure 5.1: *Schematic view of the R2487-02*

borosilicate glass window. The bialkali photocathode is sensitive to radiation in the 300 – 600 nm range, with a peak response at 420 nm and a quoted quantum efficiency of 18% at 390 nm [3]. This therefore provides a good match for the many scintillators available which emit at this wavelength, with the most two most likely to be used with this type of tube being NaI(Tl) and CsI(Na). The specified effective area of the photocathode is 55 × 45 mm (minimum) which makes up 43% of the 76 × 76 mm front face of the tube.

The electrons ejected from the photocathode are proximity focussed onto the first dynode. The dynode structure used is a 12-stage proximity mesh which is designed to maintain the spatial distribution of the electron cloud as it is amplified. The gain of the PMT is typically 10^5 at 1250V, with the maximum operating voltage being 1300V.

The anode is of the crossed-wire type, and consists of two orthogonal sets of wires, 18 along the x-axis and 17 along the y-axis. In the versions tested, each wire is linked into a chain of 1kΩ resistors which forms a charge division network, whilst in other versions of the tube, the anode outputs are available at individual connections, and may be connected to appropriate electronics to enable specialised analysis of the positional information. The operation of the charge division network supplied with the -02 version of the PMT is now described.

The charge division network

The two sets of orthogonal anode wires are interconnected as shown in Figure 5.2. Charge deposited on any one anode wire is divided between the two outputs on the resistor chain according to the resistances of the two arms of the network and hence according to the position of the particular anode wire. As signals from any number of anode wires can be superimposed to make up a single event, the position indicated by the PMT is the position of the centroid of the electron shower incident on the anode.

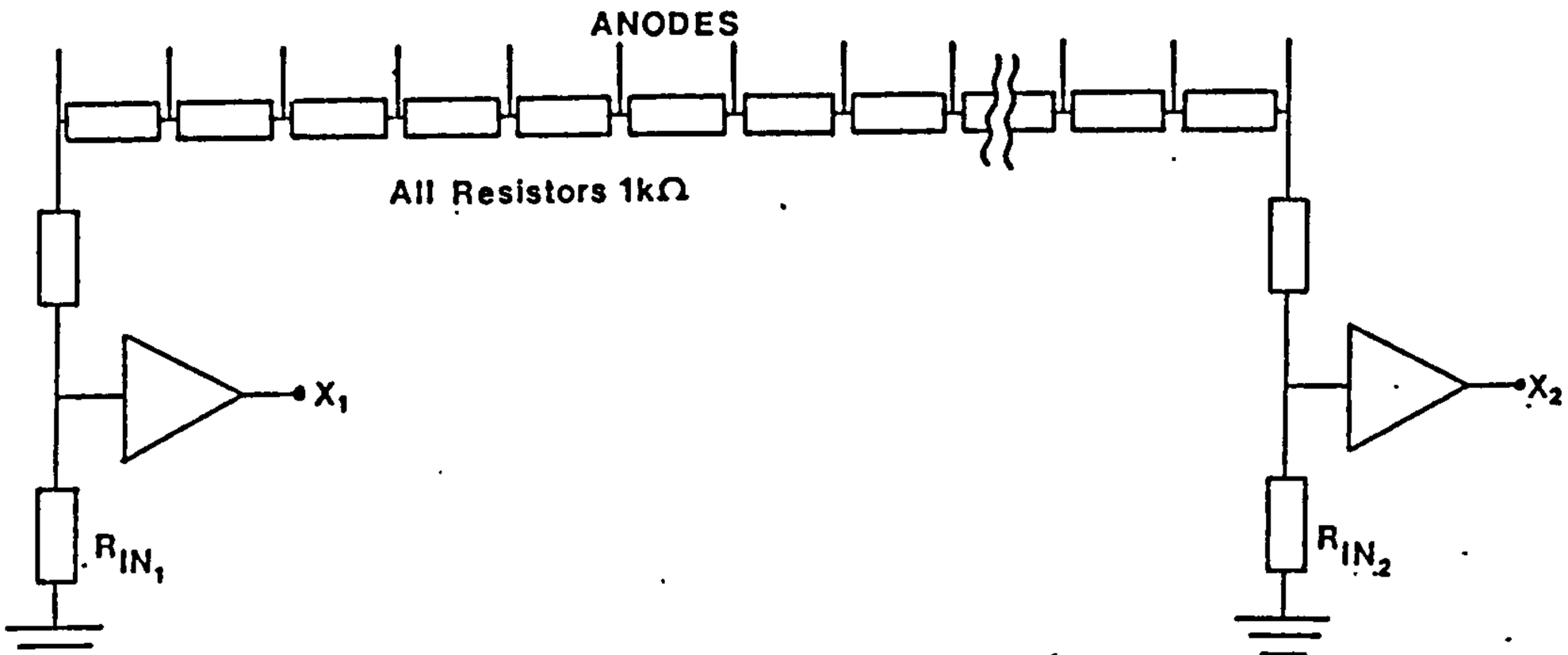

Figure 5.2: *R2487-02 resistive charge division network*

The output from the PMT therefore takes the form of 4 signals designated X_A, X_B, Y_C and Y_D. The use of appropriate algorithms enables both the intensity and position of the incoming illumination to be measured. Clearly the value of $X_A + X_B + Y_C + Y_D$ will be proportional to the intensity of the incident illumination, whilst the position of origin of a signal may be determined by the ratio of the two outputs of the resistor chain, using the following relationship:

$$S_X = \frac{X_A - X_B}{X_A + X_B} \tag{5.1}$$

where S_X is the reconstructed co-ordinate on the x-axis. Similarly:

$$S_Y = \frac{Y_C - Y_D}{Y_C + Y_D} \tag{5.2}$$

It can be seen that these algorithms give rise to values in the range of $-1 \leq S_X, S_Y \leq +1$ for an ideal charge division network.

It is also clear that any impedance introduced into the chain in the form of the input impedance of the pre-amplifiers (R_{IN}) will affect the division of the charge, with the degree of division becoming less pronounced as R_{IN} increases.

5.3 Experimental Details

Two supposedly identical R2487 photomultipliers were purchased for testing. The serial numbers of these devices were ZS0212 and ZS0514, hereafter referred to as TUBE 1 and TUBE 2 respectively. The factory test dates for the two PMTs were separated by 14 months, and so some undocumented development of the product may have occurred between the production of the two devices.

The PMT under test was housed in a aluminium casing with connections for the high voltage supply and a maximum of five signal outputs (4 anode outputs and a last dynode connection). When combined with the crystal housing, this formed a light-sealed detector unit which was convenient for laboratory tests. Mounting points for various collimators were provided on the detector housing.

The crystal used was a $80 \times 80 \times 5$ mm NaI(Tl) crystal supplied by Harshaw Chemie B.V. mounted in an aluminium housing with a 1mm thick aluminium entrance window and a 3mm thick glass exit window. This crystal was optically coupled to the photomultiplier using a standard silicon grease. The complete mechanical arrangement is shown in Figure 5.3.

The previous section outlined the calculations needed to extract the energy and position data from the raw PMT signals. In order to carry out these calculations and to allow a flexible approach to the analysis and display of results, it was decided that a computer-controlled readout system was necessary. The technique chosen employed 4 analogue-to-digital converters (ADCs) in a CAMAC system interfaced to an IBM AT compatible personal computer, the details of which will be described later. The analogue circuitry associated with the detector was used to convert the raw PMT signals to levels suitable

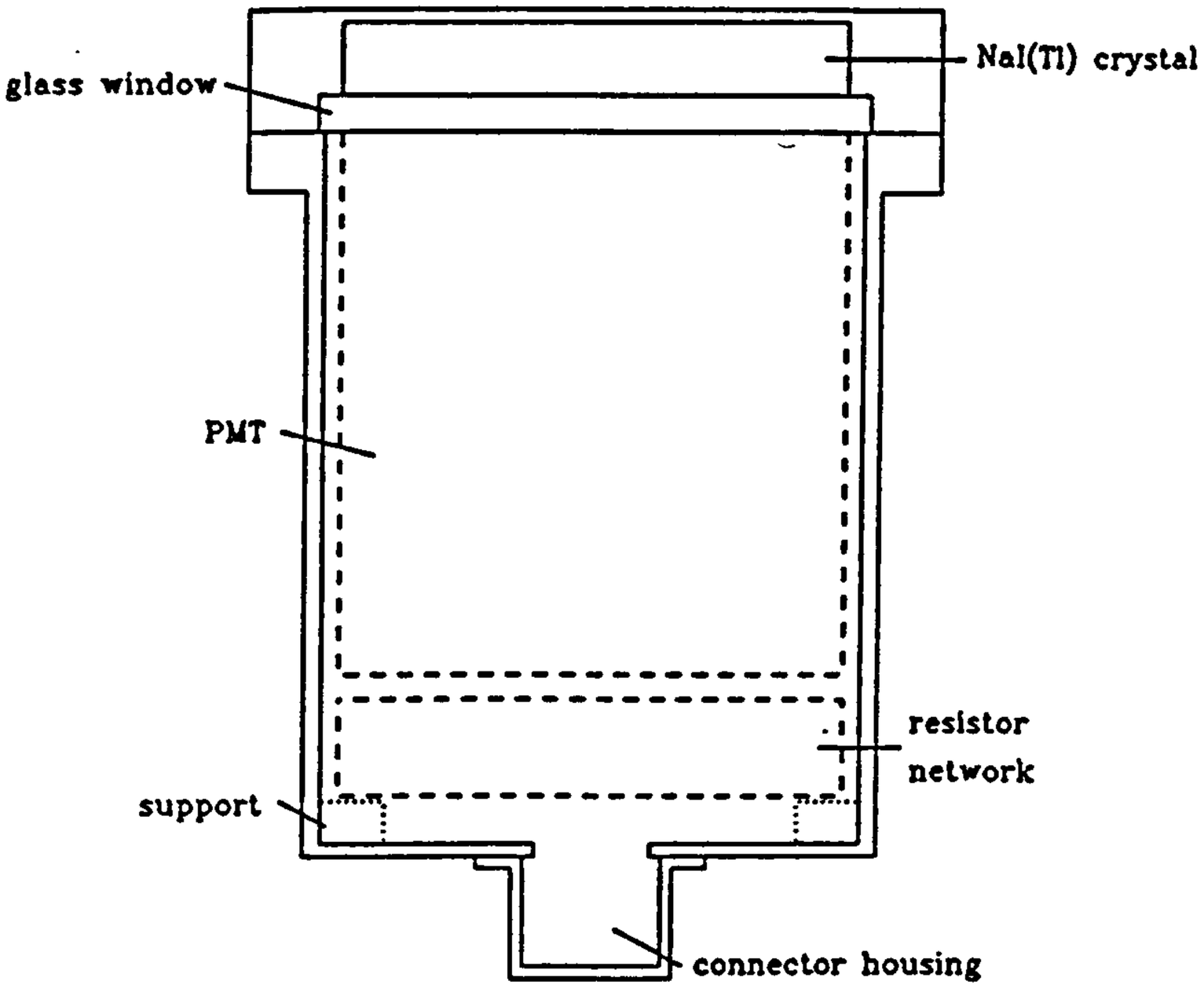

Figure 5.3: *The aluminium detector housing used in laboratory tests*

for input into the ADCs.

Two different approaches to the analogue circuitry were investigated, the differences arising from the way in which an event was recognised and the ADC conversion initiated. In the first case a signal was derived from the last dynode of the PMT, whereas in the second the individual anode signals were summed to provide a single trigger pulse.

5.3.1 Last Dynode Triggering

To enable a signal to be taken from the last dynode of the photomultiplier, the modification shown in Figure 5.4 was made to the dynode chain.

This provided an extra fast output with no position encoding which could be used as a trigger signal. Alternatively, this output could be connected to pulse shape analysis circuitry, enabling these position-sensitive photomultipliers to be used in a phoswich detector.

A schematic diagram of the analogue circuitry that was used to evaluate this system is shown in Figure 5.5. The four anode outputs were passed directly to a preamplifier

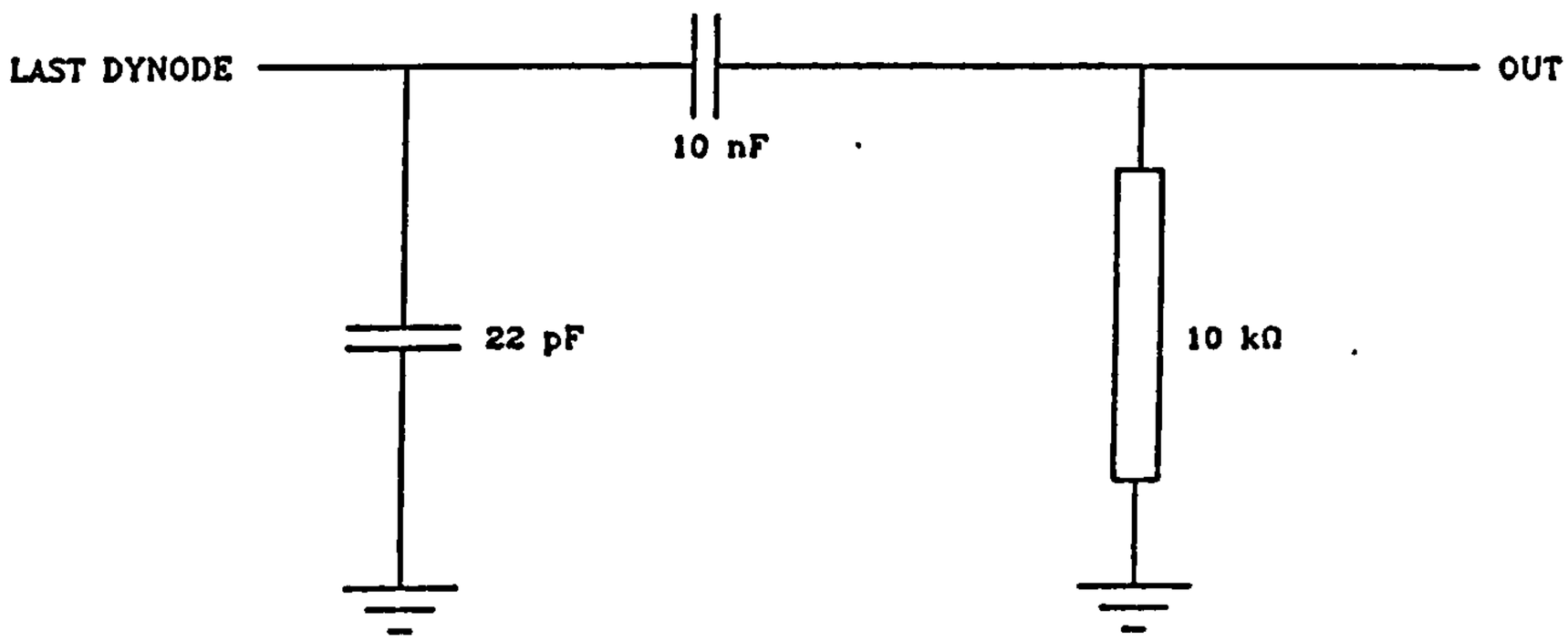

Figure 5.4: *Modification to the dynode chain of an R2487-02 to enable a signal to be taken from the last dynode*

(See Appendix 1) for a circuit diagram). The outputs from this preamplifier were at a low level, typically 60 mV, and so two further stages of amplification were required to produce a signal compatible with the $0 \rightarrow -2$V input range of the ADCs.

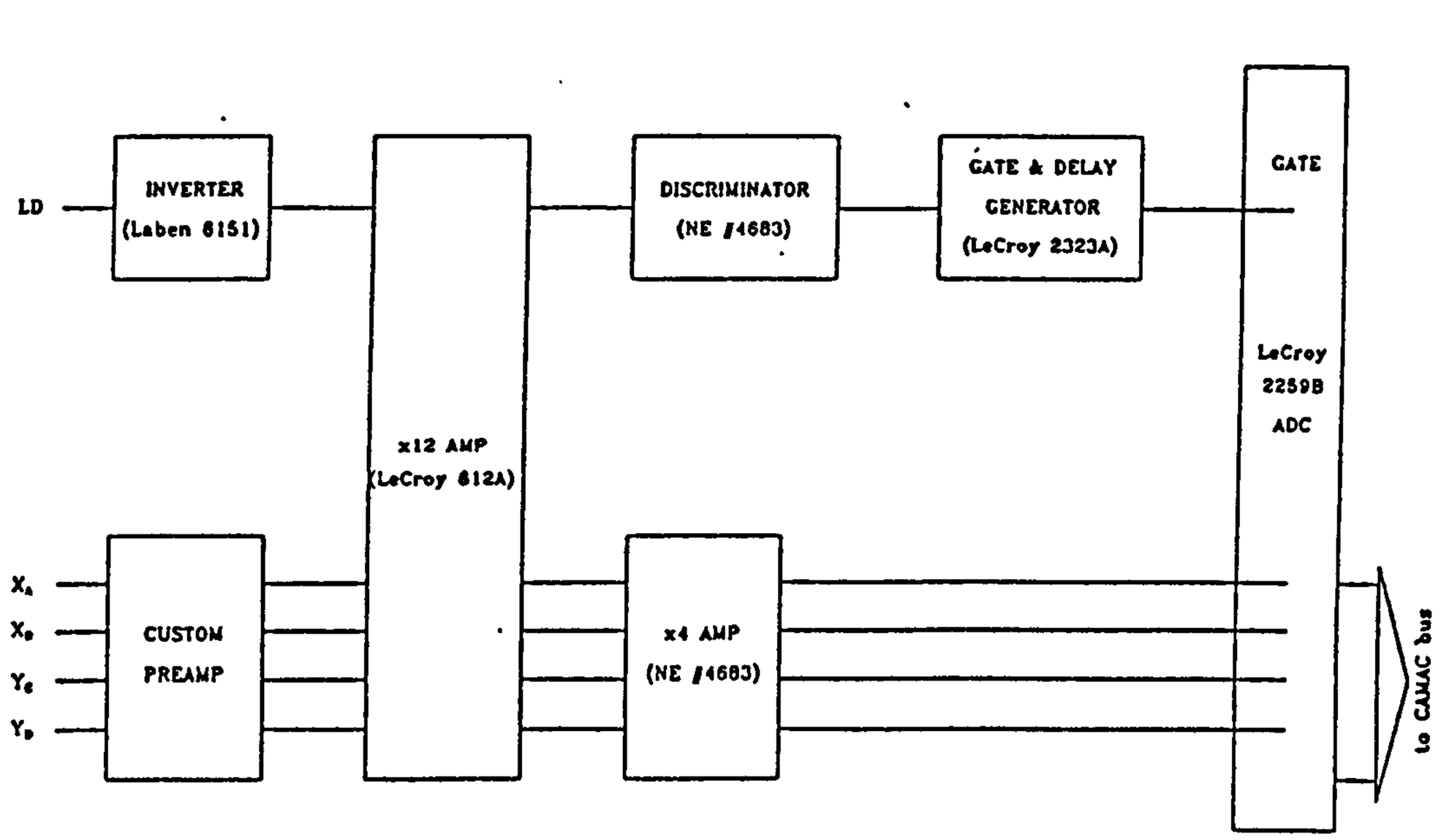

Figure 5.5: *Analogue electronics suitable for last dynode triggering*

The gate input for the ADCs was derived from the last dynode connection. This positive-going signal with a fast (15ns) rise time was first inverted and amplified before passing into a discriminator which was used to set a low level threshold for valid events from the detector. A variable delay was introduced to allow for the correct phasing of the

gate signal and the four anode signals. This analogue circuitry was used for the tests on TUBE 1 described in the following sections.

5.3.2 Anode Triggering

Deriving a trigger signal from the anode outputs rather than the last dynode has the advantages that it requires no modifications to be made to the photomultiplier base connections, and reduces the number and complexity of the analogue circuits required. A schematic diagram of the signal processing electronics is shown in Figure 5.6

The four anode outputs pass to a specially designed amplifier (see Appendix 1 for a circuit diagram) which carries out the following functions:

- Each input passes into a charge sensitive pre-amplifier with a low input impedance, which is necessary if the charge division is to occur properly. The two identical outputs from each preamplifier have a range of $0 \rightarrow 0.2$ V
- One output from each preamplifier passes into a main amplification stage with a gain of ~ 10 which inverts and amplifies the signal to provide an output compatible with the input stage of the ADCs.
- The other four outputs (one from each preamplifier) pass into a inverting summing amplifier with unity gain which produces an output which can be fed to a standard NIM discriminator.

This approach was used for the tests on TUBE 2 including the imaging tests described in Chapter 4. It is envisaged that future modifications could incorporate the discriminator into the amplifier circuit and this would further simplify the electronics.

5.3.3 Data digitisation and analysis

The ADCs used (LeCroy 2259B) were 12-channel, externally triggered, peak-sensing ADCs with a conversion time of 105μs. Peak-sensing ADCs were used as these were found to be less susceptible to the effect that source position has on the rise-time of

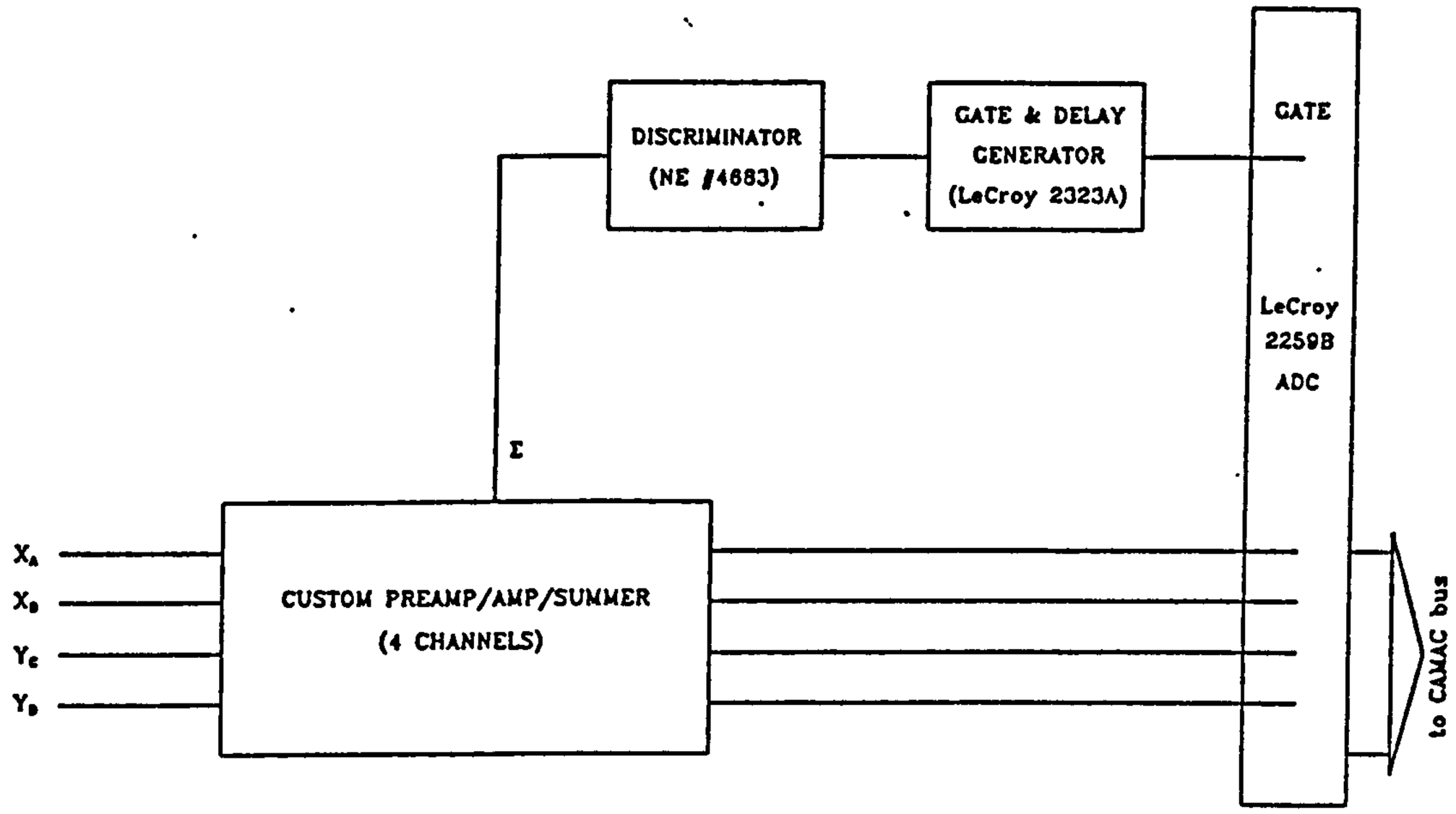

Figure 5.6: *Analogue electronics suitable for anode triggering*

the outputs. The digital values of the four anode outputs were transferred to a RM NIMBUS AX (a 12MHz AT-compatible personal computer) which was connected to the CAMAC bus via a HYTEC 1330 interface. Software written for this application allowed the collection, analysis and display of data from the detector. Applications software included:

- Pulse height analysis (of any/all of the four anode outputs).
- Utilities to aid in the calibration of the detector.
- 2-D image collection.

5.4 Preliminary Measurements

5.4.1 Energy Resolution

The energy resolution of the detector system was measured by illuminating the crystal with X-rays at two energies: 60 keV from ^{241}Am and 122 keV from ^{57}Co. Two positions were tested for each source: at the centre of the detector; and 30mm from the centre,

near to the limit of the sensitive area. By using a lead collimator, the radiation incident on the crystal was restricted to a 1mm diameter beam, this being essential to obtain a true measurement of resolution from a detector with non-uniform response.

Spectra were formed by binning the sum of the four digitised anode signals ($X_A + X_B + Y_C + Y_D$) to form a standard pulse height spectrum. This same procedure was employed for the measurements on both photomultipliers, and the results are shown in Table 5.2. In order to allow a meaningful comparison of the performance of the two tubes, the same 80 × 80 × 5 mm NaI(Tl) crystal was used for all the measurements.

		TUBE 1	TUBE 2
Am^{241}	Centre	26.7%	16.9%
60 keV	30 mm	32.0%	19.2%
Co^{57}	Centre	15.7%	12.4%
122 keV	30 mm	24.3%	16.2%

Table 5.2: *Energy resolution measurements*

A sample spectrum for a ^{57}Co source placed centrally over the crystal, measured using TUBE 2, is shown as Figure 5.7. These results may be compared with those obtained for the smaller but otherwise identical R2486 by Hailey et al [67], who measured a FWHM resolution of the form 10.8% (100 keV/E)$^{1/2}$ for a NaI(Tl) crystal.

The feature most apparent from this is the superior performance of TUBE 2. This was undoubtedly due, in part, to the improved analogue electronics employed, but there was reason to suspect that TUBE 1 was offering a poorer performance. This was later confirmed by the spatial linearity tests.

The energy resolution measured at the centre of both PMTs is good, but in each case the resolution worsens away from the centre. The spectra obtained showed this to be due to a reduction in detector sensitivity, and this dependence of sensitivity upon source position is discussed below.

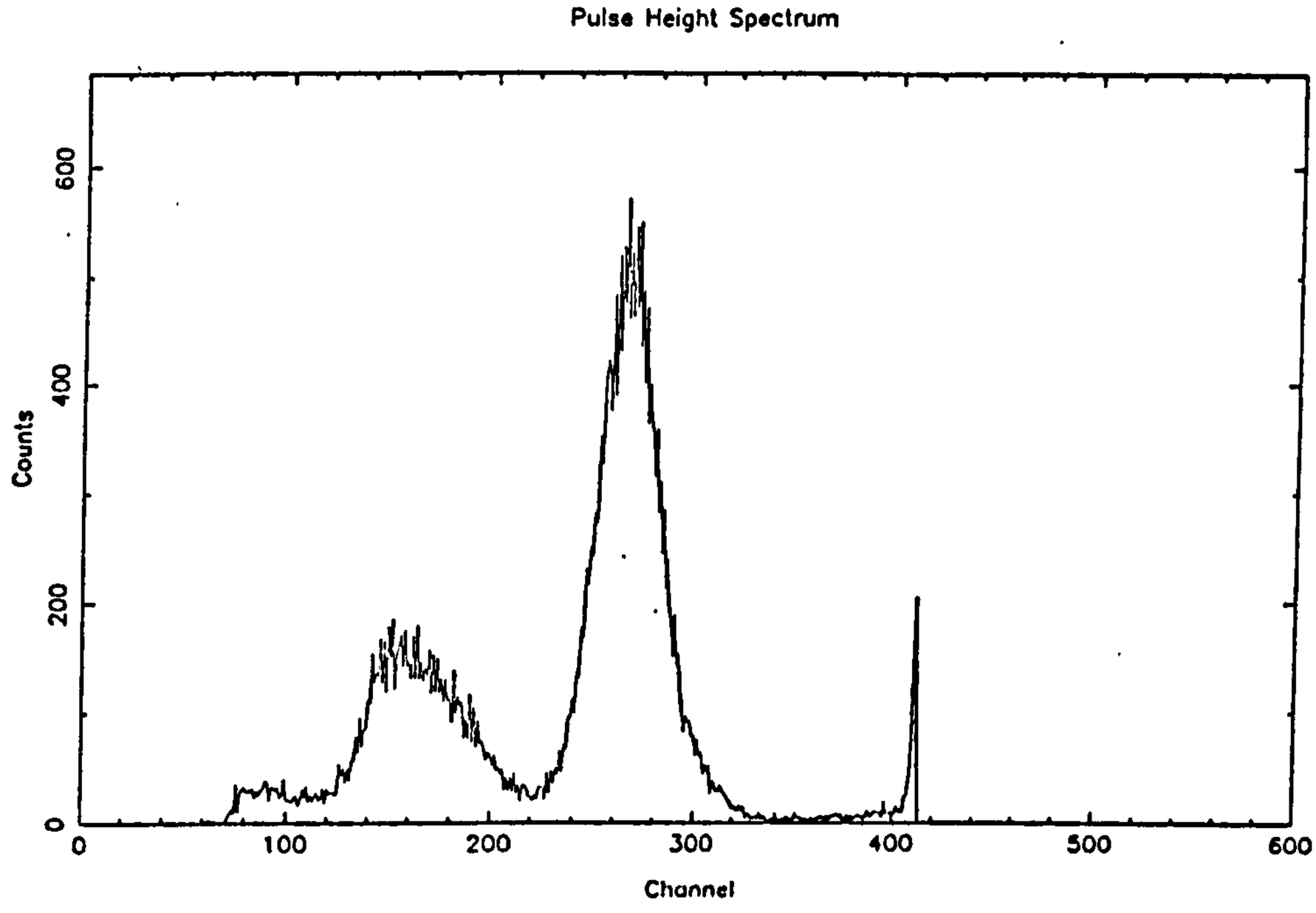

Figure 5.7: *Energy spectrum for central ^{57}Co source - TUBE 2*

5.4.2 Pulse-Height Uniformity

It became clear from the measurements of the energy resolution of the two detectors that both TUBE 1 and TUBE 2 have a non-uniform sensitivity across their sensitive areas. This effect was investigated by measuring the pulse height produced by the ^{57}Co source at points making up a 7×7 grid of points separated by 10mm on the detector face. Maps of the dependence of output pulse height on source position for the two PMTs are shown as Figures 5.8 and 5.9 and in both cases there is a marked drop in sensitivity towards the edge of the detector. In addition, the map of TUBE 2 is also noticeably asymmetric. The most important quantitative value is the peak-to-edge ratio since this determines the range of pulse heights which must be accepted by the hardware in order to ensure the detection of a given energy at any position. This value is 2.3 and 3.5 for TUBE 1 and TUBE 2 respectively.

This behaviour may be explained as a combination of several processes:

1. There are likely to be spatial variations in the quantum efficiency of the photocathode and the photoelectron collection at the first dynode. Hailey et al. [67] reported variations of ~15% when the photocathode of a similar tube was scanned

using a 100 μm diameter fibre light pulser. These variations must be intrinsic to the photomultiplier and it may be assumed that they are due to a combination of the two effects.

2. Events occurring near the edge of the sensitive area may be degraded by light losses around the photocathode or by subsequent losses of photoelectrons from the dynode structure. This effect will be dependent on the size of the light pool at the photocathode, and hence the crystal and window thicknesses.

3. Non-uniformity of the light collection efficiency at the crystal-PMT boundary is likely to be a much smaller effect.

4. There may be boundary effects due to the finite crystal size, which extends just beyond the photomultiplier casing.

Although the non-uniformity is quite severe, it is an effect which may be measured, and hence the energy information supplied by the photomultiplier may be corrected using calibration data as part of the data processing procedure carried out by the computer.

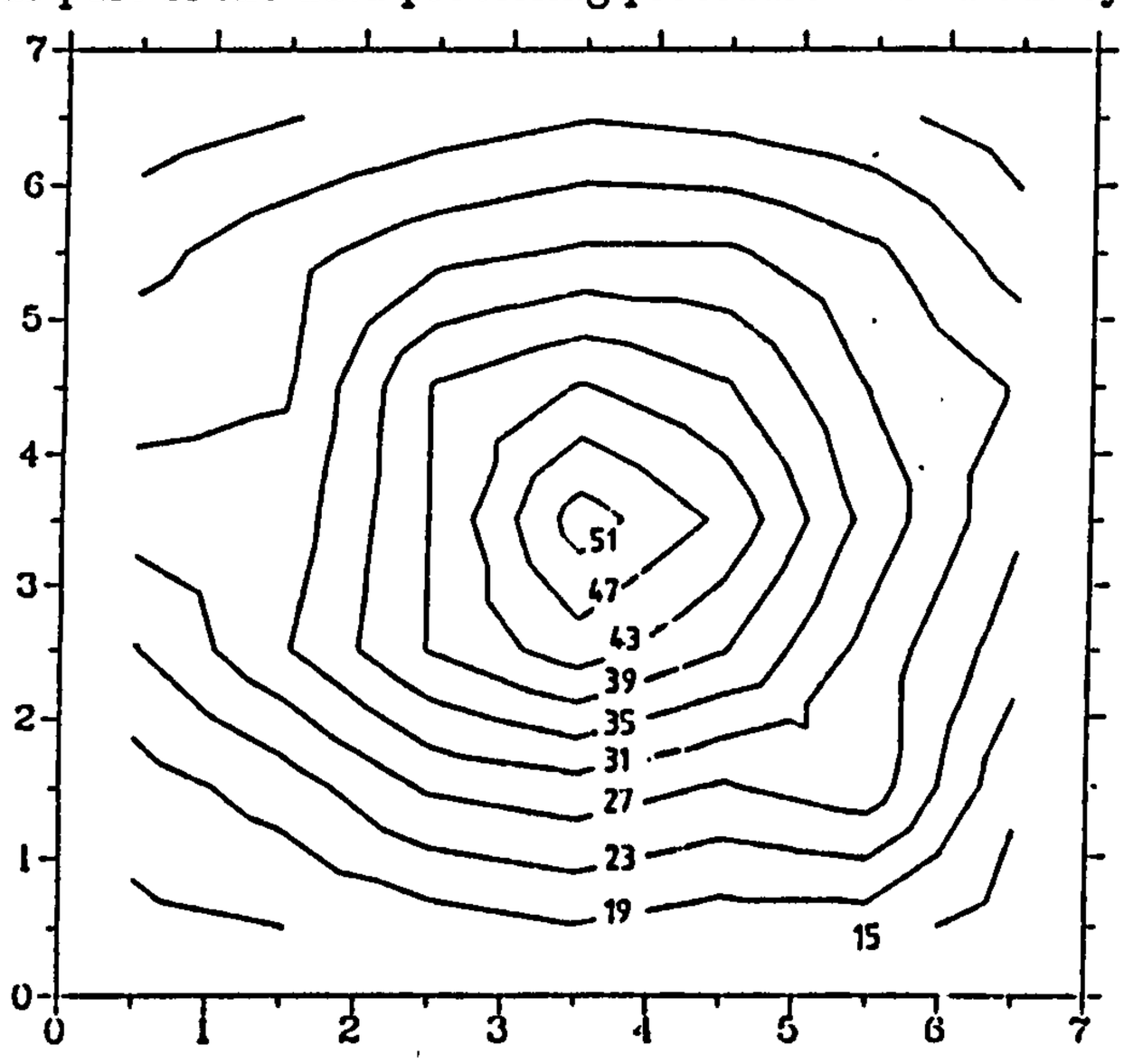

Figure 5.8: *Output pulse height as a function of source position - TUBE 1*

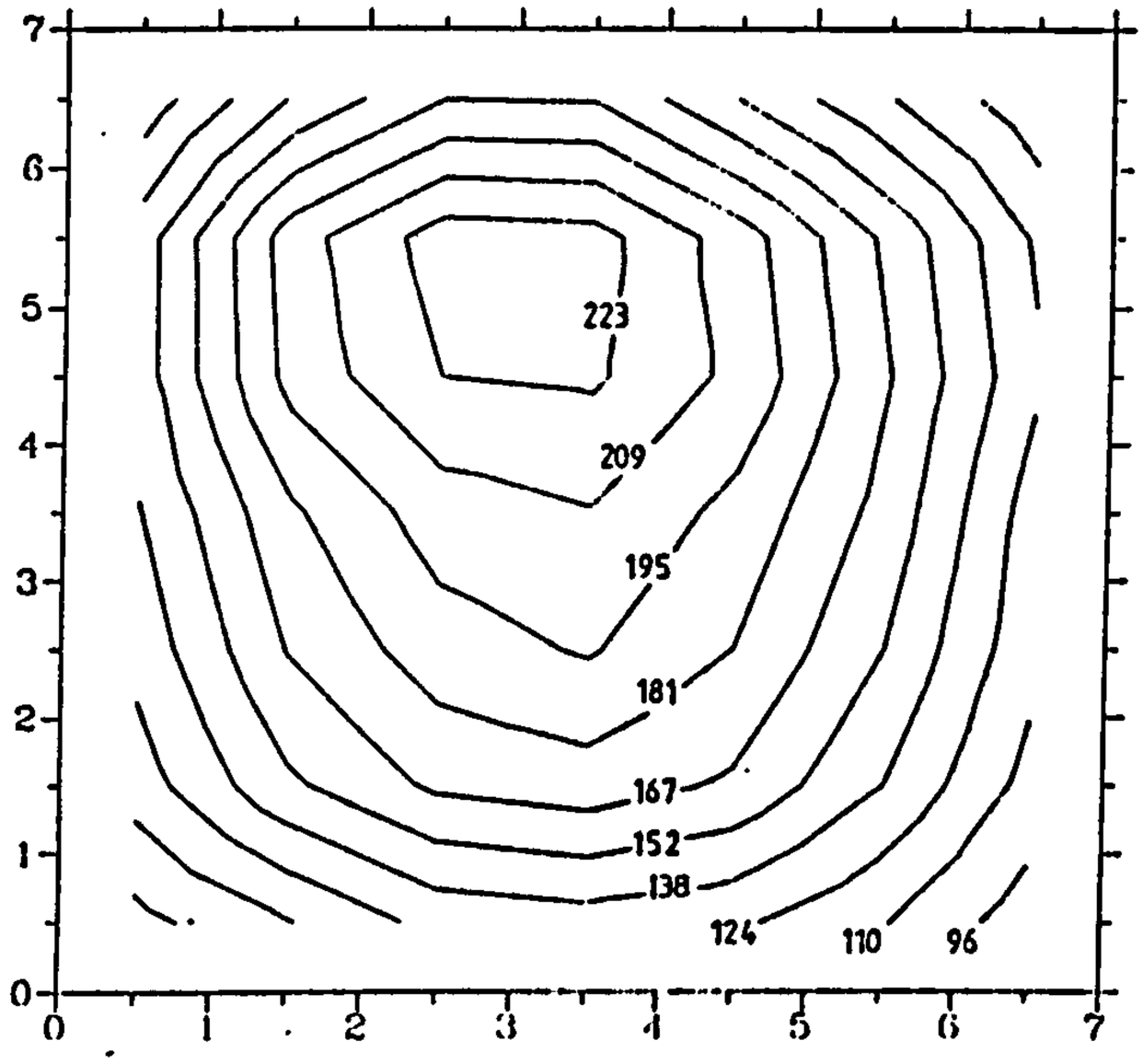

Figure 5.9: *Output pulse height as a function of source position - TUBE 2*

5.4.3 Spatial Resolution

The next important performance factor to be measured for the two PMTs was the spatial resolution. This determines one contribution towards the uncertainty in the reconstructed position of any events detected.

The measurement was made by histogramming values of S, the reconstructed position for two collimated sources separated by a known distance. In this way the widths of the two resulting peaks in the histogram can be calibrated against the distance between them. This approach makes the assumption that the spatial information given by the PMT is linear over the area being measured, and for this reason, only the central areas of the detectors were considered for this measurement. The two sources were placed at $x = \pm 8$mm, $y = 0$mm for TUBE 1 and at $x = \pm 10$mm, $y = 0$mm for TUBE 2. The collimation used was a 1mm diameter hole drilled through 20mm of lead to produce a tight 1mm beam at the crystal.

The histograms obtained for TUBE 1 and TUBE 2 are shown as Figures 5.10 and 5.11 respectively. The widths of the peaks are:

TUBE 1: FWHM = 2.54 ± 0.2 mm

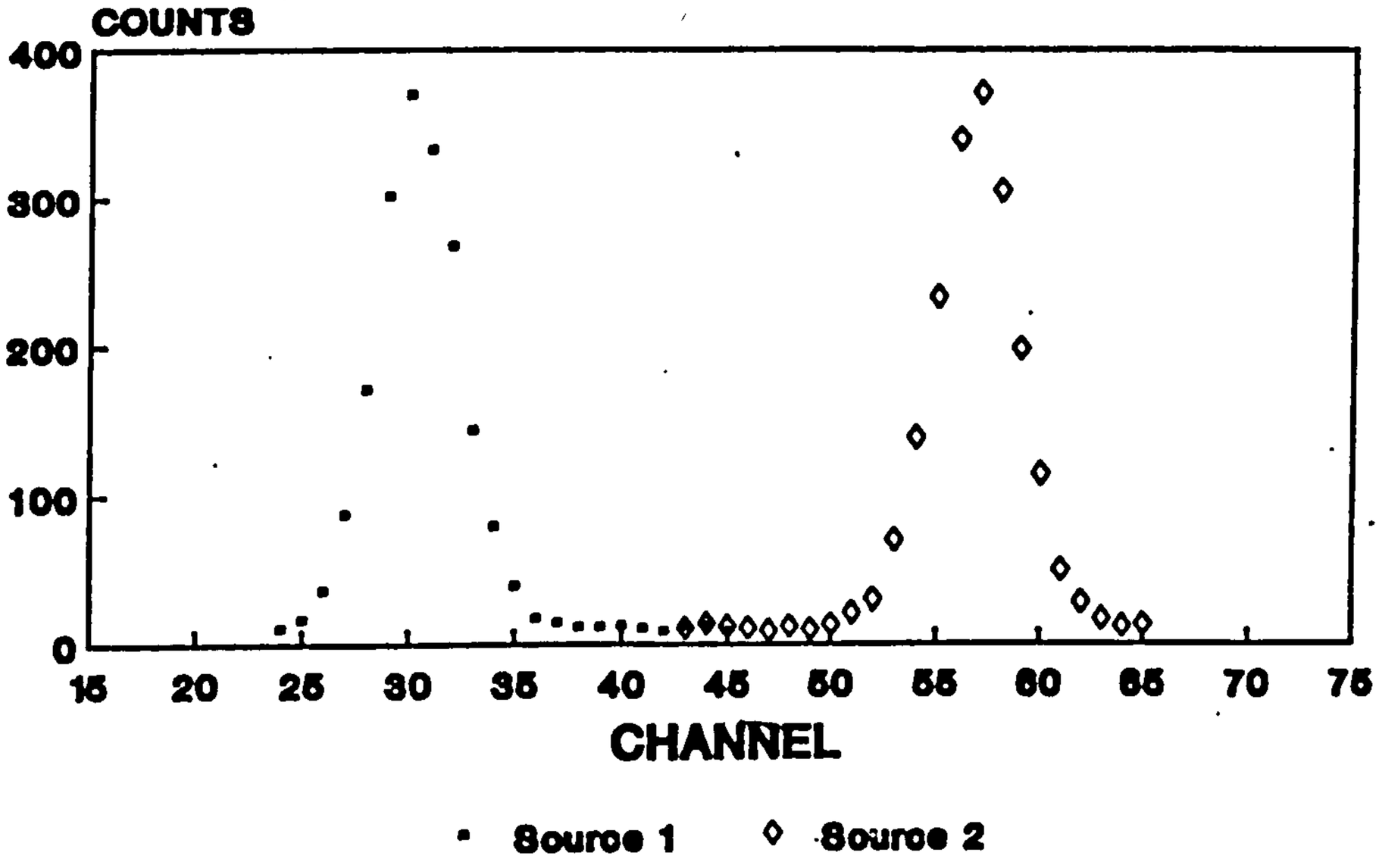

Figure 5.10: *Measurement of spatial resolution - TUBE 1*

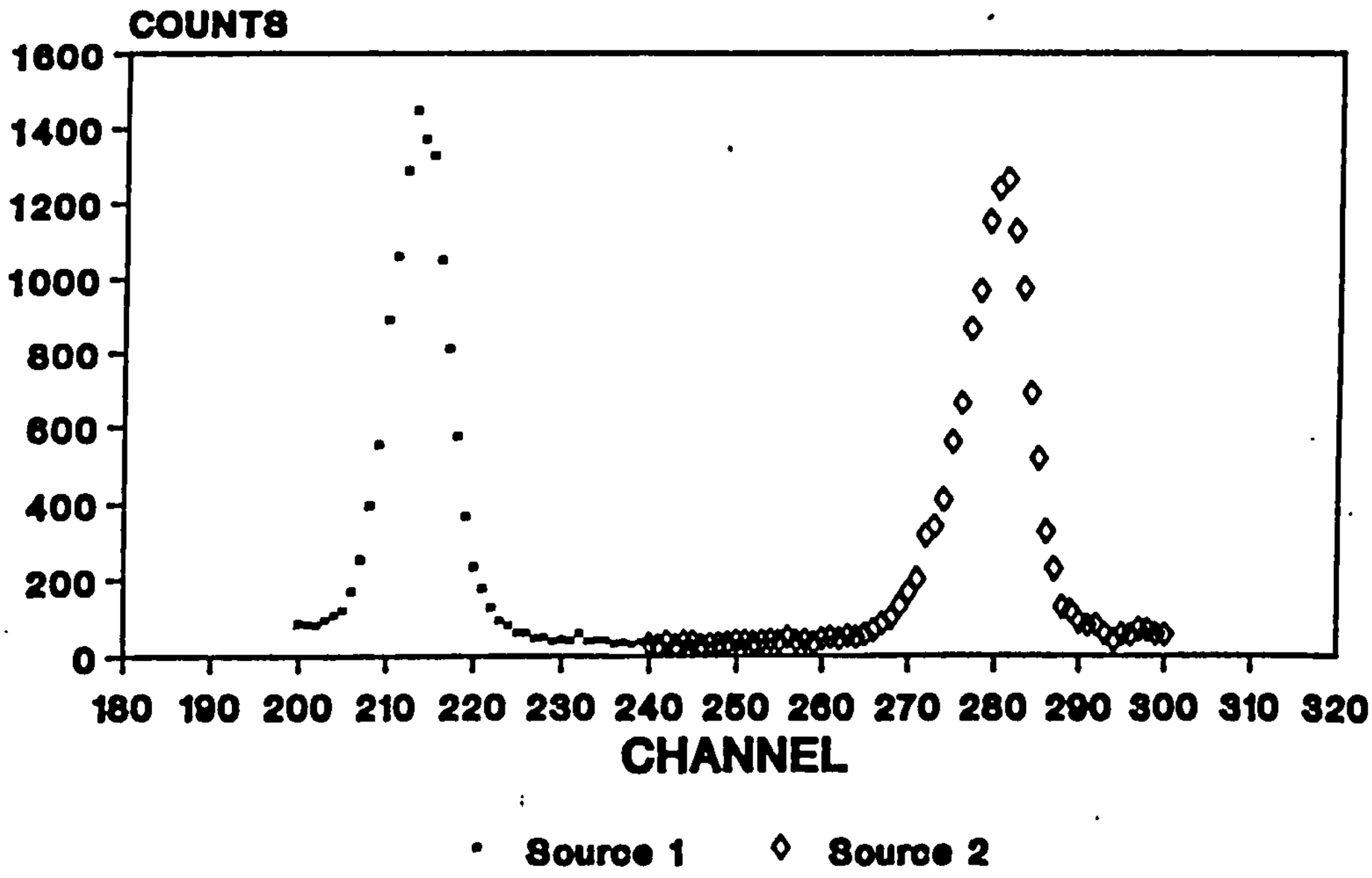

Figure 5.11: *Measurement of spatial resolution - TUBE 2*

TUBE 2: FWHM = 2.72 ± 0.3 mm

These must be corrected to take account of the width of the incident X-ray beam. The calibration curve shown in Figure 5.12 was created by the superposition of many gaussians with a FWHM determined by the true detector resolution over a distance representing the X-ray beam diameter, and examining the resultant profile. The corrected values are:

TUBE 1: FWHM = 2.33 ± 0.2 mm

TUBE 2: FWHM = 2.53 ± 0.3 mm

These values suggest that, at least at the centre where the measurements were made, the spatial resolution of TUBE 1 is slightly better than that of TUBE 2. The measurement of spatial resolution across the whole face of the tube is a more complex task, and must be combined with the correction of any non-linearities present. See Figure 7.13 for an estimate of spatial resolution as a function of source position.

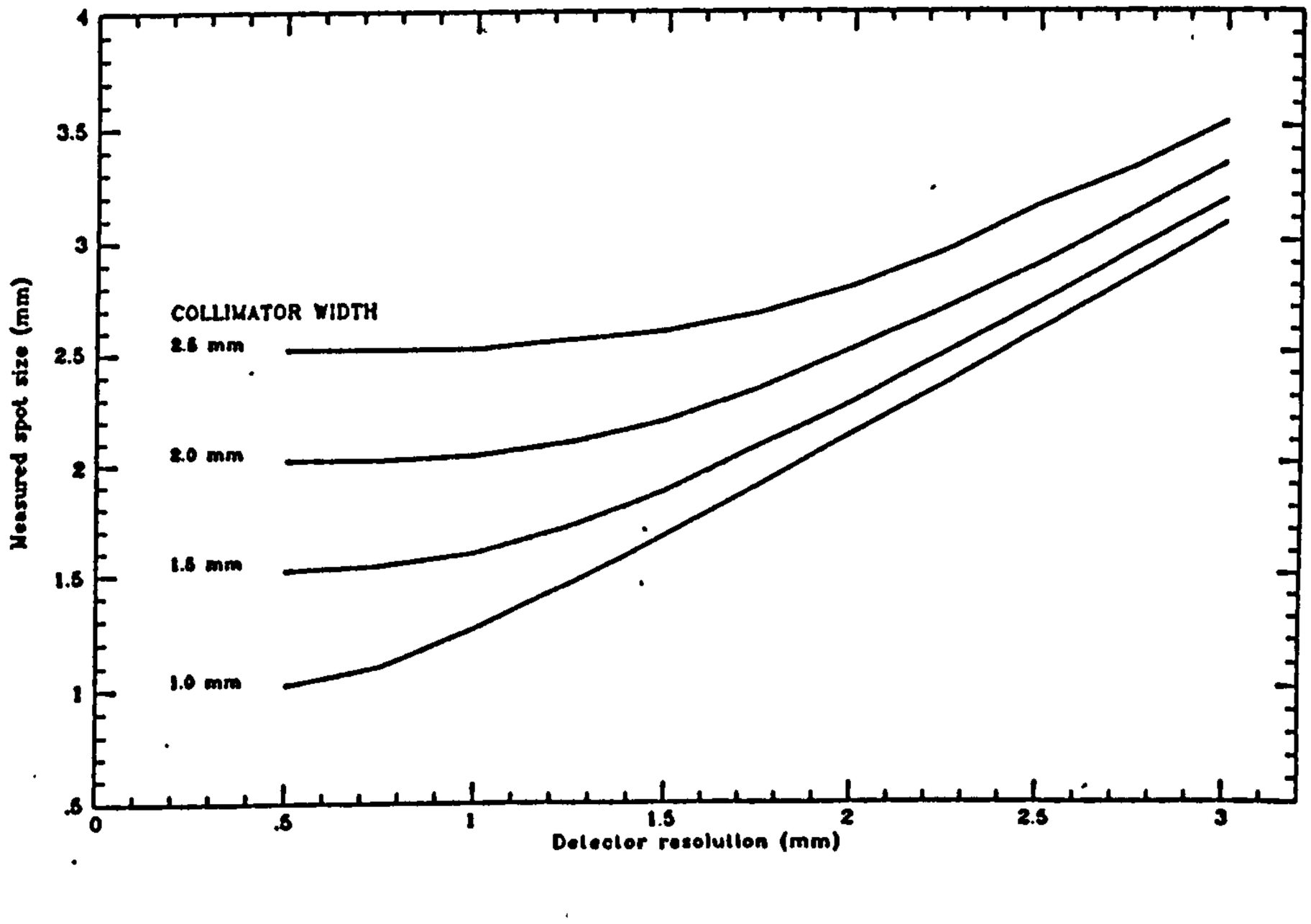

Figure 5.12: *Calibration curves to account for finite source width in spatial resolution measurements*

5.4.4 Spatial linearity

After the ability to locate and resolve point sources of illumination with good resolution, the next most important parameter that affects the value of the position-sensitive tube in imaging applications is the stability and linearity of the positional data provided. This will ultimately determine the useful area of the detector and also the amount of processing required to retrieve the true co-ordinates of an event from the raw output signals.

As described in Section 5.2, the four anode outputs X_A,X_B,Y_C and Y_D are processed according to

$$S_X = \frac{X_A - X_B}{X_A + X_B} \qquad \text{and} \qquad S_Y = \frac{Y_C - Y_D}{Y_C + Y_D} \tag{5.3}$$

where S_X and S_Y are the uncorrected x and y co-ordinates. For an ideal detector, this would result in values of S between -1 and 1, with a linear dependence upon event position. This ideal response is illustrated in Figure 5.13.

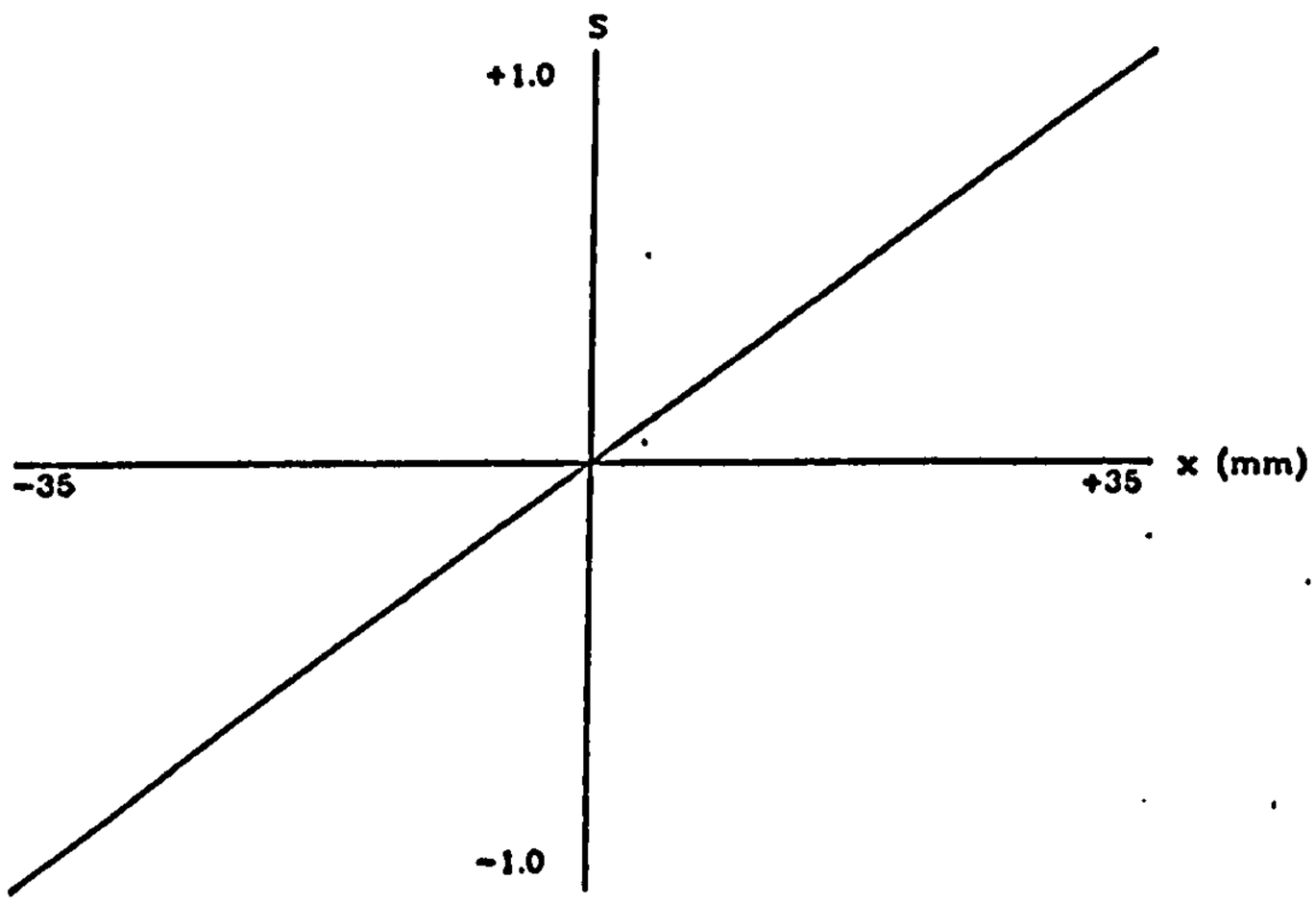

Figure 5.13: *Position response of an ideal detector*

In practice, however, light losses near the edge of the sensitive area of the photocathode impose a limit to the range of the values of S_X and S_Y. As the light pool formed by the X-ray interaction moves further from the centre of the detector, the amount of light lost increases, the reconstructed co-ordinate no longer changes linearly with position, and the

graph of S against position flattens at each end, becoming slightly S-shaped.

The graphs in Figure 5.14 plot the reconstructed co-ordinate S, against position for a source scanned along both the x and y axes of TUBE 1. Both curves show the expected general shape of a linear response with flattened ends, but in the case of the response along the y axis there is a serious problem for positions with y < -18mm. The graph is no longer strictly monotonic, and this will lead to ambiguities in the reconstructed position. As an example of this, consider the position value of 48 shown on the plot. This could be interpreted as a signal from either of two positions separated by ~15 mm. This is clearly unacceptable for an imaging detector, so the useful area must be restricted to y > 18 mm. The comparable graphs for TUBE 2 shown in Figure 5.15 indicate no such problems: both are monotonic over the measured range, allowing for unambiguous reconstruction of the position from any value of S.

It should be noted that for both PMTs the measurements were taken over a range of 60mm along each axis, which is in excess of the specified minimum useful area.

5.4.5 Distortion Maps

The measurements described in the previous section only contain information about events occurring on either the x or y axis. In order to assess a detector's imaging capability fully, it is necessary to make this type of measurement over the whole useful area of the detector. In this way, any distortions present in the detector will be discovered.

The measurements were made by determining the values of S_X and S_Y for events generated by a tightly collimated source scanned across the detector face. If contours of equal S_X and equal S_Y are superimposed, for an ideal detector they should form a grid of two equally spaced sets of orthogonal lines as shown in Figure 5.16. The maps obtained for TUBE 1 and TUBE 2 are shown as Figures 5.17 and 5.18 respectively. In each case, the broken line shows the 55 × 45 mm area guaranteed by the manufacturer.

The map for TUBE 1 shows marked deviations from the ideal performance. The problems noted on the y-axis response in Section 5.4.4 are now confirmed by the large distortions present in the area y < -10 mm. In terms of imaging capability, this distortion renders

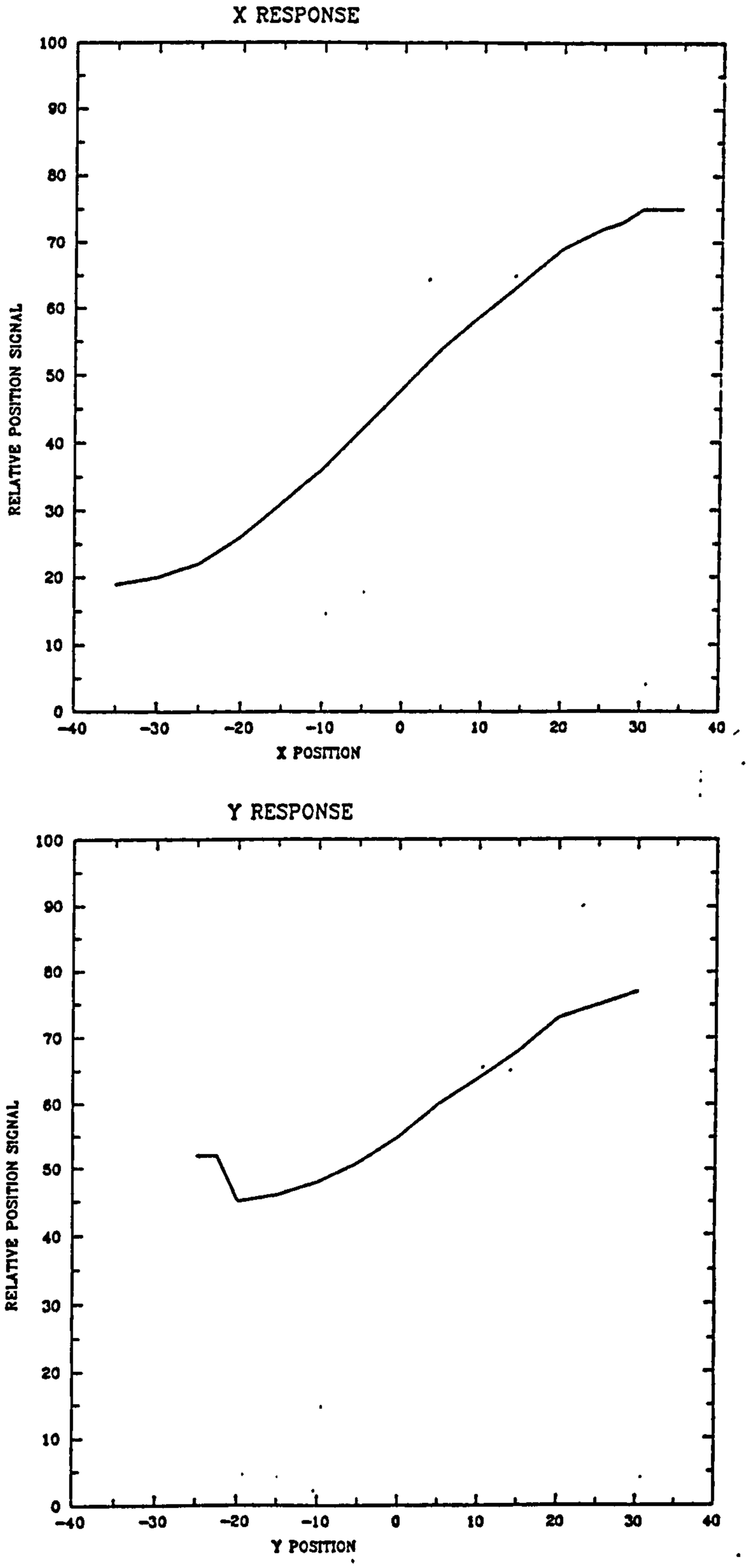

Figure 5.14: *Position response of TUBE 1 along x and y axes*

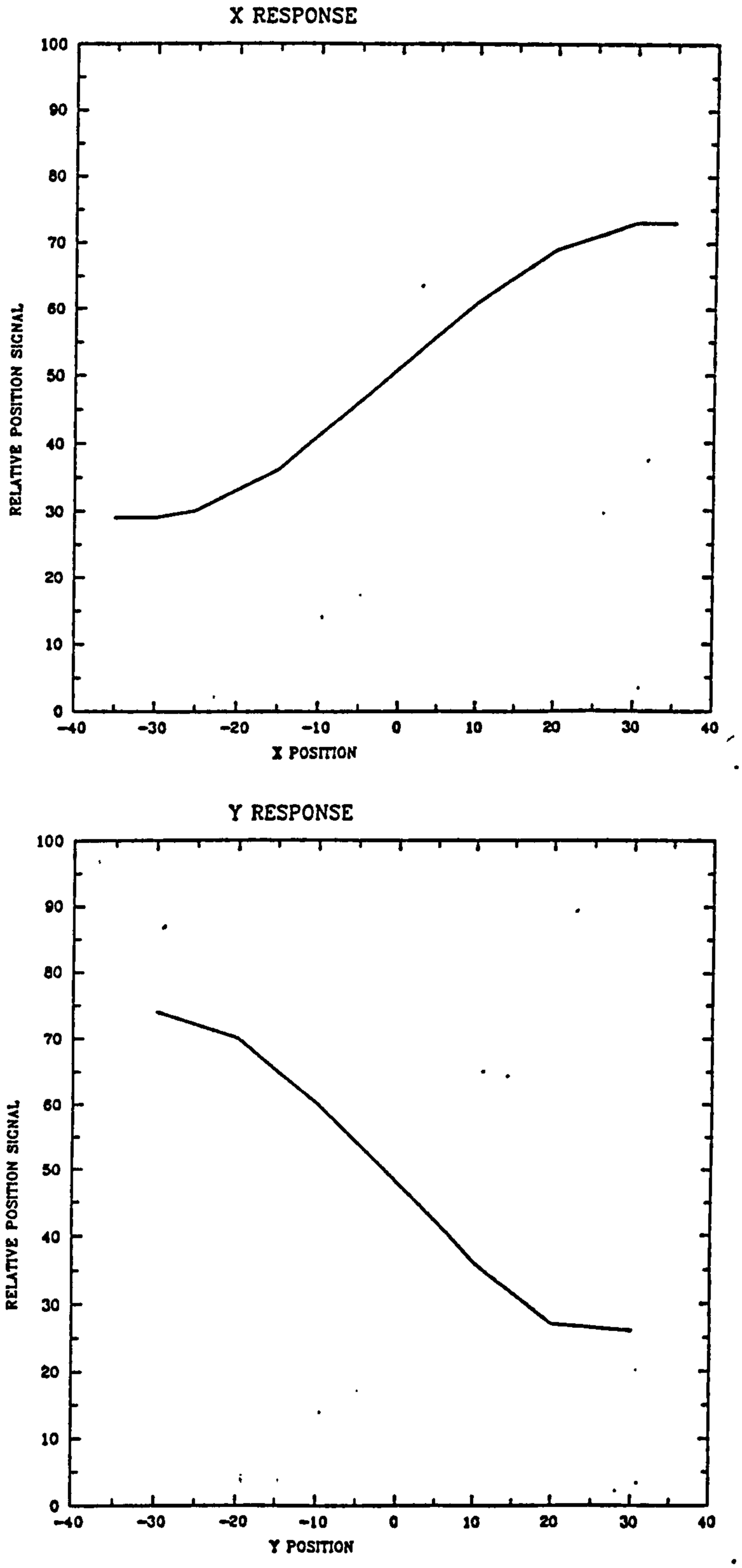

Figure 5.15: *Position response of TUBE 2 along x and y axes*

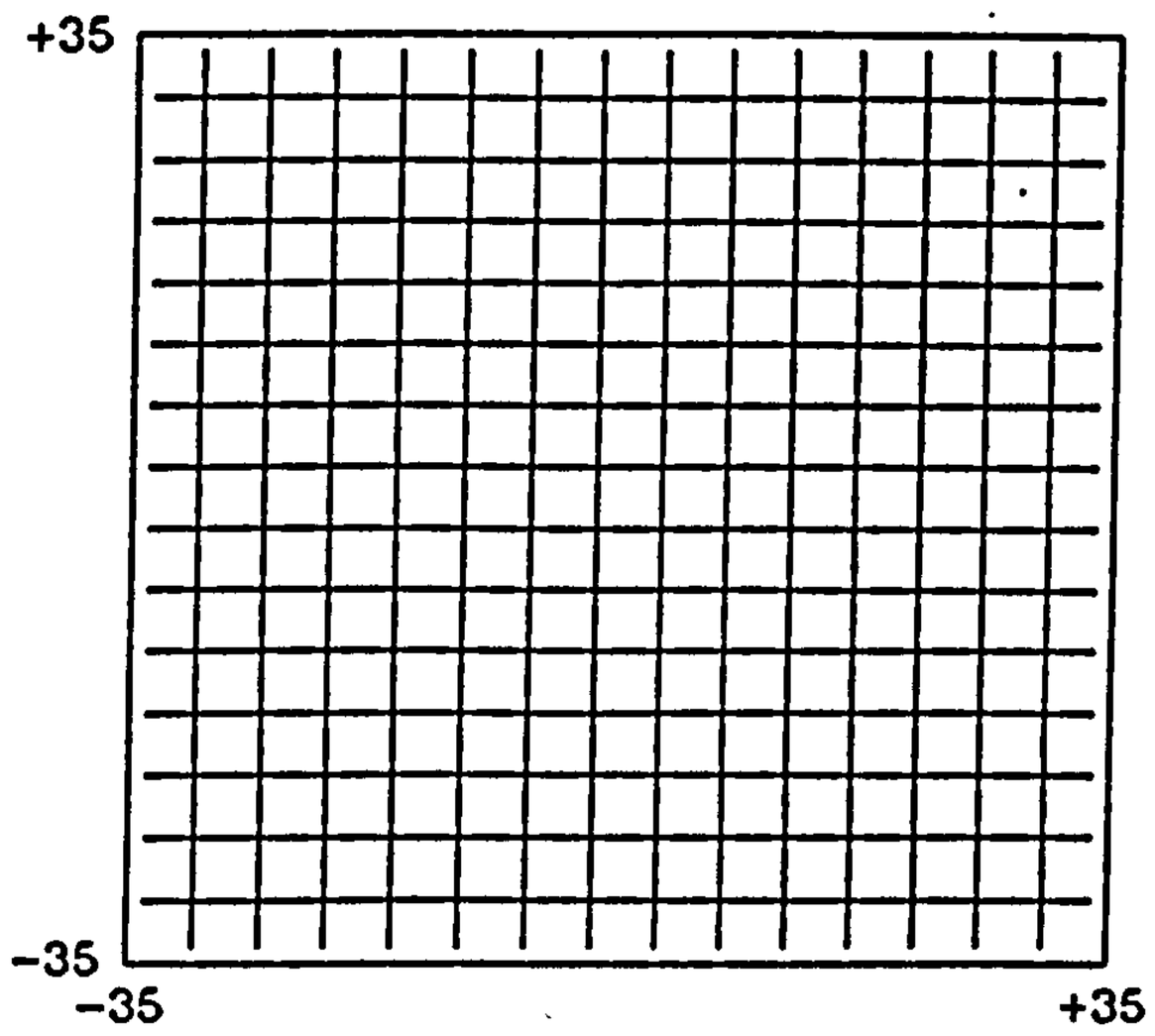

Figure 5.16: *Distortion map for an ideal detector*

the PMT useless over a large part of its sensitive area. The estimated useful area is 40 × 20 mm, only ~15% of the surface area of the detector.

In contrast, the map for TUBE 2 shows it to be useful over an area greater than that specified by the manufacturer. The distortions present are far smaller than those for TUBE 1 and are mainly due to light losses near the edge of the photocathode, an effect which is unavoidable.

5.5 Conclusions

Proving tests have been carried out on two examples of the Hamamatsu R2487-02 position-sensitive photomultiplier. The PMTs were coupled to a thin NaI(Tl) crystal for evaluation as imaging X-ray detectors. The results show large differences in performance between the two PMTs.

- In terms of energy resolution, both detectors have good resolution at the centre of the detector, but suffered due to a loss of sensitivity away from the centre. The second of the two tubes gave a better resolution for all positions (12% for 122 keV X-rays at the centre of the detector).

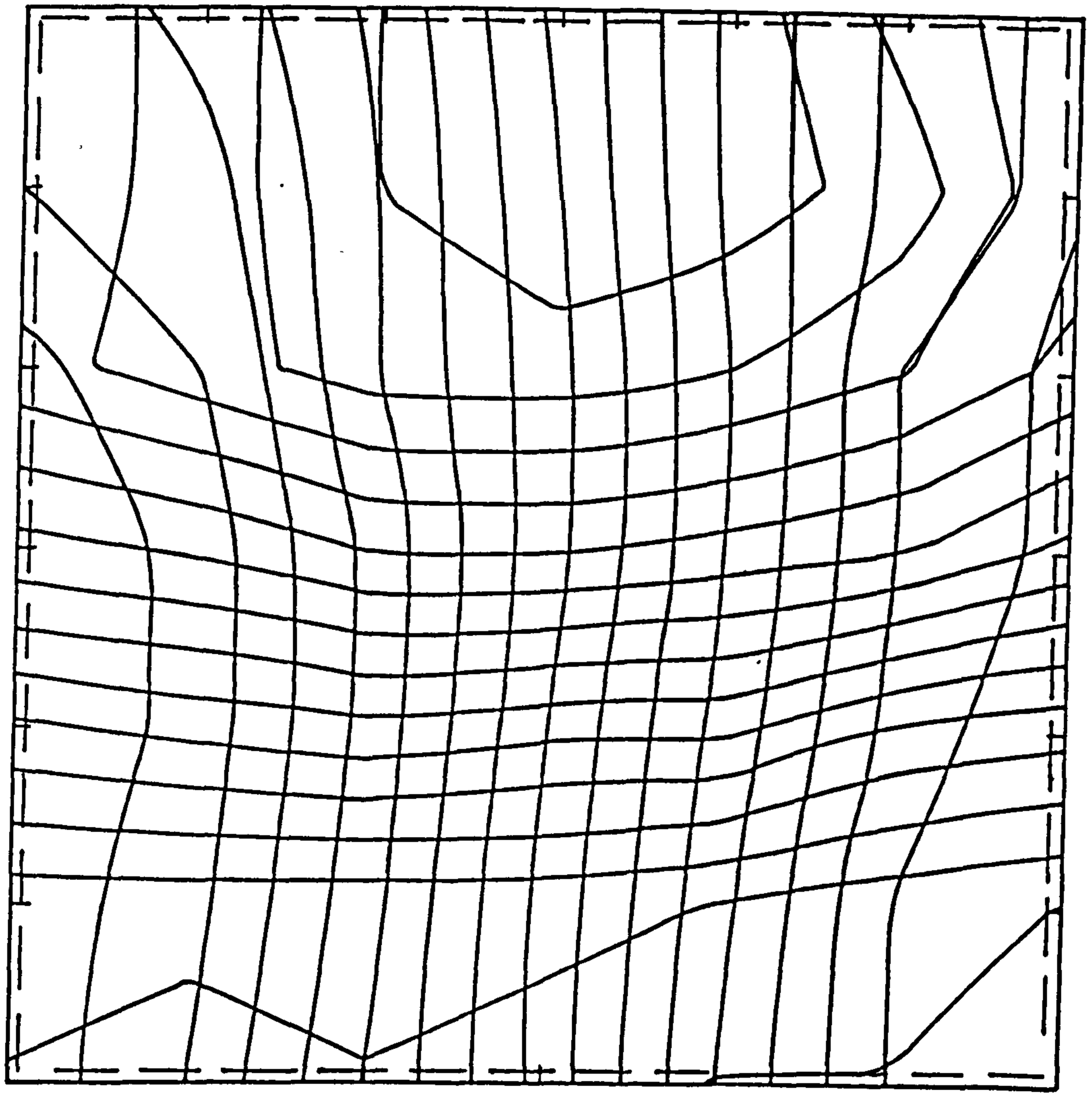

Figure 5.17: *Distortion map for the central* 55 × 45 *mm region of TUBE 1*

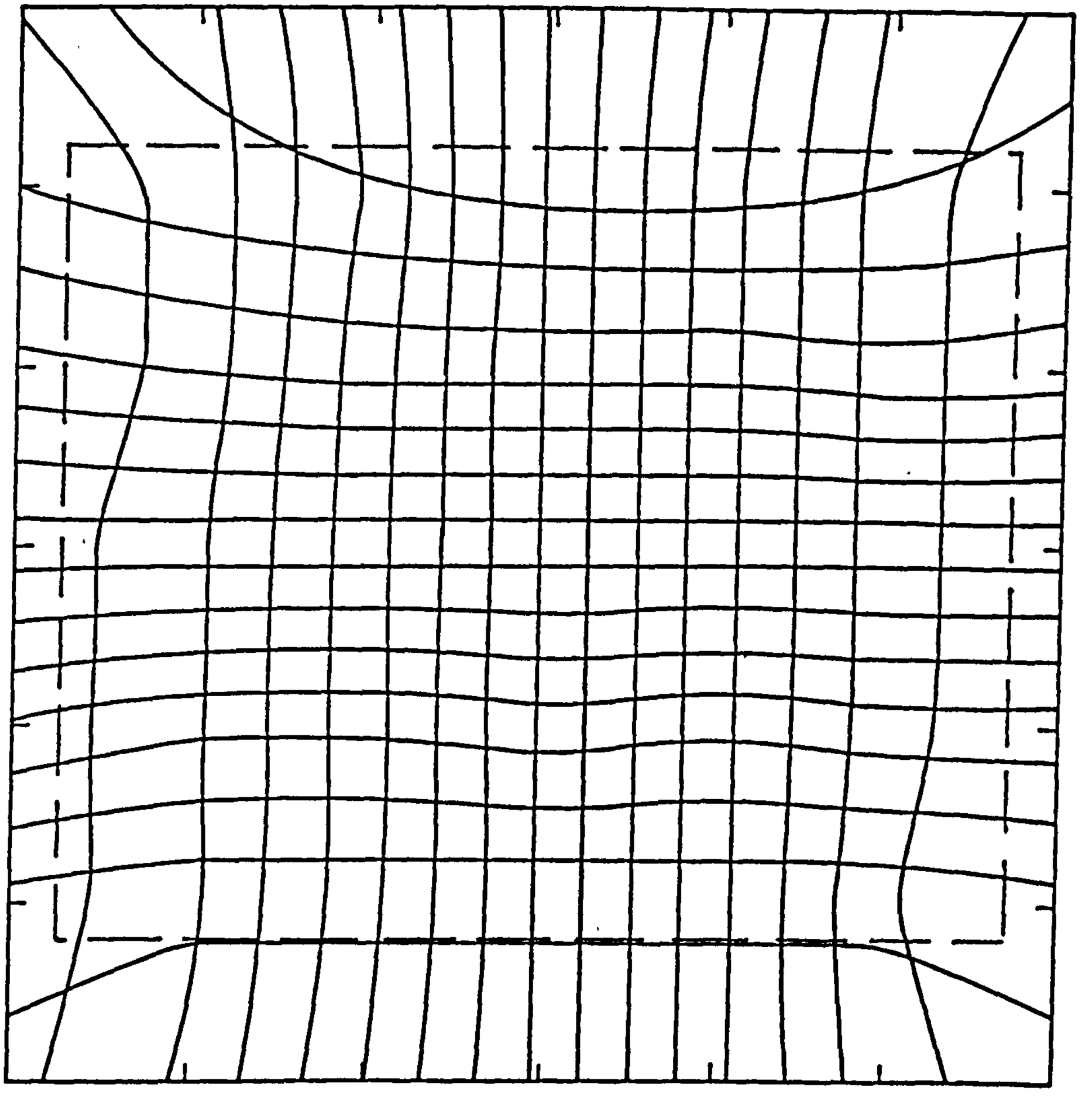

Figure 5.18: *Distortion map for the central* 60 x 60 *mm section of TUBE 2*

- The uniformity of both detectors was tested, and in this respect, TUBE 1 slightly out-performed TUBE 2, having a response which was both more uniform and symmetrical.
- Spatial resolution for the two detectors was very similar, and in the range 2.3 - 2.5 mm at the centre.
- When the spatial linearity of the two detectors was measured, it became clear that there was a problem with TUBE 1,whilst the spatial linearity of TUBE 2 was quite satisfactory. As a follow-up to these measurements, maps of the distortions present in the detectors were made. The map for TUBE 1 showed serious distortions which restricted the area useful for imaging to only 40 x 20 mm. In contrast, the map for TUBE 2 indicated that it could be used over a 60 x 60 mm region, better than the manufacturer's specifications. When approached on this matter, the manufacturers (Hamamatsu) confirmed that the PMTs produced did have some variation in performance, but were unable to explain the very poor performance of TUBE 1.

In the light of these tests, it was clear that any imaging work would only be practical using TUBE 2. It will clearly be necessary to formulate some appropriate purchasing specifications when procuring additional tubes for imaging applications. The next chapter details the methods used in assessing the imaging performance of the detector, and presents the results of the studies carried out.

Chapter 6

IMAGING WITH A POSITION SENSITIVE PHOTOMULTIPLIER

6.1 Introduction

In Chapter 5, the basic performance of two position-sensitive photomultipliers was measured. These tests included measurement of the energy resolution, and in view of their proposed application in imaging systems, the linearity and resolution of the position information. In the light of these tests, it was apparent that one of the photomultipliers was suitable for testing as a prototype imaging device. This chapter presents the results of tests carried out to investigate the use of this photomultiplier in conjunction with a scintillation crystal to form a compact imaging device for the detection of hard X-ray photons.

The purpose of these tests is twofold. Firstly, they demonstrate the intrinsic imaging capability of an X-ray detector employing position-sensitive photomultipliers, which could lead to the construction of large-area position-sensitive detection planes for use in hard X-ray telescopes. Secondly, there are several situations in which a compact X-ray imager based on a single photomultiplier could prove valuable, and the experimental set-up

employed in these tests serves as a prototype for such a detector.

Initial discussions will centre on the schemes devised to overcome the non-linearities and non-uniformities discovered during the initial tests of the photomultiplier/crystal combination. It is clear that both the energy and position information from the photomultiplier needs to be corrected if distortion-free images are to be produced.

Following this, the results of a comprehensive series of imaging tests will be presented. Both point and extended sources have been used in conjunction with a variety of apertures in order to assess the basic performance of the detector system in an imaging role. Results using the following apertures are presented:

- Simple pinhole apertures with diameters from 1 mm to 4 mm.
- A coded aperture based on a 73-element non-redundant array.
- A coded aperture based on a 361-element pseudo-noise product pattern.
- A high resolution parallel collimator.

A discussion of the relative merits of each system is given, with the emphasis being placed on the sensitivity and angular resolution attainable. Where relevant, both raw detector data and the results of suitable image processing techniques are presented side-by-side in order to give an indication of the importance of post-processing in the imaging process. For purposes of comparison, images obtained on a commercial gamma camera are also presented.

6.2 Calibration and Correction

Before a position-sensitive PMT can be used for imaging, it must be comprehensively calibrated in order to evaluate the intrinsic non-uniformities which have been shown to exist with these devices. If a detector based on a position-sensitive PMT is to be used in an imaging application, each X-ray event recorded must be corrected to remove the effects of these problems. A flow-chart showing one possible correction procedure is shown in Figure 6.1.

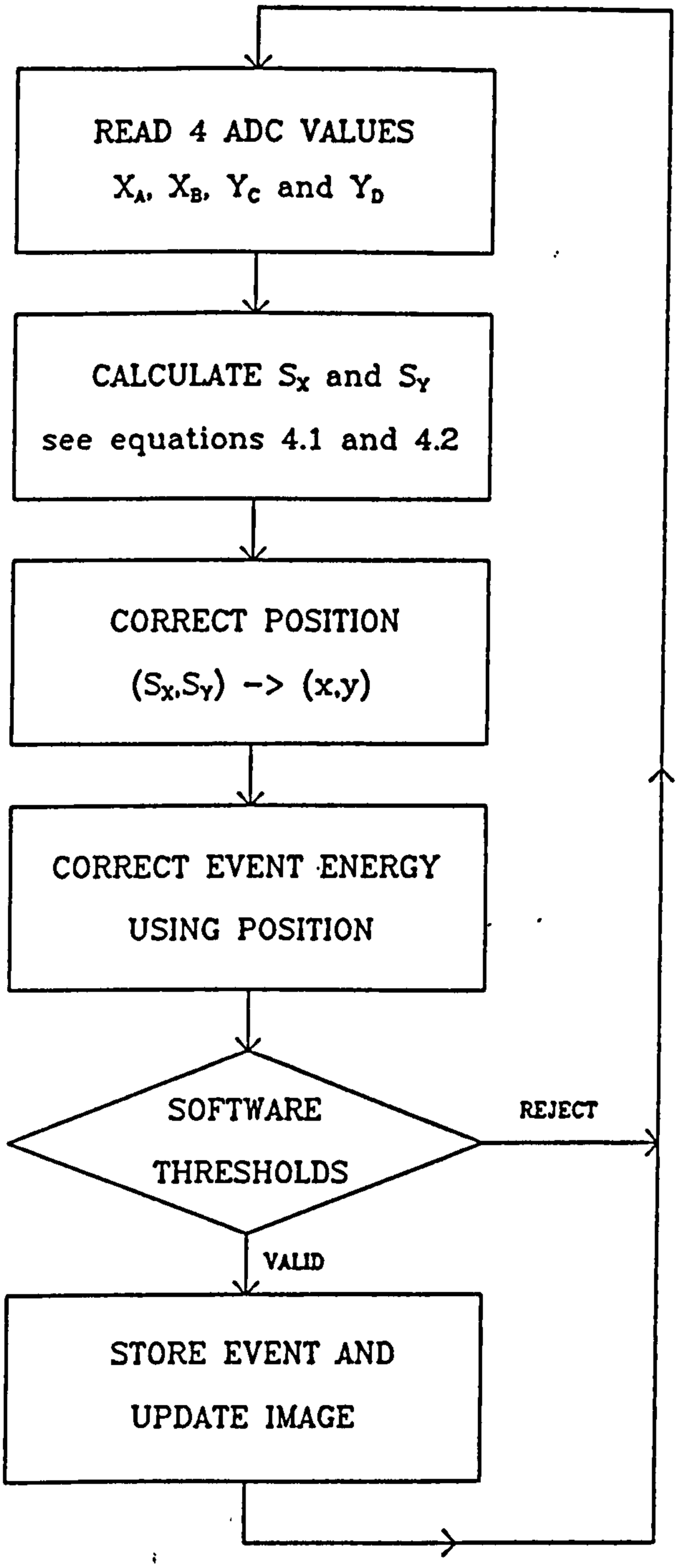

Figure 6.1: *Event correction scheme - theoretical method*

Firstly, the uncorrected positions S_X and S_Y are obtained from the digitised photomultiplier outputs according to Equations 5.1 and 5.2. These positions are then corrected into true co-ordinates using the spatial linearity calibration curves. This process is described in greater detail in Section 6.2.1. Once the true position is known, the event energy may be corrected using calibration data. It should be noted that any errors in the position reconstruction will be carried over into the energy correction. In theory, this could be avoided by carrying out the energy correction in S-space, but since this is a non-linear co-ordinate system, the correction algorithm is difficult to implement. When the energy of the event has been reconstructed, the software thresholds are applied in order to reject events falling outside the required energy window. Assuming the event is a valid one, the event may be stored and the image updated accordingly.

The major problem with this approach is that a great deal of processing is carried out before the data is passed through the threshold tests. If a significant percentage of the events are rejected by these tests, then this will introduce a large dead-time into the data collection system. Due to the relatively low count rates possible with the CAMAC-based system employed in these imaging tests, the procedure shown in Figure 6.2 was devised in order to reduce the problem of dead-times. This scheme does not correct the event energy, which allows the threshold tests to be carried out before any other processing.

Various approaches to the correction of both the energy and position information supplied by the photomultiplier will now be discussed in more detail.

6.2.1 Position Correction

It was shown in Section 5.4.4 that the event co-ordinates (S_X,S_Y) derived from the anode outputs are not linearly dependent on the source position. This means that any imaging system using these photomultipliers must be capable of correcting these non-linearities in order to produce an image free of distortion. The approach chosen to achieve this aim is as follows:

(i) It is assumed that the non-linearities measured along the x and y axes are representative for the entire sensitive area, and so the curves shown in Figures 5.13 and 5.14 may be used as calibration data. This is clearly not a completely

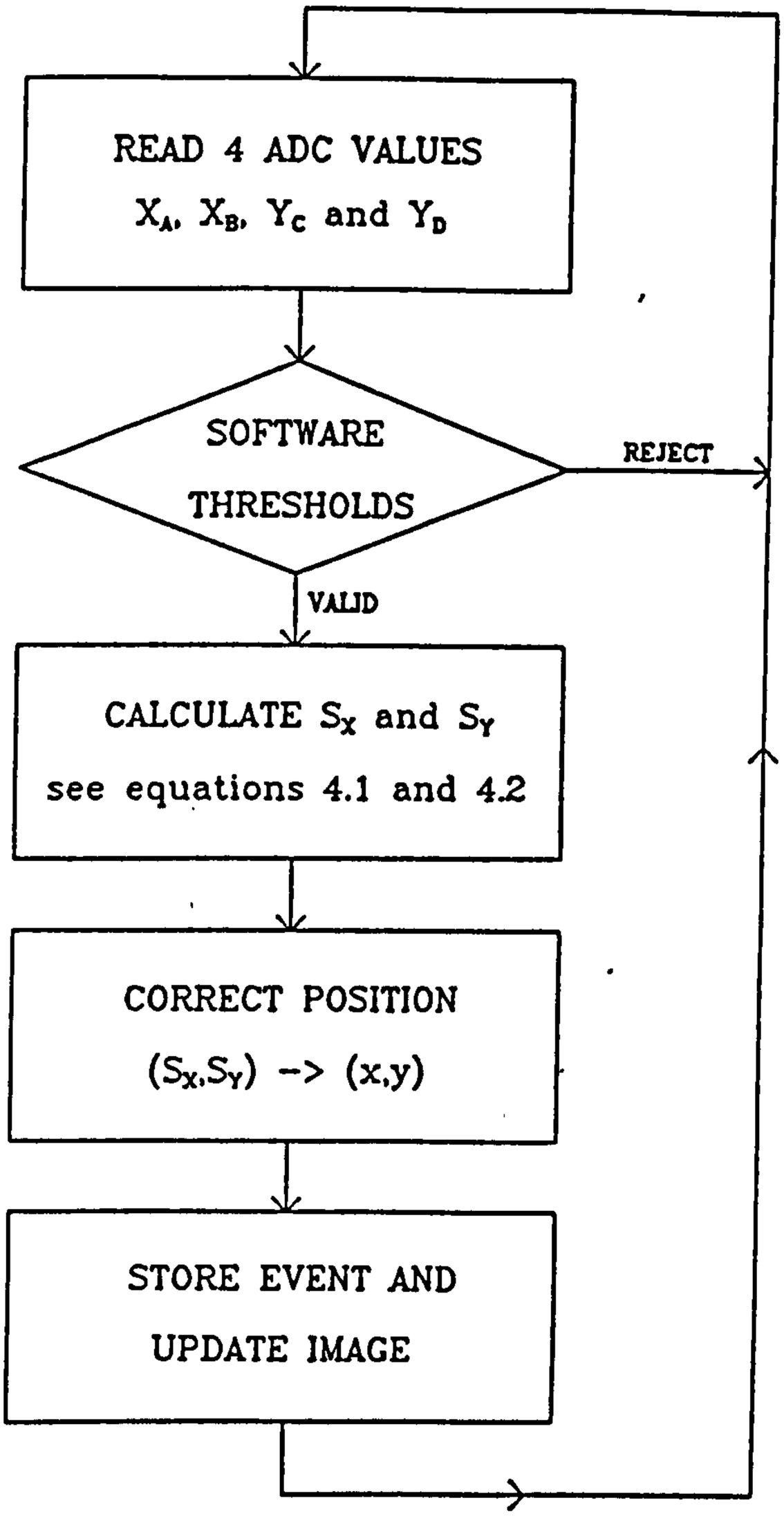

Figure 6.2: *Event correction scheme - practical method*

accurate representation of the distortions observed, but it does allow a considerable simplification of the correction algorithms.

(ii) Using the information contained within these curves, two large look-up tables (one for each axis) may be constructed such that the true position (x,y) can be obtained for any value of S_X and S_Y.

(iii) In a practical system, the image must be accumulated into an array of a given number of pixels, e.g. a 128 × 128 image. If the size of this array is known in advance of the look-up table generation, it is possible to calculate the pixel corresponding to each position (x,y), and hence each raw co-ordinate (S_X,S_Y). Therefore a look-up table can be used to convert directly from the uncorrected position to the co-ordinates of the pixel in the image which must be updated.

This process is illustrated in Figure 6.3. One considerable advantage of this approach is the saving in processing time which may be made by the use of look-up tables and the direct conversion to image pixel co-ordinates. The main disadvantage of this correction system is the assumption made in (i) above, that the non-linearities along the line y=20, for example, are the same as those measured along the x-axis. The distortion maps presented in Section 5.4.5 show that this is not the case, although the assumption only breaks down very near the edge of the sensitive area. However, it is difficult to envisage a practical system of position correction which is not based upon this assumption.

One problem which can occur as a result of this approach is caused by the linear interpolation between the known data points on the calibration curves used in the look-up table generation software. This can lead to abrupt changes in the number of positions which address a given image pixel, giving rise to 'bands' of slightly higher and lower intensity on the final image. This can be largely overcome by using a more finely sampled calibration curve to ensure that the transitions are smooth, but some of the images are still affected by this to a small degree.

One alternative approach is to fit curves to the linearity calibration data, and then use the inverse curves to correct the reconstructed position. This has the disadvantage that for all but the simplest curves, the mathematical description is so complicated that the processing time involved is considerable, and ultimately this will reduce the count rate which can be handled by the data collection system. In its favour it is not affected by

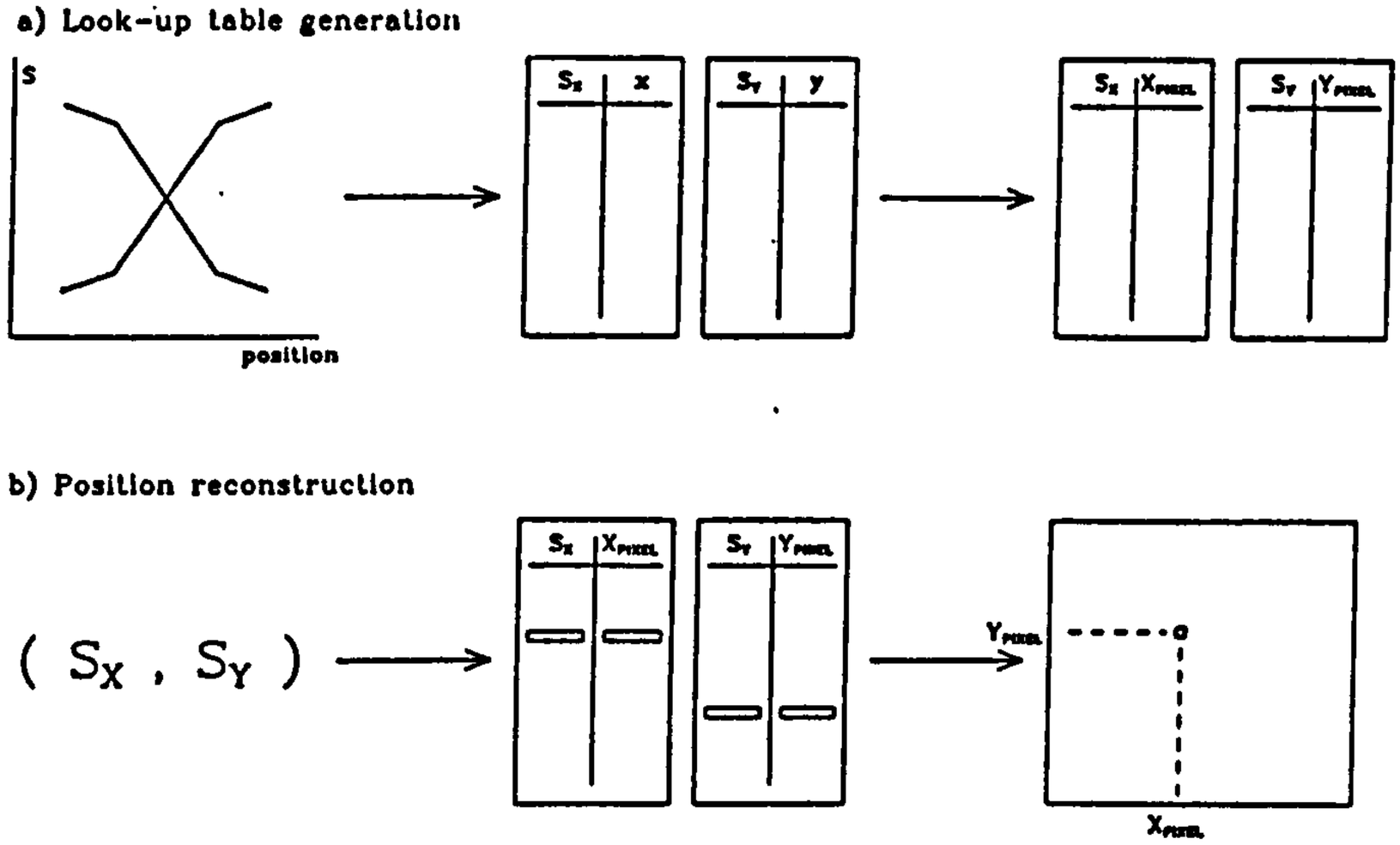

Figure 6.3: *Position correction algorithm*

the quantisation effects associated with the look-up table approach.

6.2.2 Energy Correction

The non-uniformity of the response of the photomultiplier (see Section 5.4.2) means that the energy deposited in the crystal cannot be directly measured from the sum of the four anode signals. However, the true energy may be recovered by correcting the value of $X_A+X_B+Y_C+Y_D$ using the reconstructed event location. Using the known detector response as a function of source position, the energy information can be normalised to give a response independent of position.

Again this can be achieved by creating a look-up table, in this case containing a correction factor for each position (x,y). To be effective, the spatial frequency of the look-up table would need to be ~1 mm over the entire tube area. To obtain calibration data to such accuracy requires either an automatic calibration system (which is under development), or the estimation of intermediate data by linear interpolation between a coarser series of data points which could be obtained manually.

6.3 Sources used in Imaging Tests

In the imaging tests described in the following sections, several sources, both point-like and extended were used. In order to avoid repeated descriptions, these sources will now be described.

Point Sources

The point sources used were 1 mm diameter beads encapsulated in rectangular plastic frames (Amersham type X.245). Both ^{241}Am (60 keV) and ^{57}Co (122 keV) sources were used, with activities ranging from 3 - 10 μCi.

Thyroid Phantom

Two thyroid phantom sources with identical geometries were used. The first, a Picker hollow plastic phantom, had to be filled with ^{99}Tc (140 keV) in solution. A typical initial activity introduced was 1 mCi, but the short (6 hour) half-life of the technetium meant that the source was only useful for at most two days. A more convenient source, a solid phantom (Amersham CTR.36110) with ^{57}Co distributed throughout a plastic body, was later obtained. A schematic view of the thyroid phantom is shown in Figure 6.4. The source consists of two lobes, one with half the intensity of the other. The more active 'hot' lobe contains two 'cold' regions of different size, while the colder lobe contains one hot spot and one cold spot. This distribution of intensity is achieved by varying the thickness of the source, with the hottest regions of the source being 18mm thick.

Line Source

A hollow source was built to the design shown in Figure 6.5. This source had to be filled with ^{99}Tc (140 keV) in the same way as the first thyroid phantom, and so suffered from the same drawbacks. The lines making up the source varied from 0.5 mm to 3 mm in thickness, but were all the same depth.

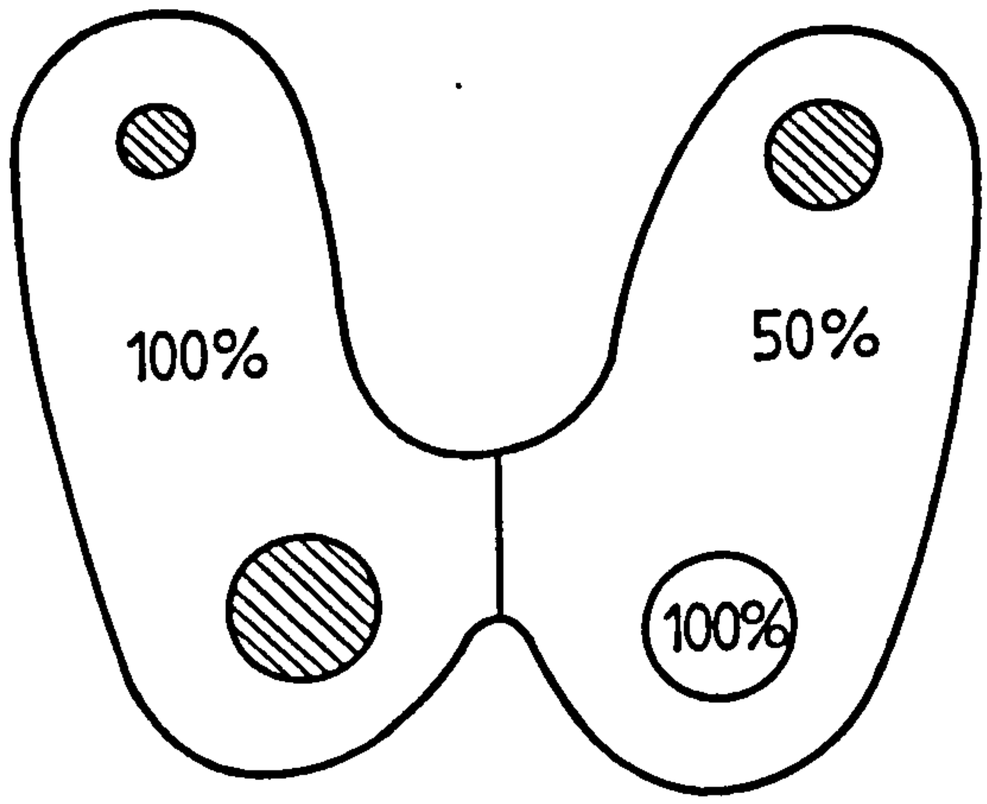

Figure 6.4: *Schematic view of the thyroid phantom*

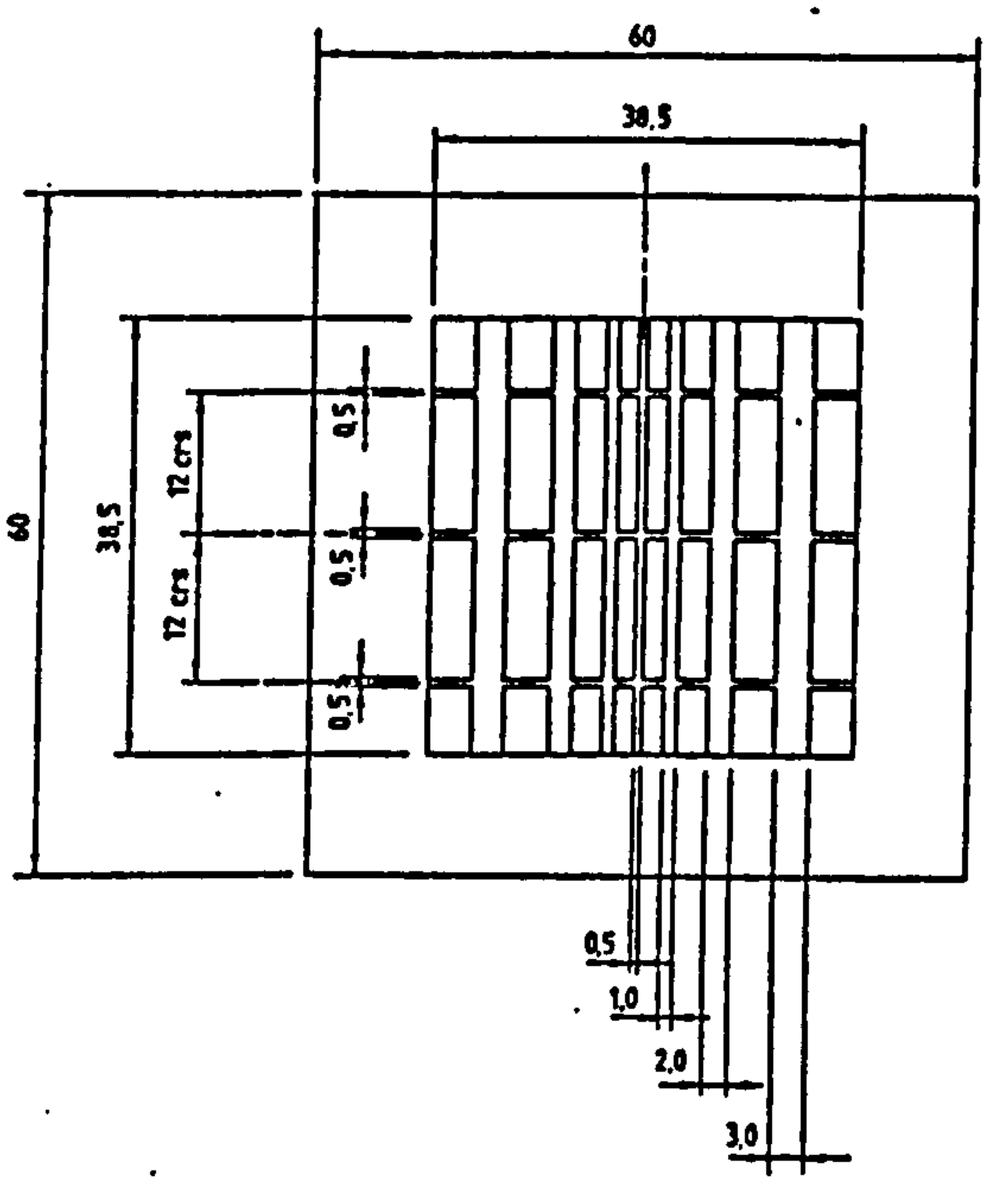

Figure 6.5: *Schematic view of the line source*

6.4 Pinhole Images

The simplest imaging system which can be envisaged uses a pinhole aperture in order to form an inverted image of the source at the detector plane.

A pinhole aperture suffers from low transmission when compared with both parallel collimators and coded aperture systems. This results in a relatively low sensitivity for the system, which can only be improved by increasing the size of the aperture and hence worsening the angular resolution of the system. One major advantage of the system, however, is the simplicity of the data recorded at the detector plane. No processing of the image is necessary unless the point-spread function is so wide as to significantly degrade the image, in which case an appropriate algorithm such as Maximum Entropy [36,66,113] deconvolution or CLEAN [73] may be applied. A further advantage of the pinhole imaging geometry shown in Figure 6.6 is that the magnification of the system can be changed, allowing a wide range of source sizes to be imaged.

Pinholes 2, 3 and 4 mm in diameter were constructed from 2 mm thick lead sheet. Initial

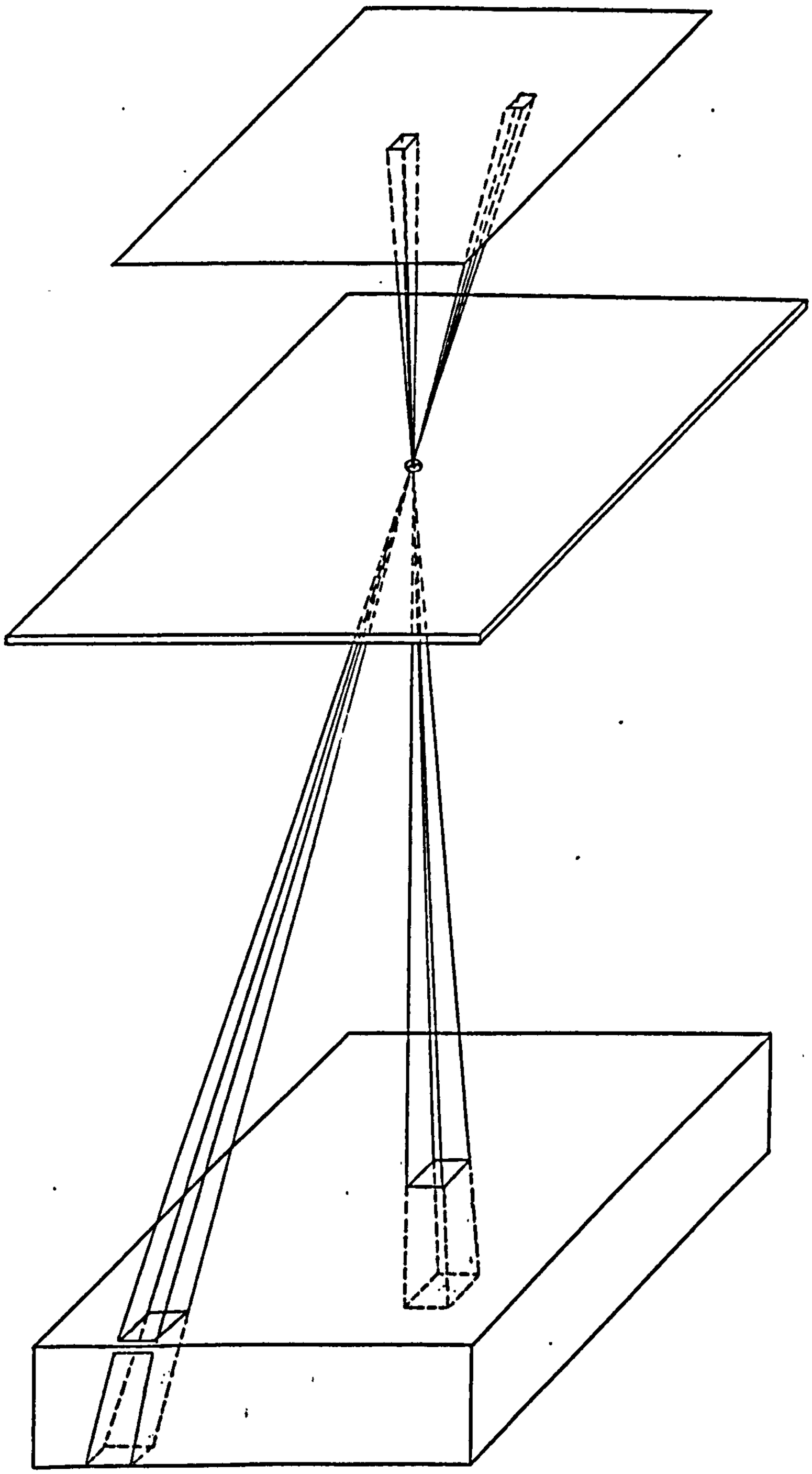

Figure 6.6: *Schematic view of the pinhole imaging system, showing the problems associated with viewing the edges of thick sources.*

tests suggested that the 3 mm pinhole offered the best compromise between transmission (and hence count rate) and image quality.

Figure 6.7 shows the raw detector data from an observation of the thyroid phantom using the 3 mm diameter collimator. Two million photons were collected into a 128 × 128 pixel array, and as can be seen the statistical quality of the image is relatively poor. However, the low data collection rates prohibited longer exposures. The most prominent feature of the image is the slope at the edge of the source, showing that the system point-spread function has degraded the sharpness of the image. However, despite being considerably blurred by the same effect, the larger features of the source are clearly visible.

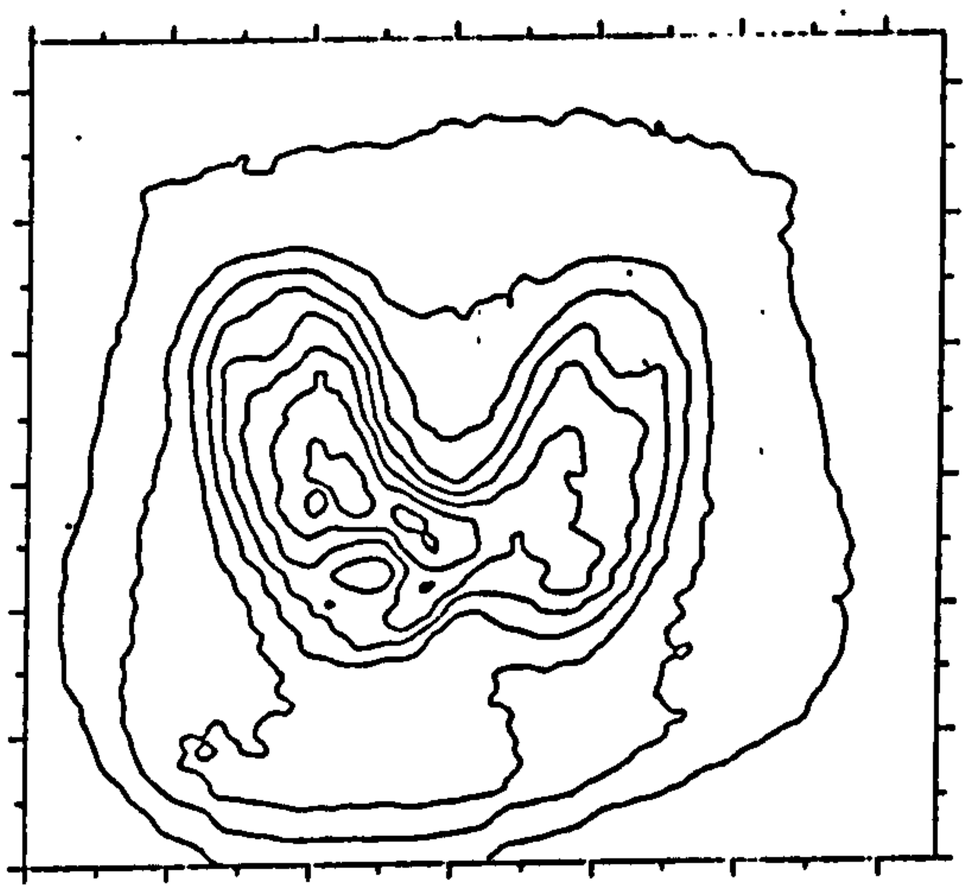

Figure 6.7: *Raw detector data from a long exposure of the thyroid phantom using a 3 mm pinhole*

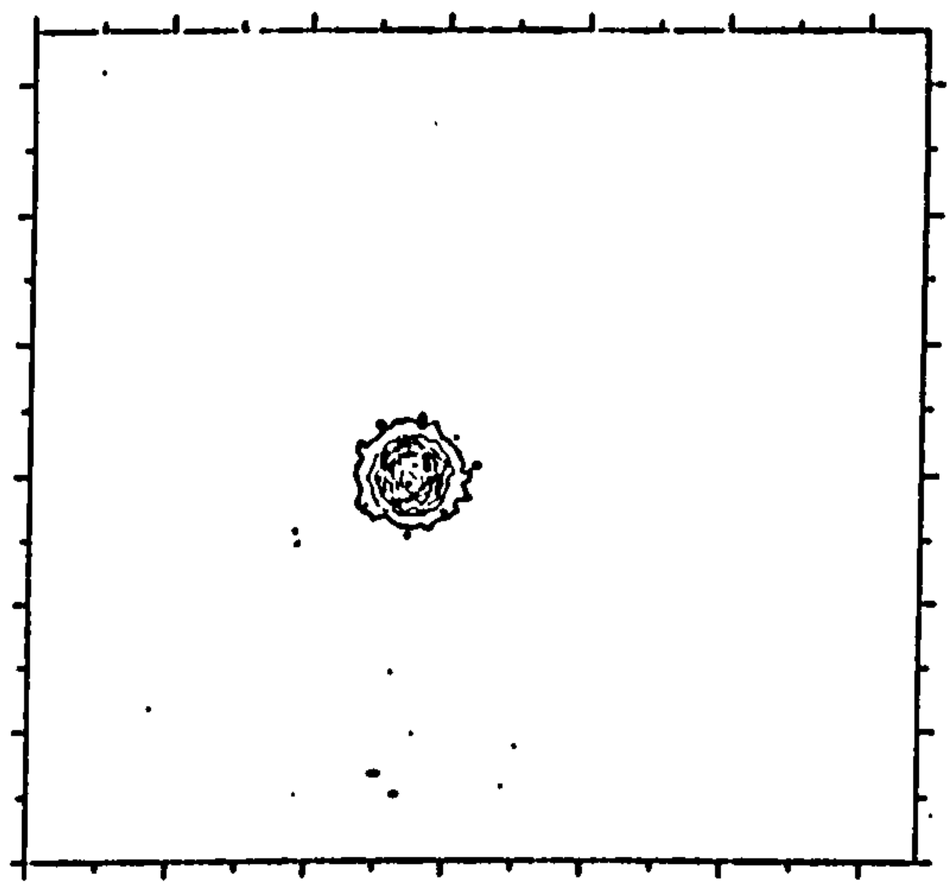

Figure 6.8: *System point-spread function for the 3 mm pinhole*

The system point-spread function was determined experimentally by collecting an image of a 1 mm point source near the centre of the field of view. This image is shown in Figure 6.8, and the peak can be measured as having a width of 8 pixels (FWHM). This point-spread function was combined with the raw detector data in a Maximum Entropy deconvolution [66], the result of which is shown in Figure 6.9. The improvements resulting from the deconvolution are clear. The edges of the image are much sharper, with the remaining slope probably being due to parallax effects associated with the finite thickness

of the source. A comparison of this image with the schematic diagram of the source in Figure 6.4 shows that both the general shape and the detailed features of the source have been imaged with a great degree of fidelity. A further comparison may be made with Figure 6.10, an image of the same source obtained on a hospital gamma camera, also using a pinhole collimator.

6.5 Coded Aperture Images

Two coded aperture masks were constructed for use in imaging tests in conjunction with the position-sensitive detector. The first was a mask based on a non-redundant array (NRA) [25,50] with 9 open elements in a 73-element basic pattern. The second was a pseudo-noise product (PNP) design [61] with a 19 × 19 element basic pattern. The two masks are shown in Figures 6.11 and 6.12, and their key parameters are summarised in Table 6.1 below:

	NRA	PNP
Basic Pattern	73 element	361 element
Transmission	13%	27%
Pixel size	3.75 mm	2 mm
Material	Lead/Antimony(4%)	Lead
Thickness	1 mm	1.5 mm

Table 6.1: *Key parameters for the coded apertures used in imaging tests*

Both masks are of relatively low transmission, 13% and 27% for the NRA and PNP designs respectively. These designs were selected for two reasons. Firstly, Fenimore [50] showed that for a source filling a large fraction of the field of view, and in the case where there is little background present, coded aperture transmissions of considerably less than 50% are optimum. For the conditions encountered in these tests, it can be estimated that the optimum aperture transmission is ~20%. Secondly, a more practical consideration, the construction of low transmission masks is simpler. Fewer apertures must be cut, and the resulting structure is more likely to be self-supporting (PNP masks are inherently

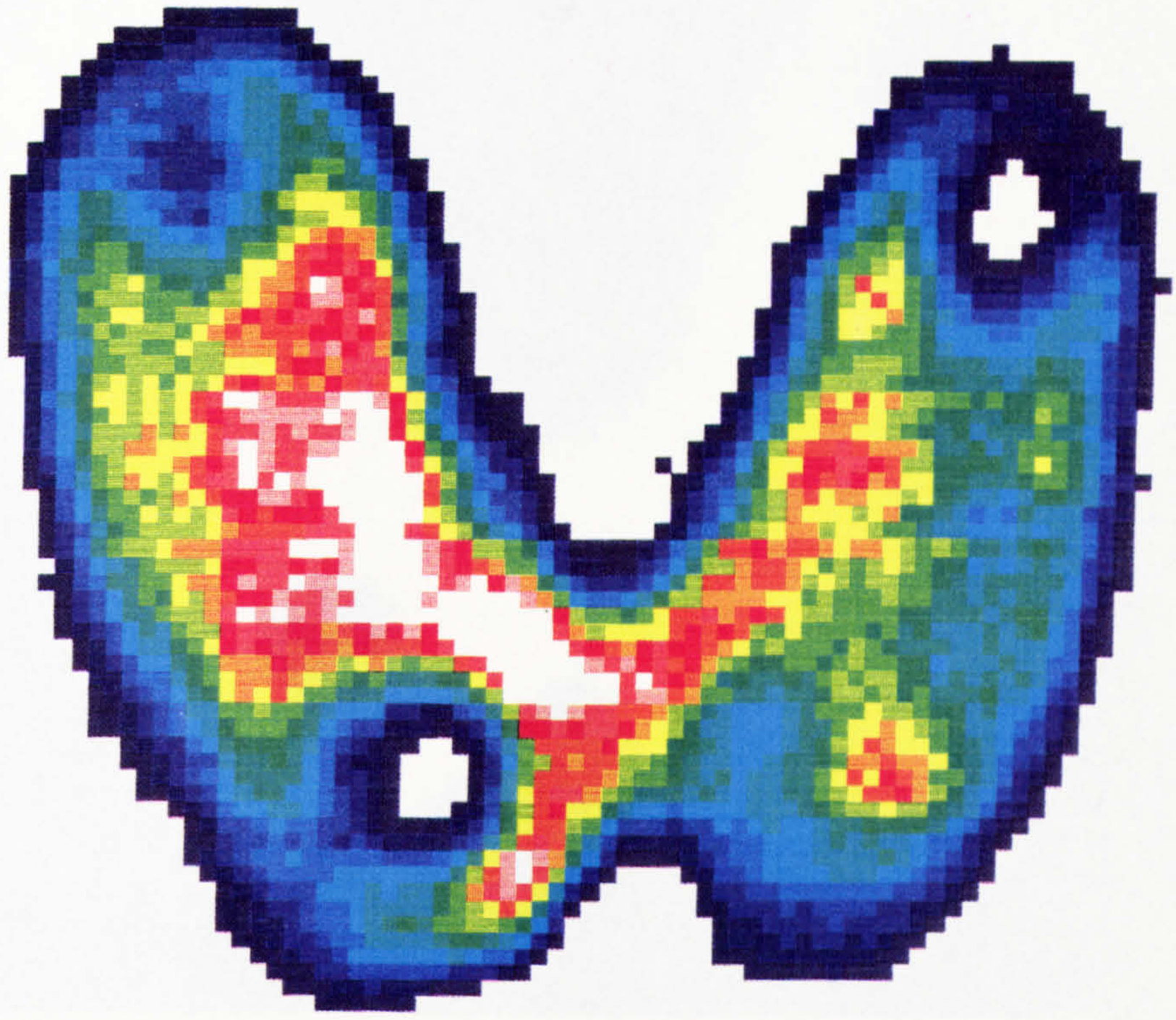

Figure 6.9: *Pinhole image of the thyroid phantom following Maximum Entropy deconvolution to remove the effects of the broad point-spread function*

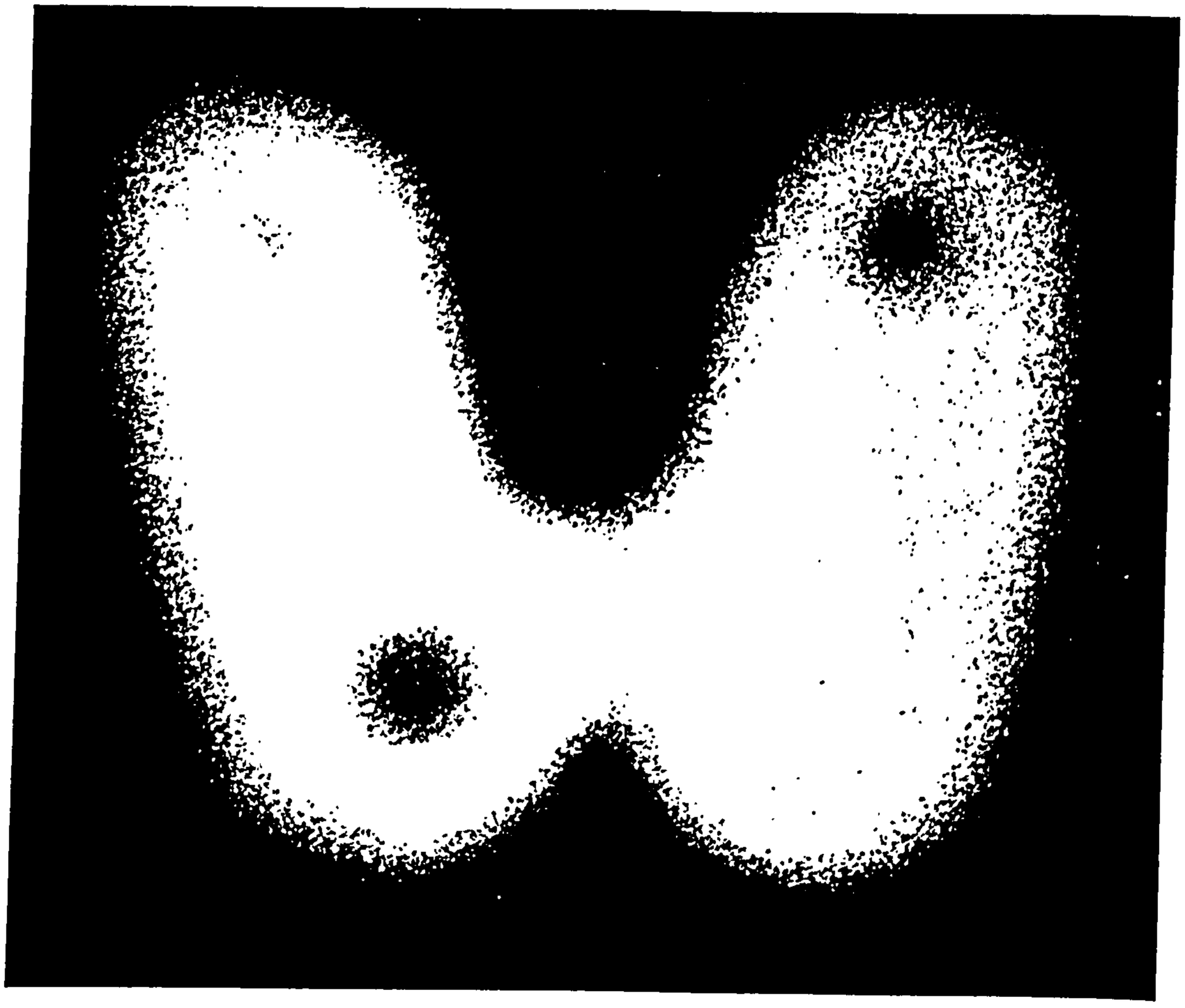

Figure 6.10: *Image of the thyroid phantom obtained with a hospital gamma camera using a pinhole collimator*

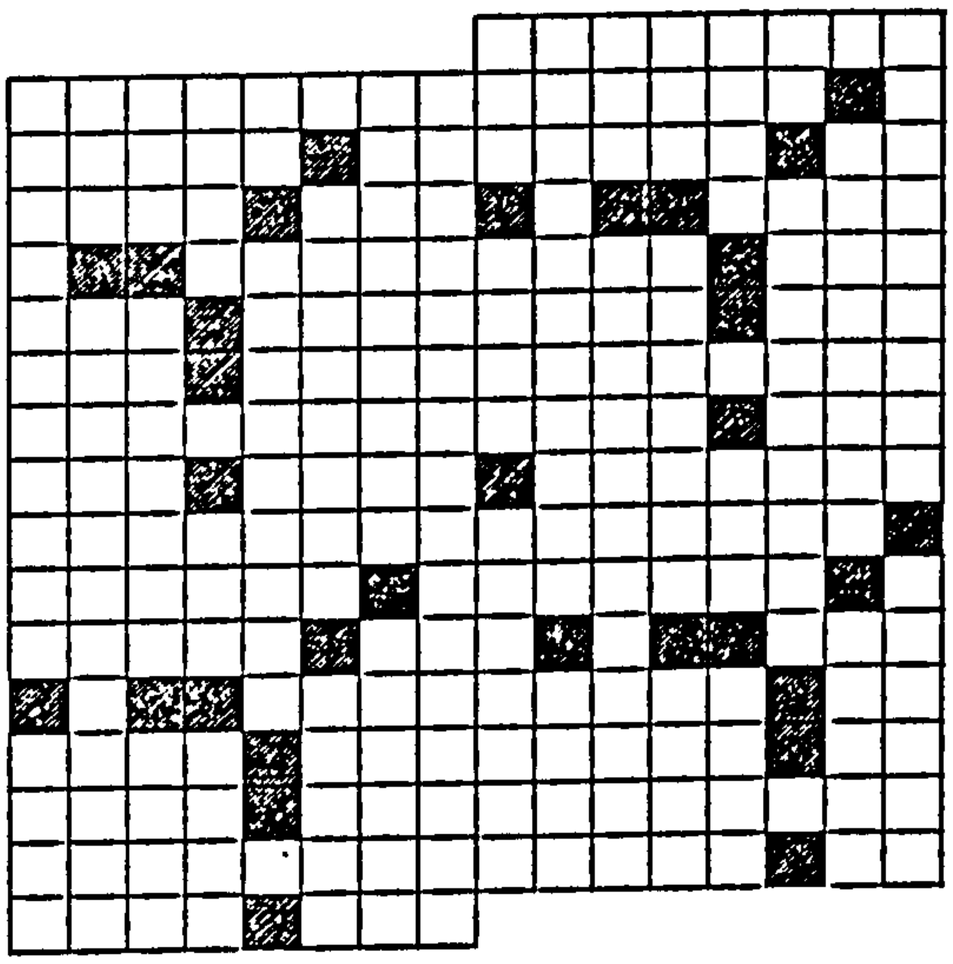

Figure 6.11: *Schematic view of the non-redundant array coded aperture used. A 73-element basic pattern is tessellated to form this, the full mask.*

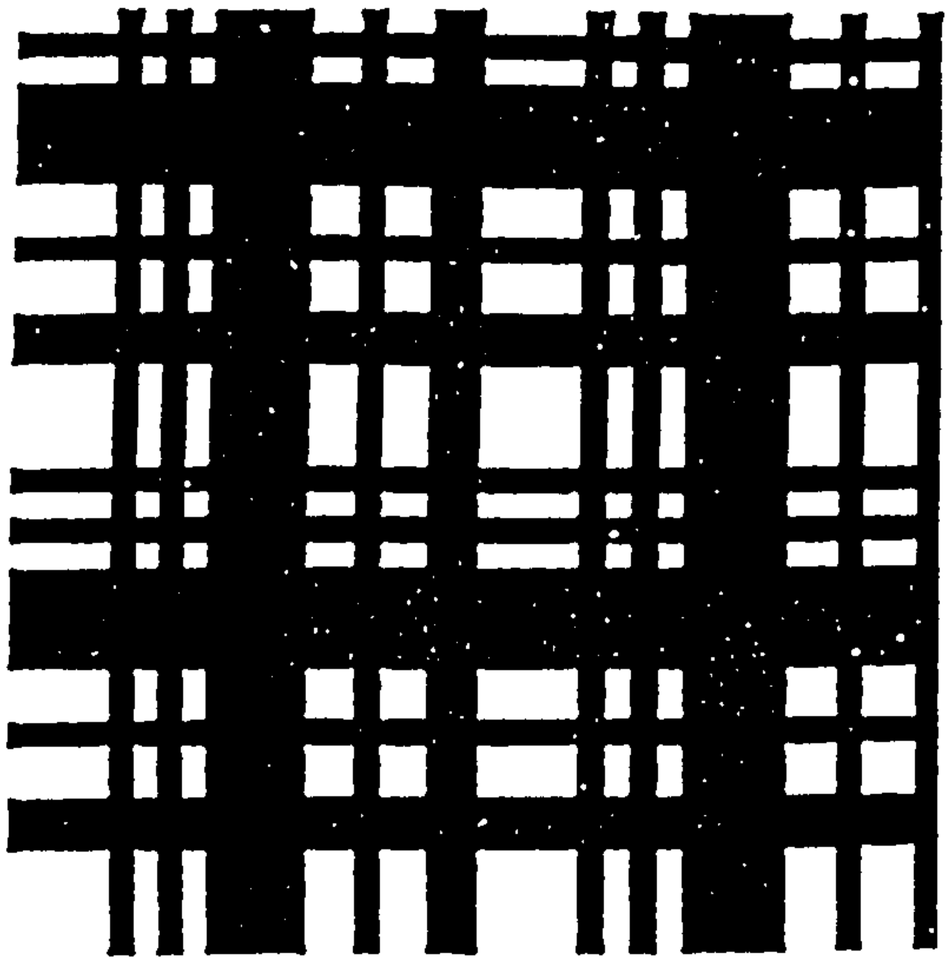

Figure 6.12: *Schematic view of the pseudo-noise product (PNP) coded aperture, formed using a* 19 × 19 *basic pattern*

self-supporting).

The pixel size of the PNP mask is almost half that of the NRA mask, theoretically giving it a considerable advantage in terms of imaging capability due to its narrower point-spread function (i.e. better angular resolution). This may be observed in the images presented later in this chapter. The combination of the higher transmission of the PNP design, and the softness of the material used in its construction meant that it was quite a delicate structure. This problem was overcome by mounting it on a thin perspex plate to add rigidity.

In both cases, the detector data was binned more finely than the size of the projected mask pixels. This sub-binning technique improves the point-source location of the system by increasing the accuracy with which the mask shadow is located. Deconvolution of the images was achieved by a standard cross-correlation method, using the decoding matrices recommended for use with each mask pattern [51,61].

NRA mask images

The NRA mask was mounted at a distance of 60 mm from the detector. Point sources were then placed at a distance of ~120 mm from the mask in order to give the correct magnification, such that the projection of the mask basic pattern mapped onto the central 50 x 50 mm of the detector. The detector data was binned such that each projected mask pixel mapped onto 16 (4 × 4) detector pixels.

Figure 6.13 shows an image of a single point source at the centre of the field of view. Although this contains only 10,000 counts, the peak is very significant ($\sim 15\sigma$). The next image, Figure 6.14 is of two sources of different activity, emitting photons at two different energies. The source in the upper left is a ^{241}Am source (60 keV), the other a less active ^{57}Co source (122 keV). The ratio of the peak heights may be explained by the activity of the two sources, and is not due to any differences in the detection efficiency between the two emission energies. In all, 500,000 counts were collected to form the raw detector data. In both images, the effect of the coarse mask can be seen in the broad peaks. Further tests were carried out using up to three point sources, an example of which is shown in Figure 6.15, with 200,000 photons detected from each of three source positions.

Following the point source tests, an attempt was made to image an extended source, namely the thyroid phantom. An image, generated from the deconvolution of detector data containing 3 million counts, is shown in Figure 6.16. The broad shape and larger features of the thyroid are visible, but the general image quality is poor. However, this is really to be expected when the following factors are considered.

- Due to the non-parallel geometry introduced into the system by the finite source distance, the projected size of any given mask pixel is different for each point in the field of view. Additionally, from any given source position, each mask pixel has a different projected size. This causes the projected mask pattern to be incorrectly sampled, leading to a reduction in image quality.
- The 'depth of focus' of the system is very small (a few mm). The projected mask pattern from any plane outside of this focussed region will again be mis-binned at the detector. The thickness of the thyroid phantom (18 mm) is much greater than

Figure 6.13: *NRA image of a single point source*

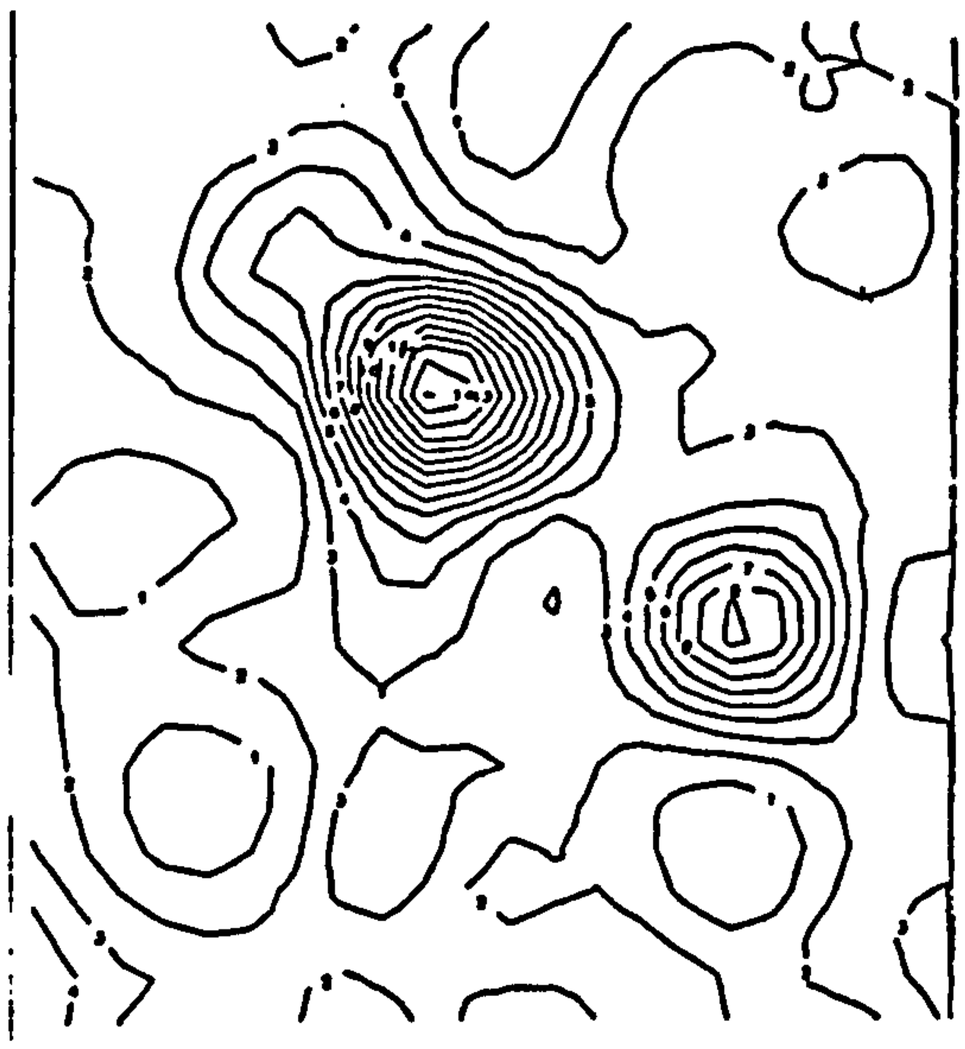

Figure 6.14: *NRA image of two point sources*

Figure 6.15: *NRA image of three point sources*

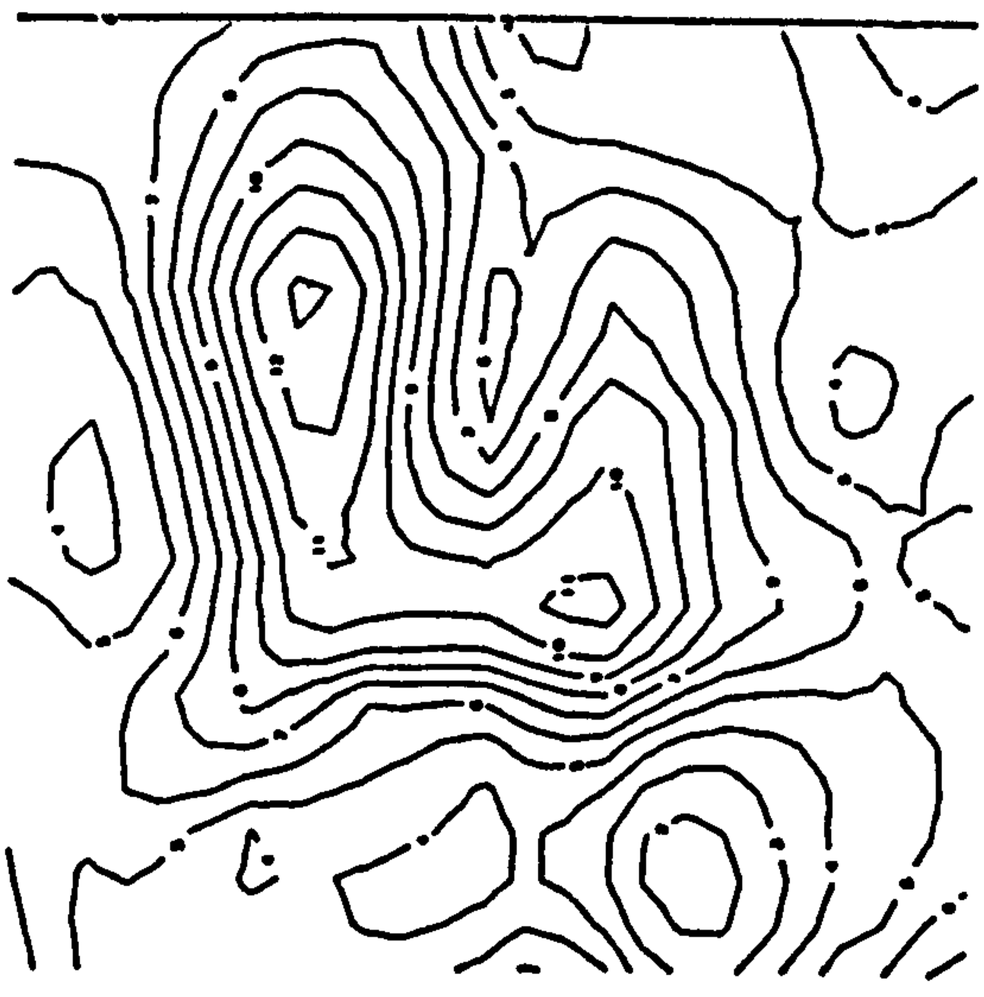

Figure 6.16: *NRA image of thyroid phantom*

the depth of focus, which has caused the image to be blurred.

- Most importantly, the angular resolution of the coarse mask used in this configuration is not sufficient to resolve the smaller features of the source. The resolution at the source plane can be estimated as ~10 mm, which is consistent with the image obtained.

PNP mask images

The pseudo-noise product mask, designed and constructed in the light of the results with the NRA mask, was then used in a similar series of tests. The distance between the detector and mask was again set to 60 mm, giving a theoretical resolution at the source plane of 6.2 mm.

A deconvolved image of a single ^{57}Co point source at the centre of the field of view is shown in Figure 6.17. When compared with the equivalent image obtained with the NRA mask, the improvement in angular resolution offered by the finer mask is clearly shown by the extent of the source peak. There is, however, a clear cross-shaped artifact present, centred on the source position. It was found that this artifact was due to mis-binning of the detector data by a very small amount, caused by both incorrect 'focussing' of the system and the unavoidable difference in projected pixel size from different points within the field of view. A vertical displacement of the source by a few mm was enough to greatly increase the magnitude of the problem.

A serious consequence of this is shown in Figure 6.18, an image of three point sources. The three peaks marked A, B and C are true sources, generated by the collection of 305000, 155000 and 240000 photons respectively. Peak D, however, a false peak which seems to be due to the superposition of positive artifacts from the two brightest sources A and C, is more significant than the true source B.

From the evidence of these two images, it was clear that the imaging of an extended, thick source such as the thyroid phantom was not a practical proposition.

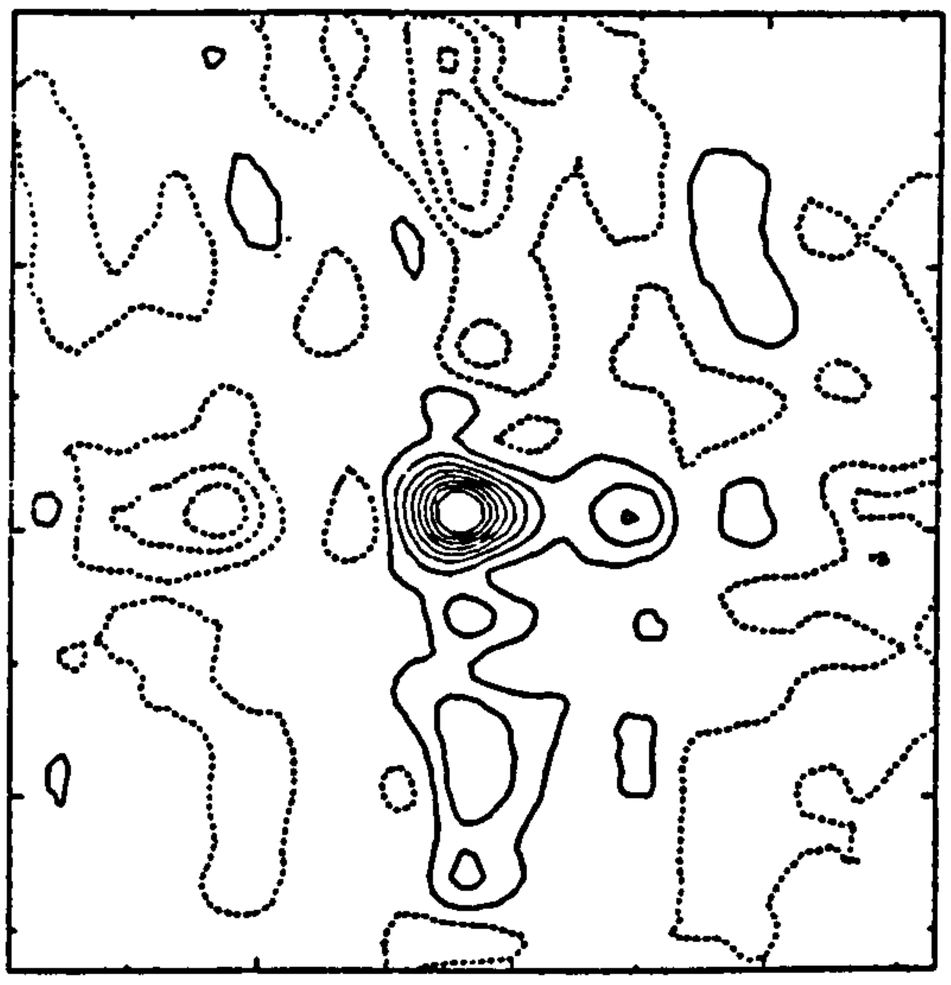

Figure 6.17: *PNP image of a single point source*

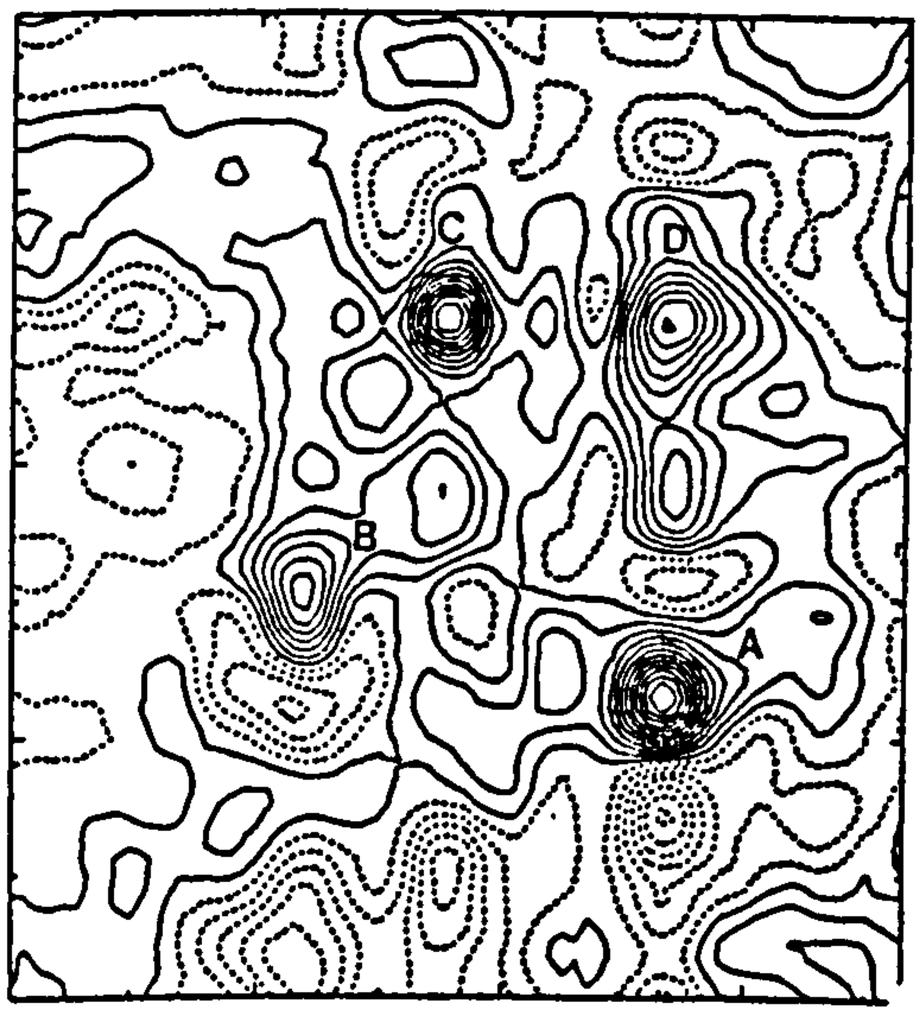

Figure 6.18: *PNP image of three point sources*

6.6 Parallel Collimator Images

In order to complete the series of imaging tests, a parallel collimator designed for use with small medical gamma cameras was obtained. This was a low-energy all purpose collimator (Searle #820-823066) designed for use at energies up to 140 keV, and with a diameter of 26 cm, it was large enough to cover the entire detector. In Table 6.2 below, the system resolution values are given as a function of source distance for detectors with spatial resolutions of 2.3 mm, the measured PSPMT performance, and 5.7 mm, the manufacturer's quoted performance figures.

The parallel collimator has the highest transmission of the apertures used in these tests, and has the added advantage that the depth of the the thyroid and line sources does not cause problems as it does with the coded mask and pinhole aperture systems. As with the pinhole aperture, no image processing is required unless the system point-spread function is wide enough to significantly degrade the image, in which case the image may be processed using a Maximum Entropy deconvolution or the CLEAN process.

Distance of source from collimator (cm)	Detector resolution	
	2.3 mm	5.7 mm
0	3.4	6.2
5	6.2	8.1
10	9.6	10.9
15	12.9	14.0

Table 6.2: System resolution with parallel collimator

Imaging tests were carried out using the thyroid phantom and the line source. In both cases the source was placed directly against the collimator in order to obtain the best resolution from the system.

Figure 6.19 shows an image of the thyroid phantom. Since the parallel collimator restricts the area of the source which can be observed to the sensitive area of the detector, only a portion of the thyroid is imaged. The field of view can be slightly increased by moving the source away from the collimator, but the angular resolution of the system degrades so rapidly that this is not practical. In order to get the best possible coverage of the source, the hot lobe of the phantom has been placed diagonally across the field of view, whilst the cold lobe is severely clipped by the right hand edge of the field of view. The quality of the image of the hot lobe of the phantom is extremely high. The shape of the source is well recorded and the features of the hot lobe are easily resolved. Some problems with the position correction algorithm may be seen in the vertical and horizontal bands present to a small degree, but this is not serious, and is a known problem which could be removed by the use of finer calibration data and a more advanced data collection system.

Again for the purposes of comparison, an image obtained on a commercial gamma camera equipped with a similar parallel collimator is shown in Figure 6.20.

An image of a part of the line source is shown in Figure 6.21. Comparison with the schematic diagram of the source (Figure 6.5) shows that the features down to 2 mm in width have been detected, and features 4 mm apart are clearly resolved. The image is dominated by counts from the outermost parts of the source, making the central narrower

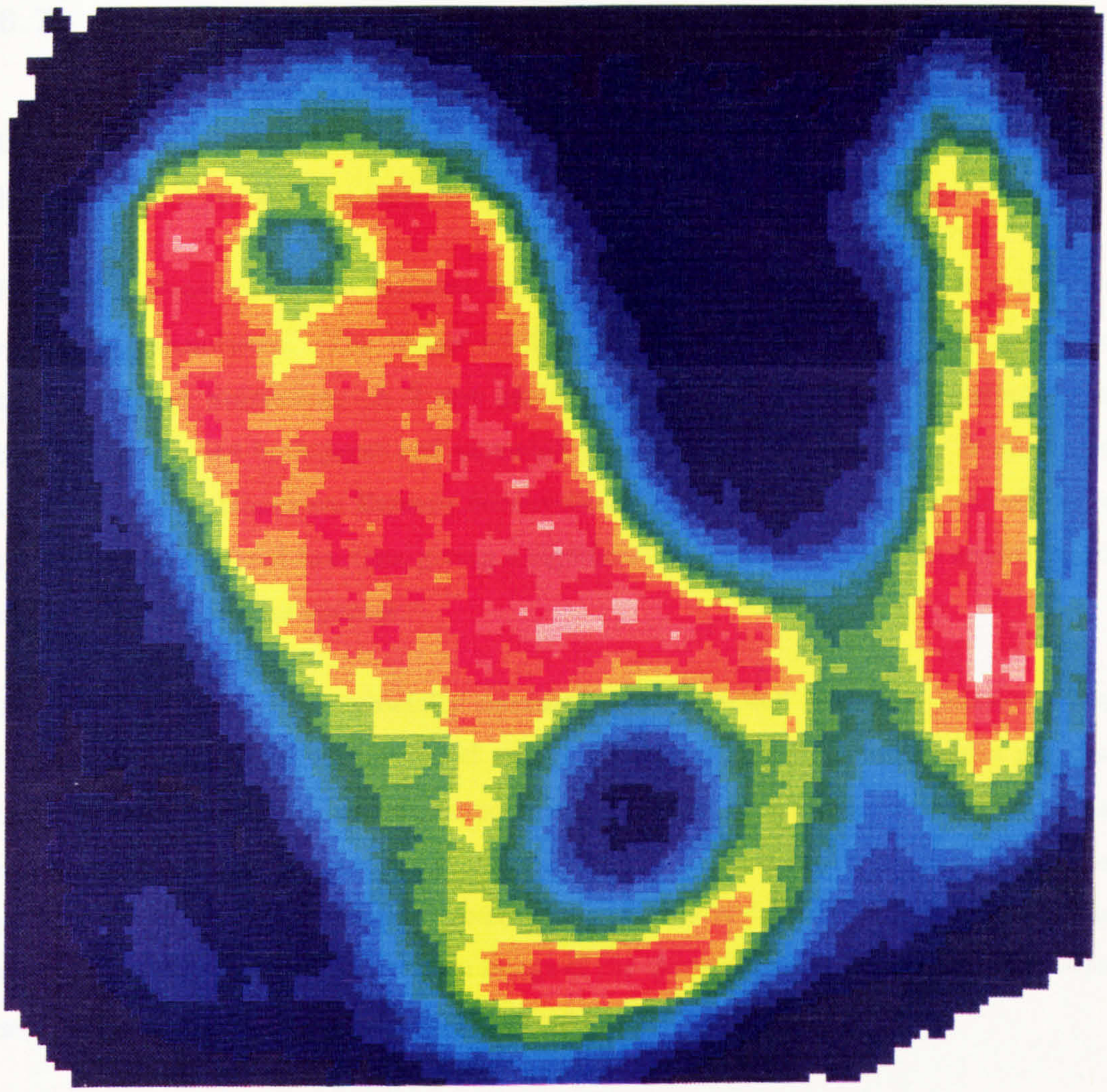

Figure 6.19: *Image of part of the thyroid phantom using parallel collimation*

features difficult to detect during a reasonable length exposure. The bottom right corner of the image is distorted due to the source being larger than the field of view. Small (4 mm) features such as the filling holes are clearly visible.

6.7 Conclusions

It has been demonstrated that a position-sensitive photomultiplier viewing a thin (5mm) NaI(Tl) crystal can act as a very effective, compact hard X-ray imaging system.

For applications where the incident flux is very high, a pinhole aperture may have adequate transmission. The image produced is inverted, but theoretically needs no complex image processing. A 3 mm pinhole aperture 60 mm from the detector has been used to image both point and extended sources with good resolution. It was found that the use of a Maximum Entropy deconvolution could be used to reduce the effects of the broad point-spread function, giving a significant improvement in image quality, most noticeably for extended sources.

The detector has been successfully operated in conjunction with two relatively low transmission coded masks, one based on a non-redundant array, the second a pseudo-noise product design. Both were found suitable for the imaging of point sources. The non-parallel geometry caused by the finite source distances (up to ~150 mm) led to problems with extended and thick sources, due to the variable size of the mask pixels when projected onto the detector. An image of the thyroid phantom consistent with ~10 mm resolution at the source was obtained with the NRA mask.

Finally the detector was used in conjunction with a parallel collimator designed for use with a small medical gamma camera. High quality images of both the line and thyroid sources were obtained. Features as small as 2 mm were imaged, with the general shape of both sources being reproduced well. However, the use of the parallel collimator served to emphasise the major limitation of the detector, the small sensitive area. Both the extended sources used were larger than the field of view, and could not be imaged in their entirety.

Chapter 8 will explore the possible applications of a small imaging detector based on a

single position-sensitive photomultiplier, but first, Chapter 7 will discuss ways of making larger area detectors based on the same devices. Many possibilities exist for extending the sensitive area of a single detector, or for forming a continuous detector of much greater area by using many photomultipliers.

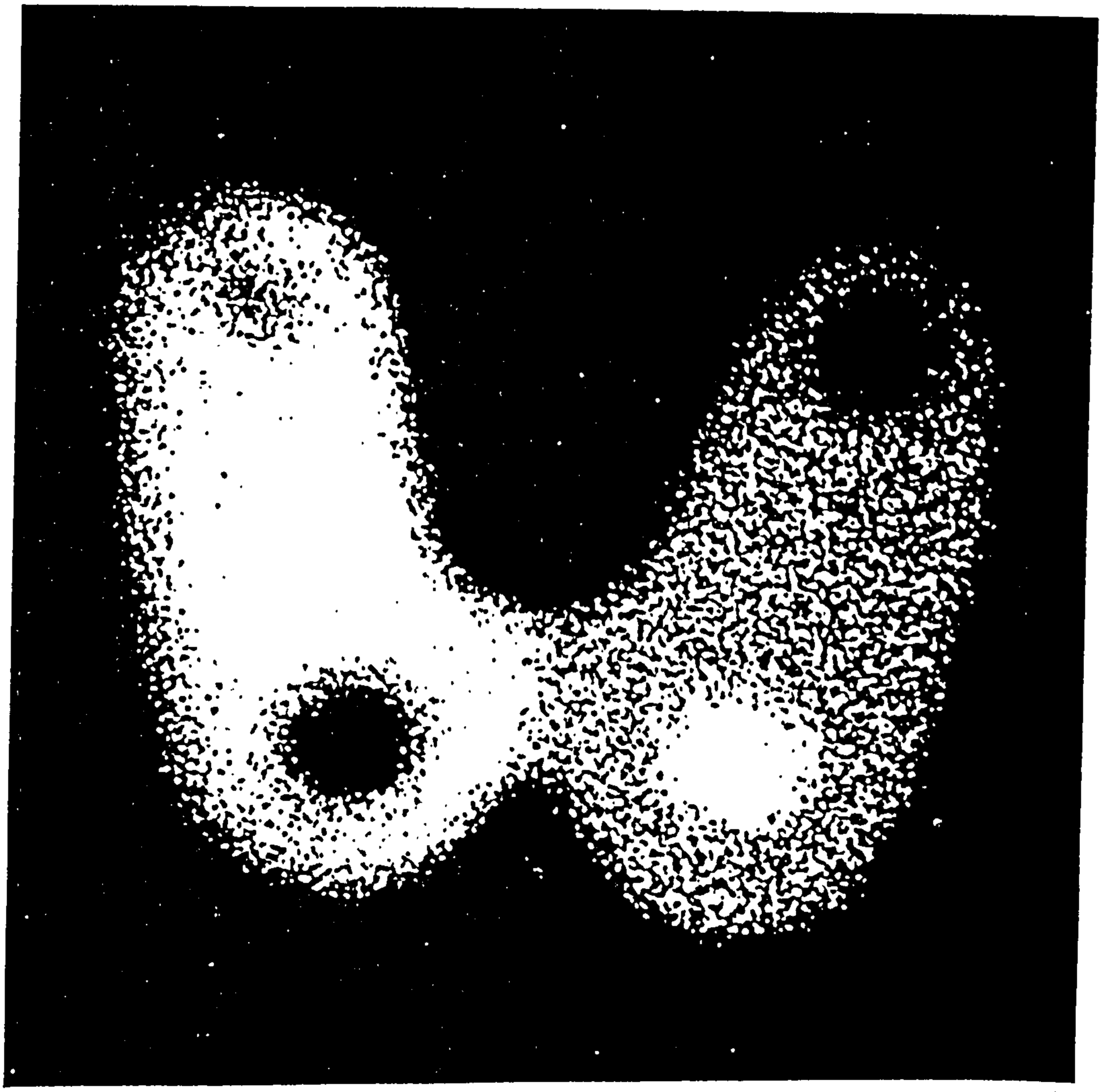

Figure 6.20: *Commercial gamma camera image of thyroid phantom using parallel collimator*

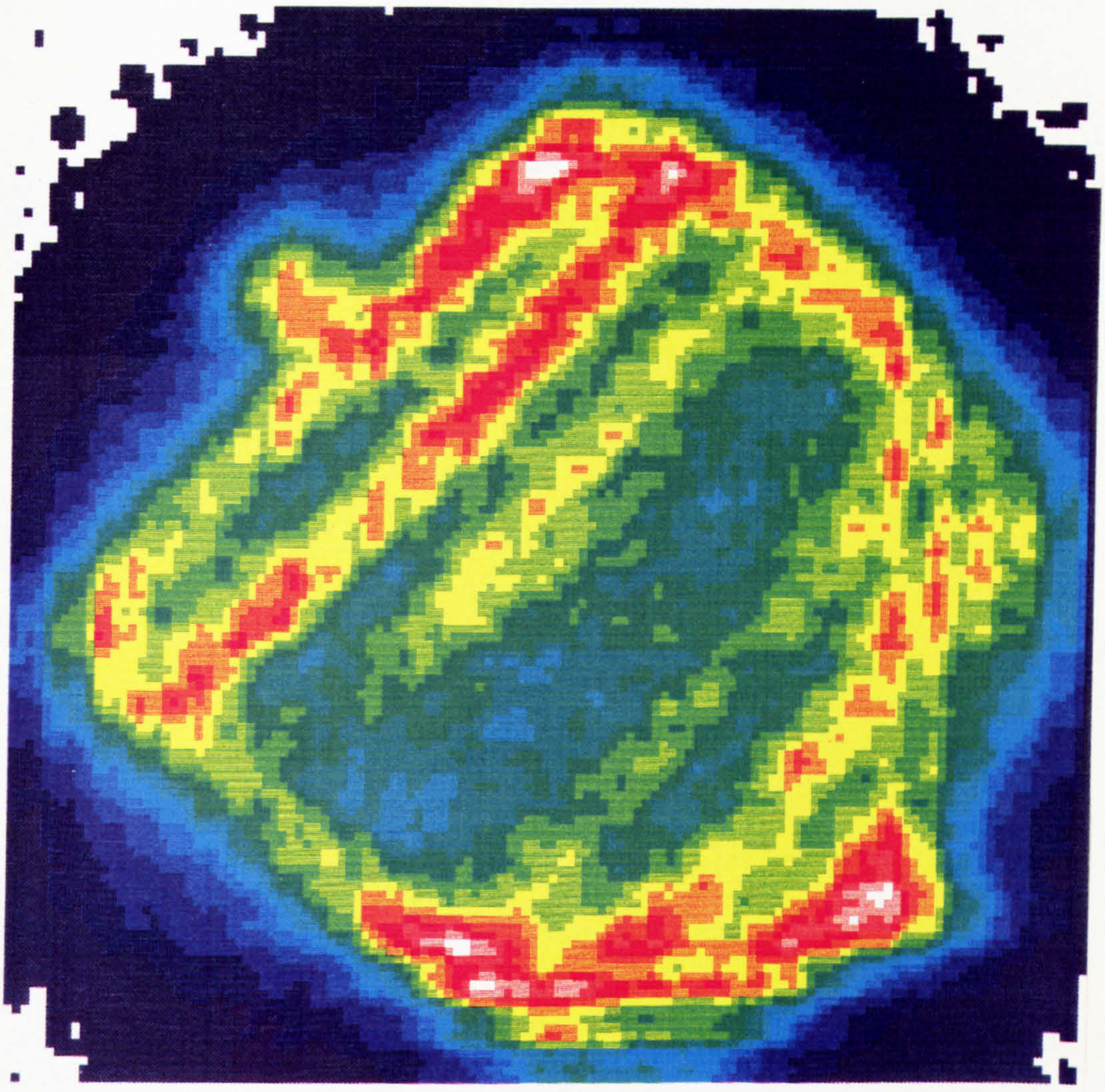

Figure 6.21: *Image of part of the line source using parallel collimation*

Chapter 7

LARGE AREA DETECTORS

7.1 Introduction

In Chapters 5 and 6, the technical and imaging performance of a detector based on a single position-sensitive photomultiplier was shown to be extremely promising for use in hard X-ray imaging. However, the largest PMT of this type currently available, a 5" diameter circular tube, has a (circular) sensitive area of only 80 cm^2. In the future, it is expected that an 8" diameter version will become available, and the sensitive area which this could provide (~250 cm^2) would represent a significant advance. Whilst detectors based on the current generation of position-sensitive photomultipliers may find some applications where there is a need for a small, light, imaging device (see Chapter 8), many uses will be made impractical by the small sensitive area.

The small sensitive area of a detector based on a single photomultiplier is particularly inappropriate for X-ray astronomy, where a large detector area (1500 – 3000 cm^2) is required to give a reasonable sensitivity due to the very low source fluxes encountered. In medical applications where the use of parallel collimation is normal, the detector area needs to be at least as great as the area to be imaged; for large-area studies such as lung performance, a similar area detector is essential.

For some applications, the translation of a single detector may be used to increase the area covered, whilst in others, suitable light guides could increase the sensitive area,

albeit at the expense of some spatial resolution. Only a moderate increase in sensitive area is possible while using a single PMT, and so to achieve a larger area detector (>100 cm^2) requires the use of an array of photomultipliers.

This chapter outlines some techniques proposed to produce larger area detectors based on position sensitive photomultipliers, and reports the results of laboratory tests carried out in an attempt to confirm the validity of these techniques.

Almost invariably, the design of a large area detector involves some light transmitting material being placed between the primary crystal and the photomultiplier, and this gives rise to the possibility of a position sensitive phoswich detector. Such a detector would have a valuable part to play in hard X-ray astronomy, and is discussed in some detail.

7.2 Scanning & rotating detectors

A simple way of increasing the coverage (but not the sensitive area) of a detector is to move the detector head whilst the image is being accumulated. This movement could be in the form of either a rotation or a linear translation.

This is likely to be of use more for high count-rate applications such as medical imaging, in those cases where a large field of view is required. Even here, however, sensitivity is important in order to minimise the radiation dose to the patient. In X-ray astronomy, there is nothing to be gained from such a technique as the sensitive area of the detector is not increased.

Figure 7.1 shows the coverage achieved by rotating both a 3" square (60 × 60 mm sensitive area) and a 5" circular (100 mm diameter sensitive area) position-sensitive photomultiplier. The curves indicate the relative viewing times as a function of radial distance, and show that the coverage of the field of view in such a system is non-uniform; a problem which would require correction during image processing by weighting pixels according to their radial distance.

The areas covered are 226 cm^2 and 314 cm^2 for the square and circular tubes, corresponding to increases by a factor of 6.3 and 4.0 respectively.

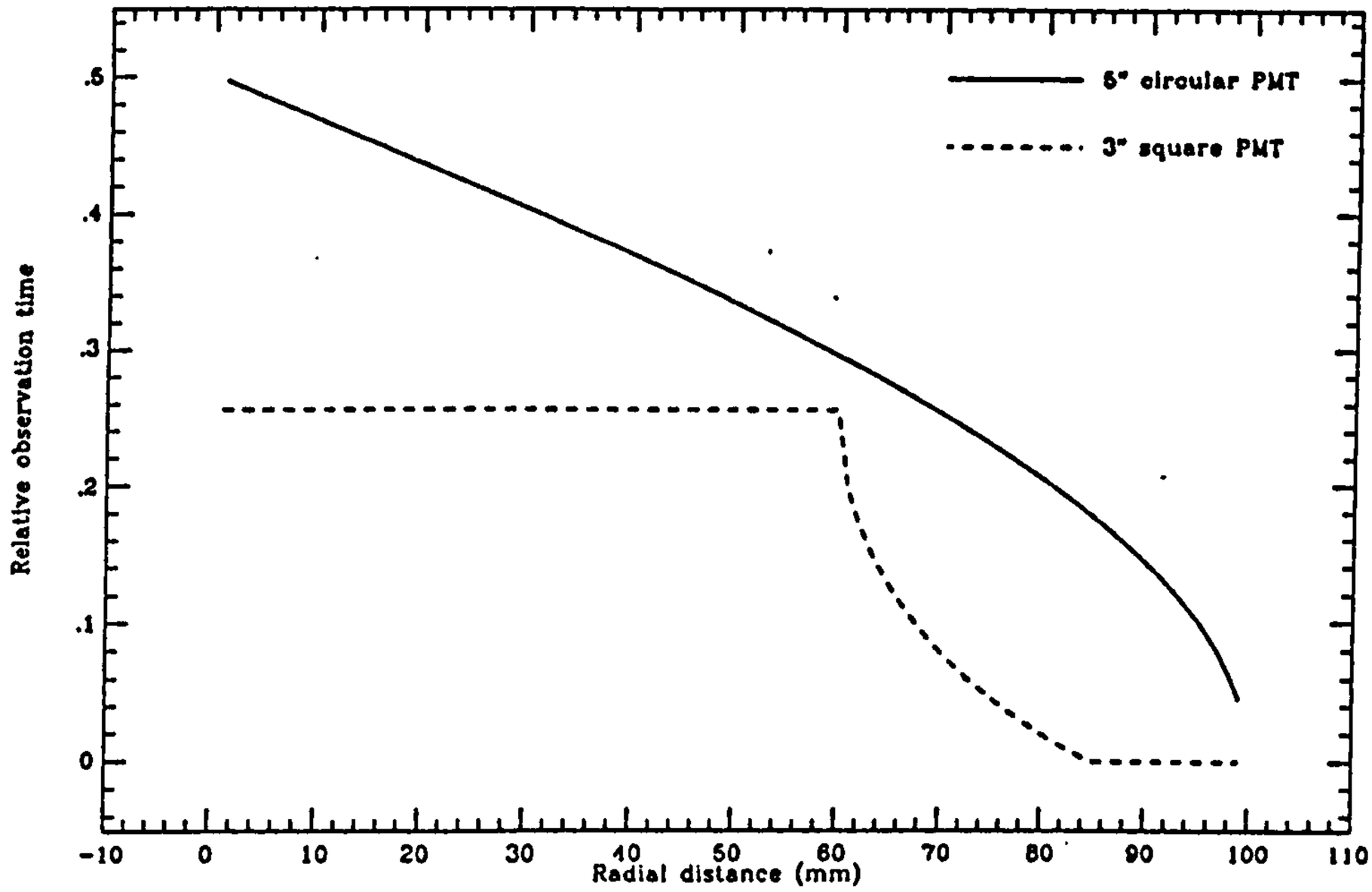

Figure 7.1: *Coverage of rotating PSPMTs*

The use of a rotating detector introduces a greater complexity to both the hardware and the image collection software. Reconstruction of each event requires both accurate knowledge of the detector position and considerable computation time.

Linear scanning detectors would slightly simplify the computation of event locations, but could prove more difficult to implement in hardware. The field of view of a scanning detector would not be limited by the PMT dimensions as it is for a rotating detector, but would depend solely on the scanning apparatus employed.

7.3 Expansion light guides

A light guide may be used in an attempt to overcome the problems caused by the small sensitive-to-physical area ratio of the Hamamatsu PSPMTs. Light guides are commonly used in scintillation detectors where a large crystal must be coupled to a smaller photodetector. When intended for use in conjunction with a position-sensitive photodetector, it is clear that any light guide should preserve the light distribution at its input surface through to the output surface without causing too great an attenuation of the light.

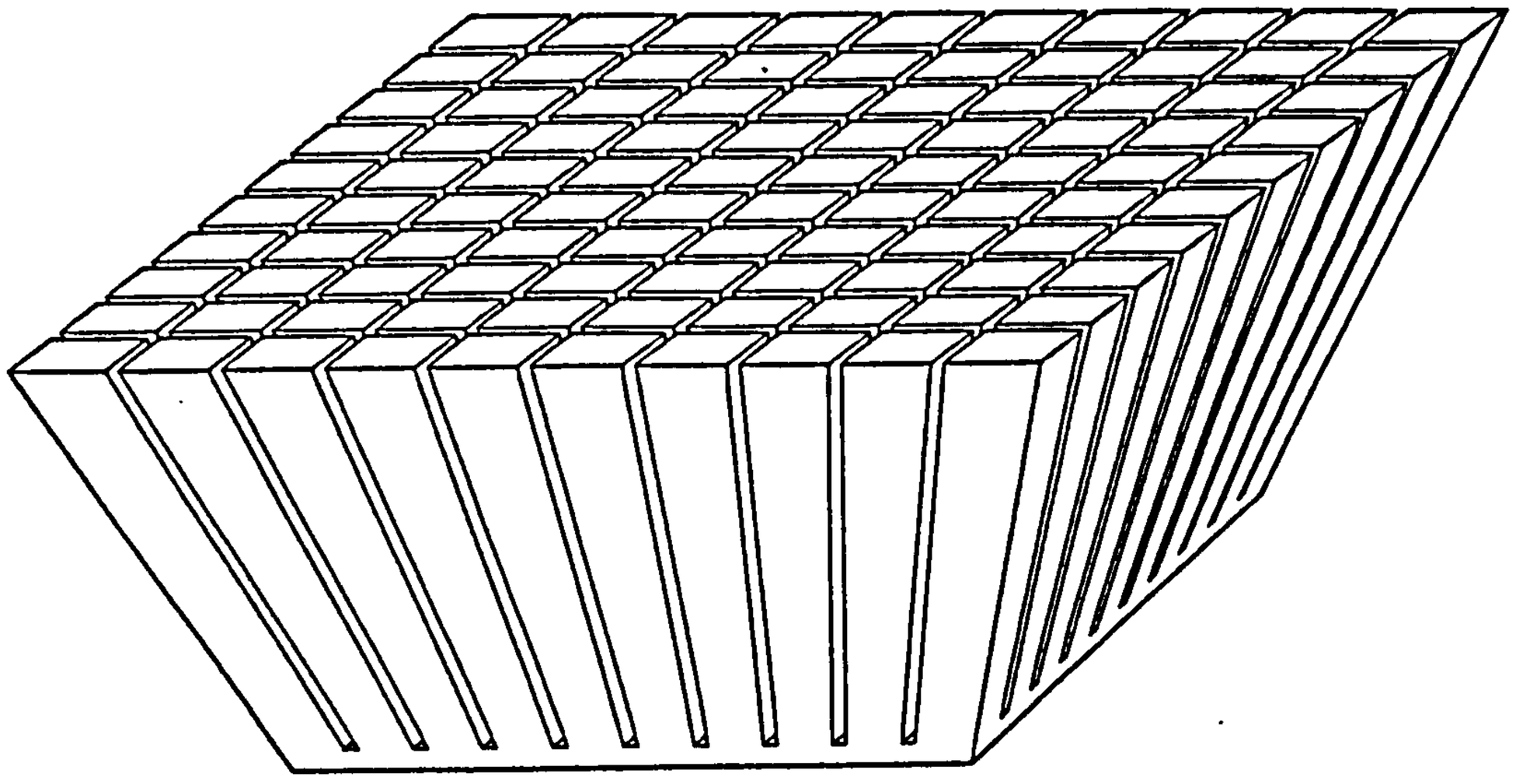

Figure 7.2: *A prototype position-sensitive expansion light guide*

A schematic view of a design which has been tested is shown in Figure 7.2. This is designed to channel light from a 80 x 80 mm crystal to the central 50 x 50 mm region of the photomultiplier via optically isolated 30 mm long perspex tapers. The theoretical performance of the light guide can be thought of as follows:

(a) The best position resolution will be for those events occurring over the junction between two segments (Figure 7.3). The division of light between the two segments, coupled with the intrinsic centroiding of the detector, should result in only a small reduction in the position resolution from that achieved without a light guide.

(b) The worst resolution will be for those events occurring near the centre of a segment (Figure 7.4). If the light is contained wholly within a single segment then the diffusive surface of the guide will cause position information to be lost.

It is therefore clear that the segment size should be chosen such that the situation described in (b) above never occurs (or only occurs for those events at the exact centre of the segment). This means that the segments should be made smaller than or equal to the spatial extent of the light cone at the interface between the crystal and the light guide. In practice, it has been found necessary to balance this desire against the need to retain a strong enough structure during the machining process.

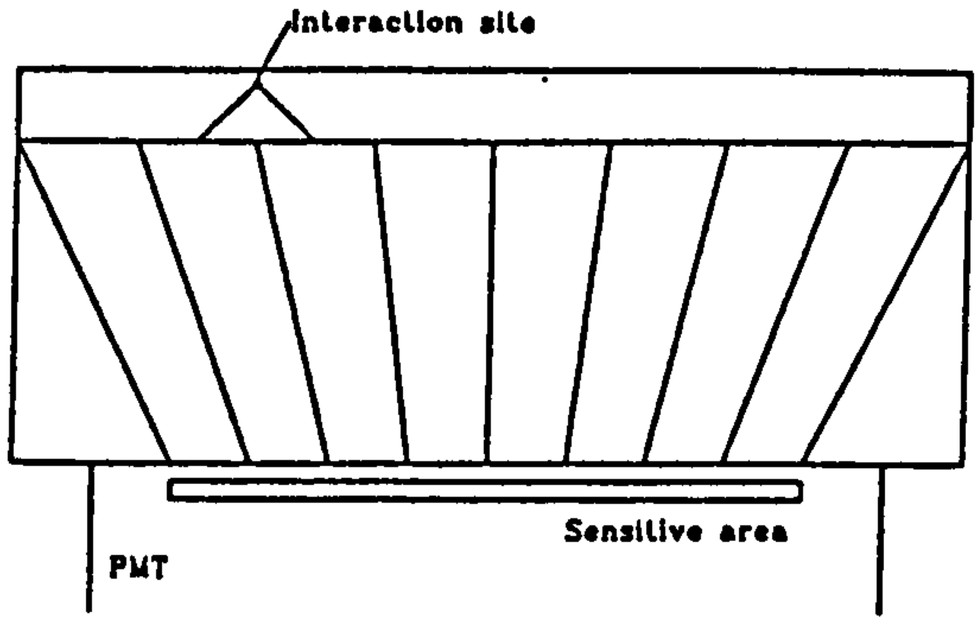

Figure 7.3: *Best case in segmented light guide*

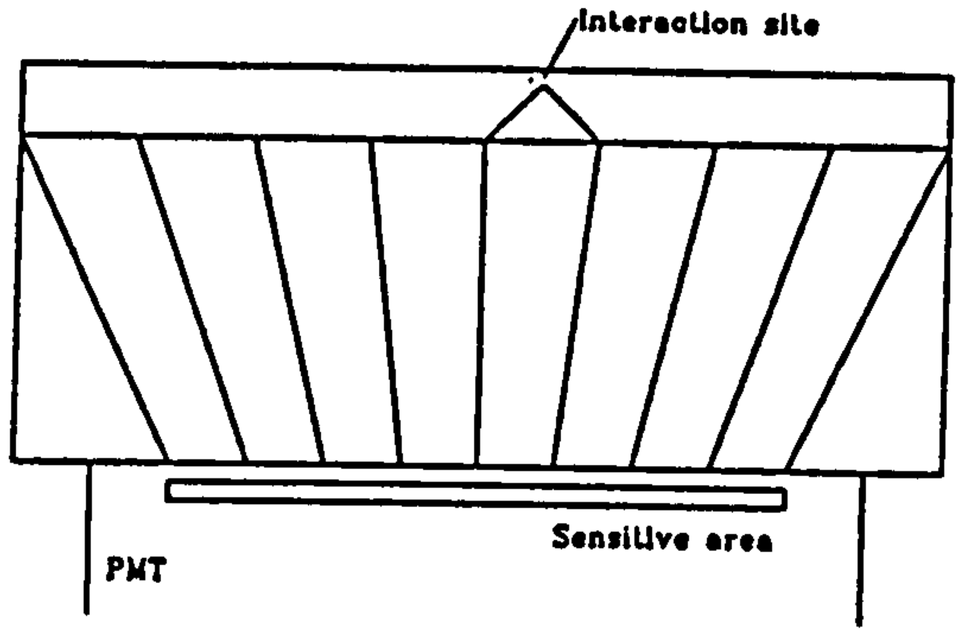

Figure 7.4: *Worst case in segmented light guide*

Two versions of this type of light guide were designed, the first coarse guide having segments defined by $p = 8$ mm, $p' = 5$ mm and the second finer guide with $p = 4$ mm, $p' = 2.5$ mm. In the coarse guide the separation between segments, c, was ~1.5 mm whilst the corresponding figure for the fine guide was 0.3 mm. If both the losses at the upper surface due to the cuts, and the adiabatic light losses in the tapers are considered, the light transmission of the guides can be estimated from the expression

$$T = \frac{(p-c)^2}{p^2} \times \frac{(p'-c)^2}{(p-c)^2} = \frac{(p'-c)^2}{p^2} \tag{7.1}$$

giving theoretical transmissions of 20% and 30% for the coarse and fine guides respectively.

The performance of the coarse light guide was first assessed without applying a diffusive coating, but simply relying on the rough machined finish of the perspex. The light guide was sandwiched between the photomultiplier glass window and the crystal, and was located centrally on both. Optical coupling fluid was used to form the optical interfaces.

Pulse height spectra were obtained using a variety of sources; an example ^{57}Co spectrum with the coarse guide is shown in Figure 7.5.

The spatial linearity of the detector was measured by scanning a source along the x and

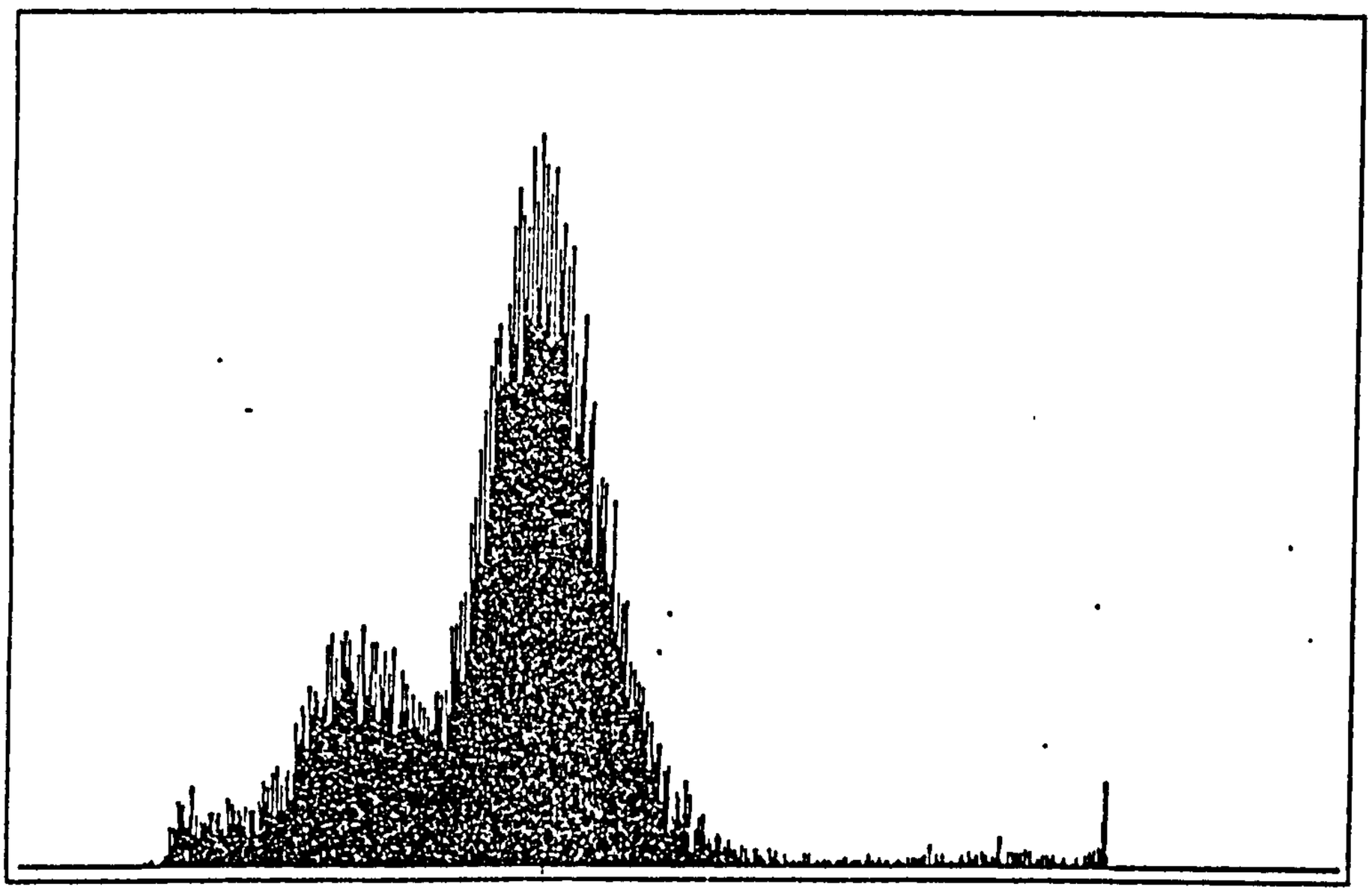

Figure 7.5: *Pulse height spectrum for a ^{57}Co source (122 keV) at the centre of the detector with the expansion light guide in place.*

y axes of the crystal as before, and plotting calibration curves of the raw position co-ordinate S against the true source position. The curves generated in this way are shown in Figure 7.6.

Once the extent of the linear region was established, it was then possible to measure the spatial resolution at the centre of the detector. This was carried out using two point sources at a known separation of 20 mm as described in Section 5.4.3.

Following these tests, the gaps between the segments were filled with white PTFE powder in order to give each segment a diffusive surface coating. Due to the intricate nature of the light guide it was impossible to do more than gradually compress the powder into the slots whilst ensuring the filling was as even as possible. Care was taken to ensure the slots were filled to ~2mm below the upper surface to reduce interaction between the PTFE powder and the optical coupling fluid. When the light guide and crystal were separated at the end of testing this appeared to have been successful.

The results of the measurements made with and without the PTFE coating are summarised in Table 7.1 below:

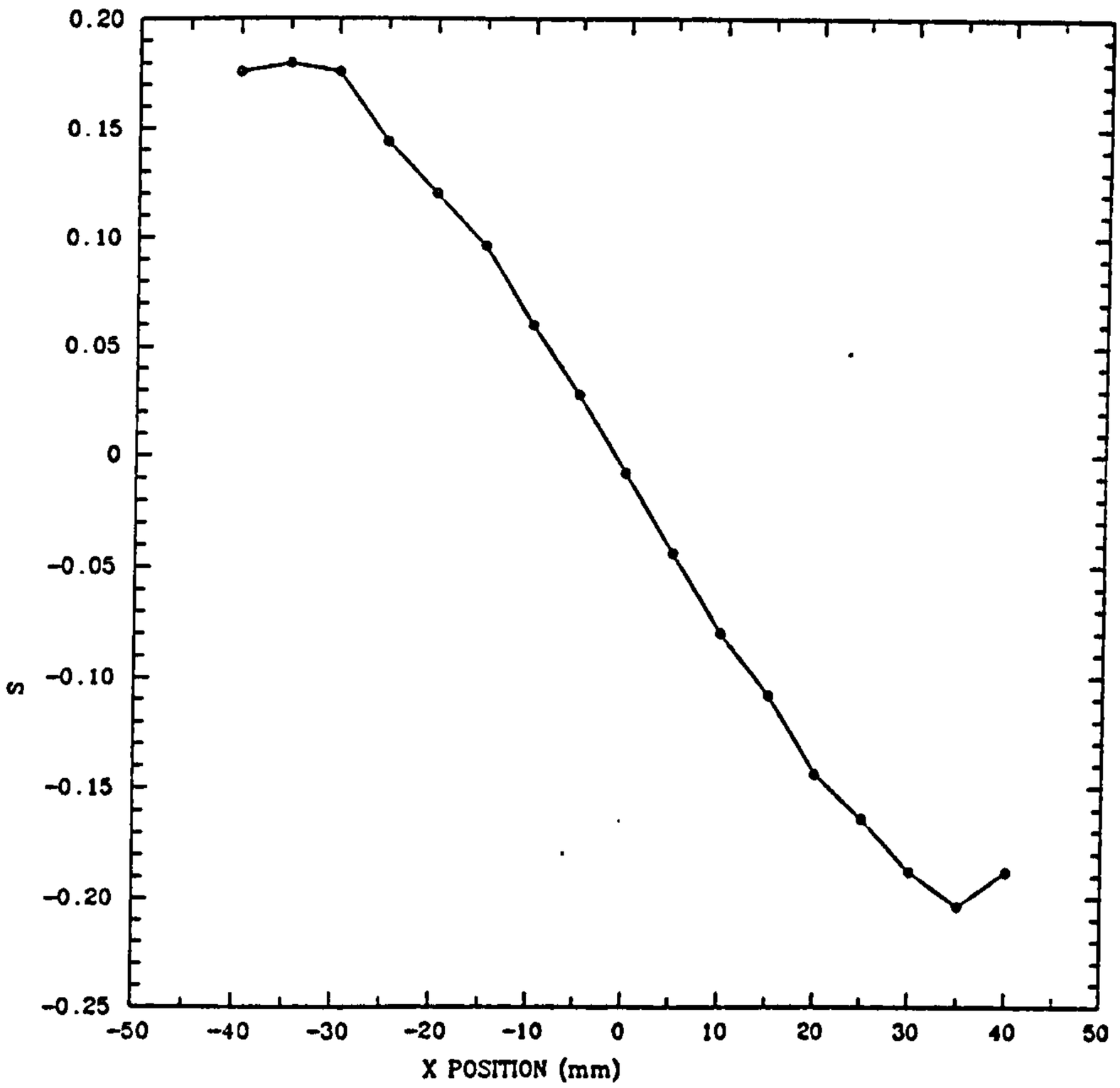

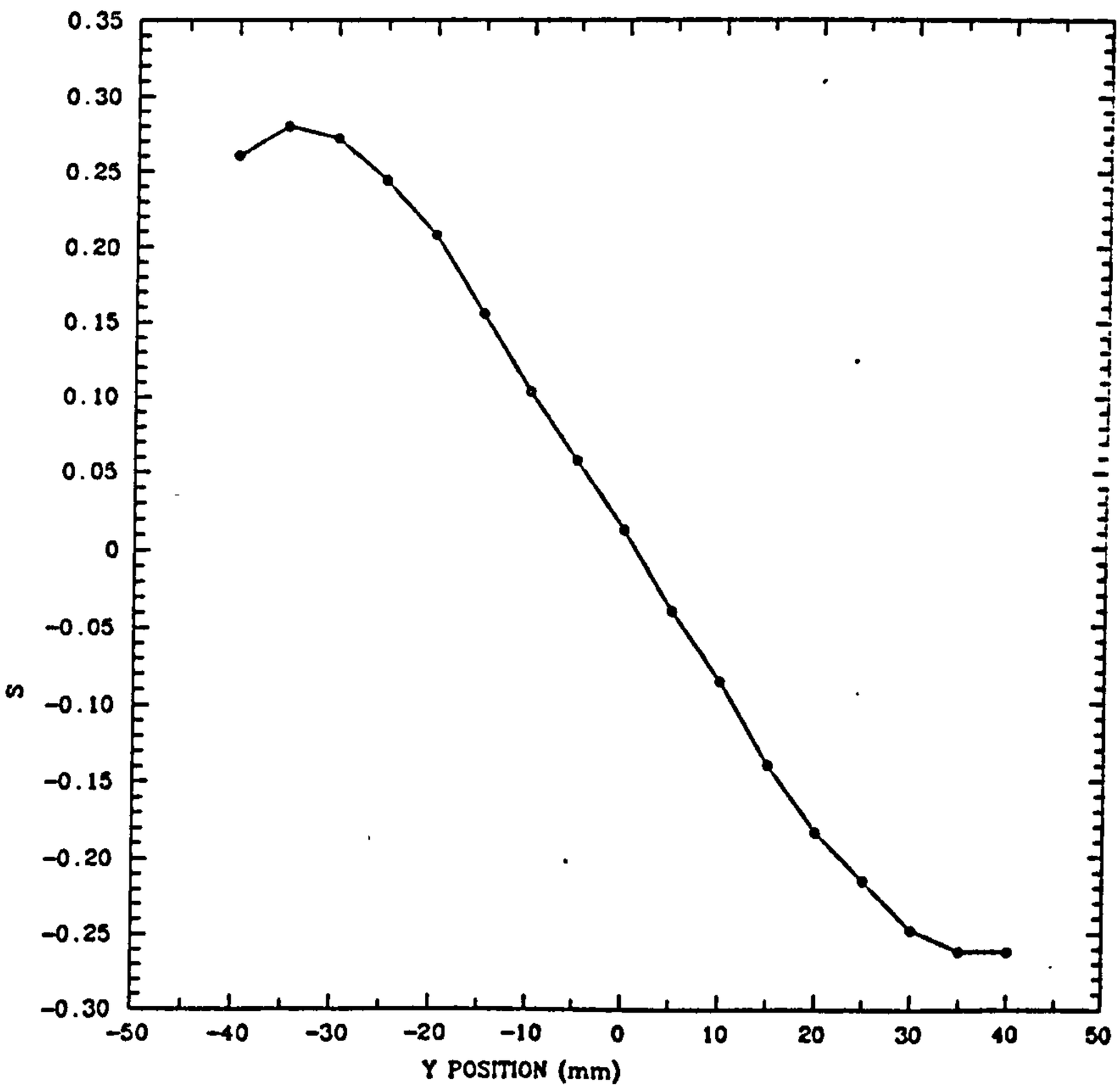

Figure 7.6: *Linearity curves for the coarse expansion light guide*

Test	Coarse guide	Coarse guide (PTFE filled)
Light transmission [1]	1.00	0.6
Energy resolution [2]	25%	35%
Spatial linearity [3]	-35 → 35 (X) -40 → 35 (Y)	-40 → 35 (X) -40 → 35 (Y)
Spatial resolution [4]	8.4 ± 0.2 mm	8.3 ± 0.4 mm

Table 7.1: *Summary of expansion light guide performance*

[1] Measured relative to the coarse guide with no PTFE filling

[2] FWHM, measured for a central 122 keV source. $V_{HT} = -1200$ V

[3] Defines the area over which there are no ambiguities in position reconstruction

[4] FWHM, measured at two points, x = ±10 mm. Figures have been corrected for collimator width

Position reconstruction look-up tables were created from the position calibration curves following the method described in Section 6.3. The detector with the light guide in place was then used in conjunction with the parallel collimator to image the thyroid phantom. An image obtained using the coarse light guide is shown as Figure 7.7. When this image is compared with Figure 6.19, the most noticeable feature of the image is that now the whole source has been imaged, indicating that the expected increase in the sensitive area, and hence coverage of the detector, has been achieved. As indicated by the preliminary measurements, however, when this coarse light guide is in place, the spatial resolution of the system is degraded to such an extent that the smaller features of the source are no longer visible.

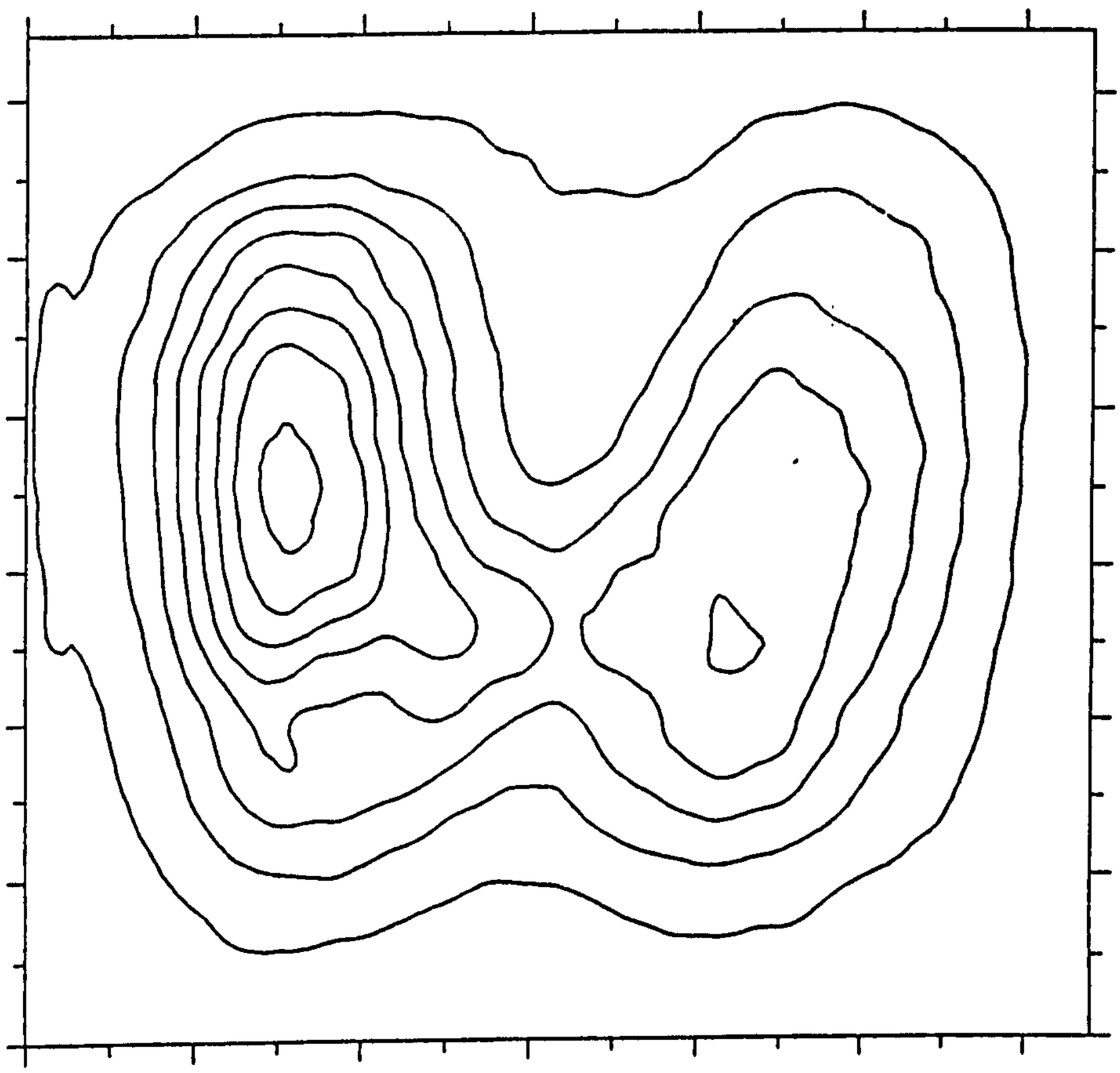

Figure 7.7: *Thyroid image using coarse light guide and parallel collimator*

Construction of a finer light guide, designed in the light of the results obtained with the coarse version, proved to be extremely difficult. An upper surface slot pitch of 4 mm was chosen to match the expected size of the light spot at the crystal exit window, but this meant that the narrowest parts of the segments were only ~2mm is size, leading to a mechanical weakness in the structure. Experiments are continuing to determine a

reliable method of construction, and potential techniques include the following:

(i) A light guide could be assembled from individually constructed component tapers. The machining of tapers of a suitable size would not be a major problem, but the final assembly could prove difficult. Depending on the materials involved, the final shape could be produced by a variety of methods such as gluing, heating under stress, or simple mechanical clamping.

(ii) An expansion light guide could also be made by pouring optical quality resin into a mould constructed from PTFE strips. When the resin hardened, the PTFE mould would remain within the transparent block, and provide diffusive optical separation of the individual segments.

The performance of the type of light guide described in this section has an important implication for the design of large area detectors based on multiple photomultipliers. If each photomultiplier can be made to view an area of crystal equal to its physical dimensions in this way, it becomes possible to form a continuous detection plane. This approach will be discussed further in the next two sections.

It should be noted that the construction of a similar light guide to maximise the use of a PMT with a circular sensitive area is considerably more difficult. Such a light guide could only be constructed by a method similar to (i) described previously, that is, by the assembly of specially shaped individual segments.

7.4 Arrays of square position-sensitive PMTs

To form a large area detector using position-sensitive PMTs is not a straightforward task. This section will assume the use of the 3" square Hamamatsu photomultiplier, the R2487. The main problem which must be overcome is caused by the non-sensitive regions around the outside of the tube envelope. The manufacturer's specified sensitive area (55 × 45 mm) covers only 43% of the PMT front surface, and even the 60 × 60 mm useful area measured in the tests in Chapter 5 accounts for only 62% of the tube area. When the PMTs are placed side-by-side in an array, this results in considerable 'dead' areas (see Figure 7.8).

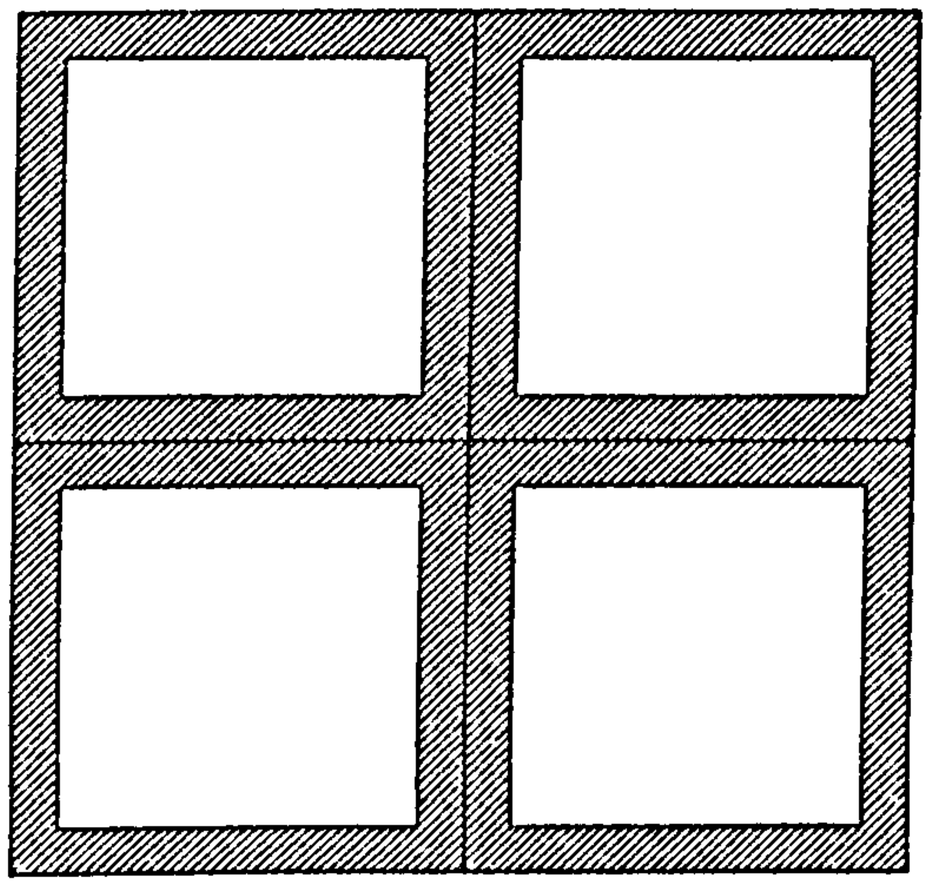

Figure 7.8: *The effect of non-sensitive regions in PSPMT arrays*

In order to prevent the light from an interaction in the crystal from falling entirely onto a 'dead' area, one approach is to physically separate the primary crystal from the detector to enable the light pool to spread sufficiently to strike the sensitive areas of the tubes. In the context of a detector for hard X-ray astronomy this is highly desirable, as the spacer between the primary crystal and the detector can be a veto crystal, enabling the detector to operate as a phoswich (see Section 7.6).

Figure 7.9 illustrates three possible configurations. In (a) the primary crystal is separated from the photomultipliers by a thick plate of transparent material, which may be optical glass, plastic or a veto crystal. It can be seen that the thickness d should be of the same order as the dead area dimensions to ensure that there is direct illumination of at least one PMT sensitive area. This type of detector could offer a continuous sensitive area, although the spreading of the light pool which is intrinsic in the technique may lead to problems with low photon statistics severely degrading the spatial information returned.

The geometry shown in (b) should overcome this problem by concentrating the light on the photomultipliers with the use of a segmented light guide. Unfortunately, the resulting detector would not offer a continuous sensitive area as the light from the shaded areas of the crystal would be channelled to dead areas of the PMTs and so this geometry is only superior to a single thin crystal in applications where a veto crystal is essential.

In order to overcome the limitations of (b) it is possible to alter the light guides to channel the scintillation light away from the non-sensitive PMT areas (c). This is the

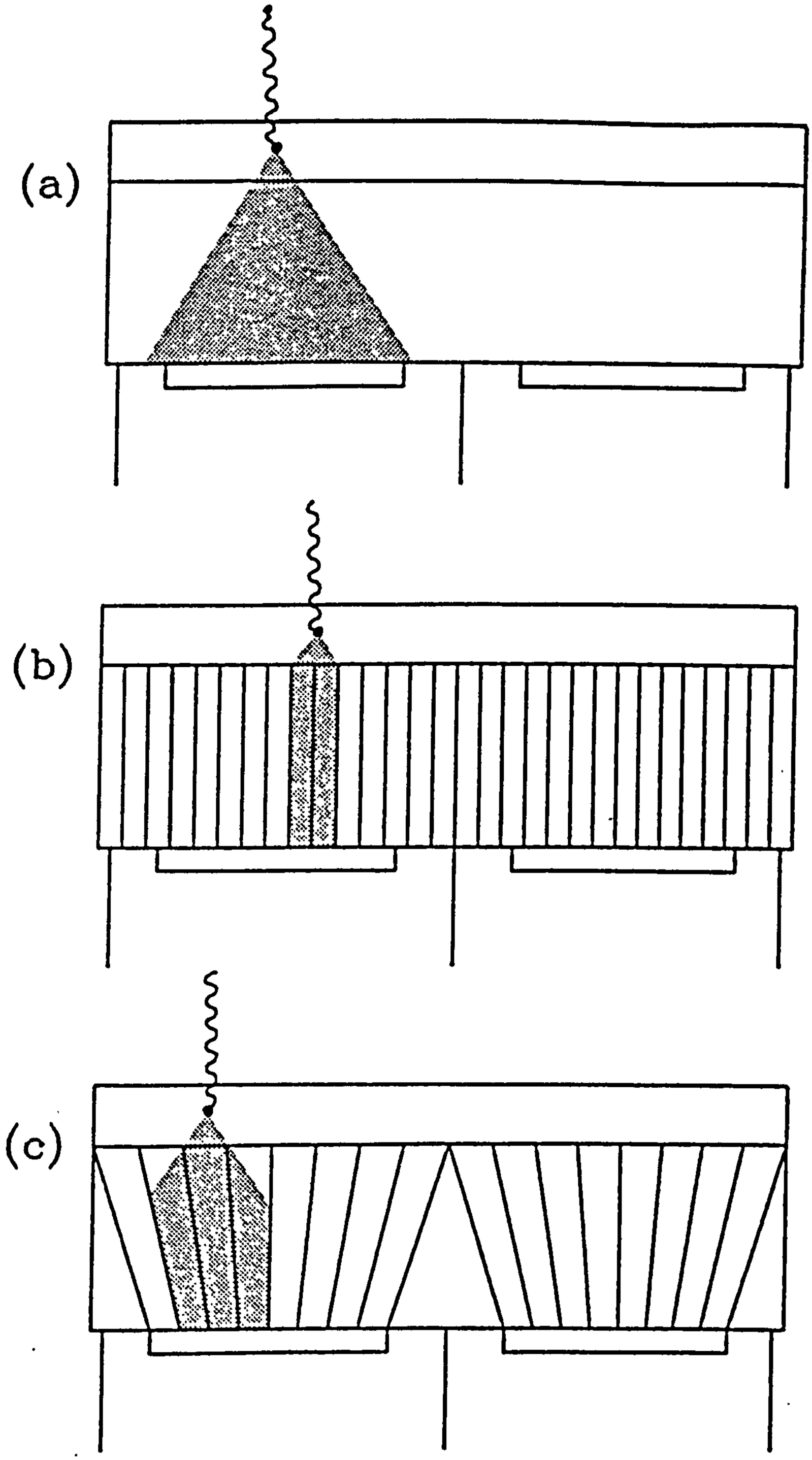

Figure 7.9: *Three possible light guide configurations*

same principle as that of the expansion light guides described in Section 7.3, modified to create an array of essentially individual detectors. The detector would be continuous, but it should be noted that if operated in phoswich mode, the veto efficiency would be degraded by the regions of the veto crystal which are viewed only by photomultiplier dead areas.

The performance of these various designs has been evaluated using Monte Carlo techniques, backed up by laboratory tests which have been carried out on the following:

- A plane perspex plate, geometry (a), of thickness 10 mm.
- Two straight light guides, geometry (b), with segment pitch $p = 4$ mm, and thickness 10 mm and 30 mm.
- An expansion light guides, geometry (c), both with and without a diffusive surface coating. These tests have been described in Section 7.3.

The planar light guide geometry (a) was evaluated using geometry-based simulation of the light transfer in conjunction with experimental measurement of systems employing guides of varying thicknesses. Figure 7.10 shows the dependence of the spatial resolution on the thickness of the crystal/window/light guide combination. Both simulation and experiment indicate that the resolution degrades rapidly with increasing light guide thickness, although the experimentally observed effect is more marked, perhaps due to some variation in the material used for the light guide. This loss of spatial resolution may be interpreted as being due to the wide spread of scintillation light over the detector, thus increasing the uncertainty in the reconstruction of the centroid of the light pool. A similar dependence upon crystal thickness, but for crystals between 1 mm and 5 mm thick, has been observed by Hailey et al. [67]. The predicted and measured light output as a function of light guide thickness is shown in Figure 7.11, and in this case the experimental and theoretical values agree remarkably well. Clearly this is a very important result, as it suggests that the use of this type of photomultiplier in conjunction with a thick crystal will always result in a trade-off between crystal thickness (and hence efficiency) and spatial resolution.

In Figure 7.12, the relative light output as a function of source position is shown for (i) the detector with no light guide, (ii) with a 10 mm perspex block in place, and (iii)

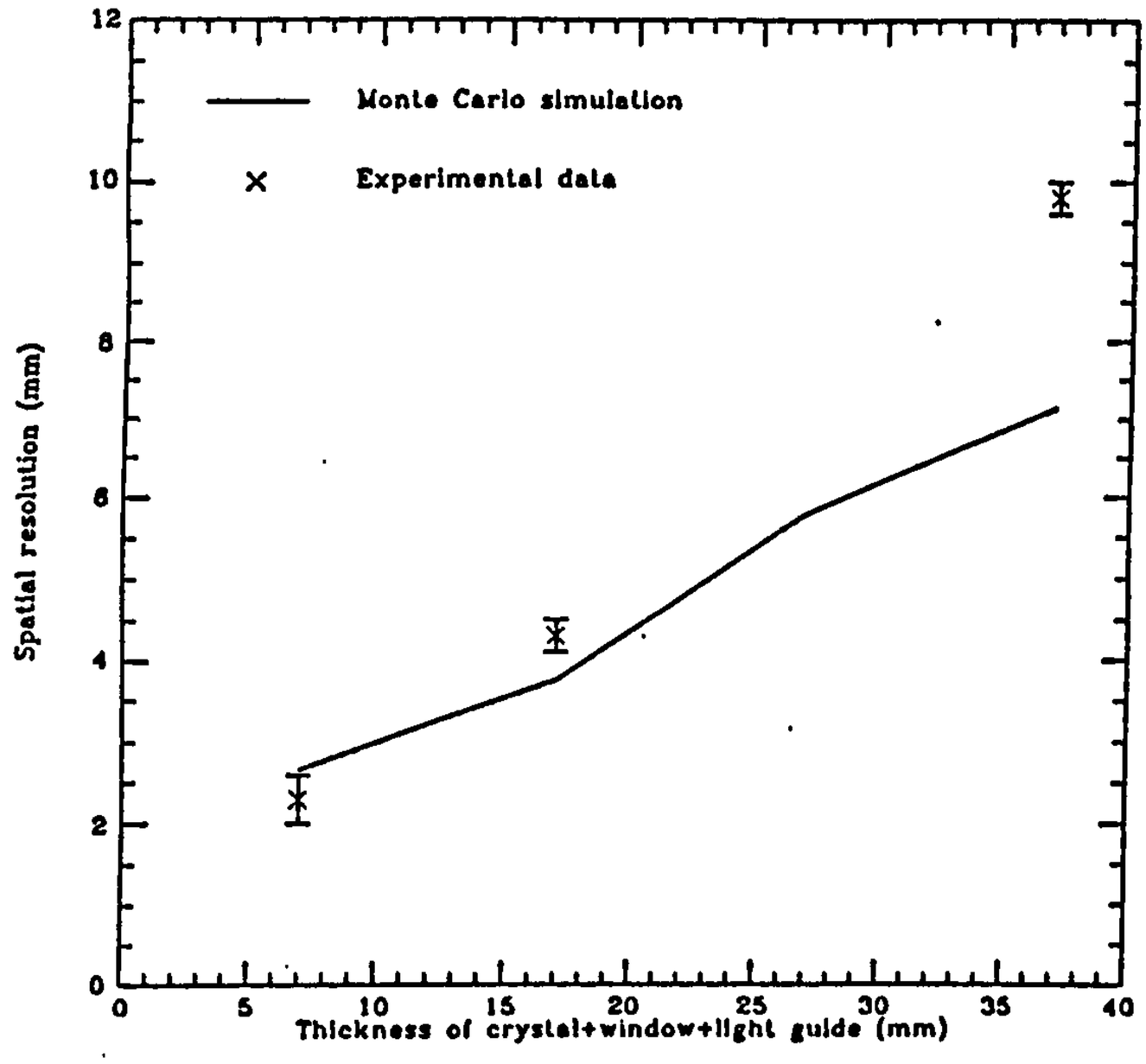

Figure 7.10: *The variation of spatial resolution with the thickness of the crystal+window+light guide combination*

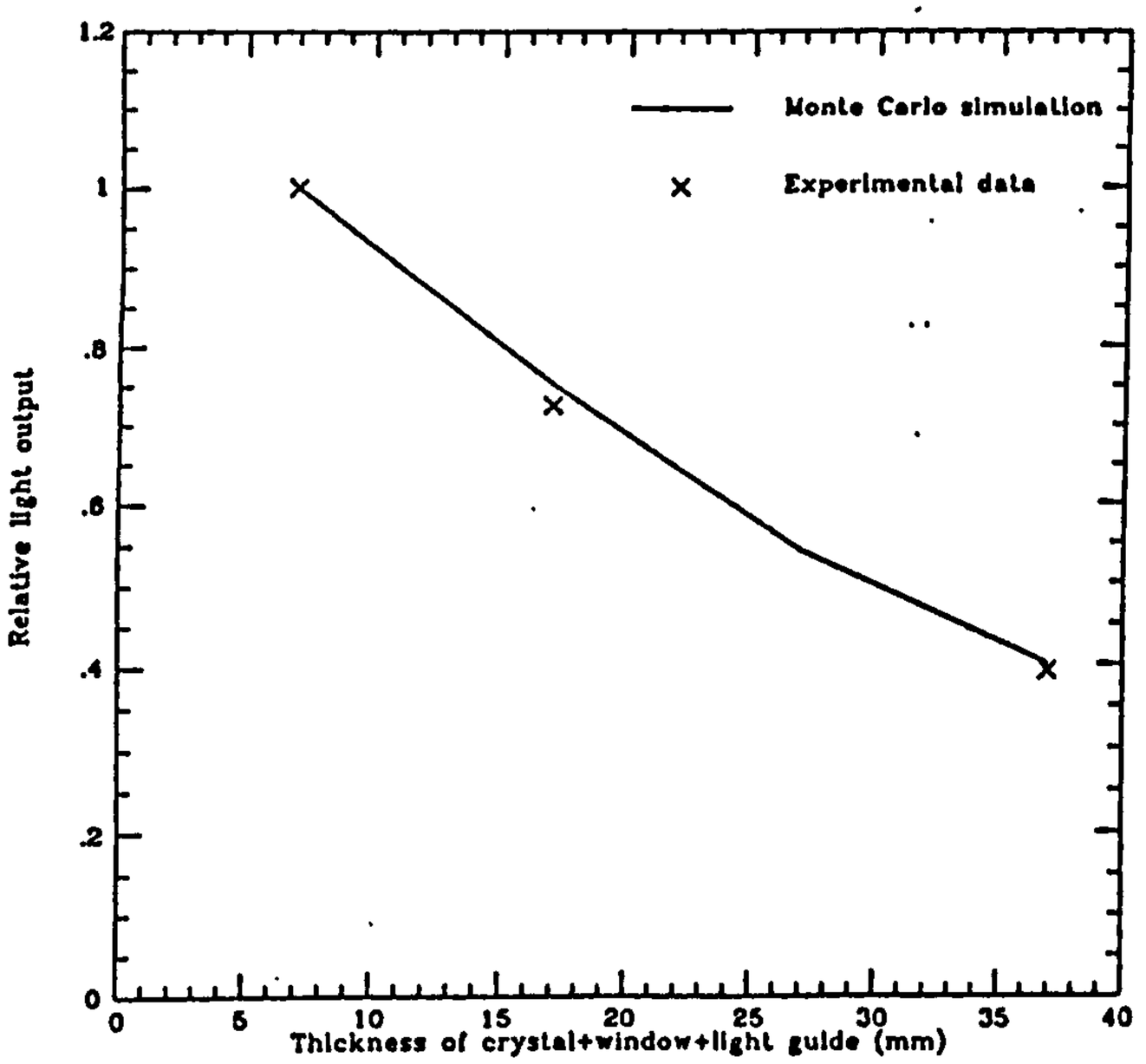

Figure 7.11: *The variation of light output with the thickness of the crystal+window+light guide combination*

with a 10mm thick straight-cut light guide. These curves may be characterised by two parameters, the values of which are summarised in Table 7.2:

i) The peak light output, which simply indicates the transmission of the light guide.

ii) The ratio of the peak light output to the light output at ±30 mm. This gives a measure of how spatially constrained the light in the guide is. A higher figure indicates tighter channelling of the light, causing a more rapid fall-off at the edges of the detector.

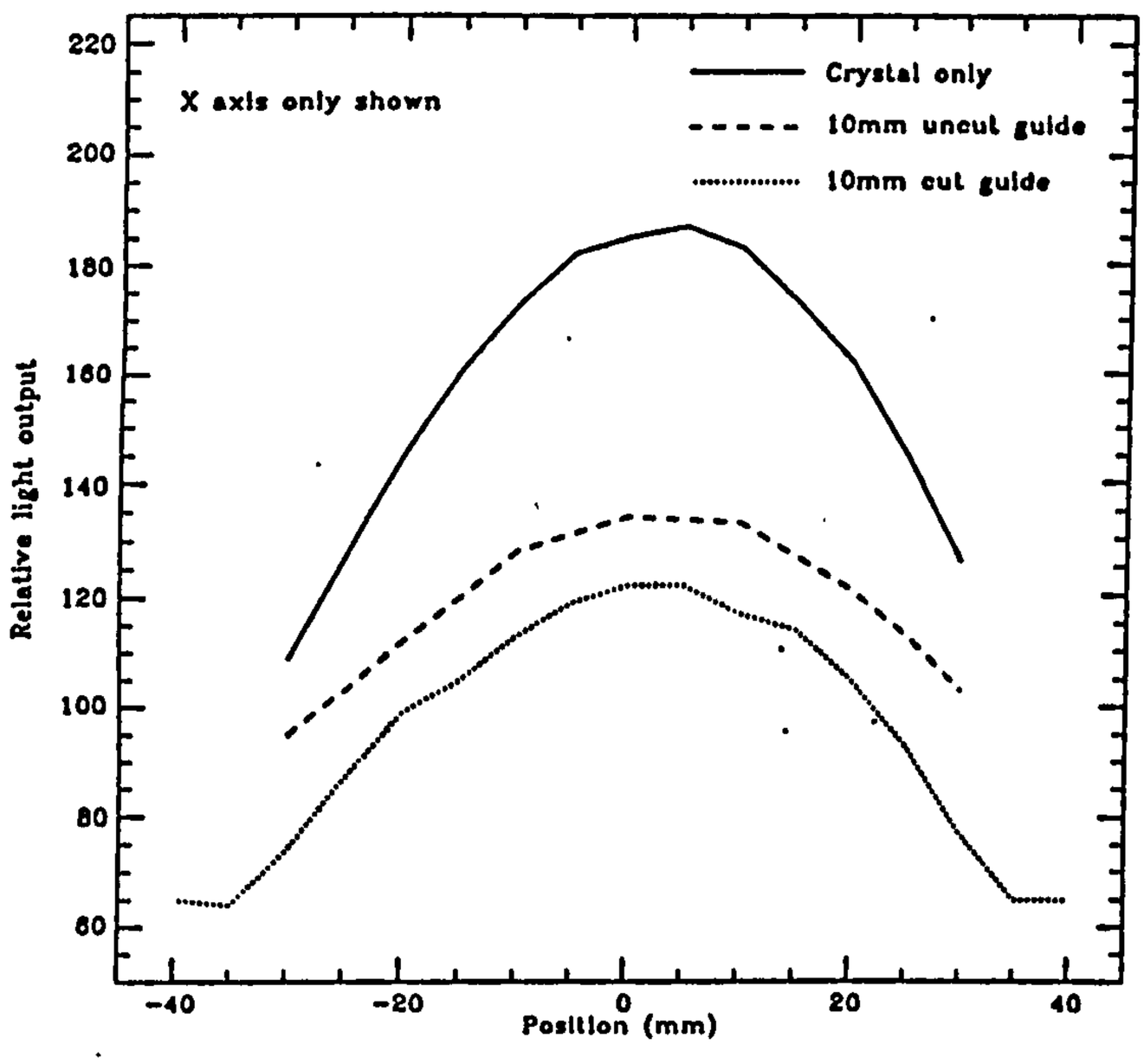

Figure 7.12: *Relative light output for detectors incorporating light guides*

With the exception of the plain crystal, the highest transmission is produced by the 10 mm perspex block. The introduction of 0.3 mm cuts into the block reduces the transmission by a further 10%, an amount consistent with the loss of surface area in contact with the crystal, i.e.

$$1 - \frac{(p-c)^2}{p^2}$$

In addition, it can be seen that the plain block allows the light pool to spread considerably, indicated by the relatively low value of $L_{PEAK}/L_{\pm 30}$. The similarity of this value for the

	L_{PEAK}	$\frac{L_{PEAK}}{L_{\pm 30}}$
Crystal only	1.00	1.59
10 mm block	0.72	1.35
10 mm straight-cut guide	0.65	1.62
30 mm tapered guide	0.23	-

Table 7.2: Transmission characteristics of light guides

cut guide and the crystal alone indicate that the 4 mm cut pitch is comparable with the size of the light pool at the crystal/light guide interface.

Figure 7.13 shows the 'spot size', that is, the convolution of the spatial resolution and the collimator beam width, for a ^{57}Co source scanned across the three detectors. The spot size increases by some 60% when the 10 mm block is introduced, which may be interpreted as due to the spread of the light pool in the perspex.

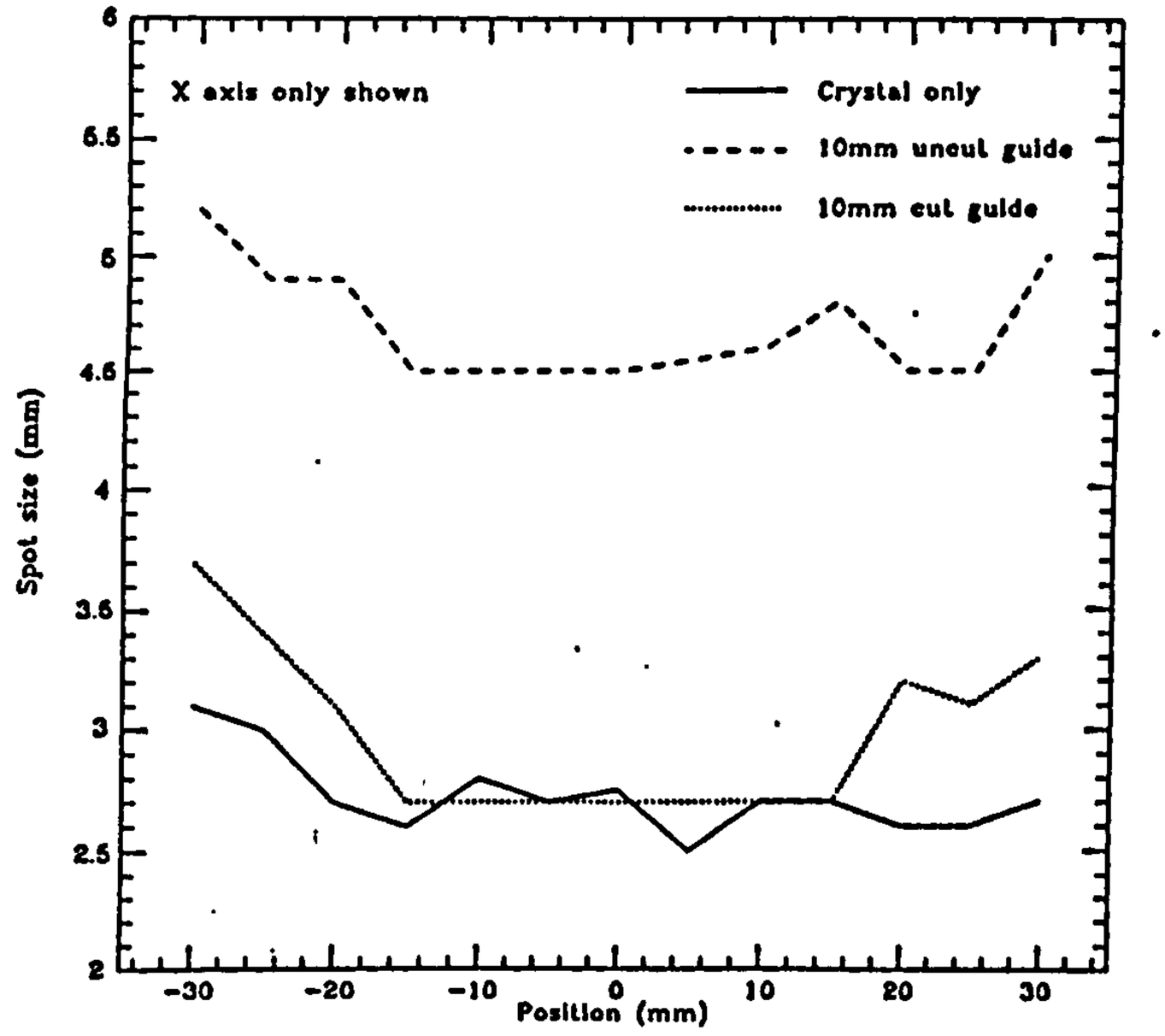

Figure 7.13: *Spot size for detectors incorporating light guides*

Conversely, when the cut block is in position, the spot size is comparable to that from the

crystal with no light guide, showing that the segmentation is successful in constraining the light pool to a concentrated region.

7.5 Arrays of circular position-sensitive PMTs

Since the development work on position-sensitive photomultipliers seems to be aimed solely at larger circular devices, it is worth considering the implications of this different geometry for the construction of larger area detectors.

- The packing efficiency of circular photomultipliers is much lower, and mechanically these devices appear less suited to an array than their square counterparts.
- Although initially appealing, the idea of operation of an array of circular PSPMTs in an Anger camera mode does have some major problems. As indicated before, the use of a thick crystal, which is necessary to avoid losing light to the dead areas of the detection plane and to allow light to fall on a group of tubes, degrades the resolution of the detector to a point at which it becomes useless. It is therefore unlikely that the use of position-sensitive tubes in an Anger camera mode will yield a significant improvement in performance, except perhaps near the edges of the detector.
- It seems that the only solution is the use of light guides once again, but the problem of coupling a square crystal area to the circular sensitive area of the photomultiplier greatly increases the complexity of this approach. If only a square part of the sensitive area is used, than a considerable amount will be wasted.

It may well be that the circular position-sensitive photomultipliers, particularly when versions as large as 8" become available, will be best suited for use in individual detectors. This will greatly reduce the mechanical difficulties, and allow a modular approach to detector design.

7.6 Position-sensitive phoswich detectors

Throughout this chapter, the major consideration has been the extension of the sensitive area possible with detectors based on position-sensitive PMTs. However, the techniques which have been considered, using light guides of various designs, suggest the possibility of a position-sensitive phoswich detector. If the function of light guide and veto crystal can be combined in one specially designed crystal, then this could prove a large step along the road to a detector of value in astronomical applications.

For use in a phoswich mode, a method must be found to distinguish between the light from the two (or more) scintillators making up the detector. The standard technique is to use two crystals with different light decay constants, and apply pulse shape discrimination to separate the signals from the different crystals. In the case of position-sensitive photomultipliers, an additional output could be obtained from the last dynode of each photomultiplier, enabling pulse shape discrimination to be applied without interfering with the positional performance of the detector.

Referring back to Figure 7.9, the depth of veto crystal required to give a high veto efficiency, of the order of 30 cm for hard X-ray astronomy, precludes the use of a planar veto crystal as shown in (a). However, if the veto crystals can be machined in a suitable manner, the geometries shown in (b) and (c) would both be consistent with the twin goals of spatial resolution and phoswich operation. It can be seen that (b) has the advantage of mechanical simplicity and could be used with square and circular detectors alike, but does not solve the problems associated with the limited PMT sensitive area. Geometry (c) overcomes this problem, but has a lower veto efficiency as part of the volume of the veto crystal is not observed by any sensitive part of the PMT array.

7.7 Conclusions

In this chapter, the construction of PSPMT-based large area detectors suitable for use in hard X-ray astronomy has been considered. The methods investigated involve the use of light guides of various designs placed between the detection crystal and the photomultiplier. Three light guide geometries have been investigated, and each found to

have individual strengths and weaknesses.

The first problem to be solved is the relatively small ratio of sensitive to physical area associated with the currently available PSPMTs. If the scintillation light is allowed to spread in a thick crystal to an extent sufficient to overcome this, then the spatial resolution achievable becomes extremely poor.

In order to maintain good spatial resolution, it is therefore important to use a light guide which constrains the spatial extent of the scintillation light. This can be achieved by using a milled light guide which is effectively made up of many individual vertical guides. Guides of this type, with thicknesses ranging from 10 mm to 30 mm have been tested.

This approach has one major problem, and that is that it cannot be used to construct a large-area *continuous* detector. For this, a more complex light guide is required, one which transfers the light from an area of crystal equal to the physical size of the PMT onto the smaller sensitive area of the tube. A design of this type has been demonstrated in conjunction with a 3" square photomultiplier, but was found to be limited by the relatively large size of the segments making up the guide. Some mechanical problems need to be overcome before finer versions can be successfully manufactured, but when available, such guides should offer excellent performance and the possibility of a large continuous detector.

If the techniques employed in the construction of these light guides can be transferred to scintillation crystals, then it will become possible to construct a detector in which the functions of the light guide are carried out by a specially designed veto crystal, resulting in a large-area position-sensitive phoswich detector.

Chapter 8

POTENTIAL APPLICATIONS

8.1 Introduction

The application of an imaging detector based on position-sensitive photomultipliers (PSPMTs) to the field of hard X-ray astronomy has been discussed in some detail in the preceding chapters. However, astronomy is by no means the only use for X-ray imaging techniques, and it therefore seems appropriate to discuss here a few representative applications in which PSPMT-based detectors may be (or already have been) put to use. The number of papers being published reporting the use of these devices is steadily increasing, indicating the interest that they are generating.

The applications which will be discussed are: the study of auroral X-ray emission, where a detector based on PSPMTs has been proposed for a hard X-ray imaging instrument; X-radiology and nuclear medicine, where there may be potential value for a compact, portable gamma camera; and tomography, a technique equally suited to non-invasive investigations in both medical and industrial applications.

In each case, consideration will be given to the benefits arising from any improvement in spatial resolution, as it is in this respect that PSPMT-based detectors are likely to outperform their predecessors.

The number of other potential applications for position-sensitive photomultipliers is

considerable, but space considerations prevent more than the following brief list: neutron detection [88], the readout of scintillating fibres [12,87], and high resolution scintillation hodoscopes [42,121].

8.2 Auroral X-ray Imaging - AURIO

The Auroral Imaging Observatory (AURIO) is a set of five instruments specifically designed to perform detailed observations of the spatial and temporal structure of auroral electron and proton precipitation, operating from the European Polar Platform at an altitude of 800 km [1]. The sensors on AURIO cover a wavelength range extending from the near infrared to the X-ray region. X-rays are produced in aurorae by bremsstrahlung emission from precipitating electrons over a broad energy range, and hence the X-ray fluxes provide a direct measure of the spectral distribution of the precipitating electrons. The flux of X-rays is related to the precipitating electron fluxes through a well-known transfer function, and hence the measured X-ray spectrum can be deconvolved to yield the incident electron spectrum.

There are two X-ray detectors proposed for the AURIO payload. The AURIO Low-Energy X-ray Imager (ALEX) consists of two variable-aperture pinhole cameras, operating in the energy range 2 - 60 keV. This is achieved using dual layer multi-wire proportional counters, with the front and rear chambers covering the ranges 2 - 15 keV and 10 - 60 keV respectively. The typical energy resolution of the detectors is 20% at 6 keV. The apertures may be adjusted to provide a trade-off between angular resolution and sensitivity, giving a selectable field of view of 100° × 60° or 25° × 25°, with spatial resolutions at the aurora of 20 km and 10 km respectively.

The AURIO High-Energy X-ray Imaging Spectrometer (AHEX) is comprised of two pairs of pinhole cameras, using position-sensitive scintillation counters as imaging detectors operating in the energy range 20 - 150 keV. A modular approach has been adopted, and with this approach, it is possible for two modules to be optimised for the energy range 20 - 80 keV and two optimised for 80 - 150 keV.

Each detector module comprises a pinhole collimator with a selectable field of view

(matching those of the ALEX detectors), and a circular position-sensitive detector. The proposed detector is based on the 5" diameter R3292 position-sensitive photomultiplier (see Table 5.1), which has a sensitive area of 80 cm^2. It was proposed to view a sodium iodide crystal through a lead-glass window or a phoswich veto crystal in order to provide some degree of shielding, a design which was conceived as a mass saving compromise in order to reduce the amount of passive shielding required at the rear of the detector. A schematic view of the AHEX instrument is shown in Figure 8.1. To achieve a high detection efficiency at 150 keV, a crystal ~6 mm thick is required, whilst the analysis in Chapter 7 suggests that the thickness of the detector and veto crystals in the low energy modules could be reduced in order to optimise the resolution of the detector. For this particular application in which one has a steeply falling spectrum, the optimisation of the energy range and detailed detector design will be an important Phase A task.

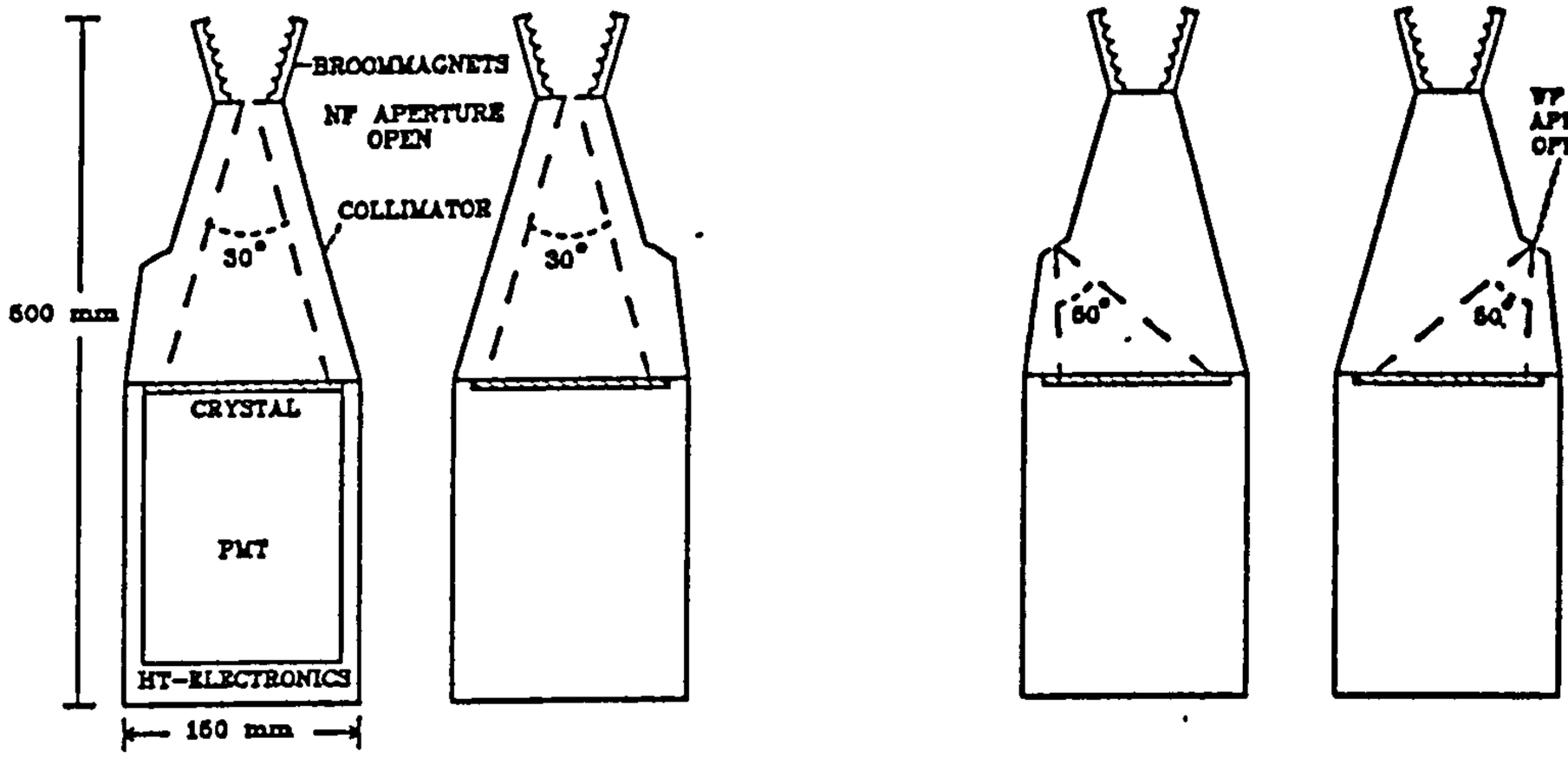

Figure 8.1: *The AHEX hard X-ray imager on AURIO*

Considerable effort is directed towards reducing the number of background events in the detectors, although one has quite a different signal to noise ratio in this application compared with a similar imager for astronomical applications. A graded shield surrounding the detector will be used to reduce the background due to energetic photons and charged particles, whilst background due to locally produced neutrons can be reduced only by minimising the thickness (and hence the volume) of the crystals. The reflected fraction of the auroral electron flux which is also incident on the aperture can

be reduced in two ways: broom magnets remove electrons with energy <100 keV, whilst a fully depleted thin silicon diode may be mounted in the aperture to veto more energetic electrons.

It can be seen from this brief description that the most critical design consideration is the thickness of the sodium iodide crystals and the windows and/or veto crystals through which they are viewed. Clearly the thinner the crystals can be made, the better the detector performance will be. However, this desire must be weighed against the background rejection requirements of the telescope. One possible solution is to use a sodium iodide crystal directly bonded onto the photomultiplier using a thin beryllium window, thus obtaining the best possible spatial resolution. In this case the graded shielding would have to be extended around the rear of the detector to replace the lost shielding effect of the lead-glass window.

Recent moves to reduce the mass allocation for the AURIO experiment still further may result in a need to combine the function of the ALEX and AHEX, either by adding a high energy extension to the ALEX or by optimising the performance of the AHEX detectors for the energy range 10 – 100 keV.

8.3 A compact imager for X-radiology & nuclear medicine

The medical uses of X-rays can be considered in two distinct areas, namely X-radiology and nuclear medicine [109,147]. X-radiology is the study of anatomical features using the transmission through the body of X-rays in the range 20 – 80 keV, whilst nuclear medicine is the study of body function using X-ray emission from selected radiopharmaceuticals introduced into the body [78]. These typically emit in the energy range 100 – 511 keV and have short half-lives in order to minimise the patient dose. Studies may be made both for diagnostic purposes, and for the monitoring of therapy.

X-radiology and nuclear medicine techniques generally result in two dimensional maps of body tissue or radiopharmaceutical uptake respectively. In addition, these methods can be extended to give 3-dimensional information (usually in the form of two-dimensional slices through the body) by tomographic techniques. These techniques, and their wider

applications, will be discussed in greater detail in the next section.

In X-radiology, film is still the most commonly used detector due to its extremely high resolution ($\sim$ 20μm) and ease of use. However, the low X-ray detection efficiency results in high patient doses, and so modern systems commonly use phosphor screens in conjunction with the film in order to greatly increase the detection efficiency and hence reduce the patient dose, whilst maintaining very high spatial resolution. One slightly more unusual medical application of radiology is very high energy ($\sim$1 MeV) radiology, which is sometimes used for real-time assessment of patient positioning during therapy. In this application, 1-D position-sensitive scintillation detectors are normal.

For use in nuclear medicine, non-imaging detectors are capable of quantitative measurements of radiopharmaceutical uptake, but are prone to errors in their positioning. The use of an imaging detector removes such problems, and allows the mapping of source distribution to be undertaken. Differential uptake within an organ can be measured and used to identify areas of dysfunction. For imaging use, the almost universal detector in use is the gamma camera. This is a standard Anger camera [126], optimised for operation in the region of 150 keV and coupled to a pinhole aperture or, more commonly, a parallel collimator. Modern gamma cameras are capable of spatial resolution in the region of 4 mm, have a high detection efficiency and can operate at extremely high count rates.

Some of the applications of nuclear medicine are:

- Static imaging of organs and glands. Radiopharmaceuticals are available which allow the imaging of, for example, the heart, kidneys, thyroid and pancreas.
- Dynamic organ imaging, and hence measurement of organ function. Dynamic studies are particularly important for observing, for example, cardiac function and lung ventilation and perfusion.
- Tumour localisation

The major drawbacks of gamma cameras currently in clinical use are their cost and size. There is therefore a possible application for a compact gamma camera with good spatial resolution which may be used as a bedside monitor or in intensive care when the patient cannot be moved to a remote gamma camera, although there is concern amongst some

regarding the use of radiopharmaceuticals in such wards.

The tests which have been carried out on the position-sensitive photomultiplier based detector have shown it to be capable of filling this role, and it is with this is mind that it is planned to carry out clinical trials of a compact gamma camera built using a 5" diameter position-sensitive photomultiplier. To be useful in a clinical environment, significant progress must be made in the area of data collection and analysis. Count rates of ~20000 counts/s are to be expected, and the data collection, analysis and display system used will be based on high-speed digital signal processing hardware.

It is proposed that the clinical trials programme be conducted in two main phases. The first stage will be conducted in the Soviet Union over a period of approximately four months. The performance of the portable camera will be compared with that of a conventional camera principally in the study of cardiac function. In particular, these studies will include:

- The measurement of the ejection fraction and filling rate.
- Functional imaging including phase and amplitude images using Fourier analysis and regional ejection fraction images.
- Study of the propagation of myocardial contractions with the ability to provide a dynamic phase display.
- Study of the motion of the left ventricular wall.

In addition to these cardiac studies, the camera will also be applied in other areas such as the study of the efficiency of lung ventilation and perfusion, kidney function, regional cerebral blood flow, the perfusion of the brain and the uptake of the thyroid gland.

These studies will be made using the normal organ imaging facilities which provide the ability to generate static and dynamic images using such isotopes as $^{99}Tc^{m}$, ^{201}Tl and ^{67}Ga. The exposures will be controlled either by pre-set time or by the required pre-set number of counts. The comparative studies will be made on the basis of colour and grey-scale image photographs and more quantitative presentations of the data.

The planned sequence of studies will require the use of an interchangeable set of foil

collimators which will provide for the high sensitivity (2.6mm), general purpose (1.8mm), and high resolution (1.6mm) requirements. The camera will also be tested in conjunction with both converging and diverging collimators.

It is expected that further trials will take place at a second institute in Moscow, followed by trials in the UK, conducted with the assistance of the Nuclear Medicine Department at the Southampton General Hospital and the Department of Medical Physics at Bristol General Hospital.

8.4 Tomography

Tomography is an important technique whereby information regarding the internal structure and function of a solid 'body' can be obtained in a non-destructive way. This is achieved by acquiring images of a source from many viewing positions, and using the information to reconstruct the original distribution of material. The primary applications of tomography are in nuclear medicine, for non-invasive study of body function, and in industry, where it can be used for quality control and the inspection of inaccessible materials [58].

Tomographic techniques can be divided into two groups [24]:

(i) Transmission tomography, where both radioactive source and detector are external to the object to be investigated. In this case, the quantity being measured is the attenuation of the radiation in the material making up the object. Most industrial applications of tomography rely on this technique, commonly known as computed tomography (CT).

(ii) Emission tomography, where radioactivity is introduced into the item to be studied, and the aim is to produce a map of the distribution of the activity within the object. Two types of emission tomography, single-photon emission computed tomography (SPECT or SPCT) and positron emission tomography (PET or PCT) are used widely in nuclear medicine.

Computed tomography (CT) is used both in industrial and medical applications, and is

based on the differential attenuation of an X-ray beam within the object to be studied. A typical medical CT system is shown in Figure 8.2, and shows how the source and detector are rotated about the patient in order to measure the many profiles needed for the tomographic reconstruction. A fan beam of X-rays is emitted from the source, allowing many lines through the source to be measured simultaneously. In industrial applications where patient dose is not a consideration, an intense, highly collimated beam may be used. In this case the object under investigation is scanned and rotated through the stationary beam.

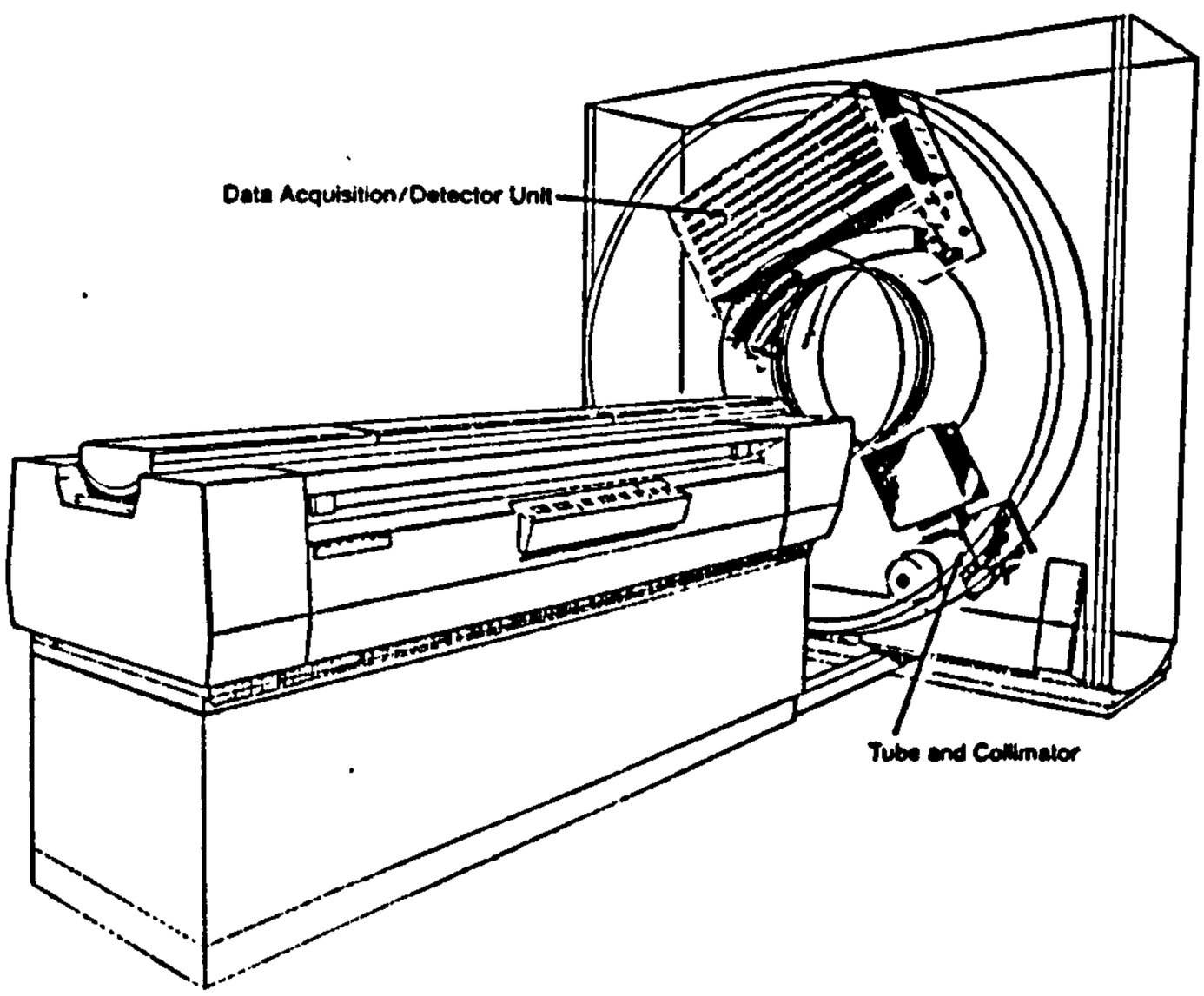

Figure 8.2: *A typical medical CT system*

CT imaging systems are capable of high resolution (~1 mm) measurements. It is unlikely that position-sensitive photomultipliers will have much impact in this field, unless two-dimensional tagged photon sources and two-dimensional detectors are used to simultaneously measure a large number of views throughout a source with considerable reduction in the scanning involved (Figure 8.3). As no collimation is required, the sensitivity of the system is greatly increased. Computer simulations of such a system viewing a source from two orthogonal directions have shown that this is indeed possible. Figure 8.4 shows slices through (a) the simulated object for study, and (b) the simulated tomographic image, obtained using a simple back-projection technique.

In SPECT (single-photon emission computed tomography) imaging, photons emitted

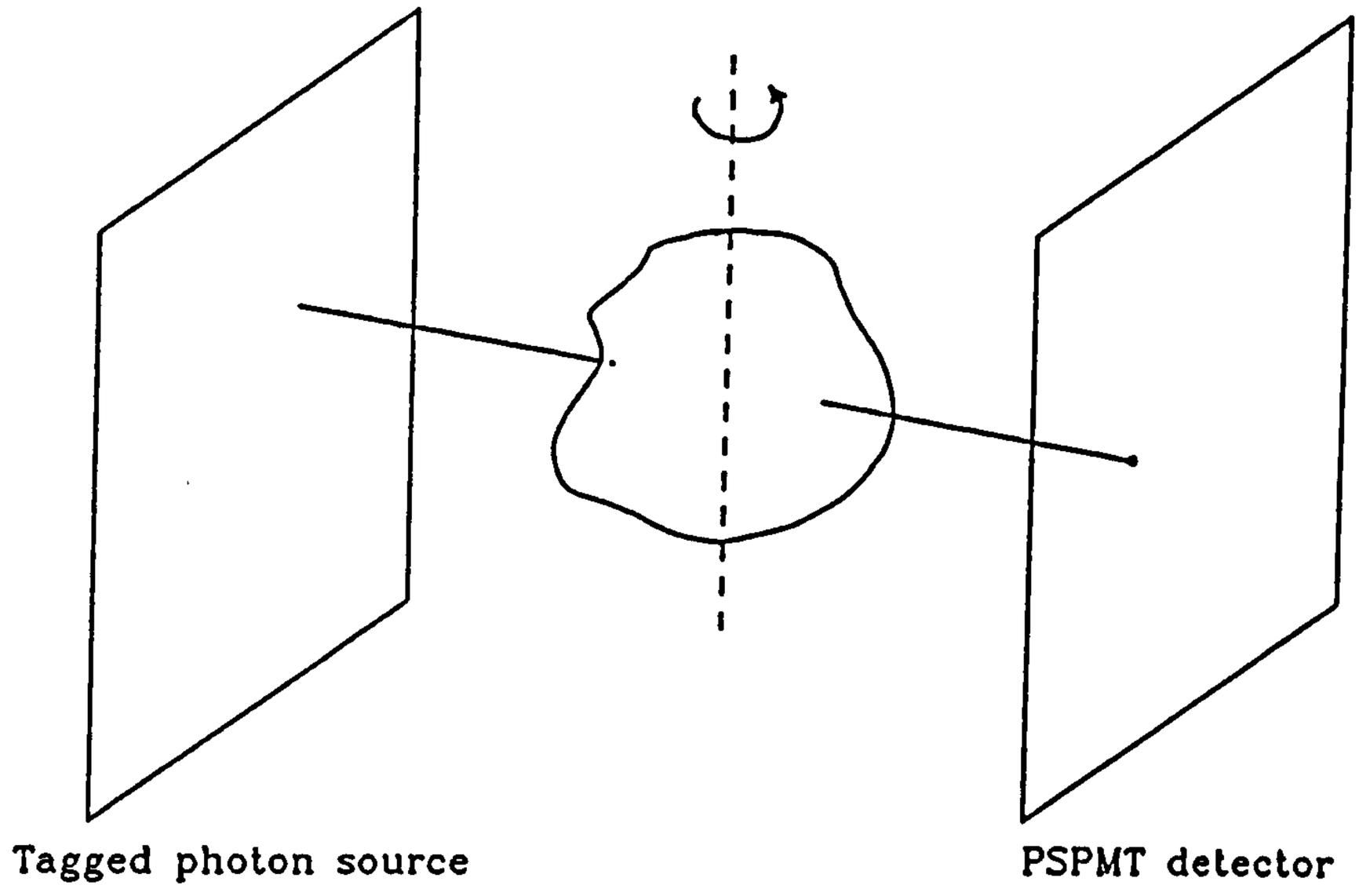

Figure 8.3: *A small CT system based on position-sensitive PMTs*

from within the object to be studied are detected by one or more collimated position-sensitive detectors. If many views are taken from various angles, the 1-dimensional profiles obtained can be used to reconstruct the distribution of the source within the body (Figure 8.5). This can be achieved by using one or more detector heads which can be moved around the source, or if higher sensitivity is required, with a fixed array of detectors surrounding the source. This simplified view of the system has two problems:

1. A simple back-projection technique as shown in Figure 8.5 leads to artifacts in the reconstructed image resulting from the superposition of activity not present in the source. This may be overcome by using a technique known as filtered back-projection.

2. The profiles recorded at the detector will have been considerably affected by attenuation of the radiation within the body being imaged. This may be corrected to a first order by the use of opposing views, requiring a detector which has a 360° coverage.

It may be shown that the resolution which can be achieved with such a system depends on the spatial resolution of the detectors, the collimators used, and the number of views taken from different angles [78].

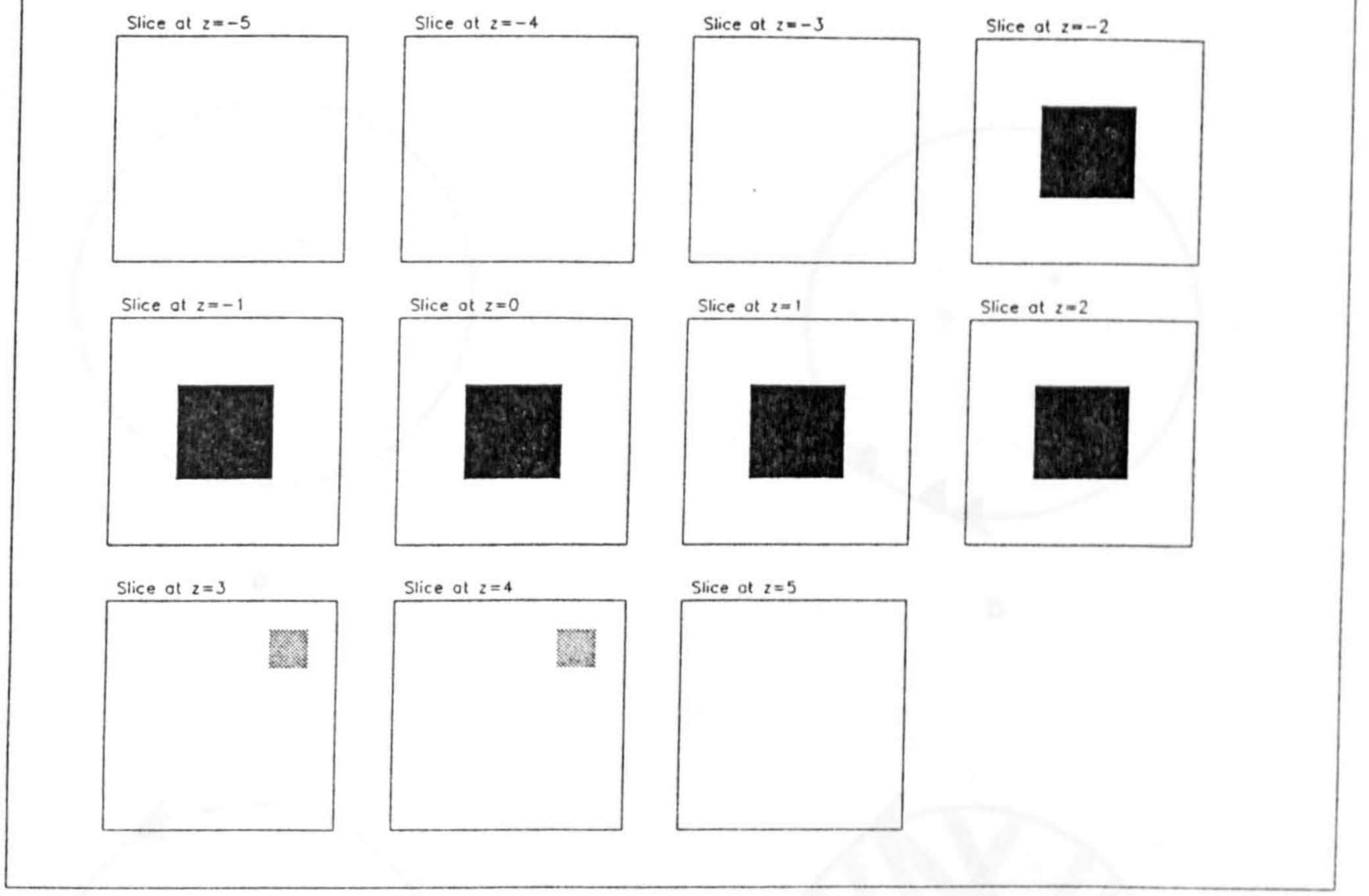

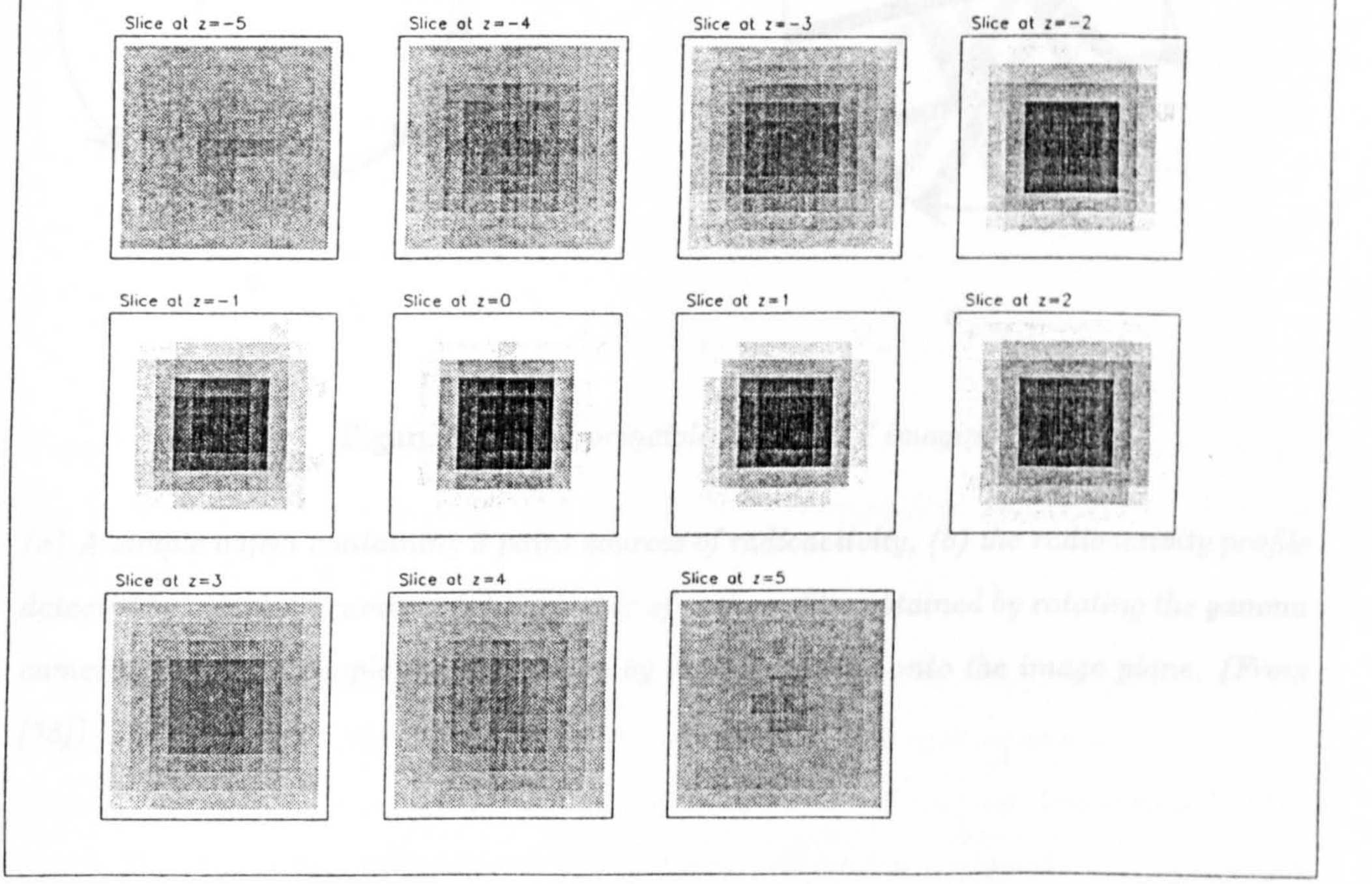

Figure 8.4: *Simulations of a small CT system based on position-sensitive PMTs (a) The simulated study object (b) Reconstruction using simple back- projection of transmission data.*

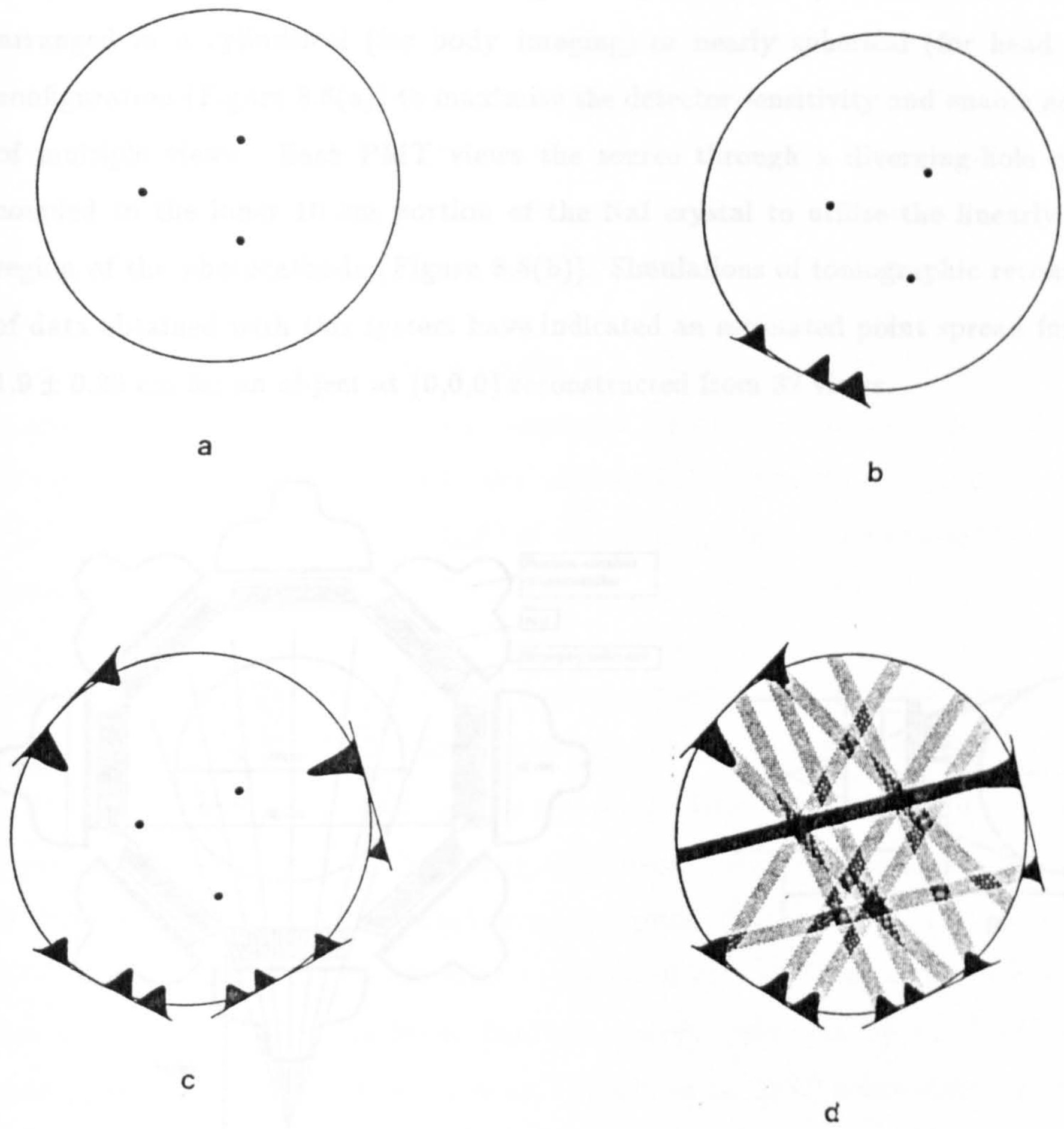

Figure 8.5: *The principle of SPECT imaging*

(a) A simple object containing 3 point sources of radioactivity, (b) the radioactivity profile detected by a gamma camera, (c) a number of such profiles obtained by rotating the gamma camera, and (d) a simple reconstruction by back-projecting onto the image plane. (From [78])

A dynamic SPECT system based on position-sensitive photomultipliers has been proposed by Singh et al. [129]. The design incorporates multiple 13 cm diameter PSPMTs arranged in a cylindrical (for body imaging) or nearly spherical (for head imaging) configuration (Figure 8.6(a)) to maximise the detector sensitivity and enable acquisition of multiple views. Each PMT views the source through a diverging-hole collimator coupled to the inner 10 cm portion of the NaI crystal to utilise the linearly sensitive region of the photocathode (Figure 8.6(b)). Simulations of tomographic reconstruction of data obtained with this system have indicated an estimated point spread function of 1.9 ± 0.25 cm for an object at (0,0,0) reconstructed from 32 views.

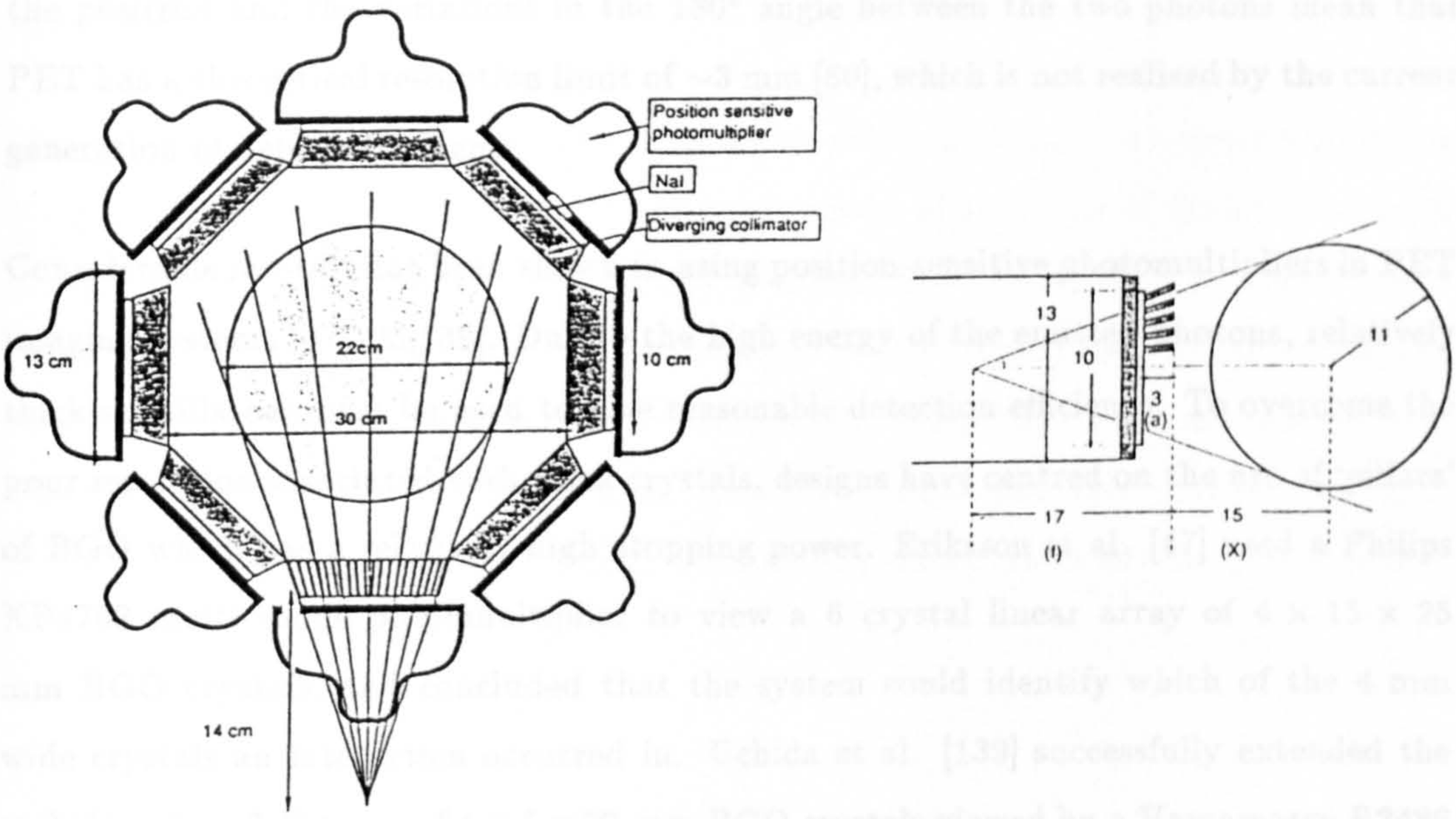

Figure 8.6: *A dynamic SPECT system based on position-sensitive photomultipliers: (a) the central ring of the instrument, and (b) the diverging-hole collimator used in the dynamic SPECT system*

Positron Emission Tomography (PET) uses positron emitting radioisotopes within the object to be imaged [80]. When a positron is emitted, it combines almost immediately with an electron to form two 511 keV gamma rays which are emitted almost exactly 180° apart. By using coincidence detectors, no physical collimation is required to determine the line along which the positron was initially emitted, and hence a map of the distribution of the positron emitter within the body can be built up.

The performance of PET systems can be further enhanced by the use of time-of-flight information. If the difference in arrival time of the two almost coincident photons is known exactly, then the position of the annihilation can be located with no further information. In practice, however, the timing resolution of the instrumentation is such that only a rough estimate of the position can be obtained. However, this information can still be incorporated into the reconstruction to improve the signal-to-noise ratio of the system.

It can be seen that the spatial resolution of a PET system depends on the spatial and temporal resolution of the detectors employed. Intrinsic limitations due to the range of the positron and the variations in the 180° angle between the two photons mean that PET has a theoretical resolution limit of ~3 mm [80], which is not realised by the current generation of detector systems.

Considerable interest has been shown in using position-sensitive photomultipliers in PET imaging systems [47,125,139]. Due to the high energy of the emitted photons, relatively thick scintillators must be used to give reasonable detection efficiency. To overcome the poor resolution associated with thick crystals, designs have centred on the use of 'pillars' of BGO which has a relatively high stopping power. Eriksson et al. [47] used a Philips XP4702 multi-anode photomultiplier to view a 6 crystal linear array of 4 × 15 × 25 mm BGO crystals, and concluded that the system could identify which of the 4 mm wide crystals an interaction occurred in. Uchida et al. [139] successfully extended the technique to a 2-D array of 5 × 5 × 20 mm BGO crystals viewed by a Hamamatsu R2486 circular PSPMT. They report an energy resolution of 38% and a timing resolution of 5.9 ns.

It is difficult to improve the resolution in such systems, because as the BGO pillars become thinner, parallax effects can lead to a deterioration in spatial resolution. A later paper by Shimizu et al. [125] suggests one way to overcome this limitation by using a detector with resolution in three dimensions. They used an array of 3 x 5 x 50 mm BGO crystals bundled together and coupled to two Hamamatsu R2487 square position-sensitive photomultipliers, one at each end of the bundle. The resolution in two dimensions is determined by the crystal dimensions, with the spatial resolution in the third dimension (along the bars) measured at ~9.5 mm.

8.5 Conclusions

Position-sensitive photomultipliers were originally designed for use in nuclear medicine and high energy physics, and it is indeed in these areas that the majority of their applications have been.

The range of position-sensitive devices is continually growing, with, for example, multi-anode photomultipliers and PMTs with microchannel plate multipliers. In addition, there is a noticeable trend towards application-specific devices with PMTs available with faceplates designed for the readout of fibre bundles and tubes designed specifically for use in PET detectors.

The increasing number of applications in which position-sensitive photomultipliers are being employed suggests that continued development of this type of device is assured. Already in the few years since they became available, position-sensitive photomultipliers have increased in size from 2 inches in diameter to the latest 5 inch diameter versions with no loss in spatial performance. Additionally, there have been indications from Hamamatsu Photonics that an 8 inch diameter position-sensitive photomultiplier is currently under development, signalling a continuing commitment to this type of device.

Appendix A

PREAMPLIFIER CIRCUITS

A.1 Circuit 1

The circuit shown in Figure A.1 is that of the preamplifier used in the testing of TUBE 1. This is a simple four-channel preamplifier, but was found to be a poor match to the photomultiplier, even following modifications to the input stage. It was replaced by the circuit described in Section A.2, and is included for completeness only.

A.2 Circuit 2

The circuit shown in Figure A.2 is that of the specially built preamplifier - summer - amplifier designed for the tests on TUBE 2. The addition of a summing amplifier facilitates triggering without making modifications to the last dynode connection of the photomultiplier, and furthermore simplifies the subsequent analogue circuitry considerably.

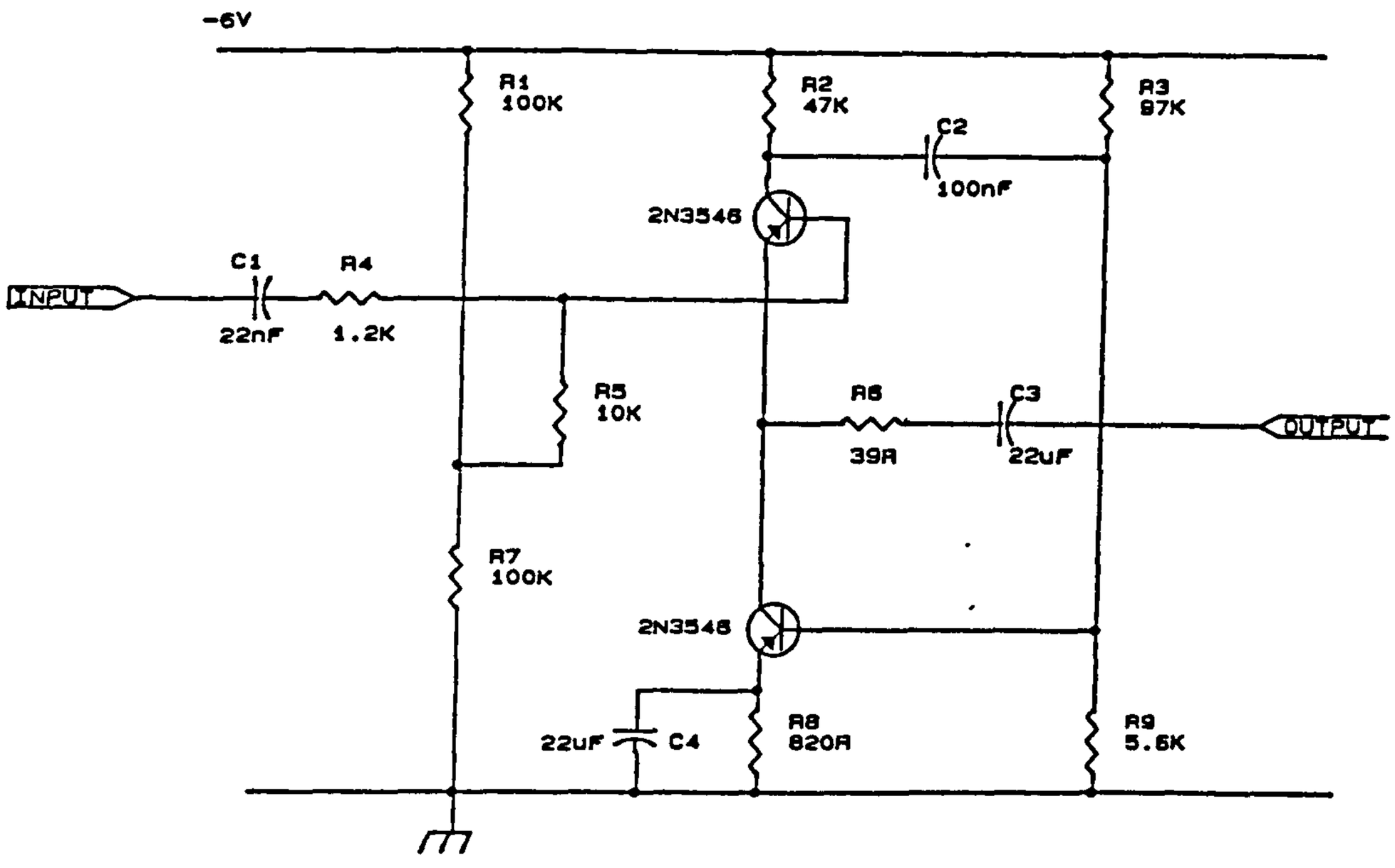

Figure A.1: *Circuit diagram for 4 channel preamplifier used in tests of TUBE 1*

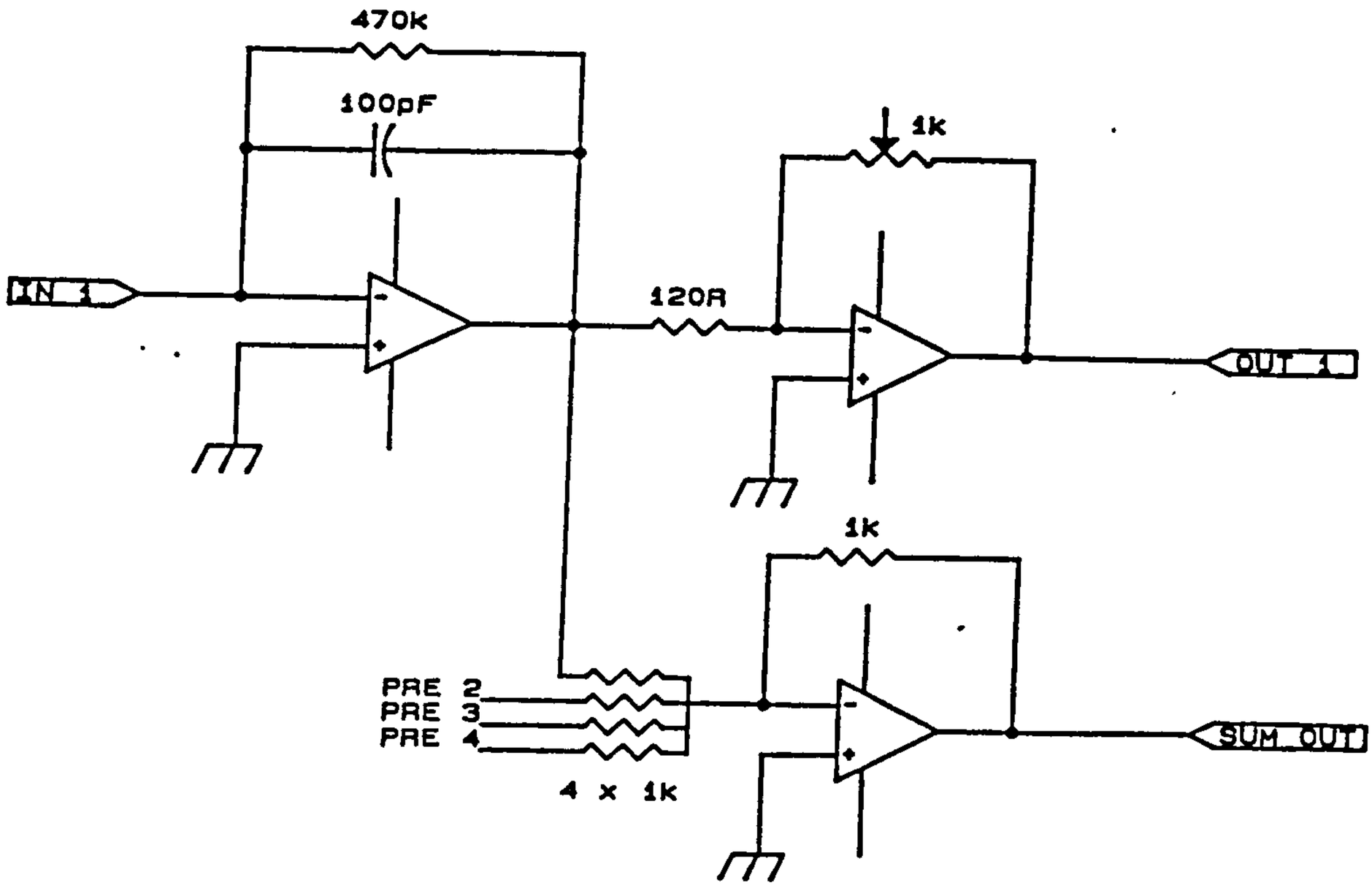

Figure A.2: *Circuit diagram for 4 channel preamplifier - summer - amplifier used in tests of TUBE 2*

Bibliography

[1] *AURIO - Auroral Imaging Observatory.* ESA, 1990. D SCI(90)1.

[2] *Harshaw Radiation Detectors.*

[3] *R2487 series technical data sheet.* Hamamatsu Photonics K.K.

[4] *ROSAT Technical Description.* 1989.

[5] Akimov, V.V. et al. In *Proc. 19th I.C.R.C*, page 330, 1985. OG 9.2-10.

[6] Althouse, W.E. et al. In *Proc. 19th I.C.R.C*, page 299, 1985. OG 9.2-2.

[7] Anderson, D.F. *IEEE Trans. Nucl. Sci*, NS-36:137, 1989.

[8] Andrews, H.C. and Hunt, B.R. *Digital Image Restoration.* 1977.

[9] Anger, H.O. *Rev. Sci. Instr.*, 29(1):27, 1958.

[10] Arnett, W.D. et al. *Ann. Rev. Astron. Astrophys.*, 27:629, 1989.

[11] Aschenbach, B. *Sp. Sci. Rev.*, 40:447, 1985.

[12] Atac, M. et al. *Proc. SPIE - Int. Soc. Opt. Eng.*, 1059:193, 1989.

[13] Baity, W.A. et al. *Ap. J.*, 244:429, 1981.

[14] Baker, R.E. et al. *Nucl. Instr. Meth.*, 228:183, 1984.

[15] Bassani, L. et al. *Adv. Space. Res.*, 3(10-12):219, 1984.

[16] Bateman, J.E. *Nucl. Instr. Meth.*, A221:131, 1984.

[17] Bazzano, A. et al. *Ap. J.*, 279:515, 1984.

[18] Bazzano, A. et al. In *Proc. 23rd ESLAB Symp.*, page 279, 1989.

[19] Bazzano, A. et al. *Nucl. Instr. Meth.*, 214:481, 1983.

[20] Beyerle, A. et al. *Nucl. Instr. Meth.*, 213:107, 1983.

[21] Bezler, M. et al. *Astron. Astrophys.*, 136:351, 1984.

[22] Blake, R.L. et al. *Rev. Sci. Instr.*, 45:513, 1974.

[23] Boutot, J.P. et al. *IEEE Trans. Nucl. Sci*, NS-34(1):449, 1987.

[24] Brownell, G.L. *Nucl. Instr. Meth.*, 221:87, 1984.

[25] Caroli, E. et al. *Sp. Sci. Rev.*, 45:349, 1987.

[26] Carter, J.N. and Charalambous, P.M. *Nucl. Instr. Meth.*, 200:601, 1982.

[27] Carter, J.N. et al. *Nucl. Instr. Meth.*, 196:477, 1982.

[28] Charalambous, P.M. et al. *Nucl. Instr. Meth.*, 221:183, 1984.

[29] Chikkur, G.C. et al. *Am. J. Phys*, 47(8):715, 1979.

[30] Cook, W.R. et al. *IEEE Trans. Nucl. Sci*, NS-32(1):29, 1985.

[31] Cook, W.R. et al. In Morris, M., editor, *The Galactic Center*, 1989. IAU Symp. No. 136.

[32] Cook, W.R. et al. *Ap. J. Lett.*, 334:L87, 1988.

[33] Crannell, C.J. et al. *Proc. SPIE - Int. Soc. Opt. Eng.*, 571:142, 1985.

[34] Cruise, A.M. *Mon. Not. R. Astr. Soc*, 170:305, 1975.

[35] Cruise, A.M. and Willmore, A.P. *Mon. Not. R. Astr. Soc*, 170:165, 1975.

[36] Daniell, G.J. *Nucl. Instr. Meth.*, 221:67, 1984.

[37] Dean, A.J. *Nature*, 308:113, 1984.

[38] Dean, A.J. et al. *Nucl. Instr. Meth.*, A273:711, 1988.

[39] Debouzy, G. *Adv. Space. Res.*, 3(4):99, 1983.

[40] Derenzo, S.E. *Nucl. Instr. Meth.*, 219:117, 1984.

[41] Dicke, R.H. *Ap. J. Lett.*, 153:L101, 1968.

[42] Ditta, J. et al. *Nucl. Instr. Meth.*, A240:69, 1985.

[43] Dotani, T. et al. *Nature*, 330:230, 1987.

[44] Eichholz, G.G. and Poston, J.W. *Principles of nuclear radiation detection.* Ann Arbor Science Pub. Inc., 1979.

[45] Ellison, J. et al. *Nucl. Instr. Meth.*, A260:353, 1987.

[46] Epstein, A. *Ap. J.*, 218:L49, 1977.

[47] Erikkson, L. et al. *IEEE Trans. Nucl. Sci*, NS-34(1):344, 1987.

[48] Fabbiano, G. et al. *Ap. J.*, 316:127, 1987.

[49] Feigelson, E.D. et al. *Ap. J.*, 251:31, 1981.

[50] Fenimore, E.E. *Appl. Optics*, 17(22):3562, 1978.

[51] Fenimore, E.E. and Cannon, T.M. *Appl. Optics*, 17(3):337, 1978.

[52] Finger, M.H. and Prince, T.A. In *Proc. 19th I.C.R.C*, page 295, 1985. OG 9.2-1.

[53] Frank, J. et al. *Accretion power in astrophysics.* Cambridge Univ. Press, 1985.

[54] Fraser, G.W. et al. *Nucl. Instr. Meth.*, A273:667, 1988.

[55] Fraser-Mitchell, J.N. *An imaging detector for hard X-ray astronomy.* PhD thesis, Southampton University, 1988.

[56] Gehrels, N. et al. *Ap. J.*, 278:112, 1984.

[57] Giacconi, R. et al. *Ap. J.*, 230:540, 1979.

[58] Gilboy, W.B. et al. *Nucl. Instr. Meth.*, 221:193, 1984.

[59] Golay, M.J.E. *J. Opt. Soc. Am.*, 61:272, 1971.

[60] Gorenstein, P. et al. *Ap. J.*, 230:26, 1979.

[61] Gottesman, S.R. and Schneid, E.J. *IEEE Trans. Nucl. Sci*, NS-33(1):745, 1986.

[62] Grabmaier, B.C. *IEEE Trans. Nucl. Sci*, NS-31(1):372, 1984.

[63] Grassman, H. *Nucl. Instr. Meth.*, A234:122, 1985.

[64] Grindlay, J.E. et al. *IEEE Trans. Nucl. Sci*, NS-33(1):750, 1986.

[65] Groom, D.E. *Nucl. Instr. Meth.*, 219:141, 1984.

[66] Gull, S.F. and Daniell, G.J. *Nature*, 272(5655):686, 1978.

[67] Hailey, C.J. et al. *Nucl. Instr. Meth.*, A276:340, 1989.

[68] Halpern, J.P. and Tytler, D. *Ap. J.*, 330:201, 1988.

[69] Hanson, C.G. et al. *Mon. Not. R. Astr. Soc*, 242:262, 1990.

[70] Harwit, M. *Astrophysical Concepts.* John Wiley, 1973.

[71] Heath, R.L. et al. *Nucl. Instr. Meth.*, 162:431, 1979.

[72] Hertz, P. and Grindlay, J.E. *Ap. J.*, 278:137, 1984.

[73] Högbom, J.A. *Astron. Astrophys. Suppl.*, 15:417, 1974.

[74] Hull, K. et al. *IEEE Trans. Nucl. Sci*, NS-30(1):402, 1983.

[75] Hurford, G.J. and Hudson, H.S. 1979. USCD-SP-79-27 preprint.

[76] Ishibashi, H. et al. *IEEE Trans. Nucl. Sci*, NS-36(1):170, 1989.

[77] Iwanczyk, J.S. et al. *IEEE Trans. Nucl. Sci*, NS-31(1):336, 1984.

[78] Jackson, P.C. *Radionuclide imaging in medicine: theory & practice.* Farrand Press, 1986.

[79] Johansen, G.A. et al. Scientific/Technical report 186.

[80] Jones, T. *Nucl. Instr. Meth.*, A273:455, 1988.

[81] Kifune, T. et al. *Mon. Not. R. Astr. Soc*, 228:243, 1987.

[82] Kinzer, R.L. et al. *Ap. J.*, 222:370, 1978.

[83] Kitchin, C.R. *Astrophysical techniques.* Adam Hilger Ltd, 1984.

[84] Knight, F.K. et al. In *Proc. 19th I.C.R.C*, page 217, 1985. OG 2.5-7.

[85] Kume, H. et al. *IEEE Trans. Nucl. Sci*, NS-33(1):359, 1986.

[86] Kuroda, K. et al. *Rev. Sci. Instr.*, 52(3):337, 1981.

[87] Kuroda, K. et al. *Nucl. Instr. Meth.*, A260:114, 1987.

[88] Kurz, R. et al. *Nucl. Instr. Meth.*, A273:273, 1988.

[89] Lapington, J.S. et al. *Nucl. Instr. Meth.*, A273:663, 1988.

[90] Lawrence, A. *Mon. Not. R. Astr. Soc*, 217:685, 1985.

[91] Lea, S.M. et al. *Ap. J.*, 246:369, 1981.

[92] Leventhal, M. et al. *Ap. J. Lett.*, 225:L11, 1978.

[93] Levine, A.M. et al. *Ap. J. Supp.*, 54:581, 1984.

[94] Longair, M.S. *High Energy Astrophysics.* Cambridge University Press, 1981.

[95] Lund, M. *Astro. Spa. Sci.*, 75:145, 1979.

[96] Makishima, K. et al. *Sp. Sci. Rev.*, 30:259, 1981.

[97] Makishima, K. et al. Modulation collimator as an imaging device. In *New Instrumentation for space astronomy*, 1978.

[98] Mandrou, P. *Adv. Space. Res.*, 3(10-12):525, 1984.

[99] Markakis, J.M. *IEEE Trans. Nucl. Sci*, NS-35(1):356, 1988.

[100] Markakis, J.M. *Nucl. Instr. Meth.*, A263:499, 1988.

[101] Marshall, N. et al. *Mon. Not. R. Astr. Soc*, 194:987, 1981.

[102] McConnell, M.L. et al. *IEEE Trans. Nucl. Sci*, NS-29(1):155, 1982.

[103] McKee, B.T.A et al. *Nucl. Instr. Meth.*, A273:911, 1988.

[104] Mertz, L. and Young, N.O. In *Proc. Int. Conf. on Opt. Instr. Tech*, 1961.

[105] Mullerworth, S.D. and Ramsden, D. Preprint.

[106] Oda, M. *Appl. Optics*, 4:143, 1965.

[107] Oi, T. et al. *Appl. Phys. Lett*, 36(4):278, 1980.

[108] Palmer, D. and Prince, T.A. *IEEE Trans. Nucl. Sci*, NS-34(1):71, 1987.

[109] Parker, R.P. *Nucl. Instr. Meth.*, 221:221, 1984.

[110] Patt, B.E. et al. *Nucl. Instr. Meth.*, A283:215, 1989.

[111] Pelling, R.M. et al. *Ap. J.*, 319:416, 1987.

[112] Persyk, D.E. et al. *IEEE Trans. Nucl. Sci*, NS-27(1):168, 1980.

[113] Ponman, T.J. *Nucl. Instr. Meth.*, 221:72, 1984.

[114] Primini, F.A. et al. *Ap. J. Lett.*, 243:L13, 1981.

[115] Prince, T.A. et al. Gamma-ray and hard x-ray imaging of solar flares. Preprint.

[116] Riegler, G.R. et al. *Ap. J. Lett.*, 294:L13, 1985.

[117] Rothschild, R.E. *Ap. J.*, 269:423, 1983.

[118] Rothschild, R.E. et al. *Ap. J.*, 250:723, 1981.

[119] Ryzhkov, V.D. et al. *Instrum. Exp. Tech*, 27(5):1045, 1984.

[120] Sakai, E. *IEEE Trans. Nucl. Sci*, NS-34(1):418, 1987.

[121] Salomon, M. et al. *IEEE Trans. Nucl. Sci*, NS-36(1):94, 1989.

[122] Salomon, M. and Marans, J. *IEEE Trans. Nucl. Sci*, NS-33(1):254, 1986.

[123] Schnopper, H.W. et al. *Sp. Sci. Rev.*, 8:534, 1968.

[124] Seller, P. RAL-87-063.

[125] Shimizu, K. et al. *IEEE Trans. Nucl. Sci*, NS-35(1):717, 1988.

[126] Short, M.D. *Nucl. Instr. Meth.*, 221:142, 1984.

[127] Simons, D.G. et al. *Nucl. Instr. Meth.*, A273:512, 1988.

[128] Sims, M.R. et al. *Nucl. Instr. Meth.*, 221:168, 1984.

[129] Singh, M. et al. *IEEE Trans. Nucl. Sci*, NS-36(1):1132, 1989.

[130] Skinner, G.K. et al. *Nature*, 330:544, 1987.

[131] Skinner, G.K. et al. *Nucl. Instr. Meth.*, A273:682, 1988.

[132] Sunyaev, R. *Nature*, 330:227, 1987.

[133] Suzuki, S. et al. *IEEE Trans. Nucl. Sci*, NS-35(1):382, 1988.

[134] Teegarden, B.J. et al. In *Proc. 19th I.C.R.C*, page 307, 1985. OG 9.2-4.

[135] Theinhardt, J. et al. *Nucl. Instr. Meth.*, 221:288, 1984.

[136] Trinchieri, G. et al. *Ap. J.*, 325:531, 1988.

[137] Tucker, W.H. *Radiation processes in astrophysics.* MIT, 1975.

[138] Ubertini, P. et al. *Nucl. Instr. Meth.*, 217:97, 1983.

[139] Uchida, H. et al. *IEEE Trans. Nucl. Sci*, NS-33(1):464, 1986.

[140] Urry, C.M. and Mushotsky, R.F. *Ap. J.*, 253:38, 1982.

[141] van der Klis, M. *Ann. Rev. Astron. Astrophys.*, 27:517, 1985.

[142] Ventura, G. et al. *Nucl. Instr. Meth.*, A226:524, 1984.

[143] Villa, G. et al. *IEEE Trans. Nucl. Sci*, NS-34(4):26, 1987.

[144] Warwick, R.S. et al. *Mon. Not. R. Astr. Soc*, 232:551, 1988.

[145] Watson, M.G. et al. *Ap. J.*, 273:688, 1983.

[146] Watson, M.G. et al. *Ap. J.*, 250:142, 1981.

[147] S. Webb. *The physics of medical imaging.* IOP Publishing, 1988.

[148] White, N.E. *Ann. Rev. Astron. Astrophys.*, 27:85, 1989.

[149] Willingale, R. et al. *Mon. Not. R. Astr. Soc*, 215:295, 1985.

[150] Zhang, S.N. and Ramsden, D. *Nucl. Instr. Meth.*, A273:673, 1988.